Modeling Cable Harness Effects on Spacecraft Structures

Kaitlin S. Spak

Dissertation submitted to the faculty of the
Virginia Polytechnic Institute and State University
in partial fulfillment of the requirements for the degree of

Doctor of Philosophy
In
Mechanical Engineering

Daniel J. Inman, Committee Chair
Gregory S. Agnes
Jeff T. Borggaard
Mary E. Kasarda
Robert L. West

June 20, 2014
Blacksburg, VA

Keywords: Cable Dynamics, Cable Vibration, Bakeout Effects,
Cable Damping, Cabled Structure

Modeling Cable Harness Effects on Spacecraft Structures

Kaitlin S. Spak

ABSTRACT

Due to the high mass ratio of cables on lightweight spacecraft, the dynamic response of cabled structures must be understood and modeled for accurate spacecraft control. Models of cable behavior are reviewed and categorized into three major classes consisting of thin rod models, semi-continuous models, and beam models. A shear beam model can predict natural frequencies, frequency response, and mode shapes for a cable if effective homogenous cable parameters are used as inputs. Thus, a method for determining these parameters from straightforward cable measurements is developed. Upper and lower bounds for cable properties of area, density, bending stiffness, shear rigidity, and attachment stiffness are calculated and shown to be effective in cable models for natural frequency prediction. Although the cables investigated are spaceflight cables, the method can be applied to any stranded cable for which the constituent material properties can be determined.

One aspect unique to spaceflight cables is the bakeout requirement, a heat and vacuum treatment required for flight hardware. The effect of bakeout on spaceflight cable dynamic response was investigated by experimentally identifying natural frequencies and damping values of spaceflight cables before and after the bakeout process. After bakeout, spaceflight cables showed reduced natural frequencies and increased damping, so a bakeout correction factor is recommended for bending stiffness calculations.

The cable model is developed using the distributed transfer function method (DTFM) by adding shear, tension, and damping terms to existing Euler-Bernoulli models. The cable model is then extended to model a cabled structure. Both the cable and cabled beam models include attachment points that can incorporate linear and rotational stiffness and damping. Cable damping mechanisms are explored and time hysteretic damping predicts amplitude response for more cable modes than viscous or structural damping. The DTFM models are combined with the determined cable parameters and damping

expressions to yield frequency ranges that agree with experimental data. The developed cabled beam model matches experimental data more closely than the currently used distributed mass model. This work extends the understanding of cable dynamics and presents methods and models to aid in the analysis of stranded cables and cabled structures.

Dedication

To Stephen, for valiantly enduring our time apart.

The shortest distance between two points is the line from me to you.

Acknowledgements

This work would not have been possible without the generous support of a NASA Space Technology Research Fellowship. Additional funding and support was provided by the Virginia Space Grant Consortium, AIAA San Gabriel Valley Chapter, Bruce J. Heim Foundation, and Southern California Braiding Company, Inc.

A heartfelt thank you to my advisor Dr. Daniel Inman, for being the best advisor a student could have. As I found out, a California girl can't live without her California sunshine, so thank you for your flexibility in my location and your excellent long-distance advising over the years. An even bigger thank you for your nationwide in-person advising, from Orlando to Boston to Waikiki and everywhere in between.

My deepest appreciation to Dr. Greg Agnes of JPL for making a place for me at JPL and mentoring me throughout my research. JPL truly is a unique place, and I would not have traded my time there for anything. Thank you for sharing the experience.

I am exceedingly grateful to Dr. Case Bradford at JPL; no matter how involved my question was, you made time to answer thoughtfully. Sure, your suggestions usually doubled my immediate workload, but I guarantee that you have made me a better engineer and this a better dissertation.

I am also indebted to Dr. Bingen Yang of USC and Dr. Dino Sciulli for their expertise with the distributed transfer function method and their willingness to share that knowledge. I am especially grateful to Dr. Sciulli, who still had his dissertation DTFM code after 16 years!

My appreciation to the countless present and past employees of JPL, NASA, Virginia Tech, and the University of Michigan who helped me along the way, offered support, expertise, entertainment, or encouragement, and went out of their way to get me where or what I needed.

To my family, thank you for your lifelong support. Mom, thanks to you, I never even knew that STEM careers weren't every girl's dream. You were always there, and you helped make me into a person who I would want to be. Dad, thank you for helping me move my half-ton pet to every new endeavor over the past decade, that means more to me than I can say. Thanks for listening to me and laughing with me. Daniel, I do fully expect you to call me Dr. Kaitlin from now on. You all mean so much to me.

Finally, my gratitude to Dr. Jiduck and Dr. Cassio, who were there from the beginning and shared the doctoral journey, and to my friend Mary, who shared the many wonderful rides.

Table of Contents

List of Figures

List of Tables

Chapter 1: Introduction

Cables appear in a wide variety of applications, in an even wider variety of sizes and configurations. From support cables made of steel and used to support thousands of pounds to small shielded copper cables used for the transfer of electrical signals, the analysis of cables has been related to the task at hand; for the support cable, the failure load is of primary importance, while the signal cable is evaluated for its electrical properties. However, as engineers design more complex structures, the luxury and simplicity of evaluating only one aspect of a material is disappearing. In cabled structures, it may soon be insufficient to know just the electrical properties of a cable; cables may be called on to provide structural support, reinforcement, or damping as well as signal or power transmission. To that eventual end, increasing knowledge about the structural properties and behavior of electrical cables and cabled structures is a logical starting point.

The purpose of this research is to investigate the dynamics of cable harnessed structures using experimental data and small-order analytical models with the goal of discovering some of the effects that attaching cables to a structure have on the dynamic behavior of the combined system. In this work, the vibration responses and damping characteristics of spaceflight cables are investigated to characterize the effects of cables attached to space structures, although the methods developed would be applicable to any stranded cables made of multiple constituent materials.

1.1 Motivation

The term “cable” encompasses everything from small twisted-pair wires to massive structural cables used for stabilization of bridges. The vibration of steel cables used for construction stabilization has been studied to prevent structural failure or collapse, but little work has been done to characterize the vibration response of smaller electrical cables, such as those used for signal transmission on space structures. Since advances in material science have increased the strength to weight ratio of structural materials used for spacecraft, the cables and wire harnesses used for space applications make up a much larger mass percentage than in the past, and vibration and movement of the cables can

affect the movement and resonance of the structure as a whole to a much greater degree than in heritage spacecraft. This work is motivated in part by previous attempts to understand the effects of cables attached to satellite structures that have not been particularly successful. In investigating this problem and studying previous efforts it became clear that the cables themselves have been poorly modeled. Hence, a good deal of the subsequent work addresses cable modeling and experimental validation. The addition of the investigated cables to a beam structure is the culmination of the progress achieved in understanding the dynamics of the cables themselves. Analysis of the cabled beam provides a stronger base for future work in the dynamics of cabled structures.

Cables have remained essentially unchanged for the duration of space exploration; although insulation and jacketing materials have been improved to reduce their weight, the conducting metallic core remains comparatively heavy. Space structures have increasingly complex signal and power requirements, so cabling is always present, and cables now make up a significant percentage of the total mass of the structure. Ten percent is a typical design value for cable mass percentage for a NASA flight center, with 4-15% of structure mass made up of cables for several small spacecraft recorded by the ESA Guidelines for Spacecraft Power and Signaling as reported in [1]. In some cases, the cable mass percentage may even be as high as 30% [1,2]. Figures 1.1, 1.2, and 1.3 show a few examples of cable harnessed space structures to illustrate the proliferation of cables across the structure in each case. Figure 1.1 shows a recently assembled spacecraft with significant cabling across its relatively lightweight aluminum panel. Figure 1.2 shows just one section of cabling on the recently deployed Mars Science Laboratory, "Curiosity"; the orange color of the cables is due to the Kapton tape overwrap. Figure 1.3 illustrates the variety of cables that may be found inside a spacecraft, as well as the cable tie attachment method commonly used.

Figure 1.1: Cables of various sizes attached to an interior panel of the SMAP satellite due to launch in 2014. Image courtesy NASA/JPL-Caltech.

Figure 1.2: Kapton-wrapped cables on the Mars Rover "Curiosity". Photo copyright Joseph Linaschke, used with permission[1].

[1] Photo accessed from www.photojoseph.com/curiosity

Figure 1.3: Cables and wires inside the ICESat spacecraft (assembled in 2002), showing the typical cable tie attachment method. Image courtesy NASA/Goddard Space Flight Center, public domain.

Traditionally, cables have been modeled as a lumped mass, where the total mass of the cable was summed and added to dynamic models as a point mass at the center of gravity. In recent years, slight improvements have been seen with distributed mass models. For these models, the cable mass is included by changing the modeled density of a structure wherever a cable is present, or by applying forces based on the weight of the cable. However, since the addition of cables to structures significantly changes both the amount of damping and resonance frequencies of the combined structure through their interaction with the structure at attachment points, it is clear that cables actually act as structural mass rather than lumped or distributed mass. Since space structures are typically controlled remotely without visual confirmation, it is important that models of the space structure reflect its movement and response accurately. In addition, dynamic testing of space structures is often performed before the structure is fully dressed with cables. Knowledge of the vibration response of a structure is necessary both for failure analysis (relevant for events such as launch or deployment), and for developing an accurate control system that relies on dynamic information about the structure.

To model cables on structures, either the insufficient and overly simplistic lumped mass model is used, or structure density is changed in an attempt to distribute the cable mass across the structure along the cable footprint. Neither of these approaches take the bending stiffness or inherent damping of the cable into account. Cable damping is poorly understood; damping mechanisms include friction between the cable wires, material damping within the wires, shear due to the viscoelastic jacketing material, and viscous damping in air, among others. Even the cable properties are difficult to determine, with past research showing that the bending stiffness of the cable varies as a function of wire interaction between layers. There is currently no reliable and predictive cable model to accurately determine the natural frequencies and damping characteristics of a cable by simply inputting geometrical cable parameters and material properties. This is partly due to the poor understanding of the damping mechanisms of stranded cables, as well as the as-built variation in cable sections of the same type and geometric arrangement, and the difficulty in determining global cable properties to begin with. Cable manufacturing can be mechanized to minimize cable variations, but the complicated wiring layouts required for space structures often require hand-built connections, splices, and splits. Hand-built cables show significant variation between test articles [1]. Cable properties are difficult to resolve into a single value for the entire cable; cables have many variables (e.g., lay angle, lay direction, wire material and composition, geometry, and shielding and jacketing material) that make it difficult to generalize results across different types of cables.

Therefore, a cable model that could predict the dynamic response of the cable within a certain confidence interval based on the cable construction and properties, rather than costly and time-consuming testing, would be a valuable tool to incorporate into cabled structure models. The developed cable model would be a valuable addition to the field of mechanical engineering and thus the motivation for this work is established.

1.2 Challenges

Cable terminology spans a vast range of cable applications, with some terms used interchangeably and other terms varying by author or source; since much past research on

cable dynamics was performed for non-conducting structural cables instead of electrical cables, terms such as "wire" and "cable" can be ambiguous. Initial research included identifying common terms for structural and electrical cables and determining where differences were implied. Identifying the similarities between spaceflight cables and wire rope was a significant step in exploring the background research and brought new insights into the current work. The available literature on cable dynamics, structural cables, and spaceflight cables that motivated specific research questions for this dissertation is discussed in detail in the next chapter.

Since cables are not homogeneous but are made up of wires that can move relative to each other, internal damping occurs due to friction. This internal damping is difficult to model, so the first challenge is to model flexible cables, including damping, accurately enough to study the effect of cables on host structures. Previous research shows that shear beam models, which take shear effects into account, are more suitable for cable models then the much simpler Euler-Bernoulli beam model [1,2,3]. This addition of shear increases the complexity of the equations of motion and solution method. One goal of this research is a useful model for design purposes, so a simple beam model is desired, although capturing all of the dynamics that are present is certainly a challenge due to a lack of higher order terms and minimal consideration of nonlinearity. The next challenge is to determine the cable properties for use in the beam model simulations, which assume a homogenous beam material. This is particularly difficult because the space cables in question have great variation in construction and geometry, and past research shows a wide range of bending stiffness values for cables that were meant to be identical [3]. Experience in the spaceflight industry provided suspicion that processes such as the heat and vacuum treatment that spaceflight cables must undergo known as bakeout may also change the bending stiffness. In addition, to prevent end connectors from becoming disengaged, cables are attached to space structures with excess slack, introducing non-linear behavior. As the final challenge, the cable property values will be included in the cable model which will be connected to a structure to yield information on the effects of the space cables on the structure. An additional complication here involves determining the stiffness and damping coefficients of the common cable

connections used in space applications, as this is an unresolved problem from past research on this topic. Throughout the research leading to this dissertation, it has been difficult but valuable to combine methods from several different fields into a coherent model that takes aspects of damping, cable modeling, and space applications into account. Since these aspects come from different fields, the scope of this research has been both broad in terms of background and methods used, and deep in terms of cable investigation.

1.3 Objectives

The focus of this research is to further the knowledge of cable dynamics, including cable frequency response, damping, and effects of cables on host structures. The work comprises both experimental studies and theoretical studies to develop the models and parameter calculation methods.

Although this research began with the intent to model the response of cabled structures, questions quickly arose based on the literature review. Previous studies used dynamic tests to deduce cable properties such as bending stiffness, but experimental testing can be expensive and time consuming; could cable properties be determined in such a way that extensive testing would not be required to predict dynamic behavior of the cable? If cable parameters are determined, could flexible cables be modeled accurately with some form of damping? What type of damping mechanisms might affect cable response? Finally, if cables could indeed be modeled to satisfaction with simple cable measurements, could these cable models be incorporated into structure models to yield useful information about the cabled structure's dynamic response? These questions provided a path forward to expand existing cable literature and build on past research. In addition, questions about determining cable attachment stiffness and reducing cable variation by reducing build-to-build variability were also raised by previous work [1,3].

The initial goal of developing a predictive model for the vibration response of cable-harnessed structures depends on an accurate cable model for spaceflight cables. Surprisingly, no sufficient cable model for this application existed to date, so developing

a damped cable model that could characterize the internal damping and vibration response of spaceflight cables was the first step for this research. However, analytical models are only as good as the model inputs, so this required determining the cable parameters and connection stiffness values to use as model inputs, as well as what type of model would be effective, and what processes (such as bakeout) might affect the cable parameters. Once that model was created, experiments to verify the physical parameters of the cable and validate the cable model were conducted, and, finally, the cable models were combined with the calculated parameters to model a cabled beam system and investigate the effects of cable attachment to a structure.

The objectives of this work are a method for establishing the parameters needed for the model based on the cable material and geometry rather than experimental testing, the development of a novel cable model that incorporates both shear effects and damping, and determination of the effect of bakeout on spaceflight cable stiffness, as well as an overall increase in the knowledge of cable dynamic behavior and the effects of cables on host structures.

1.4 Research Approach

To accomplish the research objectives, the research methodology is composed of the following tasks:

1) Model spaceflight cables
    a) Derive a simple beam-like model to model the transverse bending modes and dynamic response of cables, incorporating tension in the cable, attachment point characteristics, cable geometry, and coupling between bending and torsional modes due to the helical nature of the cable wires
    b) Identify a type of damping that can sufficiently describe the damping characteristics of the cable and incorporate it into the cable model
    c) Use the distributed transfer function method to solve the damped beam model for a variety of cable geometries
2) Perform experiments to characterize spaceflight cables

a) Scan single cables with laser vibrometer to determine the vibration response of single cables and compile a cable test database for widespread use
b) Identify physical parameters of cables, to include effectively homogenous cable parameters for use as beam model inputs through a combination of material testing and measurement
c) Compare different cable construction, geometry, and bakeout treatment

3) Develop a model for a cabled-beam
   a) Compare the experimental cable data and cable model output to confirm that a spaceflight cable model can be used in the cabled-beam model
   b) Input cable parameters based on the previous cable characterization experiments
   c) Determine values for tie-down stiffness and damping coefficients through experimental investigation
   d) Use the distributed transfer function approach to develop the cabled-beam model, incorporating tie down stiffness and cable damping
   e) Run cabled-beam experiments to determine the success and utility of the cabled structure model

Thus, the contributions of this research include a methodology for developing a damped spaceflight cable model, information on the dynamic response and damping parameters of spaceflight cables, development of an a priori method for determining homogenous cable parameters for use in beam models, experimental data for a variety of treated and untreated spaceflight cables, and a model for a cabled beam, as well as a greater understanding of the dynamics and damping characteristics of cables in general.

1.5 Dissertation Overview

Background information regarding previous cable research, the evolution of cable models of various types, and the review of existing literature can be found in Chapter 2. This includes research on structural cables, spaceflight cables, and damping mechanisms. Details about cable terminology, cable construction, and the methods designed to determine effective cable properties are presented in Chapter 3. The model methodology

is developed in Chapter 4, with an overview of the methods used and technical and mathematical background included. The development of the cable model and the cabled-beam model is found in Chapter 4 as well. Chapter 5 presents the experimental work conducted to compile a database of cable vibration responses and determine the effect of bakeout on spaceflight cable stiffness. The results for the cable parameter calculations and resulting cable models are presented and discussed in Chapter 6, as well as the results from the experimental trials, including pre- and post-bakeout comparison and the effect of adding cables to host structures. Chapter 6 also discusses the effectiveness of the cable parameter calculations and contains the comparison between cable and cabled-beam models and their respective experimental data. Conclusions, considerations, and contributions to the field are summarized in Chapter 7. Supporting material, including MATLAB programs and additional data visualization, is included in the appendices.

Chapter 2: Background and Literature Review

The influence of cables on space structures as a structural element is a growing but relatively new concern, and as such, there are only a few published studies that investigate modeling space cables specifically. However, the use and modeling of cables in general has been an increasingly relevant field, and cable dynamics and damping mechanisms are broad topics that have many applications. Combining research from all of these fields is necessary to contribute to cable influence predictions. The focus of this work is on the transverse vibration of cables for resonance considerations, but aspects of cable models used for stress and fatigue calculations were incorporated, so the review of existing cable literature will encompass several types of cable models. Reviews in cable modeling were published by Triantafyllou in 1984 [4], Starossek in 1994 [5], Rega in 2004 [6, 7], Raj and Pathasarathy in 2007 [8] and Spak in 2013 [9].

2.1 Evolution of the Cable Model

The earliest cable vibration models were based on the vibrations of tensioned strings in the eighteenth century. The rise of cable modeling began in earnest in the 1950s when engineers became concerned with both the stresses and strains that cables (or "wire ropes") would experience. It was a short time later that vibration amplitudes of cables became an area of study as well. Through the years, reviews of cable modeling studies have been published, which the reader can refer to for historical relevance. Triantafyllou reviewed the work on the dynamics of a horizontal elastic cable, covering both historical work of the 1600s to 1800s [4] and work from the 1940s through the 1980s [10]. Special note was given to Irvine and Caughey's 1974 work [11] as the point at which elasticity effects on horizontal cable dynamics were fully understood, and this work was cited in many later publications.

Cables were initially modeled as a string in tension [12, 13, 14, 15], which involves an assumption of negligible bending and torsional stiffness, sometimes known as a fiber model. Starossek included damping in work that extended Irvine and Caughey's but focused on a stiffness matrix approach [16], and later published a short review [5] that

presented the basic equations for the string-like cable model developed to date, neglecting any bending or torsional stiffness. However, the stiffness values for bending and torsional stiffness are not actually negligible for cables (especially as the overall cable diameter increases), and efforts to test and model cables using beam formulations began. In 1987 Utting published experimental results for 1X7 cables with varying lay angles that were used as a comparison standard for models as recently as 2010 [17, 18]. A leap forward in modeling came when Velinsky incorporated bending and torsion by modeling the individual wires of a cable as thin rods [19] and generalized that theory for different core geometries [20], and Costello published Theory of Wire Rope [21]. For these models, cable geometry was a major factor, cable bending stiffness was calculated simply as the sum of the individual wire bending stiffnesses, and interaction between the wires was assumed to be frictionless. The thin rod models start by summing the forces on a segment of wire to give six force or moment equations, four of which are trivial. Curvature and torsion are incorporated with the cable properties, and a stiffness matrix is used in conjunction with equations for the forces and moments to give the cable response.

Starting from cable geometry, Chiang used the finite element method to investigate six factors that affect cable stiffness and stress: radius of the core wire, radius of helical (layer) wires, helical angle, boundary condition, strand length, and contact condition between core wire and helical wires [22]. This author's work was unique at the time of publication by also looking at the interactions between the different cable parameters; for instance, in tests of a 1X7 strand, the interaction of the helix angle and boundary conditions was significant. Results compared favorably with several thin rod models.

Sathikh, Moorthy, and Krishnan introduced their thin rod model for helical wire strands with the goal of explaining the lack of symmetry in earlier models [23]. Like Huang's model [24], extension of the cable was taken into account, and there was contact between only the core wire and each layer wire. The test article was a single stiff core with one helical layer, and wire tension, bending and twist were all taken into account. The authors state that the reason for the lack of symmetry in earlier models was because the wire twist and change in curvature were not adequately modeled, which was rectified in

their model through the use of generalized strains based on Ramsey's expressions for strand loading and Wempner's expressions for curvature and torsion. The model agreed with Costello's thin rod model and Utting's experimental strand data [17], although Costello's model matched the experimental data more closely [21].

In contrast to the thin rod models, Raoof and Hobbs [25] and Jolicoeur and Cardou [26] created homogeneous (semi-continuous) models, in which each layer of twisted wire is modeled as an orthotropic complete cylinder with properties that match that of the cable layer as a whole, a process shown in Figure 2.1 Unlike the thin rod models, which follow the same basic method, semi-continuous models utilize a variety of methods, as long as each layer of wires is modeled as a cylinder. With these models, strand stiffness and interwire frictional effects were taken into account. Jolicoeur published a comparative study of these homogeneous cylinder models and found that the Raoof/Hobbs model was simpler to solve and would be preferred for tension or torsion loads, but failed to capture the range of possible bending stiffness, so the Jolicoeur/Cardou model should be used if bending will occur [27]. Raoof and Kraincanic compared the semi-continuous model to thin rod models for helical cable analysis and found that thin rod theory was more reliable for small diameter, fewer strand cables, while semi-continuous models were advantageous for large diameter wire cables [28]. Dreyer compared discrete and continuous models for static hanging cable cases and found that the continuous model was more accurate, but only slightly, and was more computationally intensive to solve [29]. Hover and Triantafyllou investigated the coupling between axial and transverse vibrations using a beam-like formulation and noted that higher *EI* values made a cable more beam-like [30].

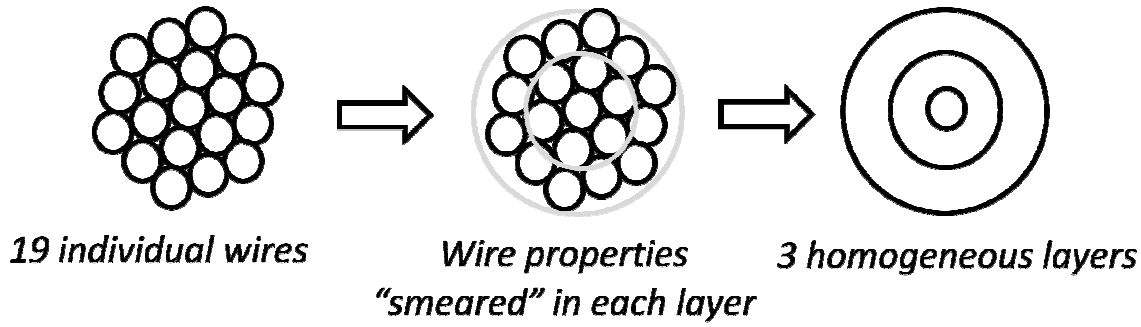

Figure 2.1: Procedure for semi-continuous models in which individual wire properties are averaged or combined over an entire layer to make a model with homogeneous layers to simplify calculations.

The beam model posits that the cable can be described using the equations for the vibration of a solid beam, with damping taken into account either through traditional damping terms that are altered to incorporate the hysteretic nature of cable damping, or through the inclusion of a non-constant bending stiffness, discussed in detail later. This model tends to work well for low-amplitude vibration modeling, as the cable is most beam-like when it has minimal curvature and the individual wires are not sliding and experiencing friction forces.

Although most models dealt with only single-helix wire arrangements, a helical strand that is wrapped into a larger helical cable actually forms a double helix shape as shown in Figure 2.2. Velinsky first investigated this, followed by Ashkenazi [31], Elata [32] and Usabiaga and Pagalday [33]. Velinsky's model calculated the tension and torque in a straight wire, and then calculated those values for a helical strand, taking the additional twist and extension into account. Then, the effect of changes of curvature of a helically wound helical strand (the double-helix) were incorporated by approximating the bending of the helical strand around the core cylinder [19, 20]. Elata went back to the fiber model to investigate the double helix, neglecting both bending and torsional rigidity of the wires, but providing a more accurate kinematic analysis of the double-helix shape which was validated with experimental data [32]. Huang and Knapp presented parametric equations for double and triple helical strands, where a helical strand in one layer becomes the centerline of a strand in the successive layer [34].

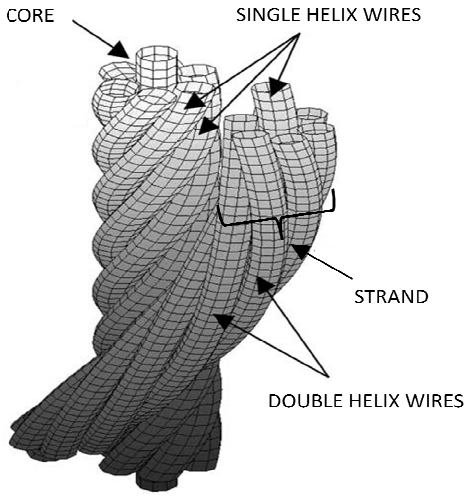

Figure 2.2: Core wire with single helix wires in first layer and core of surrounding strands and double helix wire in first layer of surrounding strands [32].

By the start of the 21st century, nonlinear cable mechanics was under serious investigation. For a detailed overview of the various nonlinear models used for cables, the reader is referred to Rega's 2004 two-part cable review [6, 7]. Rega's review covers almost exclusively cables modeled without bending stiffness and with only viscous damping, and is limited to small sag cables with low vibration amplitudes. [6] covers system modeling and methods of analysis, and [7] covers the nonlinear phenomena present, as well as bifurcation and chaos phenomena. Around the same time, Koh and Rong [35] and Srinil, Rega and Chucheepsakul [36] published work on large amplitude cable vibrations, with Srinil et al. also investigating internal resonance effects. Sun, Wang, and Zhang explored the effects of frictional contact in cables using finite element analysis and concluded that including friction in the model matched the experimental results more closely than a frictionless model [37].

A few dissertations on cable dynamics were published in the early 2000's. Sauter modeled the dynamic characteristics of slack wire cables used in Stockbridge dampers by taking into account quasi-static (velocity independent) hysteresis which is related to the bending moment of the cable [38]. Two students of Knapp wrote theses on the variable rigidity of cables; Zhong [39] and Liu [40] investigated the variable rigidity directly by using a cable software program to predict the hysteretic moment curvature relationship

rather than adding a damping term. Knapp and Liu considered friction between cable layers as a damping mechanism [41]. These are straightforward models that are good starting points for the work in damping which follows.

2.2 New and Extended Models

The semi-continuous approach was extended by Crossley, Spencer and England in 2003 [42]. Built directly on the work of Jolicoeur and Cardou, in which each layer of helical wires is modeled as a cylinder [26], Crossley et al. solve similar problems using a different method. They added bending loads to the axial and torsional loads studied previously, using a method based on stress-strain relations, and extended the work to composite cylinders and multi-layer cables using the same method. Crossley et al. also note that the values for frictionless and bonded cases are quite different, showing the need to model interwire friction to get a more accurate result.

Ghoreishi, Messager, Cartraud and Davies investigated the validity and limitations of several older analytical models by comparing them to an FE model [43]. In the comparison of the stiffness matrix components of nine models, there were two distinct result groups for the axial stiffness as a function of lay angle, both slightly stiffer than the FE model. The group of models that take the change of geometry due to Poisson's ratio into account were slightly closer to the FE results. In the case of torsional stiffness versus lay angle, the different models were not as closely grouped, but were still stiffer than the FE model (with the exception of Hruska's model, which does not take torsional stiffness into account and therefore had poor agreement with all of the other models). Overall, Costello's thin wire model showed the closest agreement to the FE model for both axial and torsional stiffness. Agreement between all models was best for lay angles less than 20 degrees [43]. Ghoreishi et al. also showed that stiffness does vary appreciably for all models for different lay angles.

The method presented by Inagaki, Ekh, and Zahrai takes friction into account [44]. A geometrical model is made assuming infinite friction, and then finite friction is added to

the model to study the transition from the no-slip condition to the full-slip condition. This model is discussed in further detail when friction damping is discussed.

Lacarbonara, Paolone, and Vestroni applied solution methods directly to the equations of motion to yield exact solutions for non-shallow cables, neglecting flexural rigidity [45]. The mode shapes depend on both the geometric and elastic stiffness, and the mode shape trends and behaviors are investigated extensively. Shortly after, Lacarbonara and Pacitti developed a model for cables undergoing both tension and bending using viscoelastic constitutive laws [46]. The authors discuss the inclusion of flexural rigidity as a way to deal with loss of tension in the cable, but noted that more study on the impact of flexural stiffness to cable behavior is needed. They compared response curves of cables modeled with and without bending stiffness, and found that as the cable tension decreases, the difference in the model curves increases. Flexural rigidity must be included to avoid numerical errors arising from low or zero tension cables.

Usabiaga and Pagalday developed a linear model for characterizing double-helix cables, but did not take Poisson's effect causing radial contraction into effect [33]. The authors built on the work of Ashkenazi et al. [31], using the thin rod model and assuming that friction between wires was so high that the wires would not move relative to each other. However, this work added additional kinematic conditions for curvature and torsion calculations. The authors assume that outer wires of the outer strand deform proportionally to the central wire's deformation, which does not agree with the Euler-Bernoulli hypothesis that plane sections will remain plane in each individual wire. Although the Euler-Bernoulli hypothesis is typical of earlier cable models, these authors posit that relaxing the planar requirement will lead to more accurate calculation of the deformation of the double-helical wires. Deformation and rotation results were compared to Costello's models [21], and agreed well enough to justify omitting Poisson's effect, with differences in torque/rotation calculation due to the additional modeling of the double-helical wires. Stress results were compared to Ashkenazi et al.'s results, showing a significant difference when the additional kinematics were included to attach material elements to the helical outer wire strands instead of the straight core. Model validation

with finite element models would be the next step, as the author notes that rigorous experimental work would be complicated and unlikely to yield complete and accurate results for the wire-wire interactions [33].

Of course, finite element models find their way into any field of study; Jiang, Warby, and Henshall developed a finite element model to analyze the complex contacts for wires that contact both the core and their neighboring layer wires under axial load [47]. This is in contrast to Huang's assumption that wires always separate from neighboring layer wires when under tension. Jiang et al. show that if contact deformation is taken into account the wires maintain contact with the adjacent wires in the same layer during tension for wires with specific core and layer radii. They also show that hysteresis must be considered when friction is included in the model. The finite element model requires fewer simplifying assumptions than current analytical models, so local contact, friction, exact geometry, and contact deformation can all be considered. This model is one of the few that specifically investigates both wire-core contact and wire-wire contact. Erdonmez and Imrak also published a finite element model for axially loaded wire rope, taking the double helix geometry, Poisson effect, and contact with both core and neighboring wires into account [18]. Their numerical results showed good agreement with both frictional and frictionless analytical results from Costello [21] and test results from Utting [17]. Jiang published another finite element model using 3D solid elements and compared the results favorably to Costello's model [48]. This model analyzes the stresses in a cable undergoing only bending, but also reverts back to the core-wire only contact that is common to most models. Jiang finds that the contact force between core and wire is negligibly small and thus, different coefficients of friction do not cause noticeable changes in the model. This is in opposition to results obtained by Papailiou [49] and is likely to be due to the idealized nature of the finite element model or the use of Coulomb friction rather than a more appropriate friction model [48]. Shibu, Mohankumar, and Devendiran also used the finite element method to solve equations based on thin-rod theory for a cable under axial tension [50]. They used the theoretical procedure developed by Sathikh et al. [23], but extended it from a core and single layer model to a core and two helical layers. A finite element model was built off of the

theoretical work, and both theoretical and FEM values were compared to published results. The finite element percent differences from values published by Utting [17] were 0.7% and 5% for axial load with fixed and free ends, respectively, but theoretical differences were 20% and 12.5% [50]. The authors found that the end conditions (free or fixed) made a significant difference in the axial rigidity.

Argatov developed a model to include the effects of Poisson's ratio and contact deformation to more accurately predict overall cable deformation [51]. Neglecting interwire contact is common in many previous models, and thus, this model extends the current work since it considers not only wire-core contact, but also contact between adjacent wires in the same layer. The author assumes that the wires remain helical and that tension, curvature and twist remain uniform and constant. Argatov found that the effect of elastic local deformations is small for lay angles less than 15 degrees, and that the deformations are large enough to obscure the Poisson's ratio deformation for lay angles of more than 25 degrees. Just as in Ghoreishi et al.'s findings [43], Argatov found that the agreement for lay angles of greater than 20 degrees was poor [51], and hypothesized that the difference was due to the effect of interwire contact. Frictional effects are neglected in this model, but the work on contact deformation may could be used to apply frictional effects in the future to further study cable damping.

Although the published models can be grouped in a variety of ways, thin-rod models, beam models, and semi-continuous models are recurring cable model types, with some papers focused just on modeling variable bending stiffness, finite element models or purely experimental results. Equations and theory to determine bending stiffness arose as aspects of other models or as equations to be applied to models in place of constant *EI*. Different models incorporate variation in bending stiffness, Poisson effects, different ways to incorporate contact between wires, strain-displacement relations, equations for wire curvature, and calculations of the normal forces between the wire, all of which lead to different final models with different assumptions and varying degrees of complexity.

2.3 Damping of Cable Vibrations

Once cable modeling became sufficiently sophisticated to predict cable motion, researchers began investigating cable damping [52, 53]. Damping was incorporated into existing and new models in a variety of ways to reflect the numerous physical damping mechanisms that contribute to energy dissipation in cables. Damping mechanisms followed the divisions of the existing cable models; thin-rod models used damping modeled as interwire friction, while damping modeled as variable bending stiffness or with a hysteretic damping term was more commonly used in beam models.

One of the earliest investigations of internal cable damping was the work of Yu in 1949 [54]. Yu noted the path-dependent (hysteretic) characteristic of internal cable damping and defined the paths as the space curves of the cable. Yu's analysis showed that only about 5% of the energy dissipation was due to internal solid friction, with the majority of energy dissipation caused by friction between the wires. Experimental data for an un-stretched cable showed damping to be much higher in a cable than in a single wire, and a shorter lay length correlated with an increase in damping capacity. This analytical model assumed a constant bending stiffness, no sag, friction due only to linear damping proportional to tension and constant damping independent of tension, both of which are due to interaction between wires. This initial model worked for small amplitudes and provided a strong starting point for further investigations into cable damping.

An interest in damping of overhead power transmission lines in the 1990s and a desire to mitigate vibrations in support cables spurred further research on cable damping mechanisms [55]. According to Otrin and Boltezar, air resistance, internal material damping, and the friction due to interwire motions were all damping mechanisms that caused energy loss in cable vibrations, and viscous and structural damping models were widely used to quantify this loss [56]. Due to their relative simplicity, linear proportional damping models were and are commonly used in which the damping is proportional to the rate of change of the displacement with the form $c\frac{dw}{dt}$. These models may be sufficient for modeling air resistance as the cable vibrates in air, but the internal damping and friction effects are not adequately captured.

The point of damping models is to describe and quantify the physical energy loss that occurs, so it is important to understand the mechanisms that are causing the losses. It is reasonable to categorize the current models into three major categories by their internal damping mechanisms; damping due to friction between the individual wires and modeled through interwire friction, damping due to changes in the cable geometry and properties and modeled as variable bending stiffness, and damping due to internal friction within the wires and modeled with internal damping or hysteretic terms. In the case of stranded cables, several damping mechanisms may be evident; both imperfection in the wire materials and internal friction between the wires make up hysteretic losses [57, 58]. Cable damping is usually reported as either a log decrement value, a ratio of energy dissipated to energy stored (loss factor), or as a percent of the critical damping value (damping ratio).

2.3.1 Cable Damping Due to Interwire Friction

This type of damping refers to the energy lost due to frictional losses as individual wires in a cable move against each other during cable motion. In an effort to show the presence of friction between wires, Urchegui, Tato, and Gomez studied and characterized the material degradation that occurred between contacting wires, using experimental testing and SEM micrographs to inspect the wear on individual wires in 7X19 steel cable with a polymeric jacket [59]. This work showed that friction wear on the core wire is significant and thus, friction forces indeed dissipate energy in cables. The authors noted that a correlation between wire wear and dissipated friction energy could be developed if the friction force and sliding amplitude between wires could be measured, which would be a valuable contribution to the study of cable damping.

The thin-rod model presented in previous sections, in which each wire is modeled as an individual curved rod, is commonly used for interwire friction analysis. Most of these models explicitly state whether the wires have frictional contact between just the core wire or the core wire and neighboring wires. Figure 2.3 shows an inter-layer contact model of a helical cable with simplified interwire friction and normal forces. One of the

first references to characterize internal wire friction in this way came from Ramsey in 1990 [60], who characterized the motion of individual wires in contact with each other, and then from Raoof and Huang in 1992, whose model gave an upper bound to the prediction of cable damping during bending [61, 62]. Contact forces were studied for both core-wire and wire-wire contact, and a theoretical model to characterize the damping of single-layer strands with axial preload subject to cyclic bending was presented. Kumar and Botsis also studied the contact forces in cables by analyzing the contact stresses, assuming only wire-core contact [63]. The material modulus of elasticity was a major factor in the stresses between wires and since these stresses are related to the contact forces, one can assume that the modulus of elasticity of the cable should be taken into account.

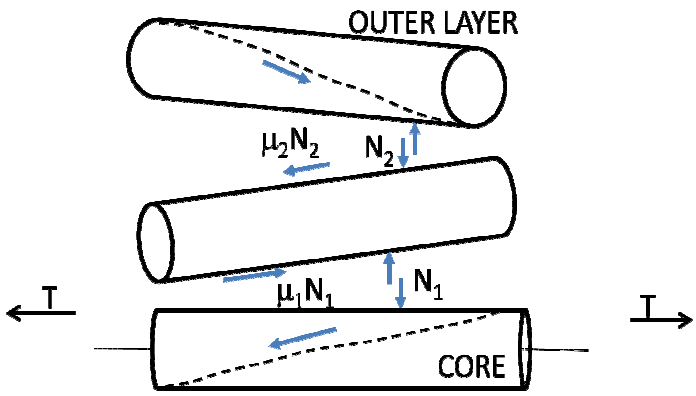

Figure 2.3: Simplified interwire contact forces. Tension on the cable as a whole results in pressure from the outer layer to each successive inner layer, causing normal forces between the wires. Sliding friction between the wires is proportional to the normal force and acts along the line of contact between the wires, shown by the dotted lines.

Models that completely neglected friction were the norm through the 1990s, and when friction was finally included, it was in an "all-or-nothing" sense; these models either assumed perfect slip and no friction, or perfect adhesion of the wires and infinite friction. Chiang ran separate cases for both sliding contact and adhesive contact between the core wire and layer wires using finite element analysis [22], and Jolicoeur and Cardou showed upper and lower bounds based on no slip and no friction cases [26]. Not surprisingly,

Elata, who used a single model with both frictionless and infinite friction cases, found that there was a significant difference in the stress results at the wire level depending on whether friction was included [32]. Usabiaga and Pagalday's model assumed infinite friction, but recommended that friction forces be determined more accurately [33], a common conclusion.

Instead of assuming a constant all-or-nothing friction value, Labrosse, Nawrocki, and Conway studied frictional dissipation in axially loaded strands by modeling the frictionless case first, and then applying a linearized "law of friction" to the thin rod model to study the frictional effects [64]. Damping was calculated as a specific loss per cycle, made up of loss due to both material energy and frictional energy. For a straight and unbending strand, the amount of energy dissipated due to frictional effects was quite small compared to other damping sources. However, although the author mentioned vibration loads, bending was not taken into account in this model, and it is likely that the interwire effects when bending occurs dissipate more energy and thus, increase damping. This model was limited to one layer with layer wires that contacted only the core, but did not assume that slip occurred or that the interwire forces were known and constant. Labrosse noted that interwire sliding occurred along the helical contact lines of the layer cables when the static frictional force was overcome, agreeing with Ramsey's earlier work [60]. He showed that specific loss values increased when cable ends were free, and as the lay angle increased. Labrosse claimed that losses from pivoting friction between wires could always be neglected when compared to losses from viscous damping and friction due to wire slippage.

Since measurement of interwire friction forces was difficult, research continued to analytically predict these forces and incorporate them into models to compare the overall cable behavior to experimental results. Huang was one of the first to model the individual wires of a helical cable separately as they deformed due to extension of the cable, and hypothesized that separation between the helical wires could occur if the cable was stretched [24]. Because the decrease in core area as the cable is lengthened is greater than the decrease in the diameter of the cylinder formed by the helical wires, separation

does indeed occur in some cases. This leads to change in the contact area between wires, which can alter the friction between wires as well as the bending stiffness due to the change in wire geometry. While Huang theorized that this separation would occur in every case, and many models do assume only core-wire contact, Jiang showed the exceptions to that assumption [47]. This research indicated that there should be some way of modeling the change in frictional force or bending stiffness as the cable vibrates or stretches. The variable bending stiffness discussed in the next section addresses these issues well.

In the category of modeling individual wires, a finite element model is worth mentioning here. Zhu and Meguid presented a new finite element to use for slack cables in [65]. Unlike most cable models, Zhu and Meguid departed from the assumption that the cable would have non-zero tension, and used homogenized Rayleigh damping to determine the damping effects of the cable. Their damping matrix takes the form $[C] = \alpha[M] + \beta[K]$. Zhu and Meguid refer to the flexural hysteresis as "flexural damping," supporting the theory that the friction between the wires and subsequent bending stiffness variability contribute to the energy dissipation of a vibrating cable.

Energy dissipation caused by sliding friction often incorporates Coulomb damping, which forms the basis for the following interwire friction damping models. Cutchins, Cochran, Kumar, Fitz-Coy, and Tinker used a Coulomb damping model to investigate the hysteretic loops of cable vibration [66]. Factors influencing the stiffness and damping of their experiments included wire diameter, number of strands, axial tension, and length of the cable. Comparison of experimental and theoretical results showed that the friction force was frequency dependent. At this time in the late 1980s, the damping characteristics of wire rope were not well understood, and design was accomplished through experimentation. The authors hoped that the results they achieved regarding the deformation behavior of the cables would help to model damping in cables due to the friction between wires.

The Coulomb model was quickly found to be limited, however. Raoof and Huang noted that frictional damping models based on a simple Coulomb rigid-plastic dashpot suffered from significant limitations when modeling cables with large radius of curvature, so elastic kickback (some amplitude diminished by elastic deflection of the system instead of transmission to the damper) must be included [61]. This elastic kickback took the form of an additional spring added to the traditional Coulomb model, as shown in Figure 2.4. This damping formulation resulted in a logarithmic decrement of:

$$\delta = \frac{4\left(\frac{aK'}{F_f} - \frac{K'}{K_f}\right)}{\left(\frac{aK'}{F_f}\right)^2 - \frac{K'}{K_f}}$$

where a is the amplitude and K', K_f and F_f are damping values from the damping model shown in Figure 2.4.

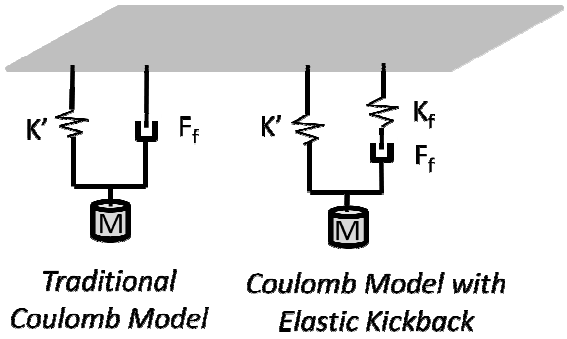

Figure 2.4: Comparison of traditional Coulomb damping model with hysteretic Coulomb damping model.

As mentioned previously, Sauter described the hysteresis and energy dissipation of a Stockbridge damper cable due to interwire friction in detail [38]. Sauter noted that the hysteretic damping mechanism in slack cables was caused by Coulomb friction between the cable wires. Sauter considered the cable as a whole rather than modeling the individual wires, and used a Masing model as shown in Figure 2.5 to evaluate the local behavior of damper cables. The Masing model was made up of linear springs with stiffness k_i and Coulomb friction elements with a maximum sticking force of h_i. This combination of elastic springs and dry friction from the Coulomb friction elements represents the static hysteresis evident in the cable damping, and is similar to the elastic

kickback damping model used by Raoof and Huang [61]. Results showed that slip in the cable was due not only to bending, but to shear effects as well, so a beam formulation which considers shear effects was more appropriate. This was confirmed with Goodding's work on spaceflight cables as well [67], and it is likely due only to the increased complexity of the beam equations that recent models still neglect shear.

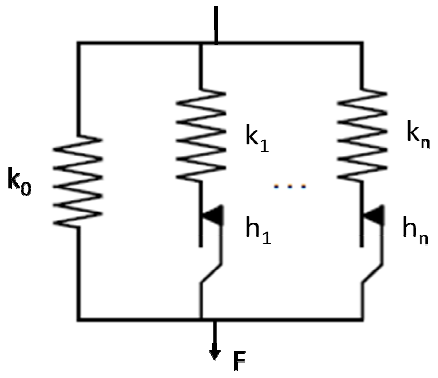

Figure 2.5: Masing-based model used to incorporate frictional damping, where k_i are spring values and h_i are the maximum stiction forces for the Coulomb element.

Trends in the data from elastic kickback models showed that for small radius of curvature, an increase in helix angle reduced damping, while increasing the number of wires or cable strain increased damping [61]. However, for large radius of curvature, an increase in helix angle actually decreased damping [61]. Kumar and Botsis found that small helix angles in the range of $\pm\frac{\pi}{3}$ resulted in larger contact stresses and led to higher damping factors, likely due to the increased contact zone between the wires [63]. A single relationship between curvature, helix angle and damping does not seem possible to formulate for a large curvature range. The authors later presented a method for use in cable design to predict the curvature value at which cable behavior deviates from the no-slip case, the maximum specific loss of the cable, and the axial and torsional stiffness by using different formulas for different scenarios to calculate the effective stiffness [68], but still, no single relationship could be found without incorporating variable bending stiffness.

Although most interwire friction models were based on thin-rod theory, a few utilized semi-continuous models. Raoof and Kraincanic examined helical models based on

orthotropic theory and thin rod theory and concluded that bending and torsion behavior of helical cables was very dependent on the contact between individual wires and layers for both thin-rod and semi-continuous models. For small cables, thin rod theory predictions were more accurate, but large diameter strands with many wires were better modeled with orthotropic (semi-continuous) theory [28]. The semi-continuous model is well-suited to larger cables because the average characteristics for each layer do not become more complex as the number of wires increases, unlike the thin rod model. In an effort to provide information of more practical use, and based on the effectiveness of semi-continuous theory for large diameter cables, Raoof and Davies next focused on specific axial and torsional losses of cables of more than 19 wires and of large overall diameter [69]. An increase in lay angle corresponded to increased axial damping and decreased torsional damping. The authors also noted that old "bedded-in" cables were significantly better behaved for prediction models, likely because the contact zones between the wires were worn in and stable.

In a contrast to calculating the frictional forces first, some authors attempted to find dissipation factors or damping characteristics directly. Otrin and Boltezar looked at vibrations of cables with no axial preload, and determined the dissipation factor [56]. Viscous and structural damping terms were included, with the viscous damping modeled as proportional Rayleigh damping and structural damping included as a dynamic modulus of elasticity, incorporated with the form $c\frac{dw}{dt} + E(1 + \eta i)$. The structural damping model produced results that more closely matched the experimental transfer function results, but still had an error of up to +/-30%.

Rawlins obtained interesting results for damping capacity directly when he compared an analytical model to untreated, pre-stretched, and pre-vibrated cables, respectively [70]. Rawlins investigated the internal damping due to movement between cable strands of cables in transverse vibration, building on work presented by Hardy and Leblond. The analytical model assumed excitation commensurate with wind-induced vibration, damping due only to internal causes (no external fluid damping considered), constant elliptical contact, and constant curvature. The specific damping capacity of the cable is

defined as the ratio of energy dissipated to the maximum energy stored, and when the cable's vibration occurs in sine-shaped loops, the damping capacity calculated using Rawlins' model was:

$$\Psi = \frac{3}{2EI\kappa^2} * f(\psi, C, F, N) + \frac{5}{4EI\kappa^2} * f(A_{elipse}, d, P, \nu, G, \mu, C, F, N)$$

where the first term corresponds to material damping and is a function of the material damping capacity ψ, material compliance C , traction force F, and number of interlayer contacts N, and the second term corresponds to frictional damping and is a function of the area of the contact ellipse between wires $A_{ellipse}$, the strand diameter d, the interwire pressure P, Poisson's ratio ν, modulus of rigidity G, coefficient of friction μ, material compliance C , traction force F, and number of interlayer contacts N. Dissipation of cable energy is difficult to measure experimentally and it is unclear whether the difficulty arises from testing procedures or overlooked cable parameters or geometry [70]. As such, the analytical model was developed to calculate baseline values and test treated cables. Expressions for the dissipation of energy per cycle and specific damping ratio were developed. The model calculated only internal damping, but the experimental damping measurements included fluid-dynamic damping due to the movement of the cable in air, as well as end-point damping from the clamped ends and elongational damping, or loss of energy through the supports due to imperfect longitudinal rigidity there. The author eliminated or corrected for these additional damping values for three groups of cables: an untreated group, a group that was subject to high tension stretch for several days, and a group that was treated with high vibration for at least 24 hours. In comparing the model and experimental data for material damping, the untreated cables measured to calculated damping ratios of around 1, but the pre-stretched cables and vibrated cables had ratios that were much higher than one, and correlation was no better than order of magnitude agreement. Despite the poor agreement between model and reality, the author's discussions and conclusion indicate several factors and mechanisms that should be taken into account for further research, and show the importance of taking cable history (such as past tension or excitation) into account since it clearly leads to varying behavior.

The most recent cable models are comprehensive, incorporating many aspects of the previously investigated models. In 2011, Gnanavel and Parthasarathy published work on the effect of interfacial contact forces in cable assemblies and developed complete models that took both tangential and normal forces into account, modeling each wire as a thin curved rod with interwire pressure, Poisson effect, and Coulomb friction effects included [71]. The authors assumed that the radial contact from the helical strands actually squeezed the core strand when the cable is under load, called the radial contact mode. Previous work showed that core-wire and wire-wire contact occurred only for lay ratios of less than 7.8 (corresponding to 15 degree lay angle), and core-wire contact only occurred for larger lay ratios. A major result of this study was relationships between lay ratios and stiffness and contact stresses: as lay ratio increased, strand axial strain was fairly constant, while contact stresses dropped dramatically but eventually leveled out.

Gnanavel and Parthasarathy [72] next differentiated between different types of contact (lateral contact, radial contact, and the combination thereof) as illustrated in Figure 2.6. Cables were modeled assuming only one contact mode at any given time and then all models were combined. The end result was an overall reduction in stiffness compared to other models that used only one contact mode for the entire loading process. They investigated a cable with combined lateral and radial contact modes, which had core-wire radial contact after a strain level threshold was reached. By including both types of contact and the transition point, Poisson's ratio and slip effects, the authors found a lower axial stiffness and higher torsional stiffness than previous models calculated. It should be noted that friction is necessary for both of these models; using a coefficient of friction of zero leads to numerical errors or an indeterminate problem [51]. These recent models provide a fairly complete study of cable damping due to interwire friction.

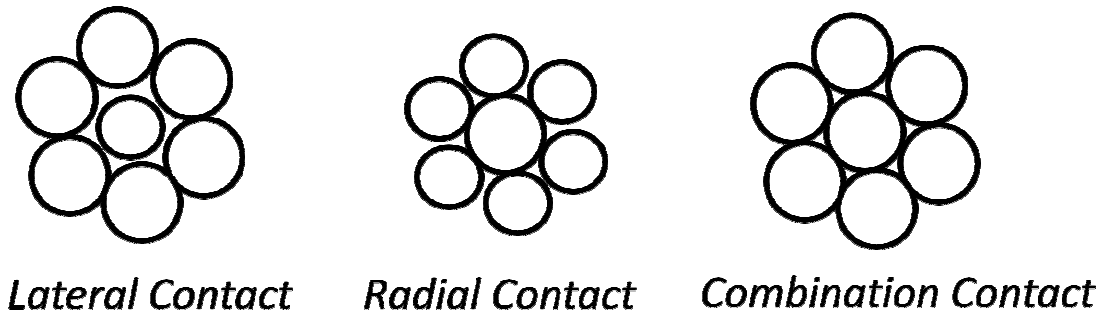

Figure 2.6: Definition of wire contact types used in Gnanavel and Parthasarathy's work [72].

There is no denying that friction plays a role in cable damping, but there are varying opinions about how much effect the coefficient of friction between individual wires has on the damping effect, with Raoff and Hobbs concluding that the maximum specific loss is independent of the coefficient of friction [25], Papailiou finding that the coefficient of friction between wire layers has great bearing on the analysis of conductor bending [49], and Dastous following Papailiou's assumption that the interwire friction forces between wires in the same layer are negligible, and finding little change in the results as the friction coefficient between layers was varied [73]. Ghoreishi et al. showed that overall cable behavior (as opposed to individual wire behavior) was not as dependent on friction [43]. However, each study made assumptions about the value of the coefficient of friction, the calculation of frictional forces, and negligibility of other factors, so the dependency of frictional loss on the friction coefficient (whether between wires or between layers) is not yet conclusive, although it trends towards requiring a friction term but insensitivity to the friction term's specific value. Frictional forces are quite variable depending on the material and geometry of the cable, and measurement of the forces between wires is not trivial. In general, including the coefficient of friction to determine cable bending stiffness (which is related to damping and thus affects the cable behavior) is necessary if the variable bending stiffness of the cable is not taken into account in other terms.

Overall, most models that seek to include the friction in between the wires are based on the thin rod theory, and try to characterize the friction forces to determine the degree of damping. These models are generally useful for stress and strain calculations.

2.3.2 Modeling with Variable Bending Stiffness

Another type of cable damping model involves investigating the changes in bending stiffness that occur if the cable is bent or stretched. A part of this effect is still due to friction, and another part is due to the movement of the wires (i.e., wire rotation). Cables can be modeled as strings, with negligible bending stiffness, or as beams, where bending stiffness is considered. Previously, bending stiffness was just calculated as an aggregate sum of the bending stiffness of each individual wire. However, research has shown that bending cables go through distinct phases of wire slippage [74].

The first phase is the adhesive or no-slip phase, where the friction forces are large enough to keep the wires in place and the cable behaves as a solid beam. Then there is the transition phase, where the static friction is overcome and the wires begin to slip, and finally the full slip phase where the wires have fully slipped to a new position. These transition points are based on curvature, wire size and material, and location of the wire in relation to the neutral axis of the cable. Figure 2.7 shows a representative relationship between bending stiffness and curvature for an arbitrary cable with a constant maximum bending stiffness value until wires begin to slip across each other, approaching a minimum bending stiffness once all wires have slipped. Lanteigne stated that slip occurs at the outer layer first [75], where bending stress is maximum and axial forces are minimum, which agrees with Raoof's experimental observations [25]. References [44, 62, 73, 74, and 76] agree that wire slip commences in the outer layer and that wires that are closest to the cable's neutral axis slip first, and both [74] and [77] agree that wire slippage reduces flexural stiffness. Studies that investigate cable damping through variable bending stiffness rather than calculation of frictional contact forces are investigated here.

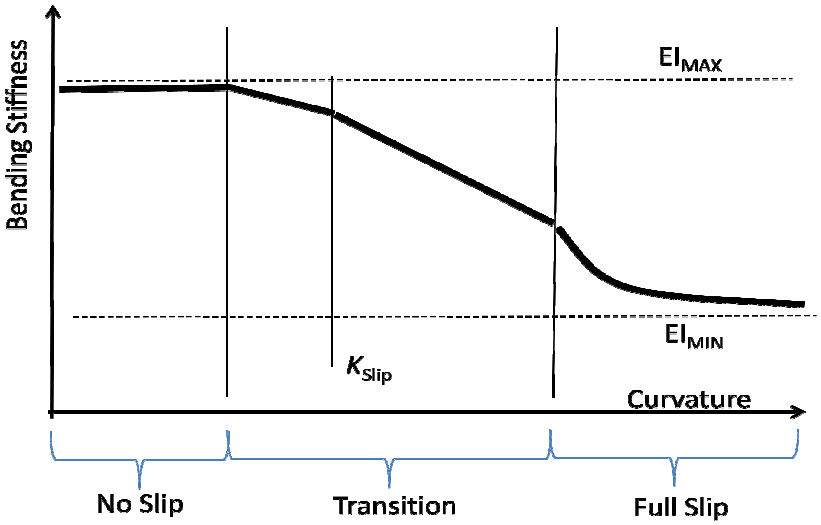

Figure 2.7: Relationship between bending stiffness and curvature; bending stiffness is constant and maximum with minimal curvature when wires are not sliding against one another. Once the wires begin to slip, they enter the transition state, where some wires are slipping and some are sticking; K_{slip} is the critical curvature that represents the average curvature between stick and slip states. When the cable experiences high curvature, all wires have slipped and the bending stiffness approaches the minimum.

Past studies showed that bending stiffness is an important aspect of cable dynamics. As Johnson and Christenson noted, cables have low inherent damping characteristics due to their long span, and high flexibility [52]. These authors were interested in incorporating cable sag, inclination, and axial flexibility, but they ignored flexural rigidity. The model that they developed includes stiffness due to tension, as well as stiffness stemming from the cable sag that only affects the symmetric modes. Johansen, Ersdal, Sorenson, and Leira modeled high-tensile cable without bending stiffness to make a non linear model that could very quickly calculate axial dynamics [78]. The experimental results were smaller in amplitude than the models, and the phase deviations grew over time as well. Neglected damping and neglected bending stiffness were two of the reasons the authors listed as explanations for the disparity in experimental and theoretical results, and it is again clear that bending stiffness is necessary for cable modeling. In a discussion about Jolicoeur and Cardou's paper, Jayakumar, Sathikh, and Jebaraj compared several thin rod models and noted that the only model that did not assume interaction between wires

(loose wire spring model) had vastly different values for both *EA* and *GJ* than all of the other models [79]. It is clear that this interaction between wires and the bending stiffness variation must be taken into account.

Many point to Papailiou for the comprehensive model for variable bending stiffness. In both a paper [49] and thesis [74], Papailiou modeled damping of a cable by characterizing the variable bending stiffness due to the frictional contact between wires under bending and tension. The model calculated bending stress due to the bending of each individual wire around its own neutral axis, but also incorporated additional stress due to the high friction that prevents slipping. Papailiou noted the solid beam behavior at maximum bending stiffness and the behavior of all wires sliding over one another at the minimum bending stiffness value, which is the sum of the individual wire stiffnesses, but went further to quantify a bending stiffness slip value to calculate the additional stiffness as wires moved in relation to each other. Table 3 gives the equations for bending stiffness, showing the relationship between curvature and bending stiffness for the transition region. The model considered the frictional forces between wire and core for single and multi-layer cables, but assumed constant axial tension and neglected friction or contact between wires within layers.

A novel experiment was performed to validate this model in which a laser distance sensor scanned the cable surface as it bent to measure the surface very carefully and construct the cross-section and center point based on that data. The experimental data and theoretical model matched very well. The calculated bending stiffness fell in between the maximum and minimum bending stiffness values for deflection curves and even exhibited the hysteresis that was hypothesized previously. The author noted that the model was sensitive to the lay angles and friction coefficient, but in later discussion, Papailiou provided more detail on the measurement of the friction coefficient and pointed out that the amplitude difference was only about 30% for a near 100% change in μ, so it was important to include, but not sensitive to the exact value. Overall, this model gives a very accurate bending stiffness value and captures much of the physical phenomena that

results in energy dissipation. It is this work that provides the basis for the stranded cable bending stiffness calculation method developed herein.

Hong, Kiureghian, and Sackman extended Papailiou's work to multi-layer structures with varying lay angles, including the nonlinear cable damping due to frictional slip between the wires and modeling the variation in bending stiffness by calculating the tension in the cable as wires slip due to bending [76]. The moment equation derived was $M = (\sum_{all\ wires} EI_i + EI_{core})\kappa_c + \sum_{all\ wires} T_i r_i \cos\alpha_{l,i} \sin\alpha_{h,i}$, where the tension value in each wire was calculated while taking slipping conditions into account. The validity of Papailiou's kinematic assumptions were confirmed, but Papailiou's early hypothesis that large cable curvature would cause the bending stiffness to reach EI_{min} independently of the friction coefficient and wire tension was not true; the bending stiffness approaches a constant value that is dependent on the interwire friction coefficient. The bending stiffness is at a maximum initially when the frictional forces have not been overcome and the wires are sticking, and then decreases as the wires start to slip. Hong et al. found that the difference between the maximum and minimum bending stiffness values could be as large as two orders of magnitude, and that the transition zone between stick and slip states was dependent on the coefficient of friction between the wires and the axial tension (which would contribute to the normal force between the wires, and thus, the frictional force). Discussion of the paper by Cardou and Papailiou allowed the authors to correct a few omissions and discuss a hypothetical "friction moment", which was dismissed as being inconsistent with reality due to the cable's friction propagation being asymmetrical [79].

Papailiou's secant stiffness method was extended by Dastous, who used a tangent stiffness method that provided discrete changes in bending stiffness as curvature changes and specific wires in the cable slip (as opposed to the secant stiffness method which resulted in a smooth curve when bending stiffness versus curvature was plotted) [73]. These discrete *EI* values made the tangent stiffness method more suitable for compatibility with finite element programs. Dastous also made a clear case for considering hysteresis in cable bending. He used a simple viscous dashpot damping

model applied to the rotational coordinate for empirical damping (a sensible choice, representing damping that is directly related to the bending of the cable and thus, the frictional slipping between the wires), but noted that different slipping conditions under higher tension would certainly need a more accurate model based on the physical damping mechanisms. Between Papailiou and Dastous, complete results were obtained for both low and high tension cables.

Inagaki, Ekh and Zahrai mention the different states of bending, namely, when the curvature of the cable is small and all of the wires deform uniformly and behave as a solid beam, and when the curvature is large and the wires slip against one another as the cable deforms [44]. The goal of this research was to calculate the bending response of cables while incorporating the frictional forces resulting from pressure from the jacket and insulation material. A frictional model extended from Papailiou's work was added to a basic geometric model. This model determined the strains at the lowest order helix and then worked outward, emphasizing the response of the cable to bending deformation, which is particularly useful for transverse beam vibration. Contact between neighboring wires within a layer was neglected. Rather than calculating *EI* directly, the authors determined the tensile forces of all wires as a function of curvature and found the bending moment. Experiments showed that the viscoelastic effect from the jacket material was small enough to be neglected. The number of wires that had slipped was plotted against applied axial tension, lay angle, and pressure from the jacket. Clear slip steps were seen as fewer cables slipped at higher jacket pressures, but the decrease in slippage as lay angle and tension individually increased was more smooth and uniform.

Raoof and Huang [62] also investigated wire slippage. They found that plane-section bending stiffness of cables was not constant, and gave upper and lower bounds, with the upper stiffness value being as much as twice as large as the lower bound. This model corrected and extended previous models by Raoof and Huang, based on the method of Lanteigne [75]. Raoof's experimental and theoretical work showed that slipping between wires started at the neutral axis and worked outwards, unless each successive layer had

opposite lay directions, which agrees with theoretical analyses of the thin rod model slippage.

Knapp and Liu opted to investigate cable damping by determining the variation in cable flexural rigidity rather than including a damping term in the equations of motion [41]. One author measured the strains due to bending that arose in a two-layer cable to test a CableCAD software model, and radial pressure within the layers was tested experimentally by measuring the force required to pull one layer out from within another layer. The authors found that no interlayer slip occurred until bending curvature reached a certain point. After this point, the outermost layer began slipping and the moment-curvature relationship increased linearly until the curvature reached the next transition point, at which the inner layer slipped and the moment-curvature relationship continued to increase but at a lower linear rate. This corresponded to a roughly exponential decrease in the bending stiffness of the cable as the cable curvature increased. To incorporate this variable bending stiffness, the authors used a finite element model in which the *EI* value was constant over a small element, but changed for each element. The authors compared their model with variable bending stiffness and experiments to work from Sauter [38] and found good agreement. These authors demonstrated that varying the bending stiffness without including a dedicated damping term is equivalent to including damping due to internal friction in the equation of motion for a cable.

In an investigation of flexural properties specifically, Filiatrault and Stearns tried to determine the bending stiffness of cables and found that the maximum bending stiffness occurred under high-tension, low-curvature conditions [80]. The authors compared their experimental results to secant conductor flexural stiffness values as well as the theoretical maximum and minimum flexural stiffnesses. This work identified the minimum stiffness as the sum of the bending stiffness of each individual wire $\left(EI_{min} = E\sum_{all\ wires}\frac{\pi d_{wire}^4}{64}\right)$ and the maximum stiffness as the bending stiffness of the cable as if it were a solid wire $\left(EI_{max} = E\frac{\pi d_{cable}^4}{64}\right)$. They calculated the maximum stiffness at about 100 times the minimum stiffness, which agrees with Hong, et al.'s findings [76]. They also found that

hysteresis effects were negligible for the static loading case, but increased when the cables were under high tension or large curvature. The authors hypothesized that the energy lost is due to friction between the wires rather than internal damping in the cables. High tension also made the cable more like a solid beam, with wires sticking rather than slipping. The authors compared their analytical and experimental values to the IEEE standard for the effective flexural stiffness of conductors where $EI_{eff} = (1 + number\ of\ strand\ layers) * EI_{min}$ and found that the IEEE recommendation is a higher bound on the real flexural stiffness.

While the variability in bending stiffness arises largely from the frictional forces from interwire contact, modeling the variability in bending stiffness rather than the frictional contacts may be a straightforward way to include damping in cable modeling.

2.3.3 Damping Due to Internal Friction and Viscoelastic Effects (Material Damping)

As discovered by Yu [54], internal damping is generally very small, but it should be considered in an exploration of internal damping mechanisms. Since most power and signal cables have insulation, investigation into insulation material damping should be incorporated to cable models as well. Today's electronics require shielded wires which may be covered with a viscoelastic insulation material with very different shear and elastic properties from the interior wire.

Yamaguchi and Adhikari investigated the increase in damping effect due to the inclusion of a viscoelastic damping layer around the outside of a cable, similar to an insulation layer [81]. The authors hypothesized that even minimal shearing through the added viscoelastic layer would increase damping. Using the Ross-Ungar-Kerwin theory and incorporating both axial and bending stiffness, they estimated loss factors for the damping-treated cable and compared them to the cable without the viscoelastic damping layer. The structural cable used in this study had a lay angle of 3-4 degrees, was wrapped in filament tape, and surrounded with a polyethylene outer cover (which was assumed to add no damping). The authors found that the viscoelastic layer did increase damping, primarily for the higher modes. Axial and bending loss due to the additional damping

layer were of the same order for a soft outer cover, but the bending loss factor could be significantly higher if a stiff viscoelastic layer was used. Yamaguchi and Adhikari continued this work by using an energy approach to evaluate the modal damping of cables with and without viscoelastic layers and investigated the relationship between jacket material and damping further [82]. They found that variation in the cable sag ratio caused significant differences in the damping ratio for both jacketed and unjacketed cables. Stiff viscoelastic material was most effective for damping of the first mode, but soft material must be used to increase damping in higher modes. Damping was not increased by a large amount due to the viscoelastic layer used in the study, but the authors presented several options to decrease the initial potential energy and thus, increase the modal damping, such as increasing the sag ratio or increasing the loss factors by changing the material or viscoelastic layer thickness. Barbieri, de Souza, and Barbieri extended the work of Yamaguchi and Adhikari to develop a reduced damping matrix [83]. Using search gradient and complex envelope techniques, they found damping ratios for the first five natural frequencies, and found that the damping ratio increased with increasing length and decreased with increasing tension.

Shear deformation losses may occur in the wires themselves as well as the cable jacket. Yu said that internal wire friction was very small compared to the interwire friction, but he also dealt only with steel cables, not jacketed cables [54]. Inagaki et al. found that the viscoelastic effect from the jacket was too small to change the overall results, but did incorporate the changed pressure on the wires due to the compression caused by the jacket and insulation [44]. It seems that more study is needed to completely characterize how and why cable insulation would change the dynamic response of a cable.

Many authors compared models to experiments to validate the models, but to truly validate, rather than calibrate, a model must be able to predict the cable behavior, not merely match it. Castello and Matt used verification and validation techniques to investigate the suitability of a simple homogeneous beam model to predict the frequency response of an overhead transmission line cable [84]. The authors cited the variability in bending stiffness and damping values as major obstacles for the use of the simple beam

model. They used an Euler-Bernoulli beam model with additional terms for tension, aerodynamic proportional damping to represent external damping (usually omitted in other models), and Kelvin-Voigt damping to represent viscoelastic internal material damping: $c_\xi I \frac{\partial}{\partial t}\left(\frac{\partial^4 w}{\partial x^4}\right) + c_\alpha \frac{\partial w}{\partial t}$. The cable used for the experimental data was about 1" thick, quite dense (more than 1.3 kg/m), long spanning, and low sag. Estimates for the bending stiffness, and alpha (external) and zeta (internal) damping parameters were calculated from the experimentally determined frequency response function, and then investigated using the methods of verification and validation. The authors found that, for a very specific narrow frequency range and given tension value, the simple model could be used to predict the time and frequency domain dynamic responses. The fact that this simple model predicted the cable response well when more complex models do poorly may be a result of the type of cable used, as a thick, single strand ACSR cable with low sag is undergoing very little bending curvature, which is what causes much of the frictional variability that gives such uncertainty for other models. Continued work on the verification and validation of cable damping models, as well as investigation of the properties and responses of different cable families, will certainly lead to more reliable and useful models.

In space, there is no supporting medium, so it is primarily internal damping that affects the system's motion. Thus, damping terms that arise from the internal movement and friction of the cable are of greatest consideration. However, because the experiments for this work were conducted in air, a viscous term was included in the model to more closely mimic the experimental results.

2.4 Dynamics of Spaceflight Cables

The literature review up to this point deals with cables in general; the past research focused on structural support cables or high tension overhead power lines. Electrical cables were not previously investigated due to their comparatively small size and the lack of precision applications requiring the mechanical properties and interactions between the cables and their host structures. However, space structures are unique in that they are both lightweight and have high precision requirements, so the addition of cables actually

does change the overall dynamics of the structure. Any structure intended for space flight undergoes much simulation and testing. Modal testing determines the resonant frequencies of the craft, or which excitation frequencies would cause the structure to vibrate uncontrollably. These frequencies are then noted and avoided or the structure is altered to change the resonant frequencies. Modal testing is often performed before the structure is fully dressed with the cables required for flight, and cable effects are currently incorporated by simply adding the mass of the cables as a single lumped mass at the center of the craft or by changing the structure density along the cable path to add distributed cable mass. The existing research on space cable dynamics was performed largely by the Air Force Research Laboratory (AFRL), resulting in a significant body of work. The AFRL undertook a study of the dynamic interaction between cables and space structures, and found that power and signal cables were incorrectly overlooked/ignored in the design and modeling of precision spacecraft, since these cable effects can be significant. Based on research from the Air Force Research Laboratory it is no longer sufficient to model cables as lumped mass [2], and flight tests showed that addition of flight cables can shift modal frequencies and cause significant increases in modal damping ratios [85]. As the field of material science advances, the materials used for space structures have become lighter weight, which is advantageous because lighter payloads are less expensive to send into orbit. The overall structure may be lighter, but the signal and power requirements are just as complex, if not even more sophisticated, requiring the same or more power and signal cables as previous spacecraft. As such, cable harnesses are making up a greater percentage of the total spacecraft mass, making up 4-15% of a structure's mass [1] and in some cases, as much as 20% [3] or 30% [1,2]. As the cable mass ratios increase, the effects of the cables become more significant. In addition, studies have shown that cables are acting in a structural capacity, adding damping and actually changing the expected resonant frequency of the system [86, 87]. The combination of a greater mass percentage and the behavior of cables as structural, rather than inert elements, make it evident that the effects of cable harnesses on space structures require greater study.

The control of a space structure relies on very precise knowledge of the structure's current position and response to propulsion systems. According to Space Vehicle Design, components for attitude determination and control of a spacecraft are demanding of "specific orientation, alignment tolerance, field of view, structural frequency response, and structural damping" [88]. Thus, since the addition of cables changes the structure's frequency response and damping, characterizing these effects is necessary for precise control of the structure. In addition, once cable damping can be accurately quantified, additional damping treatments may be rendered unnecessary if the cable damping is sufficient to prevent unwanted vibration.

The initial AFRL investigation revealed no definitive existing works on the subject of spaceflight cable effects, and only a single standard for cable attachments among five aerospace agencies [87]. Initial testing showed that the addition of cables to a structure certainly changed the structure's dynamic response, but modes were damped irregularly, if at all, and the overall conclusion was that a "simple" beam with a cable is not simple after all [87].

With the intent to quantify the effect of cables on space structures, Goodding et al. developed methods to test and model cables to determine tension and bending stiffness under transverse vibration [3]. In a departure from the typical large aluminum and steel cables usually modeled, the electric and signal cables tested were of low linear mass and under very small amplitude excitation and thus required specialized test set ups and sensitive data acquisition devices. This extensive study developed algorithms for the second area moment of inertia, shear factor and shear modulus product based on a frequency response test of the cable. A finite element model using the experimentally obtained cable parameters and calculated values was validated with experiments. Similar cables showed a high degree of variability in their experimental behavior, most likely due to the hand-made construction. The skill and attention of the technician making the cable was also noted elsewhere as being a major consideration for cable uniformity [89].

An Euler-Bernoulli beam model was used for initial modeling. To determine cable parameters, axial and lateral vibration tests were performed and estimated effective cable diameters were found to be 30-35% of the actual physical diameter [67]. This study and others also showed that elementary beam theory was not sufficient for a realistic cable model [67, 90]. Later work by Babuska et al. modeled the transverse vibration of cables with the equations of shear beams, with all of the beam parameters treated as independent quantities, not linked to the physical cable diameter or through Poisson's ratio [1]. Cable damping was included in the FE model as basic structural damping. Cable parameters were determined through axial vibration tests, but significant variability was found within each cable family, despite having the same person make all of the test cables. This work also addressed the issue of the connection tie-down stiffness for the typical aluminum TC-105 tabs and nylon cable ties used for cable attachment, referred to as "tie-downs" throughout this work. The tie-down stiffness was evaluated in several ways, but direct measurement underestimated the value badly, and more work is required to empirically determine the tie-down stiffness.

The next paper in the series extended the previous work to tests of 3-6% cable mass fractions attached to a plate panel rather than a beam [2]. Based on this and the previous works, there was a clear frequency regime where the cables act as lumped mass, a transition section, and then a frequency regime where the cables become resonant and add damping. In simple cases, like a narrow beam, the transition section is small, predictable, and straight forward, but not so with panels. This paper provided insight into the different cable models; shear stiffness was important to model cable dynamic behavior, but neglecting rotational inertia had little effect [2]. As far as cable parameters for modeling purposes, area was based on the frontal area of the copper in the cable, modulus of elasticity was calculated from axial test data, and the moment of inertia and modulus of rigidity were calculated from lateral bending tests. Again, basic structural damping was included and the tie-down characteristics were again found to take a major role. When testing was performed, the addition of cables did not change the mode shapes of the panel to a large degree. In addition, the resonance frequencies were not

significantly different, but this was explained by the fact that the cable mass ratio was much lower than typical.

Through this study series, cable modal damping was also investigated and found to average about 4% of critical as a viscous damping mechanism, although this varied from 1.8% to 4.9% depending on cable type and specimen [3]. The authors attributed deviation in the damping ratio to the lack of consistency in the cable construction due to non-mechanized cable manufacture. Experimental data showed that lower modes had larger relative motion and higher damping ratios, consistent with the hypothesis that motion between wires causes the greatest energy loss. Kauffman, Lesieutre, and Babuska also investigated damping in cables as it applies to spacecraft wiring and used a time domain, geometric rotation-based viscous damping model (based on [91]) to generate damping coefficients and compare them to existing experimental results [92]. This model was based on an Euler-Bernoulli beam with an additional transverse shear term included that shifted the resonant frequencies lower. The damping term described two internal shear forces representing the rate of change of the bending angles for the shear angle and beam: $V_v = -c_\beta \dot{\beta} - c_\varphi \dot{\varphi}$. This damping model was less frequency-dependent than previous models for the low frequency bending regime, and increased linearly with mode number in the high frequency shear regime.

Investigators at the NASA Marshall Space Flight Center also investigated the effect of cable harness assemblies on space structures; specifically, their interest was on the level of damping of a launch vehicle panel due to cable bundle installations. Initial testing of cable bundles added to the panel did increase damping [93]. The authors determined the damping parameter by optimizing a developed finite element model with a viscous damping parameter with the experimental data. This work was extended to test more cable bundles, with total bundle mass ranging from 2.37 to 21.21 pounds, giving cable mass ratios of 8.5% to 76% [93]. Of particular interest was the result that including cables on the panel resulted in greater panel damping than including a lumped mass equivalent to the cable mass. The panel response was highly dependent on measurement location, especially at low frequencies. The MSFC group also noted nonlinear behavior

in several frequency bands and found critical damping ratios to be as high as 0.08, but also noted that the modeling approach could be improved and that some of the unexpected results required further study.

Knowledge about the effects of spaceflight cables has increased from essentially nothing to results from multi-year projects staffed by teams of experts from major research labs in less than a decade. However, a consistent result from these sources was that there are still many unknown or poorly understood factors that must be investigated to complete the predictive capabilities of cabled structure models.

2.5 Literature Review Conclusions

The breadth of cable literature required careful sorting to determine the useful and applicable information. Of course the work on spaceflight cables specifically is invaluable, but several conclusions from different cable fields are worth highlighting as well. First of all, several sources note that modeling cables as a shear beam is possible for both general cables and spaceflight cables specifically. It is also clear that a cable model must include bending stiffness, and some term or mechanism to model the damping that is inherent in cables of all types. Lay angles should be restricted to 20 degrees or less for best results, and the larger the overall cable size, the more effective a beam model is for predictive uses. Cables with insulation behave as viscoelastic materials. The work to date shows that further research is required in the areas of cable parameters, cable damping and cable attachment point modeling.

A major contribution of this work is bringing together the many aspects of cable modeling to yield a coherent dynamic cable model. The current work on spaceflight cables will be extended in this dissertation by expanding the available experimental data, developing a method to calculate cable properties from basic measurements rather than dynamic testing, and improving the tie-down attachment models, as well as introducing more complex damping mechanisms into the cable model.

Chapter 3: Cables

The cable models surveyed in the previous chapter are used for many types of cable analysis, from internal force calculations to prediction of deformation. Although there are many methods to model cables, for modeling the dynamic response of a cable, a beam model has distinct advantages in terms of simplicity and effectiveness. For vibration analysis, beam models are well-studied and provide a way to incorporate the semi-continuous approach to model a stranded cable as a homogenous structure by careful calculation of the parameters used in the equations of motion. Therefore, modeling a cable as a homogenous beam is the method used herein to model dynamic cable behavior. This chapter discusses the considerations for modeling cables as beams, introduces cable terminology and the specific cables investigated, and presents the methods for calculation of cable parameters to be used in cable models.

3.1 Cables as Beams

Using a beam model is relatively straightforward and provides useful dynamic response data that can incorporate tension, internal damping and connection points. Beam models do not require determination of internal friction forces directly, but instead rely on effective beam properties such as bending stiffness and viscous damping to capture the frictional effects. Thus, determining these parameters to accurately portray the dynamic response is important. The simplest beam model is the Euler-Bernoulli model, which assumes plane sections of a beam remain plane, but for a flexible cable with viscoelastic insulation, the cable stretches and plane sections rotate, so shear effects must be included. In a shear beam model, the equation of motion contains information about the cable characteristics; specifically, the coefficients of the equation of motion include the density, area, bending stiffness, and shear term. To use a homogenous beam model to predict the behavior of a decidedly un-homogenous cable, effective parameters must be determined. As all spaceflight cable models to date have been created with cable parameters determined from dynamic response data, the calculation of cable parameters based purely on basic static measurements is a contribution that may prove useful in preliminary

spacecraft and cable design, as well as any other application that requires dynamic information about a cabled structure.

3.2 Cable Terminology

Since cable terminology differs from field to field, this section serves to define the common terms used in this work to describe spaceflight power and signal cables. A core wire surrounded by layer wires is known as a strand. Cables have a core wire or strand surrounded by helically twisted wires or strands in successive layers. Cables are designated by an "m X n" numerical designation where m is the number of strands and n is the number of wires in each strand. For example, a 7X7 cable has seven strands (a core strand and six surrounding layer strands), with each strand comprising a core wire and 6 layer wires as shown in Figure 3.1 with the core and strand labeled in the end view. A 7X19 cable would have seven strands as well, with each strand made of a core wire with 6 wires in the first layer and 12 wires in the outer layer (for a total of 19 wires per strand) as Figure 3.2 illustrates. Most cable models investigate a single strand. Cables made up of wires in multiple small strands (multi-stranded cable) are more flexible than cables made up of a single strand (single-stranded cable) with the same total number of wires.

One important characteristic that is unique to stranded cables and wire ropes is the lay angle. The lay angle is the angle that the layer wires make with the core; cable lay angles generally range from 2.5 to 35 degrees, with most mathematical analysis of cable behavior departing from reality beyond 20 degrees [43]. Helix angle and lay ratio (ratio of wind-to-twist, or length for a wire to make one full turn around the core wire) are different but also commonly used ways to quantify the amount of twist that the layer wires have around the core wire. For this work, the lay angle is used, measured in degrees and converted to radians for calculation purposes. Cables may be helical or contra-helical; a helically twisted cable has all layers wrapped in the same direction, while a contra-helical cable alternates the wrapping direction with each successive layer. The contra-helical cables are very slightly heavier, but remain straight while a helical cable will revert to a curved relaxed state. Figure 3.3 illustrates the difference between a helical cable, which hangs with a curve, and a contra-helical cable, which hangs straight

down. The core wire may be the same diameter as the layer wires, or larger, to prevent the layer wires from touching each other when the strand is unstressed. The assumption of contact between each layer wire and the core only (as opposed to each layer wire touching not only the core, but also its neighboring layer wires) is an important feature of the various friction models. Further details on cable and wire rope construction can be found in Feyrer [94].

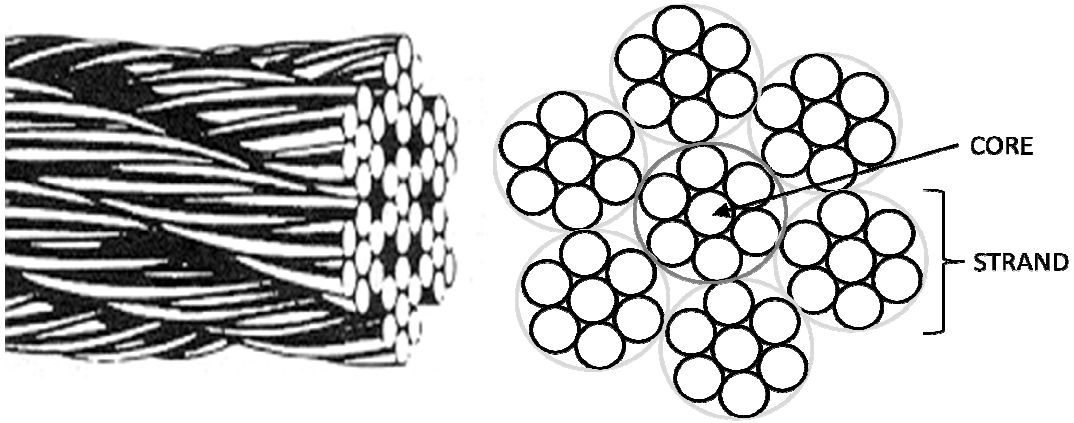

Figure 3.1: 7X7 cable side view and end view with core labeled and individual seven-wire strand identified; side view reprinted with permission from VER Sales.

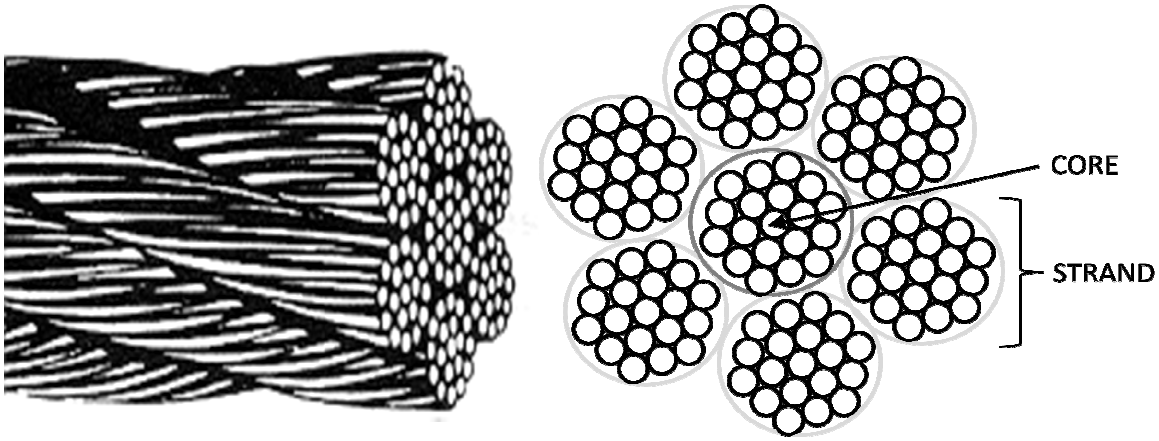

Figure 3.2: 7X19 cable side view and end view; side view reprinted with permission from VER Sales.

Figure 3.3: Evidence of inherent curvature in helical cable; in contrast, contra-helical cable hangs nearly straight.

A cable is meant for transmission of forces or signals. Cables can be categorized as either mechanical wire cables (wire ropes) for guy wires and structural use, electrical cables for signal transmission, or optical fiber cables. Mechanical wires transmit forces between locations, while signal cables transmit electrical signals [22]. Mechanical wires may be subject to much higher stresses than signal cables, while signal cables may have greater requirements for minimal vibration. Cables may be subject to axial forces causing tension, torsion, and lateral forces causing bending. Vibrations from the cable's surroundings, such as wind, water, or equipment vibration, can also cause bending and cable vibration. The outer layers, rather than the core, take most of the axial force [21]. An applied axial tension causes tension in the helical strands which causes them to apply inward radial force to the layers within [70]. Good cable models take into account the critical design factors for the specific use of the cable and make assumptions that reasonably describe the cable's properties and behavior.

3.3 Cable Component Wires and Configurations

Much of the research on cable properties deals with aluminum conductor steel reinforced (ACSR) cables as shown in Figure 3.4. But unlike ACSR cables, which are made completely of solid metal wires drawn from one material, the cables used for space

structures are generally made of an aluminum or copper core surrounded by flexible EMI shielding and some type of electrical insulation.

Figure 3.4: Aluminum conductor steel reinforced 1X37 cable, courtesy of General Cable.

Preliminary investigations were performed with an insulated 1X18 helically twisted cable made of MIL27500-26TG2T14 wires. All of the subsequent cables used in this study were also made with MIL27500-26TG2T14 wire. This wire, commonly used for space applications, consists of two 26AWG twisted wire pairs individually insulated, an EMI shield made of tinned copper, and outer Tefzel (ETFE) insulation layer. Figure 3.5 shows the components that make up the individual wires that are bundled together to make the cable.

Figure 3.5: Deconstructed cable wire, from top to bottom; Kapton wrapped cable, individual wire, and wire components: EMI shield, two 26AWG twisted wire pairs, and wire filler label.

The wire has a left hand lay and is shrink-wrapped with the Tefzel insulation, so there is an evident twist to the wire, making the wire oval in shape rather than circular. Wire size measurements were taken from published values when possible [95] and verified with actual measurement. Upon discovery that the helical twist added permanent curvature to the cable which made the frequency response dependent on the orientation of the cable in the test fixture, the contra-helical twist method, in which each layer has an alternating lay direction, was used for all subsequent test cables. The cable configurations used for test data were five sections each of 1X7, 1X19, 1X48, and 7X7 configurations, as shown in Figure 3.6, all made of the same MIL27500-26TG2T14 wire insulated with Tefzel.

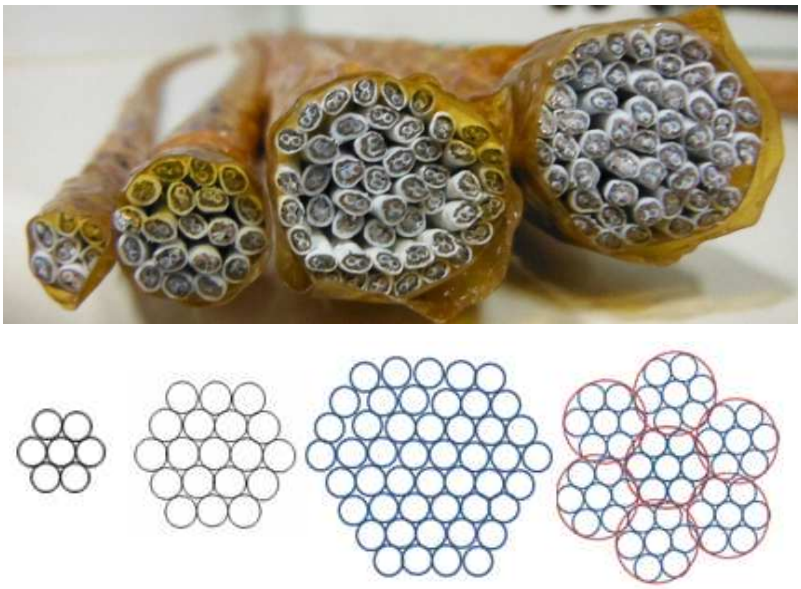

Figure 3.6: 1X7, 1X19, 1X48 and 7X7 spaceflight cable sections and the associated wire configuration diagrams.

All of the test cables were made on a planetary machine to ensure uniform construction, since previous studies noted that variability in human construction technique was evident [89] and it was desirable to eliminate this source of variation. After the wires were twisted together in the appropriate configuration, they were tied every 4-6 inches and machine wrapped with Kapton tape with a 50% overlap. The Kapton overwrap is designed to keep the wires together snugly, but is not applied with significant force. The Kapton overwrap was assumed to add no additional stiffness other than keeping the cable wires in radial contact.

The smallest cable, a 1X7 single-strand, was about 7 mm in diameter and quite flexible. The medium size 1X19 cable was similar in size to the 1X18 preliminary test cable, was about 13 mm in diameter, and had three layers, with one, six, and twelve wires in each successive layer. The two large cables were both about 22 mm in diameter (approximately one inch), but the 1X48 cable was much stiffer and more like a solid beam than the 7X7 cable. The 1X48 cable did not have a full outer layer; one, six, twelve, and eighteen wires in the full inner layers and eleven wires in the outer layer makes a total of 48 wires, a configuration chosen to correspond to the size and wire count of the multi-stranded 7X7 cable. The 7X7 cable consists of a core 1X7 strand surrounded by six more 1X7 strands twisted around the core for a total of 49 wires. Multi-stranded cables are used to provide greater flexibility, and this increased flexibility was indeed observed in the multi-stranded cable over the single stranded cable of similar size.

3.4 Property and Parameter Calculations

Modeling a spaceflight cable as a homogenous beam requires input parameters of area A, density ρ, bending stiffness EI, (comprising both the modulus of elasticity and moment of inertia), and shear rigidity κAG. To predict the cable response, these values must be correlated to cable and wire properties such as modulus of elasticity and rigidity, cable geometry, and construction, which forms the basis for this section of investigation. Bending stiffness is particularly important, since it can vary with cable curvature, tension, and wire slip. The work on stranded ACSR cables provided a sound starting point for cable parameter calculation, but because most power and signal wires include several different materials within each wire, composite material methods had to be introduced for these purposes. Up to this point, cable properties for beam models were determined by running dynamic tests and then working backwards to yield the appropriate mass and stiffness terms. Ideally these parameters would be determined simply by using the geometry and constituent materials of the cable, without using complicated equipment or having to measure individual cable sections. To show that this is possible, direct calculations for each parameter were developed, and maximum and minimum parameter values were determined. Models using these parameter ranges were compared to extensive dynamic testing with the objective being to bound the range of cable responses

with the model responses. Table 3.1 gives the average basic measurements for each cable type. Note that these observations required only basic measuring tools (scale and ruler or calipers) with no sophisticated testing required. Figure 3.7 shows the overall relationship between the measured inputs, material properties, and calculated values that will be presented here.

Table 3.1 Cable parameters measured or observed for each cable.

		1x7	1x19	1x48	7x7 (multi-strand)
Number of Wires	N	7	19	48	49
Number of Layers	n	1+core	2+core	3.5+core	1 layer of six 1-layer strands + core strand
Number of Strands	N_S	1	1	1	7
Mass	m	0.0708 kg	0.1905 kg	0.4481 kg	0.4944 kg
Length	L	0.7692 m	0.7782 m	0.7744 m	0.7744 m
Lay Angle (radians)	β	0.3417	0.2873	0.3217	0.3037
Outer Diameter	D	0.0074 m	0.01272 m	0.0204 m	0.0216 m

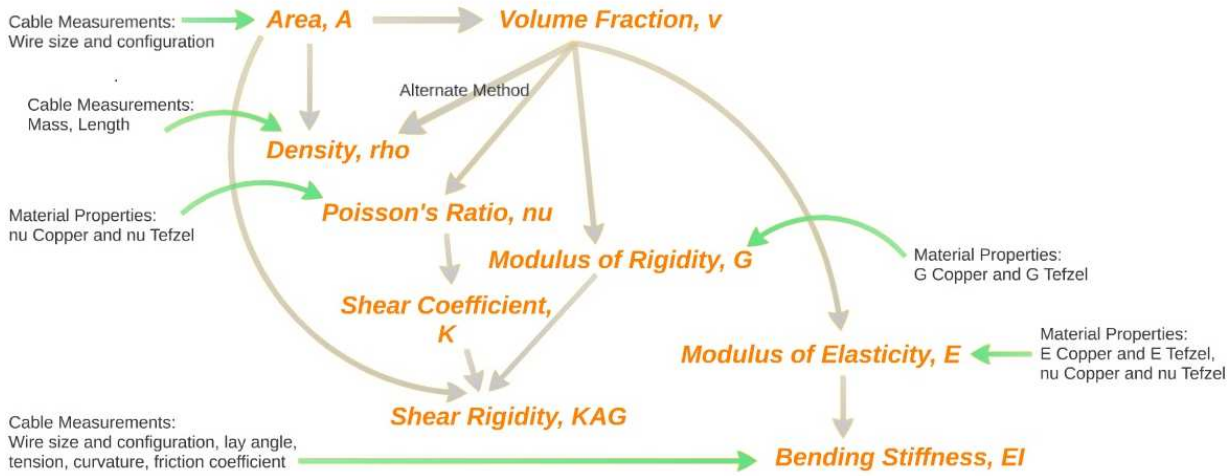

Figure 3.7: Relationships between and inputs for cable property calculations to determine cable parameters $\rho, A, \kappa AG,$ and EI used to model a cable as a beam.

In the figure, green arrows represent inputs from material properties and cable measurements, and grey arrows represent the resulting calculations. Area is calculated first, using information about the wire size and configuration, which yields values for

density and volume fraction. Copper and Tefzel material properties of Poisson's ratio and shear and elastic moduli are input to calculate the wire Poisson's ratio and then the wire shear and elastic modulus. Area, Poisson's ratio of the wire to get the shear coefficient, and the wire modulus of rigidity are combined to yield the cable's shear rigidity. Finally, the wire size and configuration, lay angle, tension, curvature, and friction coefficient are combined to calculate the bending stiffness for the beam equation from the wire moduli.

3.4.1 Wire Component Material Properties

The wires are made up of essentially two components: copper, which makes up the conductor cores and EMI shielding, and Tefzel, the insulation for interior and exterior wires. Table 3.2 shows the material properties used for the copper and Tefzel of the investigated cables. These values are used in subsequent calculations to determine the overall wire properties.

Table 3.2 Material properties for cable components.

Property	Copper	Tefzel
Poisson's Ratio	0.343	0.46
Modulus of Elasticity	110 GPa	1.2 GPa
Modulus of Rigidity	45 GPa	0.41 GPa
Density	8930 kg/m^3	1700 kg/m^3

3.4.2 Area

A section of cable used for the preliminary testing was disassembled into the two 26 AWG twisted pairs, shielding material, and Tefzel coating, as shown in Figure 3.5, and each component was measured and compared to published wire specifications [95]. There are three defendable ways to calculate the area parameter of the cable: the overall area as calculated based on the outer cable diameter, an over-estimation; the overall area of the wire as calculated based on the outer wire size, multiplied by the number of wires; and the sum of the area of the individual copper and Tefzel components, which is an under-estimation. These calculations provide maximum, middle, and minimum values for the area parameter. Examination of the wire used shows that the twisting lay of the two 26 AWG wires inside makes for an elliptical wire shape overall. Calculating the area of the wire using this elliptical shape for the EMI shielding and outer Tefzel jacketing

(rather than a circular shape) resulted in a smaller parameter range and increased agreement between experimental and model data. In the following equations, *d* indicates wire diameter, r_x and r_y indicate the x and y axes radii of the elliptical wire shape (essentially either 1/2 or one times the diameter of the 26 AWG wire plus the thickness of the shielding plus the thickness of the jacket), and *D* indicates cables outer diameter, measured from crown to crown (widest point).

$$A_{min} = N * (2 * (area\ of\ copper\ cores + area\ of\ 26AWG\ jackets) + area\ of\ EMI\ shield + area\ of\ outer\ jacket)$$

$$A_{mid,circular} = N * \left(\pi \left(\frac{d}{2}\right)^2\right)$$

$$A_{mid,elliptical} = N * (\pi * r_x * r_y)$$

$$A_{max} = \pi \left(\frac{D}{2}\right)^2$$

Figure 3.8 shows an idealized circular layout of the wire with measurements used for initial calculations, and Figure 3.9 shows the elliptical layout with the same 26 AWG wire size and shielding and jacketing thickness. Note that Figure 3.8 and Figure 3.9 are not to scale. Table 3.3 provides the resulting area calculations for the four different cable types.

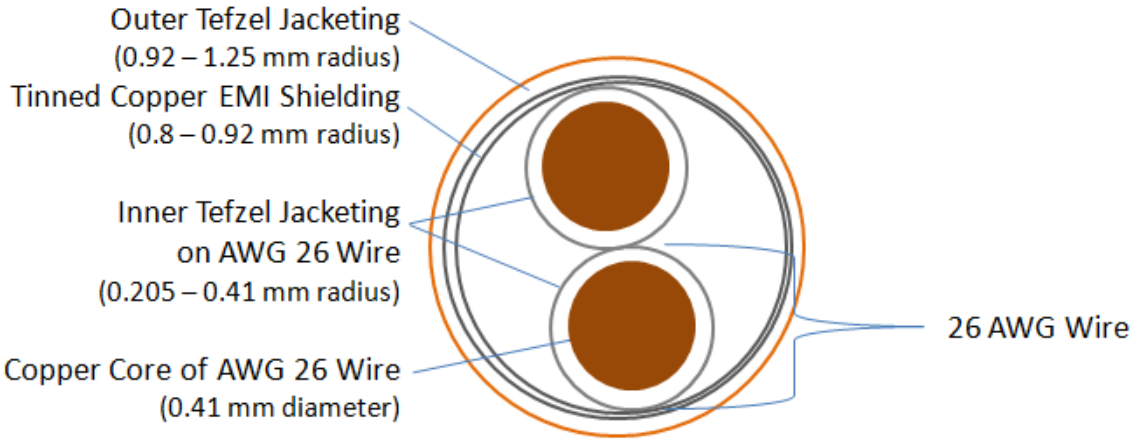

Figure 3.8: Idealized circular internal anatomy of MIL27500-26TG2T14 wire used for circular wire area calculations.

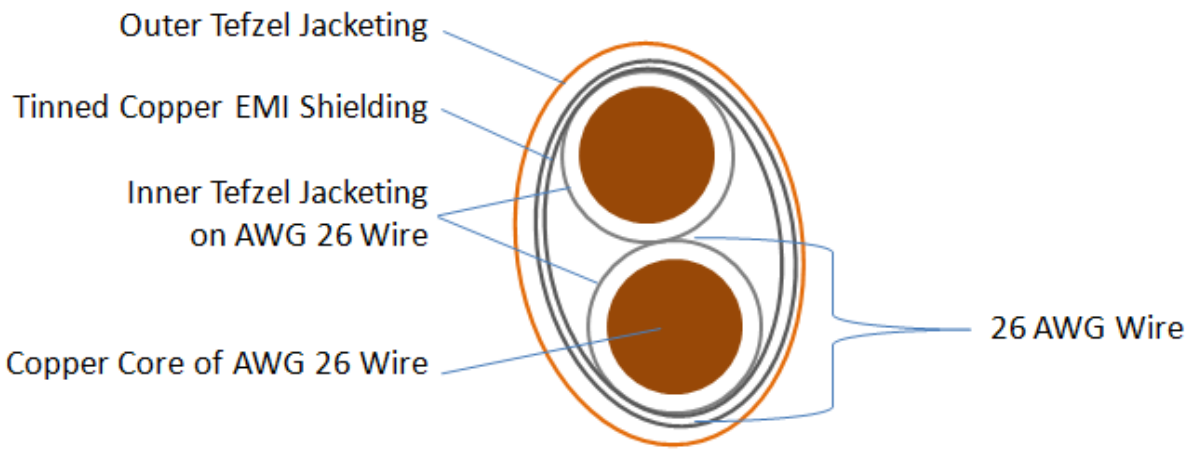

Figure 3.9: Elliptical internal anatomy of MIL27500-26TG2T14 wire for elliptical area calculations.

Table 3.3 Area calculations for four cable types, in m^2.

	1X7	1X19	1X48	7X7
A_{max}	4.35E-05	1.27E-04	3.27E-04	3.66E-04
$A_{mid,circular}$	3.44E-05	9.33E-05	2.36E-04	2.40E-04
$A_{mid,elliptical}$	2.95E-05	8.03E-05	2.03E-04	2.07E-04
A_{min}	2.77E-05	7.51E-05	1.90E-04	1.93E-04

The area calculation is also used to determine the volume fraction used for many of the subsequent calculations. These expressions depend on the volume fraction of the copper in the wire, which was calculated by dividing the copper area (based on the area of the wire conductors and tinned copper shielding) by the area of the wire as a whole as determined by either its outer diameter or the sum of the component areas. Since the materials have the same length, volume fraction for each material can be determined by dividing the area of each material by the total area. Again, there are multiple approaches to this calculation that make sense: one way is to use the total area of the wire in the denominator, which takes voids in the wire into account, and another way is to sum the component areas for the denominator, which assumes a wire without voids. Initially, these were calculated assuming that the wire was circular, but using an elliptical wire shape matched the physical wire and resulted in less variation between the two methods,

which in turn reduced the overly large range that resulted from a first round of calculations [96, 97]. Table 3.4 lists the volume fraction results for each approach. Note that volume fraction is calculated for a single wire, and is therefore the same for each cable since they are all made of the same type of wire.

Table 3.4 Volume fractions used for cable property calculations.

	With Void Space, Circular Wire (Material Area / Circular Wire Area)	With Void Space, Elliptical Wire (Material Area / Elliptical Wire Area)	With No Void (Material Area / Sum of Material Areas)
Copper	0.185	0.216	0.231
Tefzel	0.620	0.720	0.769
Void Fraction	0.194	0.064	0

3.4.3 Density

Density calculations for the cables could be calculated for each cable using the measured mass and calculated areas, or through a rule of mixtures (RoM) approach, which would yield the same density for all cables. Density was determined by weighing the cables and dividing the total mass by the volume, where the area was chosen to correspond to either the overall area, yielding a minimum density, the area calculated by summing the area of the wires, or the area calculated by summing the measured components comprising the wires, yielding a maximum density.

$$\rho = \frac{mass\ of cable}{area\ of\ cable_{min,\ mid\ or\ max} * cable\ length}$$

Thus, the smallest ρA value is given by using the maximum area to get a minimum density. Previous work assumed all cable parameters to be completely independent of each other [1,2], but since area calculations would be used to determine the density, this author felt that consistency throughout the calculation was necessary.

Density could also be calculated using a rule of mixtures approach. The rule of mixtures is a weighted mean used for multi-component or composite materials to determine overall properties based on the component properties. For this calculation, all cables would have

the same density since all of the cables were made of the same wires and have the same volume fraction. The cables were transversely loaded, so the lower bound for the rule of mixtures is used, given by

$$\left(\frac{vf_{Cu}}{\rho_{Cu}} + \frac{vf_{Tefzel}}{\rho_{Tefzel}}\right)^{-1} \leq \rho_{cable}(RoM)$$

where vf_{Cu} and vf_{Tefzel} could be the volume fraction calculated with or without voids as described in the previous section, and the density values are the published values for pure copper or pure Tefzel as indicated. Those values were within the limits of the mass and volume density approach for all other cables, with the exception of the minimum value for the 1X7 cable. Table 3.5 presents the density values for both methods.

Table 3.5 Density values calculated for each cable, in kg/m^3.

Density Term	1X7	1X19	1X48	7X7
ρ_{min}	2117.1	1926.5	1770.5	1742.3
$\rho_{mid,elliptical}$	3110.6	3049.7	2853.7	3084.1
ρ_{max}	3323.4	3258.4	3048.9	3295.0
ρ_{min} (RoM)		2090.6		
ρ_{max} (RoM)		2233.6		

The density calculation was verified experimentally by using Archimedes's principle; a short section of 1X18 cable was weighed in air and then weighed in water as shown in Figure 3.10, both immediately after submersion and several days after submersion. The immediate result was 2163 kg/m^3, and after waiting for 72 hours to allow the water to permeate every void of the cable, the result was 2557 kg/m^3. These were both within the range of the similarly-sized 1X19 cable density calculations using cable mass and areas and RoM, which lent confidence to these density calculation methods. Since the rule of mixtures approach resulted in density values that were within the range of all other cables, the mass and volume density calculation technique was used for maximum and minimum ρA values, except for the minimum of the 1X7, which used the RoM minimum value.

Figure 3.10: Cable in water for measurement of density based on Archimedes's principle of buoyant force.

3.4.4 Concentric Composite Wire Properties

The real contribution here comes from the calculation of the modulus values. Obviously, a stranded cable is quite different than a homogenous beam. The existing ACSR research only considered wires made of a single material, so for an insulated and shielded wire made up of several components, additional calculations are required to determine the single modulus of elasticity term for a single non-homogenous wire. The field of composite materials yielded useful approximations for wire properties; specifically, the individual wires that make up the cable could be modeled as a concentric cylinder composite, in which the copper conductor takes the role of the strengthening fiber and the Tefzel insulation takes the role of the matrix. Since the Tefzel insulation is tightly bonded to the conductor, the wire can reasonably be considered a composite material. Modulus values were based on a modified rule of mixtures for parallel fibers in a concentric matrix [98]. These expressions depend on the volume fraction of the copper and Tefzel in the wire, calculated for maximum and minimum values as described previously.

To determine the wire modulus of elasticity, the concentric composite model uses the core material as the fiber and the surrounding material as the matrix, so for cables, copper is the fiber and Tefzel is the matrix. For a beam in bending, the longitudinal modulus of elasticity is required, given by

$$E_L = v_f E_f + v_m E_m + \frac{2(\nu_f - \nu_m)^2 E_m E_f v_f (1 - \nu_f)}{E_m(1 - \nu_m)(1 - \nu_f - 2\nu_f^2) + E_f((1 - \nu_m - 2\nu_m^2)v_m + (1 + \nu_m))}$$

Note that the Greek letter ν, representing Poisson's ratios, and the symbol v for volume fraction look very similar in the elastic modulus equation and must be distinguished carefully. Using the two volume fraction cases results in the upper and lower bounds for the base longitudinal modulus for a single wire. However, this expression applies for straight parallel fibers; in the case of a twisted conductor pair, the modulus of elasticity is reduced by as much as 10% [98]. Thus, a 0.9 factor is included in the wire elastic modulus to take into account this fiber curvature effect. The minimum and maximum values for the wire modulus of elasticity are determined by using the volume fractions with and without voids, respectively.

The shear modulus of a composite consisting of parallel fibers in a concentric matrix is given by

$$G = \frac{\left((1 + v_f)G_f + (1 - v_f)G_m\right)G_m}{G_f + G_m - v_f(G_f - G_m)}$$

where v_f is the volume fraction of the fiber and G_f and G_m are the shear moduli for fiber and matrix, respectively, where the copper acts as fiber and the Tefzel acts as matrix. This shear value is used for the cable as a whole. The cable model is relatively insensitive to the shear modulus value; it is important that the term be included, but large changes in *G* yield only small changes in the frequency response.

Poisson's ratio for the cable is required for the calculation of the shear coefficient κ, and is also calculated from the concentric composite model using

$$\nu = \nu_m - \frac{2(\nu_m - \nu_f)(1 - \nu_m^2)E_f v_f}{E_m(1 - v_f)(1 - \nu_f - 2\nu_f^2) + \left((1 - \nu_m - 2\nu_m^2)v_f + (1 + \nu_m)\right)E_f}$$

where v_f, ν_f and E_f are the volume fraction, Poisson's ratio, and the elastic modulus of the fiber (copper), and v_m, ν_m and E_m refer to the same properties for the Tefzel matrix. Note that the symbols for volume fraction and Poisson's ratio must be carefully distinguished. Table 3.6 gives the calculated wire properties from the concentric composite model, with the values based on the volume fraction with or without void space making the minimum or maximum value. These values form the basis for the shear and bending terms to follow.

Table 3.6 Wire material properties calculated using concentric composite model.

	With Elliptical Void	No Void
E_L with straight fiber	24.6 GPa	26.3 GPa
E_L with curved fiber	22.1 GPa	23.6 GPa
G	0.63 GPa	0.65 GPa
Poisson's Ratio, ν	0.433	0.431

3.4.5 Shear Rigidity

At this point, calculated parameters include maximum and minimum values based on two methods of volume fraction calculation for the wire modulus of elasticity, the wire modulus of rigidity, and the wire Poisson's ratio. These properties can now be combined to build the remaining cable parameters required for the beam model. The importance of shear effects for cables was noted by several sources [2, 3, 84, 90], and it is the inclusion of the shear terms rather than the exact shear term value that is significant. The developed cable model is relatively insensitive to the specific shear value, but is very sensitive to whether it is included. The shear rigidity term κAG requires the calculation of κ, the shear coefficient, as well as area and modulus of rigidity. The shear coefficient represents the distribution of the shear stress profile across the cross-section of a beam. Reference [99] focuses on shear coefficient calculation for circular shear beams, and gives the equation for shear coefficient of a circular beam as

$$\kappa = \frac{6(1+\nu)^2}{7+12\nu+4\nu^2}$$

where ν is Poisson's ratio. For the wire Poisson's ratio limits, the result for κ is 0.9517 and 0.9514, so the rounded value of 0.95 is used for all calculations. This is higher than the typical Timoshenko value of 0.9 for a circular beam, indicating that more shear is occurring in the stranded cable than a typical solid beam, which seems reasonable. The concentric cylinder model values for the modulus of rigidity are combined with area calculations and the shear coefficient to determine the shear rigidity term.

Although further investigation could refine this value based on the interaction of individual wire shear profiles, both the previous research [3] and this study's findings show that the model is not very sensitive to the shear term value, so an order of magnitude change in the shear modulus value made little difference and the calculated value works as is. Since the cable model is insensitive to the shear term, and κ has been shown to round to the same value for each limit case, the difference between choosing the maximum or minimum area makes is very slight. Figure 3.11 shows the modeled difference in frequency response function for G values differing by orders of magnitude. Differences are minor all the way through the fifth frequency, and even the higher frequencies are simply shifted.

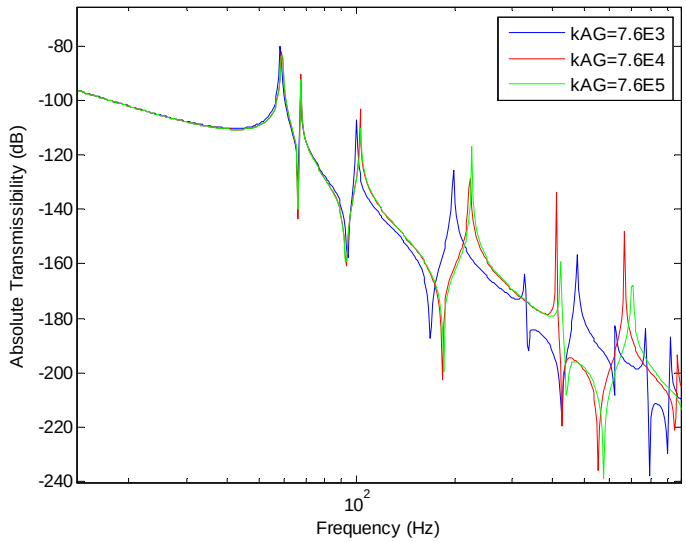

Figure 3.11: Slight variations in frequency response for massive changes in shear rigidity value.

3.4.6 Bending Stiffness

The AFRL work limited cable modeling to commercially available finite beam elements and determined elastic modulus and moment of inertia values through axial dynamic tests and lateral bending tests, both requiring dedicated test equipment. The approach outlined here allows for calculation of bending stiffness based purely on the cable geometry and published material values. Bending stiffness of cables is considerably more complex than for a homogenous beam; research shows that the bending stiffness of a beam is variable when the beam is a multi-stranded cable [41, 49]. For a solid homogenous beam, bending stiffness is made up of the product of the modulus of elasticity *E* for the solid material and the moment of inertia *I*, which is easily calculated for simple solid shapes. For a stranded cable, neither of these properties is simple. Instead of determining *E* and *I* directly, the overall bending stiffness is considered based on the work of Papailiou concerning the bending stiffness of ACSR overhead transmission line cables. According to Papailiou, cable bending stiffness must take into account not only the stiffness of each individual wire, but also the secondary stiffness due to the friction between the wires. The secondary stiffness varies depending on whether the surrounding wires have slipped against the core wires or not, which is generally dependent on the amount of cable curvature. When a cable is straight and all of its wires are in an initial position, it has a maximum bending stiffness. As the cable is bent or displaced, wires begin to slip against each other, and when all wires have slipped, a minimum bending stiffness is achieved [49]. The difference between the minimum and maximum bending stiffness value may be orders of magnitude apart [76, 80], and the bending stiffness value can be any value in between depending on the curvature of the cable. The bending stiffness for a stranded cable is given by Papailiou as the sum of the minimum bending stiffness plus additional stick or slip terms summed from each wire [49]. The minimum bending stiffness is

$$EI_{min}^{wire} = E_L \pi \frac{d^4}{64} \cos\beta$$

where E_L is the wire longitudinal modulus of elasticity (which itself must be determined by modeling the wire as a composite as described previously), d is the diameter of the

individual wire, and $\beta$is the lay angle. This is similar to the usual bending stiffness calculation where the moment of inertia is πr^4 , but includes a cosine term to take the angle of the wires into account. The additional term to include the sticking between wires is

$$EI_{stick}^{wire} = E_L A(r \sin\phi)^2 \cos^3\beta$$

where *A* is the wire area, *r* is the layer diameter, ϕ is the angle that the individual wire's position makes with the horizontal (neutral) axis, and β is the lay angle. The equations for EI_{min}^{wire} and EI_{stick}^{wire} give the lower and upper bounds for the bending stiffness value for a single wire, which for the cables investigated here, can be an order of magnitude apart and thus give too large of a range for useful prediction. By including the curvature of the cable (for this case, based on the static displacement of the cable due to excitation tension), a more precise value can be obtained by adding a bending stiffness slip term:

$$EI_{slip}^{wire} = \sigma_T A\left(e^{\mu \sin(\beta)*\phi} - 1\right)(r \sin\phi)\cos\beta\,/\kappa_c$$

Here, σ_T is the stress in the wire due to tension, μ is the friction coefficient between wires, κ_c is the curvature of the cable, and other variables are the same as in the previous equations. The friction coefficient is taken as 0.35 for the insulated wires based on the friction coefficient for Tefzel, given by MatWeb as 0.3 to 0.4, DuPont as 0.23 (between metal and Tefzel), and Omega Wiring as 0.4. This value could be improved through experiments to find the coefficient of friction for the specific wires used, but according to discussion about [49], small changes in the friction value will not cause large changes in the overall bending stiffness [79].

For the case where the cable wires have not begun to slip and the cable stiffness is at a maximum, the bending stiffness is given by

$$EI_{max} = \sum EI_{min}^{wire} + \sum EI_{stick}^{wire}$$

Otherwise, if the cable wires have begun to slip, the cable bending stiffness is a function of curvature and tension and is given by

$$EI_{slip} = \sum EI_{min}^{wire} + \sum EI_{slip}^{wire}$$

The bending stiffness is summed over all of the wires; for the wire minimum bending stiffness, this simply requires multiplying the *EI* wire minimum term by the number of wires in the cable, but for the wire slip and wire stick terms, the ϕ angle will change for each wire, and the layer radius changes for each layer, so these calculations must be done carefully.

Figure 3.12 shows the end layout of a 1X7 cable in which the layer diameters are noted in terms of the wire diameters, and the wire angle ϕ is shown starting at 0 radians at the horizontal axis and moving counterclockwise. Figure 3.13 shows a similar layout for a 1X19 cable. The bending stiffness is calculated as the sum of the minimum stiffness, plus the stiffness of each additional layer. Table 3.7 gives the number of wires or strands required to make up a full layer, as well as the associated ϕ angle spacing for each layer, regardless of cable size.

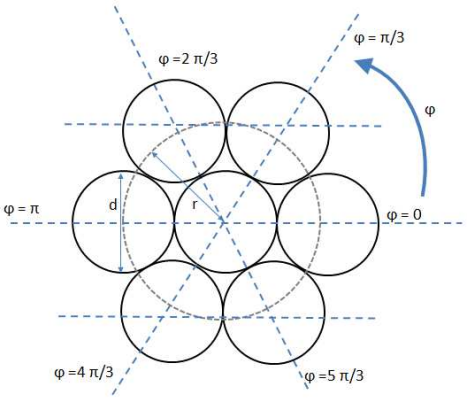

Figure 3.12: 1X7 cable layout showing ϕ angle.

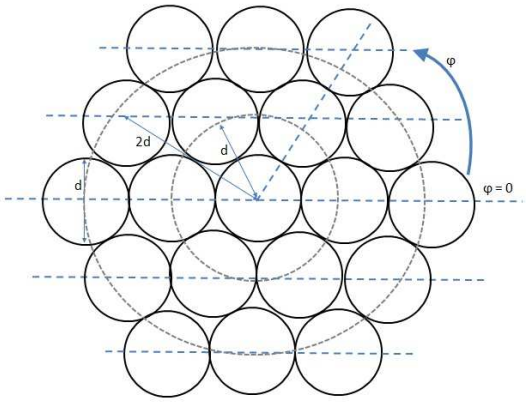

Figure 3.13: 1X19 cable end layout showing layer diameters.

Table 3.7 Number of wires and associated ϕ angles for first five cable layers.

Layer Number	Number of Wires or Strands for a Full Layer	ϕ Angle Division (degrees)	Layer Radius in Terms of Wire Diameter, *d*
0 (Core)	1	N/A	0
1 (Innermost Layer)	6	60	*d*
2	12	30	2*d*
3	18	20	3*d*
4 (Outermost Layer)	24	15	4*d*

In the case of the 1X48 cable which does not have a complete outer layer, the individual wires wrap around the cable, adding inertia around the cable unevenly. Thus, the average value between minimum stiffness (in which the additional layer wires are at the neutral axis) and maximum stiffness (in which additional layer wires are at the top and bottom of the cable) is used. Figure 3.14 shows the layout for the minimum and maximum stiffnesses with the associated outer layer ϕ angles of 0, 15, 30, 45, 150, 165, 180, 195, 210 330, and 345 degrees for the minimum and 60, 75, 90, 105, 120, 135, 240, 255, 270, 285 and 300 degrees for the maximum.

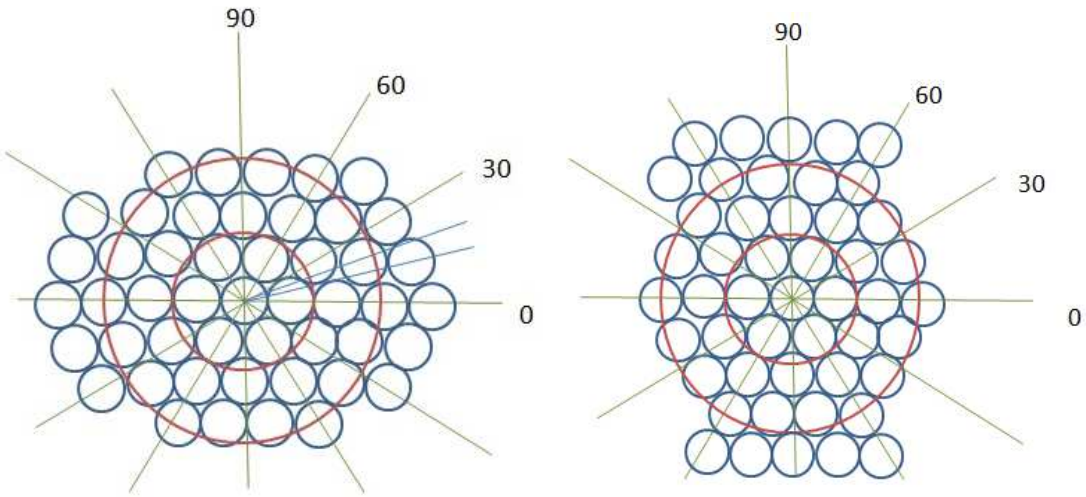

Figure 3.14: 1X48 cable with minimum configuration (wires aligned near neutral axis) and maximum configuration (wires away from neutral axis).

The above bending stiffness equations are only applicable to single stranded concentric cables; for the multi-stranded 7X7 cable, the equations were modified to take into

account the strand behavior of the outer layer. For the multi-stranded cable, the core *EI* is calculated as a single 1X7 strand and the outer strands are treated as large individual wires; in the *EI* wire stick formula, the base *E* value is used, the area is the area of the 1X7 strand, *r* is the distance to the center wire in each strand, ϕ is the wire angle for the six outer strand center wires and β is the lay angle for the six layer strands, not the individual wires. Figure 3.15 shows the end layout for a 7X7 cable with the layer radius of 2.5*d* and ϕ angle divisions of 60 degrees shown. This approach, though novel, worked well; considering the outer strands to be large wires resulted in a lower overall bending stiffness for the multi-stranded cable than the similarly sized single stranded cable, which agreed with experimental data and theory.

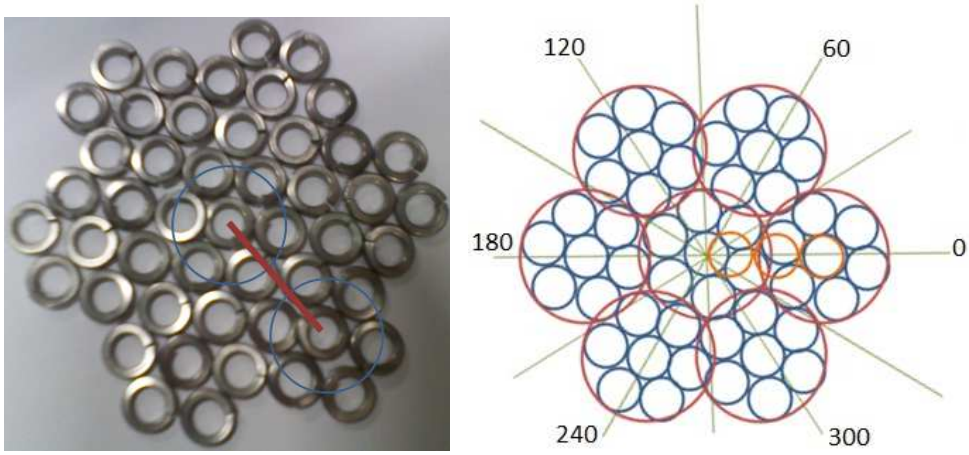

Figure 3.15: 7X7 cable layer distance of 2.5d shown by red line and orange circles; strand ϕ angles shown to be 60 degrees apart.

Table 3.8 lists the maximum, slip, and minimum bending stiffness values for the four cables used, as well as the "traditional" bending stiffness calculation determined by multiplying the elastic modulus by the moment of inertia calculated for the wires based on the parallel axis theorem. The maximum and minimum values in the table are based on calculated maximum and minimum wire E_L values of 23.7 GPa and 22.1 GPa as determined previously using the concentric composite model. The curvature for the slip state was based on the static displacement of the cable due to the excitation force; the values listed in Table 3.3 are based on the curvature values for the two-point fixture. Radius of curvature for the two-point fixture were 25, 80, 450, and 200 m for the 1X7,

1X19, 1X48, and 7X7 cables respectively, and were 50, 200, 900, and 700 m for the four cable types for the four-point fixture, each determined based on the measured maximum displacement of the cable due to the static force applied by the excitation attachment. The curvature values for the four-point fixture were lower due to larger radii from smaller displacements due to the shorter span, so the corresponding bending stiffness was higher as anticipated. Although the displacement of the cables in both fixtures was small (0.1 to 1.6 mm), it was enough to cause wire slipping based on calculations for critical curvature from [49]. Based on the cable maximum and minimum bending stiffnesses, it is clear that the traditional approach for bending stiffness calculation does not agree with the range calculated for most cables. In addition, the multi-stranded 7X7 cable is significantly more flexible than the 1X48 cable, which is reflected correctly in the cable bending stiffness calculations, but not by the traditional approach. The minimum to maximum (stick) range does span an order of magnitude as reported by previous authors. Overall, the approach suggested by Papailiou for bending stiffness calculation [49, 74] incorporated the physical parameters of the cable and took the friction between the wires into account, giving a more complete bending stiffness calculation than determining the modulus and inertia values independently.

Table 3.8 Bending stiffness values calculated for four cables types using minimum and maximum E wire values.

	1X7		1X19		1X48		7X7	
	Minimum	Maximum	Min.	Max.	Min.	Max.	Min.	Max.
EI Stick	1.65	1.87	13.82	15.72	93.60	106.71	74.05	84.38
EI Slip (4 Pt)	0.40	0.44	1.55	1.71	7.52	8.13	2.60	2.82
EI Slip (2 Pt)	0.34	0.37	1.08	1.18	4.73	5.10	2.14	2.30
EI Min	0.28	0.30	0.77	0.83	1.94	2.07	1.96	2.10
Traditionally Calculated *EI*	2.84	3.04	6.25	6.67	148.91	159.09	154.39	164.95

3.4.7 Damping Mechanisms and Coefficients

A few damping mechanisms are at work in all cables, which also have coefficients that must be determined as model inputs. As listed in the literature review, cable damping mechanisms sampled to date include viscous damping, Kelvin-Voigt damping, structural

damping, and geometric damping. Comparison of simple damping mechanisms showed that viscous damping alone was not effective for modeling damping in cables [97, 100].

Viscous damping occurs due to the friction between the beam and the surrounding medium (for our purposes, air) as the beam moves transversely. This term is likely to be very small for a small cable, and non-existent in space, but it is included in the model as the simplest form of damping.

$$viscous\ damping = cv\frac{\partial w}{\partial t}$$

where *cv* is the viscous damping coefficient. Another common form of damping is structural damping, which includes both damping due to friction and material damping effects. It is generally more effective at modeling experimental damping than viscous damping, and can be included by using the form

$$structural\ damping = \alpha\frac{\partial w}{\partial t} + \beta EI\frac{\partial^4 w}{\partial x^4}\frac{\partial w}{\partial t}$$

where α and β are the structural damping coefficients.

Hysteretic damping occurs in viscoelastic materials, which the literature review has shown to be the case for the insulation around spaceflight cables. Hysteretic damping was investigated for cables in [57] and experimental observations concluded that the 1X19 cable investigated had hysteretic damping that was frequency and amplitude dependent. Hysteretic damping can be incorporated through many forms, including spatial hysteresis and time hysteresis. Time hysteresis specifically includes damping from stress that is proportional to strain plus the past history of the strain. Time hysteresis damping can be incorporated through the equations of motion [101] where the hysteretic damping term is included as

$$time\ hysteretic\ damping = \int_0^t g(t-\tau)w''(x,\tau)dt$$

and $g(t)$ is a kernel that represents the hysteresis model. A particularly effective hysteretic kernel for frequency-dependent viscoelastic materials is the Golla-Hughes-McTavish (GHM) method, where additional spatial coordinates are incorporated through

the representation of the material modulus as a series of damped mini oscillators [102, 103]. The viscoelastic material properties are approximated by a curve fit of the form [104]

$$G(s) = \frac{\alpha s^2 + \gamma s}{s^2 + \beta s + \delta}$$

where the Laplace transform has already been applied and $\alpha, \beta, \gamma,$ and δ are the damping coefficients that can be experimentally determined through dynamic mechanical analysis [105]. Experimental analysis is required for damping coefficients, so the damping coefficients are determined through curve fitting of experimental data. The cable damping expression for each cable was determined by adjusting the four hysteretic damping coefficients in the cable model until the first four frequency amplitudes for the experimental data were matched by the cable model. Those coefficients were then used in the four-point model for the same cable to confirm that the damping coefficients still approximated the first few amplitudes reasonably well. Those damping coefficients were then applied to the damped cable portion of the cabled beam model.

Cables may experience heavy damping, so approximations for light damping should not be used to determine cable damping ratios. The modal damping from a hysteretic damping model can be calculated for a particular mode using the mobility frequency response function and the viscous half-power bandwidth method. This gives an equivalent viscous modal damping ratio added by the GHM damping method. To determine the modal damping ratio for a particular frequency, the derivation from Ewins [106] is used, which results in the expression

$$\zeta = \frac{\omega_1^2 - \omega_2^2}{2\omega_r(\omega_1 + \omega_2)}$$

where $\omega_1 \; and \; \omega_2$ are the frequencies at the point 3 dB down from the maximum amplitude at mode r, and ω_r is the natural frequency at mode r. This expression can be used for any level of damping.

It should be noted that using variable bending stiffness can also incorporate damping; for a cable that is experiencing slipping states, variation of bending stiffness as a function of

curvature produces damping of vibration without requiring an explicit damping term in the equation of motion for the cable [41]. Thus, the use of a bending stiffness term that includes the dependence on curvature as well as additional viscous and hysteretic damping terms should give a reasonable approximation for the damping exhibited by stranded cables.

3.5 Cable Bakeout Correction Factor

So far, the geometry, wire configuration, and wire material have been the major factors that influence cable parameters. However, for spaceflight cables, another factor that can influence cable dynamic behavior is bakeout treatment. The investigation of spaceflight cables so far has been limited to cables constructed for the purpose of testing. Cables that are constructed for actual flight must go through additional preparation and test, including "bakeout," a combination of heat and vacuum treatment designed to expedite the initial outgassing of flight hardware for contamination control [107]. Bakeout requires both high temperature thermal treatment and near-vacuum pressure, and may take anywhere from a few hours to several weeks, depending on the item's intended destination and mission. All components of a space structure must go through bakeout to become flight ready, but components may be baked out separately and assembled in a clean room prior to launch. It is common for cables to be baked out separately from the main structure, which also means that vibration testing usually occurs before cables are added to the structure and thus provides further motivation for accurate modeling of cabled structures since additional testing may be difficult once the structure has entered the clean assembly room. Anecdotal reports from cable technicians suggest that cables seem stiffer after going through the bakeout process, but no study existed to affirm or quantify this difference. Since there is no existing literature on the effects of bakeout on flight cables, and quantification of cable dynamics is important for space structure modeling, additional experiments were conducted to determine whether bakeout affects cable dynamics and spacecraft structural models that include cables. An additional bakeout correction factor can be included in cable models to take the effects of bakeout into account [108]. Based on experiments run, the bakeout factor to include for the bending stiffness of baked out cables would be between 0.8 and 0.95.

3.6 Cable Parameter Conclusions

Combining the theory for bending stiffness of stranded cables with the material properties for concentric composites yielded reasonable bending stiffness terms for stranded cables. Extending these ideas allowed for calculation of multi-stranded cable parameters by considering the outer layer strands as large wires. The bending stiffness of each cable was dependent on curvature; even small displacement in the static position of the cable was enough to cause wire slippage and subsequent lowering of the bending stiffness value. Calculation methodology for ranges for area, density, and shear terms were presented, as well as the form of the cable damping term. Table 3.9 presents the equations for the maximum and minimum values of the cable parameters required for cable modeling that are calculated directly. Table 3.10 lists the equations to determine the maximum and minimum parameters required for the calculation of bending stiffness and shear rigidity.

Table 3.9 Equations for minimum and maximum values for cable parameters $A, v,$ and ρ.

Parameter	Parameter Minimum	Parameter Maximum
Area, A	$N(2(A_{Cu\ Core} + A_{Tefzel\ 26AWG\ Jacket}) + A_{EMI} + A_{Jakcet})$	$N\pi\frac{d_{wire\ min}}{2} * \frac{d_{wire\ max}}{2}$
Copper Volume Fraction, v_{Cu}	$\frac{2A_{CuCore} + A_{EMI}}{(2A_{CuCore} + A_{EMI} + 2A_{Tefzel\ 26AWG\ Jacket} + A_{Jacket})}$	$\frac{2A_{CuCore}+A_{EMI}}{\left(\pi\frac{d_{wire\ min}}{2}*\frac{d_{wire\ max}}{2}\right)}$
Tefzel Volume Fraction, v_{Tefzel}	$\frac{2A_{Tefzel\ 26AWG\ Jacket} + A_{Jacket}}{(2A_{CuCore} + A_{EMI} + 2A_{Tefzel\ 26AWG\ Jacket} + A_{Jacket})}$	$\frac{2A_{Tefzel\ 26AWG\ Jacket}+A_{Jacket}}{\left(\pi\frac{d_{wire\ min}}{2}*\frac{d_{wire\ max}}{2}\right)}$
Density, ρ	$\frac{m}{L * \pi R_{cable}{}^2}$ or $\left(\frac{vf_{Cu}}{\rho_{Cu}} + \frac{vf_{Tefzel}}{\rho_{Tefzel}}\right)^{-1}$	$\frac{m}{A_{Minimum}}$

Table 3.10 Equations for minimum and maximum values for cable parameters for bending stiffness and shear rigidity terms.

Parameter	Equation	To Use For Minimum Value	To Use For Maximum Value
Poisson's Ratio, ν	$\nu_m - \frac{2(\nu_m - \nu_f)(1-\nu_m^2)E_f\nu_f}{E_m(1-\nu_f)(1-\nu_f-2\nu_f^2)+\left((1-\nu_m-2\nu_m^2)\nu_f+(1+\nu_m)\right)E_f}$	$\nu_m = \nu_{Tefzel\,min}$ and $\nu_f = \nu_{Cu\,min}$	$\nu_m = \nu_{Tefzel\,max}$ and $\nu_f = \nu_{Cu\,max}$
Modulus of Rigidity, G	$\frac{\left((1+\nu_f)G_f+(1-\nu_f)G_m\right)G_m}{G_f+G_m-\nu_f(G_f-G_m)}$	$\nu_m = \nu_{Tefzel\,min}$ and $\nu_f = \nu_{Cu\,min}$	$\nu_m = \nu_{Tefzel\,max}$ and $\nu_f = \nu_{Cu\,max}$
Shear Coefficient, κ	$\frac{6(1+\nu)^2}{7+12\nu+4\nu^2}$	$\nu = \nu_{min}$	$\nu = \nu_{max}$
Modulus of Elasticity, E	$\nu_f E_f + \nu_m E_m + \frac{2(\nu_f-\nu_m)^2 E_m E_f \nu_f(1-\nu_f)}{E_m(1-\nu_m)(1-\nu_f-2\nu_f^2)+E_f\left((1-\nu_m-2\nu_m^2)\nu_m+(1+\nu_m)\right)}$	$\nu_m = \nu_{Tefzel\,min}$ and $\nu_f = \nu_{Cu\,min}$ and $\nu = \nu_{min}$	$\nu_m = \nu_{Tefzel\,max}$ and $\nu_f = \nu_{Cu\,max}$ and $\nu = \nu_{max}$
Bending Stiffness, EI (Single Stranded)	$\sum_N E\,\pi\frac{d_{wire}^{\,4}}{64}\cos\beta + \sum_N \sigma_T A\left(e^{\mu\sin(\beta)*\phi}-1\right)(r\sin\phi)\cos\beta\,/\kappa_c$	$E = E_{min}$ and $A = A_{min}$	$E = E_{max}$ and $A = A_{max}$
Bending Stiffness, EI (Multi-Stranded)	$N_S * EI_{MinStrand} + \sum_N \sigma_T A_{min}\left(e^{\mu\sin(\beta)*\phi}-1\right)(r\sin\phi)\cos\beta\,/\kappa_c$	$EI_{MinStrand} = EI_{Min}$ for single strand using E_{min} value	$EI_{MinStrand} = EI_{Min}$ for single strand using E_{max} value

For the parameters listed in Table 3.10, the equation is the same for maximum and minimum cases, but the input values used in the equations will be the maximum or minimum values for volume fraction, modulus of elasticity (or strand bending stiffness in the case of the multi-stranded cable), area, or Poisson's ratio, as required by the equation. Determining effective cable values for the area, density, bending stiffness, shear terms, and damping terms enables the development of a beam model for cables, which is constructed in the next chapter.

Chapter 4: Modeling Methodology

Of the cable models introduced in Chapter 2, the beam model has many advantages for the purpose of vibration analysis. The beam model can be used directly to solve for dynamic response information, and can incorporate bending stiffness and shear, which must be considered for cable modeling. However, there are aspects of the semi-continuous model that are valuable as well; the beam model assumes a homogenous cross-section, and a stranded cable made up of jacketed wires is certainly non-homogenous. An important contribution of this work is the determination of equivalent homogenous beam parameters that describe the cable response accurately without resorting to dynamic experimental testing of the cable. Thus, once cable parameters are determined as described in Chapter 3, they can be incorporated into an equation of motion for the now effectively homogenous cable system. There are many methods to solve a beam model equation of motion, but the method used here is the distributed transfer function method (DTFM). The DTFM is an exact method that determines dynamic response through the use of exponential matrix calculations rather than eigenvalue solvers. The DTFM has been used for beam modeling and shown to be more accurate at determining natural frequencies than the Rayleigh Ritz method [109]. The DTFM divides a system into a series of subsections and nodes, similar in some respects to a finite element method, but with nodes only placed at joints, force locations, boundary constraints, or other points of interest. Unlike the finite element method, the DTFM only requires nodes at points where different components are connected, constrained, or excited, so the elements remain as large as possible. This leads to similar accuracy, but much less computation time than the finite element method [110]. For this reason, the DTFM is well-suited to the repeating nature of cables attached to structures, and works well with the damped equations that describe cable motion and the tie-down constraints. This chapter begins with an overview of the DTFM and then describes the work done to develop the cable model and the cabled beam model.

4.1 Distributed Transfer Function Method

The distributed transfer function method may be unfamiliar to some readers, so the method will be described in general terms before going through the cable and cabled-

beam cases. The method related here is based off of the work of Yang [111, 112, 113], who used the DTFM for multi-section Euler-Bernoulli beam systems [111] and Sciulli [114], who used the approach for the case of two Euler-Bernoulli beams connected by spring-damper systems. The response $w(x,t)$ for a distributed beam system is governed by a fourth order linear partial differential equation and boundary conditions such as

$$\left\{A\frac{\partial^2}{\partial t^2}+B\frac{\partial}{\partial t}+C\right\}w(x,t)=f(x,t), x\,\epsilon\,(0,1), \qquad t>0$$

$$M_j w(x,t)|_{x=0}+N_j w(x,t)|_{x=1}\ =\gamma_j(t),\ \ t\geq 0, j=1,2,3,4$$

where *A*, *B* and *C* are differential operators derived from the equation of motion comprising constant coefficients related to the physical properties of the system and spatial derivatives, and *M* and *N* are operators based on the boundary conditions of the system. The equation of motion and boundary conditions are Laplace transformed with respect to *t*, and cast into state space form

$$\eta'(x,s)=F(s)\eta(x,s)+v(x,s)\ \ x\,\epsilon\,(0,1)$$

$$M(s)\eta(0,s)+N(s)\eta(1,s)=\gamma(s)$$

where

$$\eta(x,s)=\{W(x,s)\ W'(x,s)\ W''(x,s)\ W'''(x,s)\}^T$$

$$v(x,s)=\left\{0\ 0\ 0\ \frac{q(x,s)}{a_n s^2+b_n s+c_n}\right\}^T$$

$$\gamma(s)=\{\gamma_1(s)\ \ \gamma_2(s)\ \ \gamma_3(s)\ \ \gamma_4(s)\}^T$$

for a fourth order beam equation. The size of the solution vector $\eta(x,s)$ is dependent on the order of the equation of motion. The solution to the state space equation is

$$\eta(x,s)=\int_0^1 G(x,\xi,z)v(\xi,s)d\xi\ +\ H(x,s)\gamma(s) \qquad\qquad x\,\epsilon\,(0,1)$$

where

$$G(x,\xi,z)=\begin{cases} e^{F(s)x}\left(M(s)+N(s)e^{F(s)}\right)^{-1}M(s)e^{-F(s)\xi}, & \xi<x \\ -e^{F(s)x}\left(M(s)+N(s)e^{F(s)}\right)^{-1}N(s)e^{F(s)(1-\xi)}, & \xi>x \end{cases}$$

and

$$H(x,s)=e^{F(s)x}\left(M(s)+N(s)e^{F(s)}\right)^{-1}$$

with $e^{F(s)x}$being the fundamental matrix using the state space matrix *F(s)* created from the equation of motion and sized according to the order of the equation of motion, and $G(x,\xi,z)$ and $H(x,s)$ known as the transfer functions of the subsystem.

However, this is only the solution for a single subsystem, and the value of the DTFM for cabled structure research is the ability to connect many subsystems to model a cable attached at many points. Thus, for any number of interconnected subsystems, displacement and strain vectors are described by

$$\alpha(x,s) = \{W(x,s) \;\; W'(x,s)\}^T$$
$$\epsilon(x,s) = \{W''(x,s) \;\; W'''(x,s)\}^T$$

and the solution vector $\eta(x,s) = \{\alpha^T(x,s) \;\; \epsilon^T(x,s)\}^T$. An internal force vector is assumed to be

$$\sigma(x,s) = E(s)\epsilon(x,s)$$

where *E(s)* is a constitutive matrix, which is the elastic modulus in the case of a beam model. Set

$$\gamma(s) = \{\alpha(0,s) \;\; \alpha(1,s)\}^T$$
$$M(s) = \begin{bmatrix} I_2 & 0 \\ 0 & 0 \end{bmatrix}, \;\; N(s) = \begin{bmatrix} 0 & 0 \\ I_2 & 0 \end{bmatrix}$$

where α are nodal displacement vectors at each end of a subsystem and I_2 is a 2x2 identity matrix that either links subsystems or incorporates boundary conditions and constraints as described later. Constraints such as springs between subsystems can be incorporated through either the boundary condition matrices or the global stiffness matrix created through subsystem assembly. The subsystems are assumed to have a unit length, so the fundamental matrix must be multiplied by the length of the subsystem for subsystem lengths other than one.

Combining all of these equations and partitioning the *G* and *H* matrices appropriately yields solutions of

$$\alpha(x,s) = \int_0^1 G_\alpha(x,\xi,s) f(\xi,s) d\xi + H_{\alpha_0}(x,s)\alpha_0(s) + H_{\alpha_1}(x,s)\alpha_1(s)$$

$$\sigma(x,s) = E(s)\int_0^1 G_\epsilon(x,\xi,s)f(\xi,s)d\xi + H_{\epsilon_0}(x,s)\alpha_0(s) + H_{\epsilon_1}(x,s)\alpha_1(s)$$

These solution equations depend on specific portions of the transfer function matrices which are partitioned as shown.

$$G(x,\xi,s) = \begin{bmatrix} G_\alpha \\ G_\epsilon \end{bmatrix}, \qquad H(x,s) = \begin{bmatrix} H_{\alpha 0} & H_{\alpha 1} \\ H_{\epsilon 0} & H_{\epsilon 1} \end{bmatrix}$$

Once the nodal displacements are known, the response of the system is completely determined. To determine the nodal displacements, the subsystems must be assembled to make a stiffness-like matrix as follows.

Assuming the total system has *N* nodes, located at $x_k, k = 1,2 \ldots N$ where the subsystems are connected, the displacement vector of the system at location x_k is called $u_k(s)$. Multiple subsystems can be connected at each node, as well as pointwise constraints of the form $-C_k(s)u_k$ and external forces. Force balance at the node x_k requires

$$Q_A(s) + Q_B(s) + \cdots + Q_D(s) - C_k(s)u_k(s) + p_k(s) = 0$$

where *Q* vectors are the vectors of the forces applied at node *k* by the subsystems and p_k is the vector of nodal external forces. The force $Q_A(s)$ for subsystem *A* is

$$Q_A(s) = -R_A\sigma_A(x_k,s)$$

where R_A is a coordinate transformation matrix for that subsystem. The subsystem nodal displacement vectors $\alpha_A(x_l,s)$ and $\alpha_A(x_i,s)$ are related to global nodal displacements $u_l(s)$ and $u_i(s)$ by coordinate transformation matrices so that

$$\alpha_A(x_l,s) = S_A u_l(s)\ , \qquad \alpha_A(x_i,s) = T_A u_i(s)$$

The subsystem nodal displacement vectors are put into the appropriate terms for the left and right side of the subsystem (α_0 or α_1) in the solution vector, and the solution vector is put into the force term. Combining the solution and coordinate transformation equations in this way yields

$$Q_A(s) = -R_A\left(E\int_0^1 G_\epsilon^A(x_k,\xi,s)f(\xi,s)d\xi + H_{\epsilon 0}^A(x_k,s)\alpha_0(s) + H_{\epsilon 1}^A(x_k,s)\alpha_1(s)\right)$$

$$Q_A(s) = -R_A\left(E\int_0^1 G_\epsilon^A(x_k,\xi,s)f(\xi,s)d\xi + H_{\epsilon 0}^A(x_k,s)T_A u_i(s) + H_{\epsilon 1}^A(x_k,s)S_A u_l(s)\right)$$

$$Q_A(s) = -R_A(H_{\epsilon 0}^A(x_k,s)T_A u_i(s) + H_{\epsilon 1}^A(x_k,s)S_A u_l(s) - f_l^A)$$

and when this equation is compared with the form of stiffness matrix times displacement, with *k* as the node of interest *l*,

$$Q_A(s) = -K_{li}^A(s)u_i(s) - K_{ll}^A(s)u_l(s) - f_l^A$$

it is shown that the elements of the stiffness matrix are

$$K_{li}^A(s) = R_A H_{\epsilon 0}^A(x_l,s)T_A \quad , \quad K_{ll}^A(s) = R_A H_{\epsilon 1}^A(x_l,s)S_A$$

for the subsystem A. However, these equations assume that $x_i < x_l$ (essentially $x_i = 0$ and $x_l = 1$), and must be rederived otherwise, switching the nodal displacement substitutions. Deriving the equations for reversed subsystems results in different combinations of the elements of the *H* transfer matrix with the transformation matrices.

After the force balance is determined for each node, an equilibrium equation similar to the typical finite element method can be formulated as

$$K(s)u(s) = q(s)$$

where the stiffness matrix, displacements, and forces are in global terms. This equation can be solved for the displacements of each subsystem, which can then be substituted back into the solution equations to determine the response of each subsystem.

To get eigenvalues and the resulting natural frequencies, the external forces are set to zero so that

$$K(s)u(s) = 0$$

and the nontrivial solution for $u(\lambda_k)$ is found by solving $\det[K] = 0$ to give the natural frequencies. The displacements are calculated for each natural frequency, and these displacements can be substituted into the solution equation, again assuming applied

external forces are 0, to give the mode shape for each subsystem for each natural frequency.

Frequency response functions can also be created from this method. Assuming that a harmonic forcing function is applied at frequency ω, the nodal displacements are determined as

$$u(j\omega) = K^{-1}(j\omega)q(j\omega)$$

where the forcing function is assumed to be a harmonic input. Again, the displacements are substituted into the solution equation to get the frequency response as a function of $j\omega$. Appendix A contains the detailed equations for the construction of the global stiffness matrix $K(s)$for a simple beam divided into three subsystems as an example of the DTFM approach.

4.2 Equations of Motion

The distributed transfer function method begins with the equation of motion for a system. For the simplest case of an Euler-Bernoulli beam in which plane sections remain plane, the equation of motion is

$$\rho A \frac{\partial^2 w(x,t)}{\partial t^2} + EI \frac{\partial^4 w(x,t)}{\partial x^4} = q(x,t)$$

where $w(x,t)$ is the transverse displacement of the beam and $q(x,t)$ is an externally applied forcing function. The coefficients ρ, A, and EI represent the density, area, and bending stiffness parameters that describe the beam material and shape. The Euler-Bernoulli beam equation is sufficient for the aluminum beam used as a host structure. However, since the cables under consideration are constructed of a metal core and outer insulation layer, they do not experience constant shear across the cross-section, and are more like a sandwich or composite beam in their behavior than a solid beam. Therefore, a simple Euler-Bernoulli model does not adequately capture the cable behavior, and a shear beam model must be used. Derivation of the equation of motion for a shear beam can be determined from Timoshenko's work [115]. In the Timoshenko beam equations, variables include both the transverse displacement of the beam and the rotation of a plane section of the beam due to both bending and shear, taking shear effects into account as

well as rotational inertia. A Timoshenko cable model was developed as part of this research, but rotational inertia effects were small compared to shear effects, and the additional complexity of the Timoshenko beam was unwarranted, corroborated by both this author's findings [100] and others. Since multiple sources note that shear effects must be included [2, 90] and the cables could be under tension, a shear term and tension term are included in the governing equations and the equation of motion for an undamped cable is more accurately described by

$$\rho A\frac{\partial^2 w(x,t)}{\partial t^2}-\frac{EI\rho A}{\kappa AG}\frac{\partial^4 w(x,t)}{\partial t^2\partial x^2}+EI\frac{\partial^4 w(x,t)}{\partial x^4}+T\frac{\partial^2 w(x,t)}{\partial x^2}=q-\frac{EI}{\kappa AG}\frac{\partial^2 q(x,t)}{\partial x^2}$$

where T is the tension in the cable and again, the property coefficients can be terms that describe the cable as a beam. Going further along the path towards reality, cables experience damping through a variety of mechanisms, including viscous damping and hysteretic damping. For this case, the equation of motion is derived from governing equations with damping included. Hysteretic damping is incorporated through the stress strain relation for a viscoelastic material [101]

$$\sigma(x,t)=E\epsilon(x,t)-\int_0^t g(t-\tau)\epsilon(x,t)d\tau$$

where E is the elastic modulus, $\epsilon(x,t)$ is the strain, and $g(t)$ is the hysteretic damping kernel. From the work of Timoshenko [115], the equations for a beam are

$$\rho A\ddot{w}(x,t)=-\frac{\partial V(x,t)}{\partial x}+q(x,t)$$

$$\frac{\partial M(x,t)}{\partial x}=V(x,t)$$

which are used in conjunction with the definition of the moment and shear terms for a beam that experiences bending and shear, which are

$$M=EI\frac{\partial \psi}{\partial x}$$

$$V=-\kappa AG\left(\frac{\partial w}{\partial x}-\psi\right)$$

where the moment, shear, transverse displacement and total rotation are all functions of x and t for those and all subsequent equations until the Laplace transform is taken for the DTFM form. As discussed previously, cables experience hysteretic damping. Since the stress of the beam therefore has a hysteretic component, the moment becomes:

$$M = EI\frac{\partial\psi}{\partial x} - \int_0^t g(t-\tau)\frac{\partial^2 w}{\partial x^2}d\tau \text{ OR } M = EI\frac{\partial\psi}{\partial x} - \int_0^t g(t-\tau)\frac{\partial\psi}{\partial x}d\tau$$

Using the form in which hysteresis is applied to w, substitution of the shear definition and new moment equation into the governing beam equations yields:

$$\rho A\frac{\partial^2 w}{\partial t^2} = -\kappa AG\frac{\partial\psi}{\partial x} + \kappa AG\frac{\partial^2 w}{\partial x^2} + q$$

$$EI\frac{\partial^2\psi}{\partial x^2} + \int_0^t g(t-\tau)\frac{\partial^3 w}{\partial x^3}dt - \kappa AG\psi + \kappa AG\frac{\partial w}{\partial x} = 0$$

The tension term is then added, as is a viscous damping term since inclusion of aerodynamic damping was recommended to more closely match energy dissipation of stranded transmission line conductors [84]. That work also notes that friction among conductor wires depends on time rate of change of wire curvature during bending vibrations (time hysteresis), so the combination of viscous and hysteretic damping could be an effective damping model. With tension and viscous damping included, the governing equations for shear and moment are:

$$\rho A\frac{\partial^2 w}{\partial t^2} = -\kappa AG\frac{\partial\psi}{\partial x} + \kappa AG\frac{\partial^2 w}{\partial x^2} + c\frac{\partial w}{\partial t} + q$$

$$EI\frac{\partial^2\psi}{\partial x^2} + T\frac{\partial w}{\partial x} + \int_0^t g(t-\tau)\frac{\partial^3 w}{\partial x^3}dt - \kappa AG\psi + \kappa AG\frac{\partial w}{\partial x} = 0$$

These equations are combined as shown in Appendix B to obtain a single equation in terms of the transverse displacement $w(x,t)$. Thus, a viscously and hysteretically damped viscoelastic cable in tension can be described with the equation of motion:

$$\rho A\frac{\partial^2 w}{\partial t^2}-\frac{\rho EI}{\kappa G}\frac{\partial^4 w}{\partial x^2\partial t^2}+EI\frac{\partial^4 w}{\partial x^4}+\frac{cEI}{\kappa AG}\frac{\partial^3 w}{\partial x^2\partial t}+T\frac{\partial^2 w}{\partial x^2}-c\frac{\partial w}{\partial t}+\int_0^t g(t-\tau)\frac{\partial^4 w}{\partial x^4}dt = q-\frac{EI}{\kappa AG}\frac{\partial^2 q}{\partial x^2}$$

4.3 Damped Shear Beam DTFM Model

Once the equations of motion of the cable as a beam are derived and the equivalent cable parameters calculated, the next step is to use the equations of motion to find information about the cable response, including natural frequencies, damping ratios, mode shapes, and frequency response functions. The distributed transfer function method (DTFM) is an exact solution method based on the fact that the transfer function of a system has all the information needed to determine the dynamic response of that system. By determining the transfer function of a system and putting it into a specific form, the desired information is obtained. For the case of cable-harnessed structures, DTFM is advantageous because it is easily segmented and allows for the building of cable-harnessed structures very easily since connections between systems are easily handled. Different forms of damping can be modeled by incorporating the damping mechanisms into the equation of motion, as evidenced by [116] for Euler-Bernoulli beams. Since an end goal of this work was to create a cable-harnessed beam model, setting up the cable model with the DTFM method makes for complete and straightforward integration of the developed cable model into a cable-harness structure model.

The cable system of interest consists of a single length of cable held in place through connections to ground, under slight tension and with both ends free. Figure 4.1 shows the cable system for the two-point fixture and the four-point fixture, with the attachment points modeled through both linear and rotational stiffness and damping. These models corresponded exactly to the experimental cable set ups for the two-point fixture and four-point fixture that will be discussed in Chapter 5.

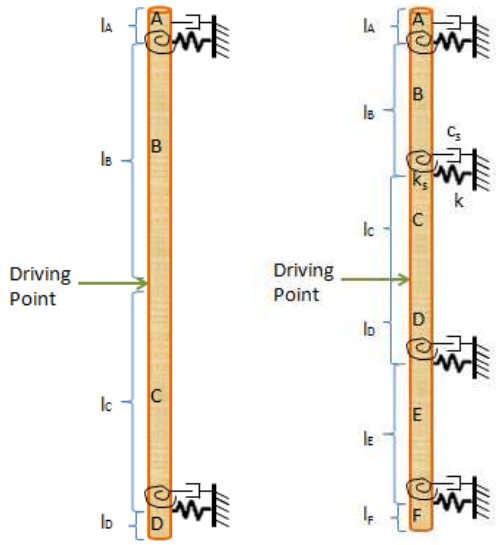

Figure 4.1: Cable model diagram showing linear spring and damper and rotational spring at attachment points for two-point and four-point models with nodes located at ends, attachment points, and excitation (driving) point.

For the two-point fixture model, the cable is divided into four unequal subsystems with five nodes; one node at each end, one node at each connection point, and one node at the excitation point. The four-point fixture model has six subsystems with nodes at the two ends, four connection points, and excitation point for a total of seven nodes. The stiffness matrix multiplies the nodal displacement vector, so the full matrix size is based on the number of nodes of the model. Thus, the stiffness matrix for the two-point model is a 10X10 matrix and the four-point model requires a 14X14 matrix. The MATLAB programs included in Appendix C contain the information for each subsystem and node as part of the input file for each model.

The equation of motion for the cable as a damped shear beam from the previous method provides the starting point for the distributed transfer function method. The solution $w(x,t)$ is assumed to be separable, so the partial derivatives are applied and are henceforth indicated by dot notation for temporal derivatives and prime notation for spatial derivatives.

$$\rho A\ddot{w} - \frac{EI\rho}{\kappa G}\ddot{w}'' + EIw'''' - \frac{EIc}{\kappa AG}\dot{w}'' - \int_0^t g(t-\tau)w''''dt + c\dot{w} + Tw'' = q - \frac{EIq''}{\kappa AG}$$

Taking the Laplace transform,

$$\rho As^2W - \frac{\rho EI}{\kappa G}s^2W'' + TW'' - \frac{EIc}{\kappa AG}sW'' + csW + EIW'''' - \frac{1}{s}G(s)W'''' = Q - \frac{EI}{\kappa AG}Q''$$

and rearranging the equation yields

$$W'''' = \frac{(-\rho As^2 - cs)}{\left(EI - \frac{1}{s}G(s)\right)}W + \frac{\frac{\rho EI}{\kappa G}s^2 - T + \frac{EIc}{\kappa AG}s}{\left(EI - \frac{1}{s}G(s)\right)}W'' + \frac{Q}{\left(EI - \frac{1}{s}G(s)\right)} - \frac{\frac{EI}{\kappa AG}Q''}{\left(EI - \frac{1}{s}G(s)\right)}$$

which is now an appropriate form to create the fundamental matrix used as the heart of the DTFM. Setting the equation of motion into the form

$$W' = FW + Q$$

gives the fundamental damped shear beam matrix for a cable subsystem,

$$F_{Shear_{Damped}} = \begin{bmatrix} 0 & 1 & 0 & 0 \\ 0 & 0 & 1 & 0 \\ 0 & 0 & 0 & 1 \\ \frac{(-\rho As^2 - cs)}{\left(EI - \frac{1}{s}G(s)\right)} & 0 & \frac{\frac{\rho EI}{\kappa G}s^2 - T + \frac{EIc}{\kappa AG}s}{\left(EI - \frac{1}{s}G(s)\right)} & 0 \end{bmatrix}$$

which is multiplied by the length of the subsystem. This fundamental matrix contains coefficients that represent physical information about a specific cable; the solution for a different cable simply requires changes in the fundamental matrix rather than the entire

method [117], so computing results for a variety of cables is straightforward. Boundary conditions of the system are incorporated through the use of matrices from the equation

$$M(s)\eta(0,s) + N(s)\eta(1,s) = \gamma(s)$$

which are determined from the boundary condition equations for each subsystem. Since the cable ends in each fixture are free, the beam is suspended to approximate a free-free condition, and the cable attached to the beam is free at the ends, the boundary conditions used for both the cable and cabled-beam model end subsystems require the bending moment and shear force to vanish at the ends, so the equations and corresponding boundary condition matrices are

$$EI\frac{\partial^2 W}{\partial x^2} = 0, \qquad \frac{\partial}{\partial x}\left[EI\frac{\partial^2 W}{\partial x^2}\right] = 0$$

$$M_{Free} = \begin{bmatrix} 0 & 0 & EI & 0 \\ 0 & 0 & 0 & -EI \\ 0 & 0 & 0 & 0 \\ 0 & 0 & 0 & 0 \end{bmatrix}, N_{Free} = \begin{bmatrix} 0 & 0 & 0 & 0 \\ 0 & 0 & 0 & 0 \\ 0 & 0 & EI & 0 \\ 0 & 0 & 0 & -EI \end{bmatrix}$$

The interior subsystems simply use boundary condition matrices created from the identity matrix, which ensures compatibility between displacement and slope on each side of each node. For this internal compatibility, the equations require the deflection and slope to be the same for each subsystem attached at the same node, so corresponding boundary conditions are

$$W_k^- = W_k^+ = W_k = 0, \qquad \frac{\partial W_k^-}{\partial x} = \frac{\partial W_k^+}{\partial x} = \frac{\partial W_k}{\partial x} = 0$$

$$M_{Interior} = \begin{bmatrix} 1 & 0 & 0 & 0 \\ 0 & 1 & 0 & 0 \\ 0 & 0 & 0 & 0 \\ 0 & 0 & 0 & 0 \end{bmatrix}, N_{Interior} = \begin{bmatrix} 0 & 0 & 0 & 0 \\ 0 & 0 & 0 & 0 \\ 1 & 0 & 0 & 0 \\ 0 & 1 & 0 & 0 \end{bmatrix}$$

The attachment points between cable and ground or cable and beam are modeled as spring and damper constraints incorporated in the global stiffness matrix and are

discussed in the next section. Displacements, mode shapes, natural frequencies, and frequency response functions are found as related in section 4.1. Appendix C contains the MATLAB program files for the cable models; input files for each model are listed first and contain the node and subsystem information for each model, followed by several function files that determine the boundary condition and constraint matrices, assemble the global stiffness matrix, determine the eigenvalues for the system, and finally find and plot the mode shapes and frequency response functions for the system.

4.4 Cable Tie-Down Attachment Point Modeling

A common method of attaching cables to structures involves the use of cable ties and mounting hardware. Aluminum TC105 tabs and cable ties are used for attaching cables to space structures as shown in detail in Chapter 5. As noted in [3] and confirmed in this body of work, pinned and fixed boundary conditions were not adequate for representation of these attachment points between cable and structure. Previous cabled structure models created by the Air Force Research Laboratory used a commercially available spring stiffness element for the attachment stiffness, but noted concern about the quality of the input value and recommended a better method to estimate tie-down properties [1].

The flexible cable tie, although tightened uniformly, allows some give within the cable. In addition, the cable tie is not fixed at one point in the hardware, so rotation is possible and requires surprisingly little force for even a very tight cable tie. Therefore, an attachment model that included both linear and rotational stiffness, as well as linear and rotational damping was developed. To do so, constraint equations are written in terms of the nodal displacements and included as part of the global stiffness matrix.

The cable model uses a constraint to ground and the cabled-beam model uses a constraint between subsystems. For the cable model, the constraint to ground representing the TC105 attachment with stiffness is modeled as a spring connected to a massive mass representing ground. For the spring-mass constraint, Sciulli gives the equation of motion for the rigid mass and develops the constraint matrix [114]. For a beam in transverse vibration, the displacement of the node that the mass (or ground) is connected to is

$u_i(s) = \begin{Bmatrix} w(x_i, s) \\ w'(x_i, s) \end{Bmatrix}$ and the force is $f(s) = \begin{Bmatrix} M_m(x_i, s) \\ F(x_i, s) \end{Bmatrix}$ which makes the constraint matrix term

$$C_i(s) = \begin{bmatrix} 0 & 0 \\ \dfrac{ms^2(cs+k)}{ms^2+cs+k} & 0 \end{bmatrix}$$

The same procedure is followed to add rotational stiffness and rotational damping, but the equation of motion for the rigid mass is based on the sum of torques rather than forces, which adds an additional term to the constraint matrix to multiply the slope in the displacement vector. Thus, the complete constraint matrix for the cable attachments is

$$C_i(s) = \begin{bmatrix} 0 & \dfrac{Is^2(c_\theta s + k_\theta)}{Is^2 + c_\theta + k_\theta} \\ \dfrac{ms^2(cs+k)}{ms^2+cs+k} & 0 \end{bmatrix}$$

where linear and rotational stiffness and damping terms are included, and $c, c_\theta, k,$ and k_θ are the linear damping, rotational damping, linear stiffness, and rotational stiffness coefficients of the attachment point mechanism, which must be determined experimentally. For the cable attachments to ground, both *m* representing the rigid mass and *I* representing the mass inertia must be very large to approximate the constraint condition correctly. Since the constraint matrix multiplies the displacement vector, it can be added into the global stiffness matrix when the force balance at each node representing each attachment point is determined.

For the cabled beam, the cable is connected to additional model subsystems representing the beam, rather than the ground. For this constraint matrix, the nodes of the cable and the nodes of the beam must be included. Thus, the constraint matrix must fulfill the form

$$\begin{Bmatrix} Q_{cj} \\ Q_{cl} \end{Bmatrix} = -\begin{bmatrix} C_{jj}(s) & C_{jl}(s) \\ C_{lj}(s) & C_{ll}(s) \end{bmatrix} \begin{Bmatrix} u_j(s) \\ u_l(s) \end{Bmatrix}$$

where the forces are represented by Q, and j and l are the nodes for the two subsystem nodes connected through the spring attachment. The C matrices are the transfer functions that describe the attachment point with a linear and rotational spring, determined to be

$$C = \begin{bmatrix} 0 & k_\theta + c_\theta s \\ k + cs & 0 \end{bmatrix}$$

The attachment force affects both the beam and the cable, so the force balance for each node connected to an attachment point, whether it is on the beam or the cable, will have components from the attachment constraint matrix.

Figure 4.2 shows the frequency response function for the developed model with linear and rotational stiffness as compared to a pinned-end model, both shown in comparison to the experimental data for a solid steel rod using the same rod parameters. Experimental data is matched quite well by the undamped model that includes rotational and linear stiffness for the attachment points, but the undamped pinned model shows a larger discrepancy than should be expected for this simple case of a solid material with known properties. It is clear that the TC105 tab and cable tie attachment cannot be described adequately with a pinned connection. The pinned model is clearly inferior in terms of natural frequency agreement, underestimating the natural frequency for all three major modes shown.

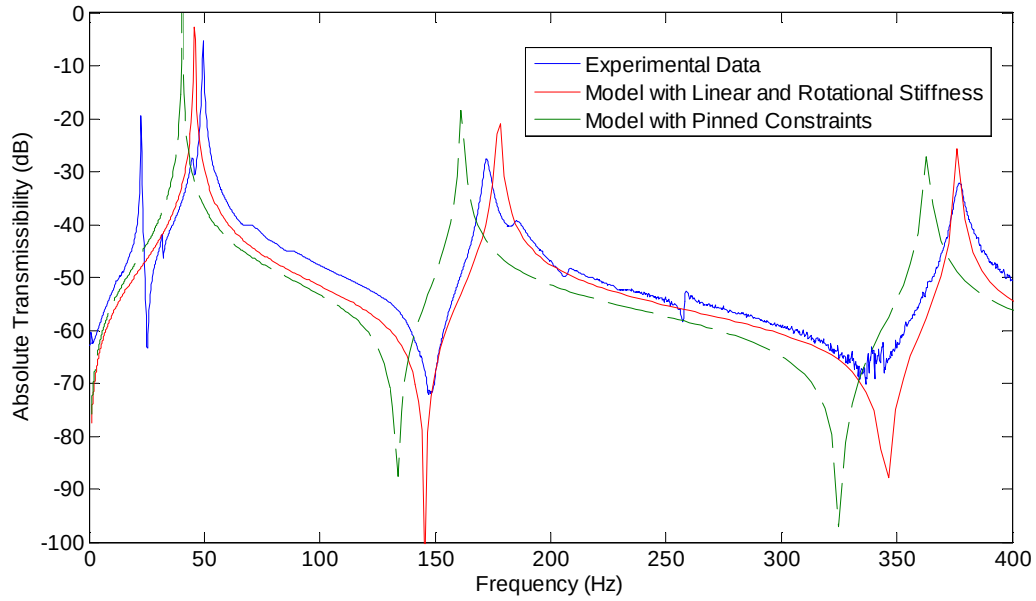

Figure 4.2: Comparison of pinned constraint with linear and rotational stiffness constraint model against experimental data for steel rod in test fixture, showing superiority of linear and rotational stiffness method in terms of natural frequency agreement.

Previous studies used a higher linear stiffness value than the values required for the tests herein, but this could have been needed to compensate for the lack of rotational stiffness, which adds stiffness, but in a different degree of freedom. Higher rotational stiffness shifts all frequencies up uniformly, while higher linear connection stiffness increases frequencies proportionally. Figure 4.3 shows the effect of including rotational stiffness on the model frequency response function for a 1X7 cable; even low values for rotational stiffness have the capacity to change the model response appreciably and may be able to capture the non-standard stiffness character of the cable attachment points. Chapter 5 contains details about the experiments that were conducted to determine the inputs for linear and rotational attachment stiffness used for the model constraints.

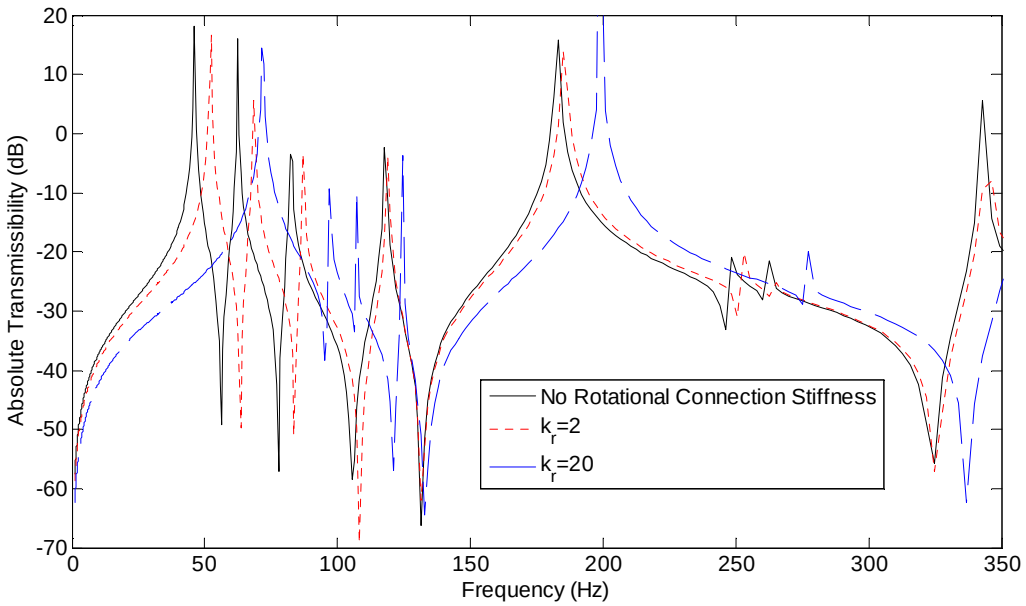

Figure 4.3: Effect of adding rotational stiffness to constraint matrices; adding rotational stiffness changes the model frequency response function even for small rotational stiffness values.

4.5 Sensitivity Analysis

In attempting to model cables on structures, there are a surprising number of factors that affect the results; of course the cable parameters have an effect on the cable response, but the input for the attachment point method also had a major effect. The frequency response was already shown to be insensitive to changes in shear modulus value in Chapter 3. Bending stiffness and mass terms have a greater effect. Figure 4.4 shows the difference for the full range of bending stiffness and mass values for an arbitrary cable. An increase in bending stiffness and decrease in density and area increases the natural frequency values with a steady shift.

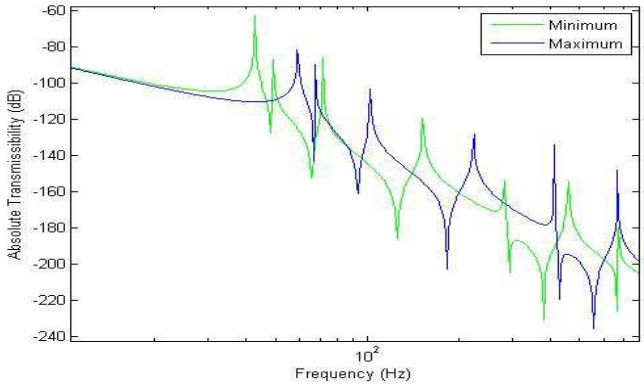

Figure 4.4: Frequency shift due to full range change in cable properties.

Even an order of magnitude change in bending stiffness did not change the first frequency appreciably, as shown in Figure 4.5. For this graph, the mass value was held constant and only the bending stiffness was varied.

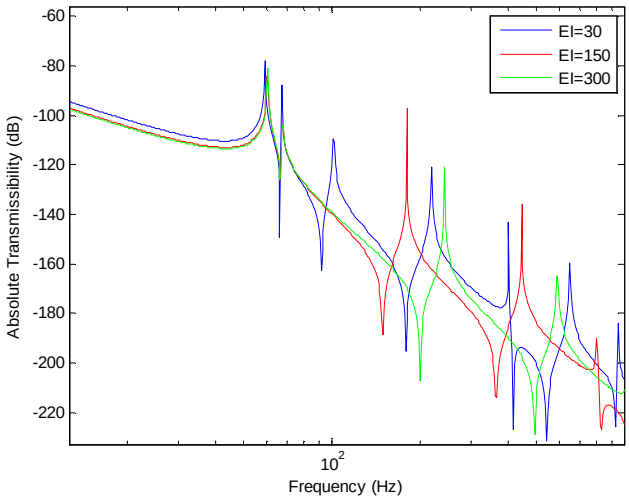

Figure 4.5: Order of magnitude changes in bending stiffness do not change the first frequencies appreciably, all other frequencies are simply shifted.

It was apparent from the preliminary investigation that the cable attachment points did not behave as an ideal pinned connection, so each connection was modeled as a spring and damper as described in the previous section. Past research hypothesized that the human construction factor was the cause of cable response variability, so for this study all of the cables were made on a planetary machine to ensure uniformity. However, there

was still variation from section to section for each cable type whenever the cable was reattached to the test fixture. This led to an investigation of the tie-down attachment stiffness described previously which found that the cable attachment stiffness varied by an order of magnitude over the frequencies of interest. Figure 4.6 illustrates the drastic difference due to attachment stiffness; rather than just shifting values, frequencies are split or combined as well.

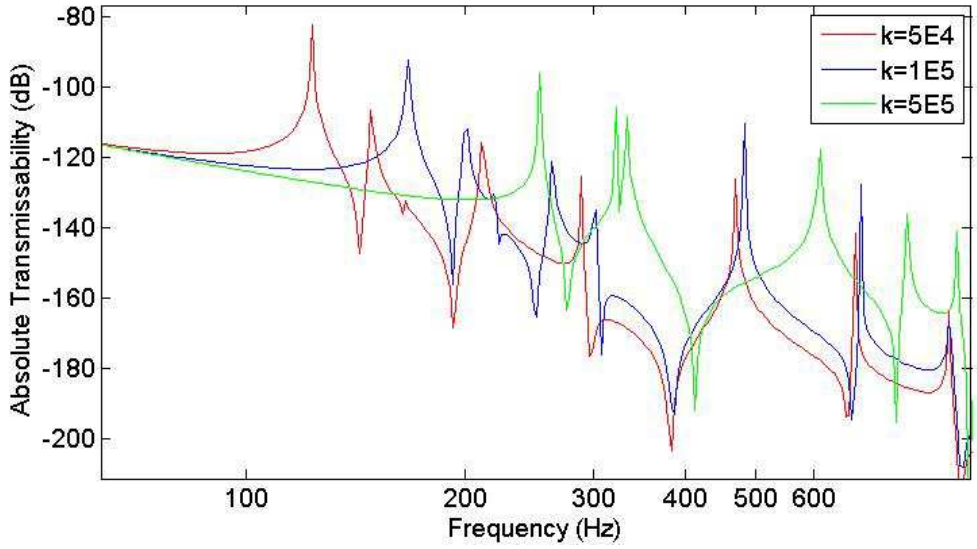

Figure 4.6: Order of magnitude changes in attachment point stiffness DO cause frequency shifts, splits, and combinations, even in the lowest modes.

4.6 Cabled-Beam Model

A great advantage of the distributed transfer function method is that it lends itself well to a system with many connection points. Therefore, once the cable model is made, it can be easily extended to model a cable attached to a structure as discussed in this section.

Figure 4.7 shows the model for the cabled beam structure with the driving point shown by a green arrow. This model was designed to match the experimental cabled beam structure discussed in the next chapter and shown with node locations labeled in Figure 4.8. The cabled-beam model consists of 8 nodes and 7 subsystems on the beam, and 8 nodes and 7 subsystems on the beam for a total of 16 nodes and 14 subsections. The ends of both the beam and the cable are modeled as free ends, and the attachment points were

modeled with linear and rotational stiffness as described in the previous section. Cable parameters were determined as introduced in Chapter 3.

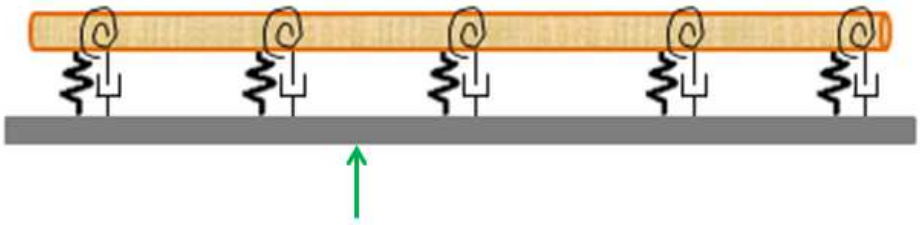

Figure 4.7: Top view of model for cabled beam with excitation point shown by arrow.

Figure 4.8: Cabled beam with node locations labeled; node 4 indicates excitation point.

The cabled beam model is run in exactly the same way as the cable model, one of the advantages of the DTFM; the major differences are that instead of the constraints that represent the attachment points being connected to ground, the constraints are connected to additional subsystems on the beam using the constraint matrices developed for spring connections between subsystems. Appendix C contains the MATLAB program files for the cabled beam model.

4.7 Model Verification for Known Cases

Before delving into modeling unknown cable responses, it must be shown that the developed method works for known cases, such as homogenous Euler-Bernoulli beams with various end conditions and multi-span beams. To that end, the cable model was run with arbitrary parameters and compared to published analytical solutions [118, 119, 120]. Table 4.1 shows the agreement between the first few natural frequencies of the modeled cases and published values. The Euler-Bernoulli cases had nearly identical natural frequency results, regardless of which type of end condition was modeled, and the five-section multi-span beam matched published results [120] very well considering the pin supports at the connection points were actually modeled with very stiff springs (spring

stiffness on the order of 10^9 was found to be a good approximation for a pinned end). The shear beam had to be compared to Timoshenko published beam values, and when considering that the Timoshenko beam also includes rotary effects, the agreement is good enough to instill confidence in the model to proceed forward. Changes in length and tension were also checked, and the model predicts frequency increases as expected for decreases in length and increases in tension.

Table 4.1 Verification of DTFM model for known cases.

	Published Value	**DTFM Model Value**	**% Difference**
Euler-Bernoulli Beam, Simply Supported [118] ρA=12.56 , EI = 179200, length=1			
1st Mode	187.48	187.51	0.01%
2nd Mode	750.03	750.03	0%
Euler-Bernoulli Beam, Free Ends [118] ρA =12.56 , EI = 179200, length=1			
1st Mode	425.10	425.06	0.01%
2nd Mode	1171.70	1171.70	0%
Published Timoshenko Beam, DTFM Shear Beam [119] ρA =12.56 , EI = 179200, $\kappa AG = 1.1016E8$, length=1			
1st Mode	184.70	186.00	0.70%
2nd Mode	707.83	726.99	2.71%
Euler-Bernoulli Multi Span Beam, 5 Equal Pinned Sections [120] ρA =1.1746 , EI = 138, length=0.7742			
1st Mode	26.81	26.79	0.08%
2nd Mode	27.44	27.42	0.07%
3rd Mode	126.53	126.38	0.11%
4th Mode	157.62	157.40	0.14%

Published values for double beam models are difficult to find in multi-span configurations, so verification of the cabled beam model was checked by comparing the cabled beam model with the attachment points unattached against the experimental beam

results. As a visual indication of agreement for the cabled beam model, Figure 4.9 shows the agreement between the model with no cable attached and the bare beam experimental data. Agreement for bending natural frequencies is excellent. Comparison of the model with solid rods attached to the beam provided further verification of the cabled beam model as discussed in Chapter 6.

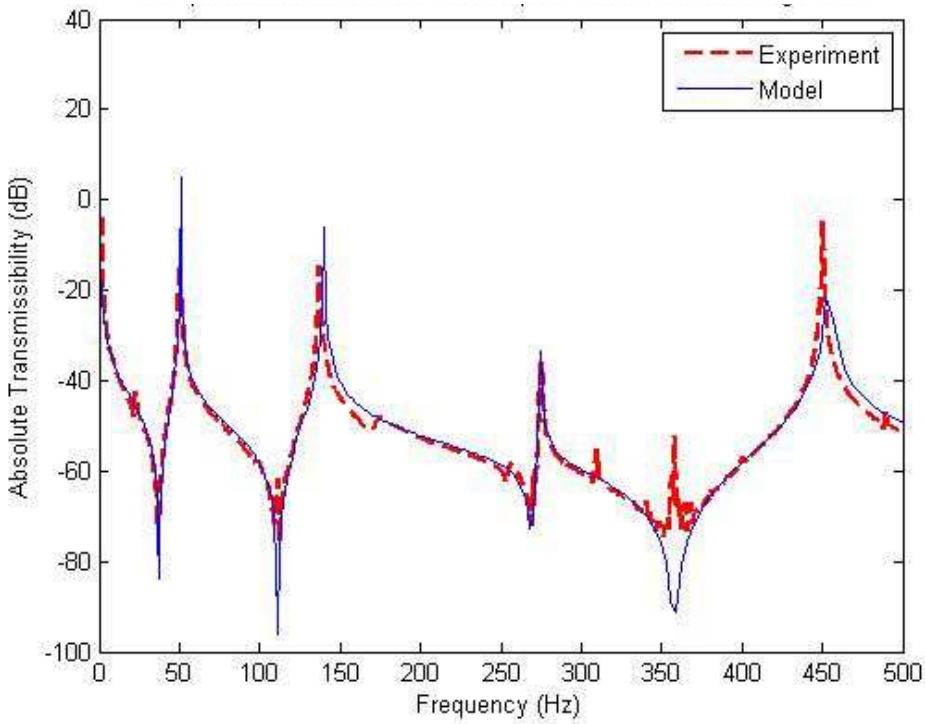

Figure 4.9: Comparison of bare beam model and experiment to show agreement before cable attachment.

4.8 Model Summary

The DTFM is well-suited to the investigation of cabled structures for its efficacy and accuracy for structures with repeated patterns and non-standard boundary conditions. This chapter presented an overview of the DTFM approach, the DTFM method for shear beams, the new equations derived to describe cables as shear beams with damping terms and tension included, and the addition of rotational stiffness and damping to the connection point model. In addition, the cabled-beam model was introduced, which built off of the cable model by incorporating the cable as a shear beam attached to an Euler-Bernoulli structure with connection points between the cable and beam that can include

linear and rotational stiffness and damping. The cable model was checked by comparing known shear and Euler Bernoulli values with the same inputs, and the cabled beam model was checked by comparing the model FRF of the bare beam (made by separating the cable portion of the model by removing the connection constraints) to the experimental FRF of the bare beam. Agreement was excellent for the tested cable and cabled beam models when run with known inputs and compared to published results for the same inputs. Combining the models developed herein with the cable parameters determined in Chapter 3 allows for complete modeling of cable and cabled beam frequency responses.

Chapter 5. Experimental Methodology

To gauge the utility of the cable parameter calculation methods and cable models, the model results must be compared to experimental data. This chapter discusses the various experiments conducted in support of this research. Experiments were performed not only for model comparison, but also for determination of attachment values and damping coefficients.

5.1 Preliminary Verification of Cable Effects

Although many sources cited the increasing influence of cables on lightweight structures [1, 2, 85], first-hand observation of cable effects were necessary before embarking on this multi-year study. A few common laboratory wires and cables were mounted to a simple aluminum beam with the TC105 tabs and TyRap 525M cable ties typically used for spacecraft cable management. A microfiber composite piezoelectric patch was bonded to the beam and used to excite the structure, and the response was measured at multiple locations with a non-contact laser vibrometer. Figure 5.1 shows the result for a cable that was approximately 7% of the total system mass, well within the limits for common spacecraft cable design. The frequencies are not merely shifted or damped for the cabled beam case; in some cases frequencies are split, heavily damped, or virtually undamped, with no immediately discernible pattern. This preliminary test showed that addition of cables to beams required further study.

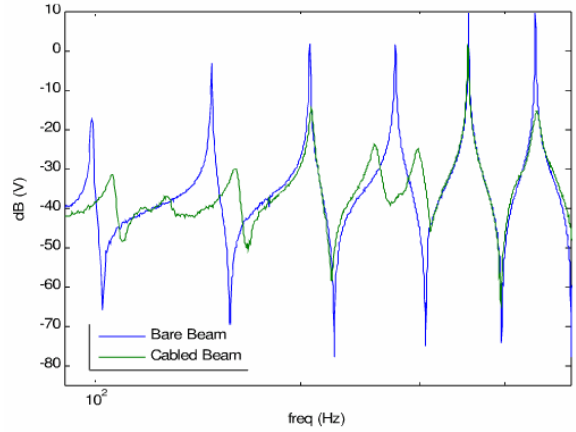

Figure 5.1: Comparisons of bare and cabled beam experimental frequency response functions showing variety of cable effects.

Additional experiments run at this time included variation of the number of tie-downs used for the cable mounting, different size cables, and comparison between cables and solid rods. The results made it clear that a beam's natural frequencies and damping ratios would certainly be affected by the addition of cables on the structure.

5.2 Experimental Setup and Development of the Standard Run

There are many factors that can affect a cabled system response; of course the cable properties themselves are an obvious factor, but the test fixture, cable attachment point technique, excitation input, and even the orientation of the cable in the test fixture all were found to have an effect [121]. Previous studies showed that cables had high variability between sections [3, 89], so it would be necessary to run many trials for each cable section to observe the range of responses. As such, initial experiments were designed to develop the "standard run" set up and procedure that would eliminate variations from test to test.

The spaceflight cable experiments described here were performed at the NASA Jet Propulsion Laboratory in a controlled environment to eliminate the low-frequency noise that plagued the experiments run previously at Virginia Tech. Working at the Jet Propulsion Laboratory also allowed access to test bed spaceflight cables for the preliminary studies, as shown in Figure 5.2, which made this work much more useful for space structures. Different cables were tested to find typical and well-behaved cables that showed repeatable frequency response functions. A scanning laser vibrometer was used to gather data over the entire cable, and a tensioned string was used as the attachment point from the shaker to the cable. The shaker was suspended by long chains so that vibration from the shaker would not travel through the inertial table to the cable test fixture. A load cell attached to the cable measured the input force from the shaker. Figure 5.3 shows the test set up for flight-suitable cables, and Figure 5.4 gives a closer view of the shaker connection through the load cell and the cable attachment point with a cable tie and TC105 tab. This mounting method was used both because it was theoretically similar to a pinned condition for modeling purposes, and because securing

cables to TC105 tabs with cable ties is common practice on space structures, and therefore has real application value as well.

Figure 5.2: Flight cables and test cables available for preliminary testing at JPL.

Figure 5.3: Preliminary cable testing of 1X18 test cable with suspended shaker.

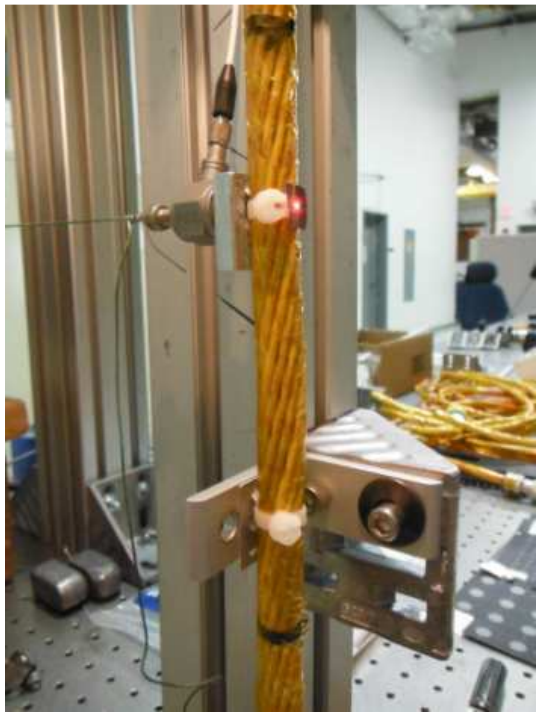

Figure 5.4: View of input force attachment method.

The natural frequencies of the suspended shaker and supporting structures were measured to ensure that they were not close to the cable frequencies of interest. Additional attachment points were set at 0.205 m above and below the 0.255 m test section to provide buffer zones that served to both mitigate end effects and mimic the reality of a cable harnessed structure. An additional laser vibrometer was set up perpendicular to the primary vibrometer to measure transverse frequency responses. The helical preliminary test cables were always fastened into the test fixture in the same way, with the inner side of the natural cable curve (coil plane) facing the shaker. Response was measured at the driving point for both the excitation plane and the perpendicular plane. Preliminary tests were run on a variety of cables to determine frequencies of interest and what parameters might need to be varied. For development of the standard run, a 1X18 (medium sized) heater cable made of M27500-26TG2T14 wire was cut into five sections of about 0.8 m each. From these tests, a "standard" test run was developed, which included the following controlled characteristics:

- 0.254 m test section length secured by cable ties tightened to setting 5 on cable tie gun (tight)

- 8.89 N of tension in the cable (hose clamp secured to top end of cable to distribute applied weight evenly)
- White noise excitation applied at 0.3 Volts
- Excitation applied at 8.3 cm from bottom of test section via 0.24 m tensioned string at medium DC offset
- Static cable displacement due to excitation string tension less than 1.6 mm
- Low pass 5kHz filter and Hanning window applied, 30 averages per test run

On each day of testing, the cable response was also scanned once at intervals of 0.9 centimeters, encompassing the entire test section, to visualize the mode shapes and ensure that the cable transverse modes were identified correctly. Figure 5.5 shows the test set-up for the four-point cable fixture, with the modal exciter (shaker) and tensioned string labeled, as well as the test section and buffer sections.

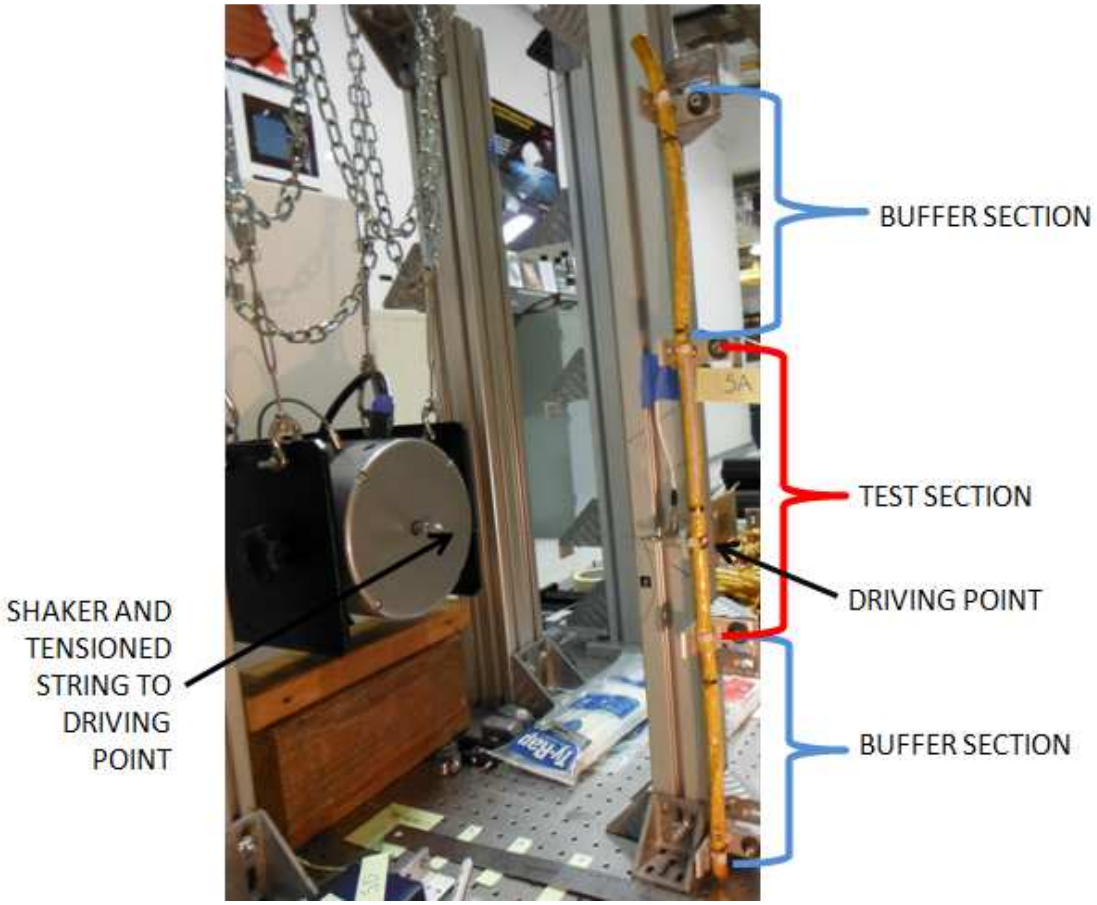

Figure 5.5: Four-point labeled cable fixture test set-up.

The various standard run tests deviated from the standard run only by the variable of interest for each test. The varied parameters were the type of excitation, the tension and length of the string used for the excitation connection, the tension in the cable, the type and tightness of the cable ties used at the test section ends, and the orientation of the cable in the test fixture.

5.3 Results from Preliminary Experiments

Initial investigation began with the test fixture and excitation connection. A slender narrow solid metal stinger was rejected in favor of a tensioned string after determining that the response was basically equivalent, but the string did not support a moment or lateral force, so only transverse force was received from the shaker.

Preliminary experiments on cables of varying sizes showed that some method was needed to quantify cable curvature caused by displacement from the excitation connection since initial research showed that cable bending stiffness is related to cable curvature. A laser displacement system was set up to measure the static displacement of the cable once the shaker string was attached and tensioned. Although it was initially hypothesized that the nearly straight cables would not experience wire slippage, the experiments showed that even the small amounts of curvature in the cables cause by the tensioned wire would cause some slippage. Curvature was largest for the smallest diameter cables.

All cables were wrapped with Kapton tape, but one in the preliminary tests was tied with lacing ties every 16 cm. This cable had less variability in its measured responses than non-tied cables, so this cable was chosen for testing variation. Lacing ties were included in all subsequent test cables as well.

A full set of tests was performed each day on cable section A over the course of two weeks; this full set included comparisons of excitation methods, excitation string length and tension, cable tension, and cable tie attachment. The responses of sections B, C, D, and E were also measured each day, and were run five times each at the conclusion of the

test to provide additional data. Testing of the cable orientation for each section occurred afterwards as it became apparent that the orientation may shift the frequency response.

5.3.1 Excitation Method Comparison

In an effort to verify that the excitation methods were not influencing the cable response in unexpected ways, a variety of excitation connections, methods, and signals were investigated. A random signal had to be used because the damped cable is a non-linear system and non-linear systems generate periodic noise. Signals for white noise and burst random from the shaker via the tensioned string were compared with hammer impacts, with the idea being that a similar response from the hammer impact would verify that the shaker connection was not affecting the response significantly. A Hanning window was applied for white noise signal and a rectangular window was applied for the burst random signal and hammer impacts. Hammer responses were tested with and without the load cell on the cable. As shown in Figure 5.6, the white noise and triggered burst random signals yielded nearly identical responses. The hammer impact responses bounded the string excitation responses, with the cable and load cell response showing a slightly lower natural frequency and the cable without the load cell attached showing a slightly higher frequency, as expected.

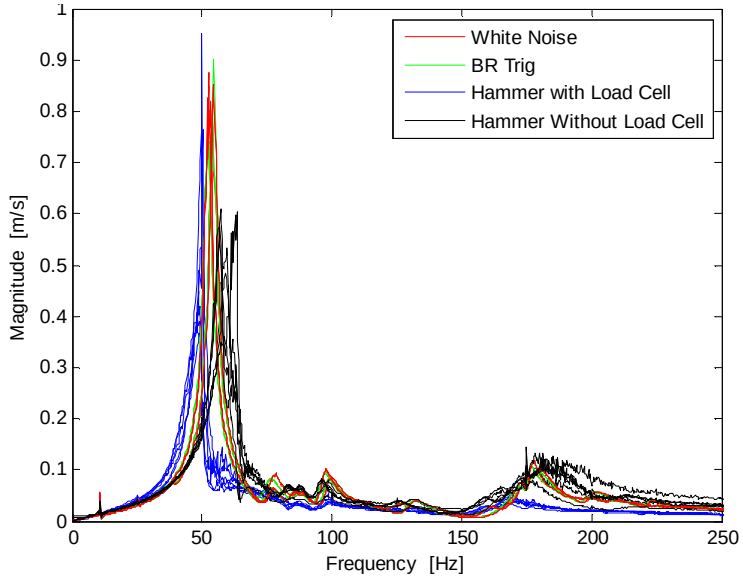

Figure 5.6: Frequency response functions of cable undergoing various excitation signals.

5.3.2 Excitation String Length and Tension Comparison

To determine whether the excitation string was adding frequencies to the cable's frequency response, the excitation string length was tested at 4, 10, 17, 24, and 45 centimeters, with the DC offset kept constant and distance between cable fixture and shaker varied as the string length varied (thus ensuring constant tension in the excitation string). At 24 cm and 45 cm, the DC offset was changed to measure the response for high, medium and low tension values, within the constraint of cable static bending less than 1 millimeter. Figure 5.7 shows the results from changes in string length for one representative day of testing; it is clear that string length is not affecting the cable response. Different string tensions had negligible effects as long as the cable was not displaced drastically due to the change in the string tension.

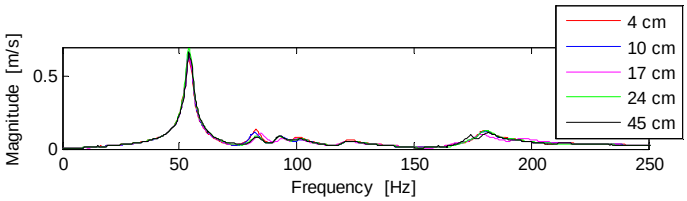

Figure 5.7: Comparison of excitation string length, showing no frequency dependence on string length.

5.3.3 Cable Tension Comparison

It is well-known that strings and beams exhibit higher frequencies at higher tensions, so it was expected that this same trend would be evident in cables. This test measured the cable response with tension in the cable of 1 lb, 2 lb, 3 lb, and 4 lb, and also tested a slack cable (0 lb) and a "hand tight" cable, designed to simulate the tension a cable would experience if it was pulled snugly during space structure assembly. It turns out that "hand tight" fit within the test weights used, which lends credibility to the use of these results for real world application. Figure 5.8 shows one of the test sets where the dissimilarities between the slack and tensioned cables are evident, especially around the second mode between 150 and 200 Hz. Figure 5.9 enlarges the response near the first mode for one of the test sets to show that increasing tension does shift the frequency higher, though not as uniformly as a single wire (based on previous tests). Again, the cable pulled hand tight appears to give a similar response and the slack cable's first natural frequency is lower than the others.

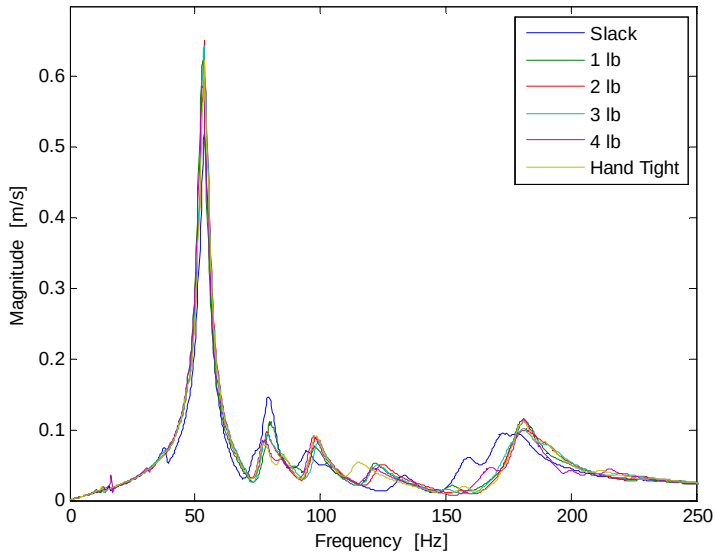

Figure 5.8: Representative cable tension test showing the difference between slack cable (blue line) and tensioned cables.

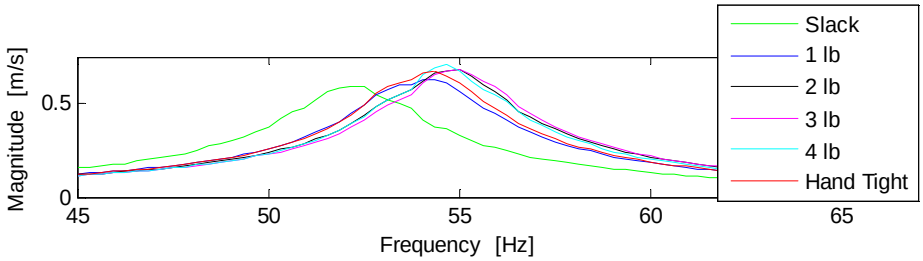

Figure 5.9: Cable response at first natural frequency showing the effect of cable tension.

5.3.4 Cable Tie Attachment Comparison

Cable ties (also known as zip ties) are commonly used for cable management on space structures. However, there is no universal standard for how to fasten these cable management ties, so the effect of different types and tightness of cable ties were investigated. Results for this test show that the type or size of cable tie is not nearly as important as how tightly the cable tie is fastened. Cable tie guns can be adjusted to fasten cable ties to a specific tightness; for this test, "tight" implies setting 5 on a Thomas & Betts Adjustable Tension Installing Tool WT-199 and "loose" implies setting 2. A "hand-loose" case was also tested, in which a cable tie was barely tightened enough to keep the cable from moving. This may simulate more of a pinned case as it allows the cable to pivot more. The hand loose case was significantly different near the second

frequency, as shown by the red line in Figure 5.10. Figure 5.10 shows the frequency responses for three trials for cables fastened with loose cable ties and cables fastened with tight cable ties; in contrast, Figure 5.11 shows the responses from cables attached only with tightly fastened cable ties, where "TR", "GB" and "Small" refer to different brands and sizes of cable ties. The tighter cable tied cables yield more uniform and repeatable results, despite the fact that the ties varied in type and size.

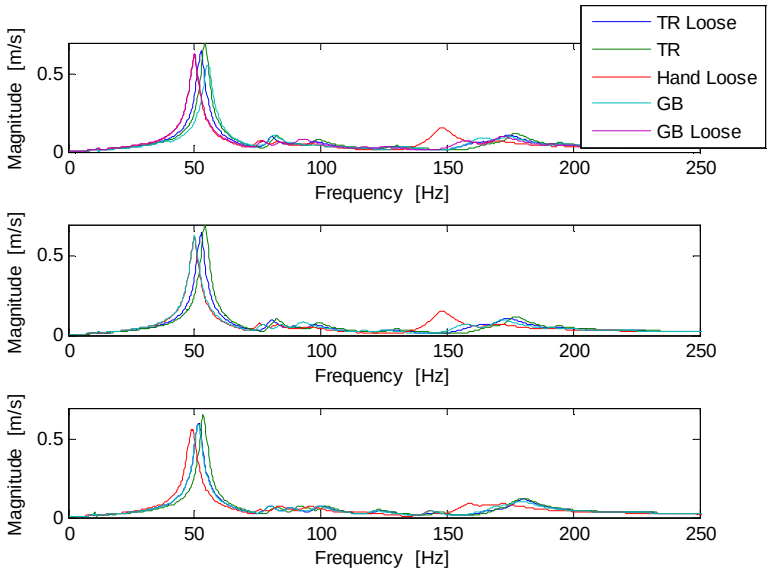

Figure 5.10: Comparison of loose and tight cable ties showing the variation due to cable tie tightness and the significant difference for hand-loose attachment (shown by red line).

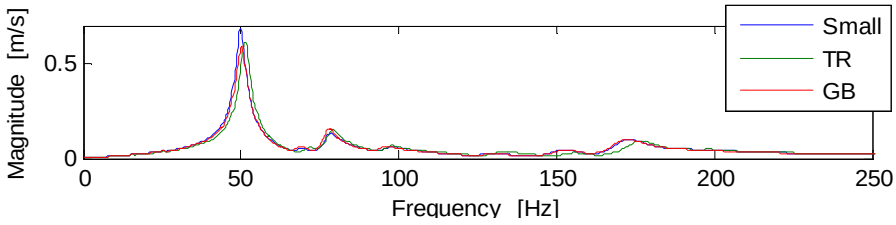

Figure 5.11: Comparison of tightly fastened cable ties of different size and type exhibiting the increased agreement between test runs as compared to loosely tightened cable ties.

5.3.5 Effect of Cable Orientation in Test Fixture

Although every effort was made during testing to orient the cables in the same way, with their natural coil toward the shaker, testing consistently showed two first frequency

response patterns which dictated further investigation of the effect of cable orientation. The tests show that the cable orientation in the test fixture was responsible for a significant frequency range near the first natural frequency. This variation in the first natural frequency was similar to the variation between cable sections as discussed in the next section. Figure 5.12 shows the frequency response function for two trials of a single cable with 90 degrees of rotation difference between trials. Figure 5.13 shows the shift in first natural frequency as compared to the angle of cable orientation in the test fixture; 0 degrees was intended to be the coil-plane parallel to the excitation with the coil facing toward the shaker, but shifting the 0 degree point for the cables showed greater similarity in the frequency-angle relationship shape. This is a good indication that the differences between cable sections shown in the next test may be due to different internal stresses in the cable; although all were aligned in the same way, different sections of cable may have varying internal stress tensors arising from their location in the overall cable and coiled storage. To eliminate this issue for the standard run, contra-helical cables were obtained that had no induced natural curvature from the wire lay direction. The cables procured for later testing were stored straight and never bent so that no inherent curvature would be developed.

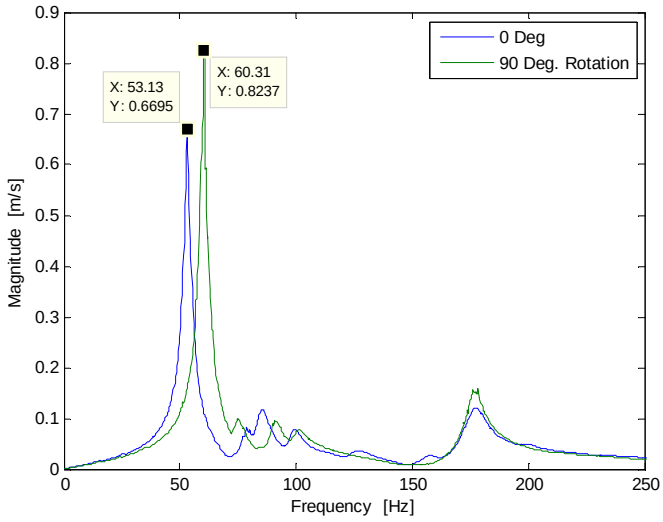

Figure 5.12: Frequency response function for a single cable at coil plane and 90 degree rotation from coil plane.

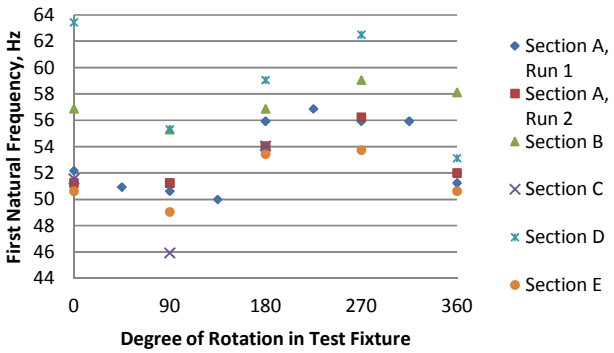

Figure 5.13: Approximately sinusoidal relationship between first natural frequency and cable fixture angle; chart angle shifted to show aligned sinusoidal trend pattern.

5.3.6 Comparison of Cable Sections

As the preliminary tests were run, it was evident that the run-to-run variation even for a standard run of the same cable section was significant. Therefore, standard runs for the same cable section and different sections of the same cable were compared. Figure 5.14 shows the five cable sections, all from the same length of cable, cut into five equal (and assumed identical) sections. The next figures show the results, with a very clear separation between natural frequencies for the A,C and E cables as a group and the B and D cables.

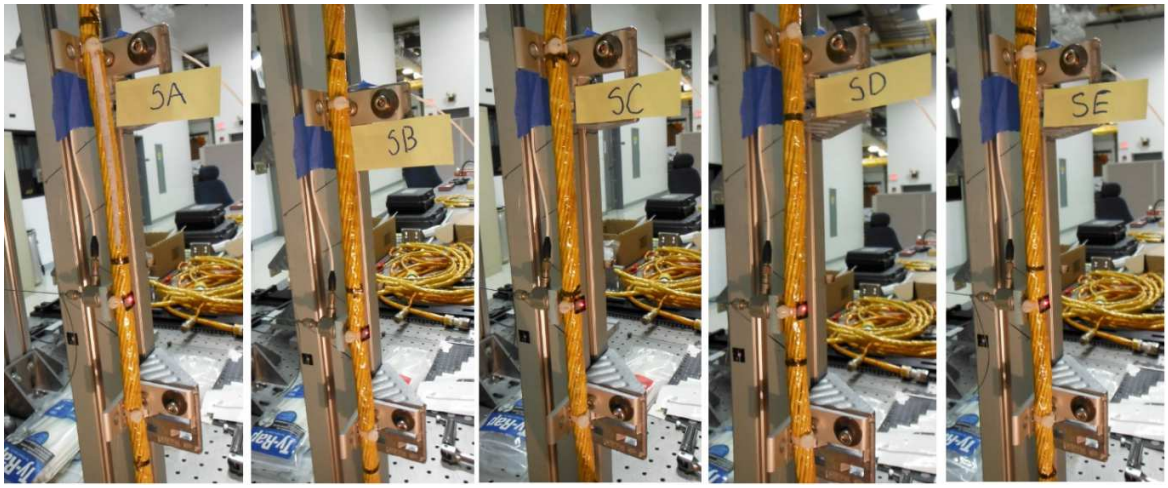

Figure 5.14: The five sections of 1x18 cable used for section comparison testing.

Figure 5.15 shows the variation for a single section of cable (Section A, the section used for all variability tests). While the first and second natural frequencies appear in roughly the same place, there is slight variation in the frequency values and significant variation in the amount of damping (as represented by peak height). The modes between 70 and 100 Hz showed great variation in amplitude and number of frequency peaks.

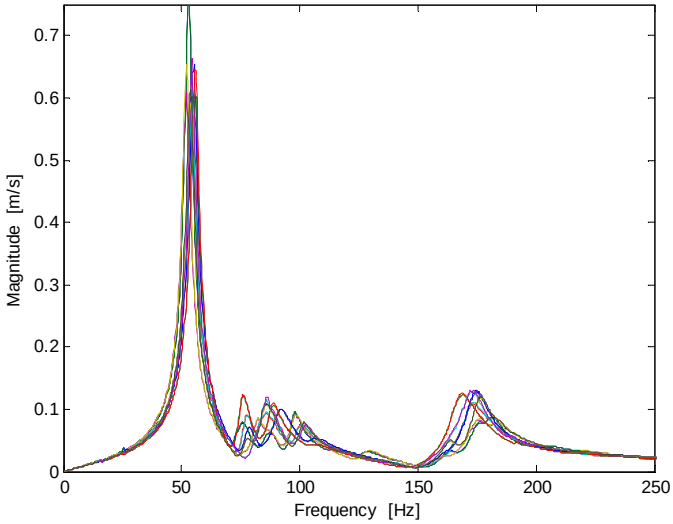

Figure 5.15: Frequency response functions for 14 standard runs of cable section A, showing the variation of response even for a single cable section, particularly in the intermediate modes between 70 and 100 Hz.

Figure 5.16 shows the comparison between different sections of the same cable. As evidenced in Figure 5.14, the only noticeable difference in these cable sections was the location of the black cable lacing ties relative to the driving point location. The sections were cut sequentially from a single 3.8 m piece of spaceflight-like cable, and the Kapton overwrap and lacing ties kept the helical cable structure intact. Lay angles were similar for all cable sections, and no visible differences were apparent. All cables were kept in a clamped test fixture overnight before first testing, and were stored hanging to prevent excessive curl from being stored coiled. The same amount of testing runs were performed on cables B, C, D and E, with A tested more often due to its use in the variability testing. Overall, cables A and D showed the most similarity from run to run, and cable C showed the least. Figure 5.16 plots the runs of all cables together, where all

runs of the same cable section are plotted in the same color, clearly showing the two frequency peaks near the first mode and three frequency peaks near the second mode. All of these tests were run on the same day with the cable removed from the test set up and reattached between each run.

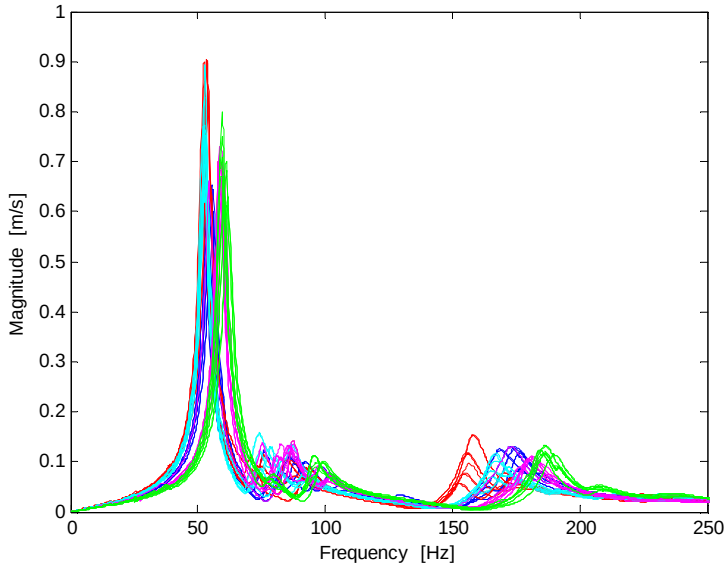

Figure 5.16: Frequency response functions for 10 runs of each 1X18 cable section showing the dependence of frequency on cable section.

The cable scans were valuable in verifying the first and second major mode shapes and thus, natural frequencies. The trends for each test were fairly clear when analyzed at the conclusion of each day's testing, but when responses and frequencies were compared from day to day, there was great variation, even between "standard" runs. It was evident that tests which required the cable to be removed and then replaced in the test fixture had the greatest variation, showing that the attachment point characteristics have a significant impact. Variation due to changes in the test set up were not significantly larger than variations between cable sections.

An interesting result from the simultaneous measurement of the perpendicular vibrations was the observation that the symmetrical-appearing helical cable does not have the same natural frequencies in both directions. The cable is actually stiffer in one plane, which is not intuitive. It is hypothesized that the twisting of the cable, coiled storage and/or

Kapton overwrap method may be responsible for this lack of symmetrical response. The cables obtained for testing were contra-helically laid, kept straight throughout their manufacture and testing, and were wrapped with Kapton by machine, thus eliminating the frequency dependence on fixture orientation.

5.3.7 Preliminary Test Summary

Conclusive results were obtained for the tests involving string length and tension, cable tension, and cable tie attachment. It was clear that for small cable deflections, the length of the excitation string and tension in the string were not affecting the cable's dynamic response. Cable tension did change the frequency response slightly, with a general trend of higher tension corresponding to higher natural frequencies. This test also showed that "hand-tight" cables were on par with 1-4 lbs of tension in the cable, and that slack cables behave differently and may have more non-linear attributes. Cable tie brand, type and size were not important factors, but the tightness of the cable tie attachment was. Therefore, cable tension and cable tie tightness should be controlled for future testing to reduce variation between standard runs. In addition, cable angle in the test fixture should be noted, as comparison between cables may require different orientations to test the same cable plane. Later testing used contra-helical cables which did not show the same dependence on orientation in test fixture.

The excitation method of the cable went through several iterations, starting with a long solid stinger, hinged stingers, and eventually settling on the tensioned string used for these tests because of its lack of support for moments or lateral forces, keeping these unwanted inputs from being applied to the cable. The hammer tests bounded the tensioned string random excitation results, which indicated that the shaker attachment was not unduly affecting the test set up. The tests conducted yielded good representations of the cable dynamics, with little interaction from the support structures. Table 5.1 lists the findings from the preliminary cable tests.

Table 5.1 Conclusions from preliminary cable tests and development of standard run.

Test Parameter	Conclusion	Option Used for Standard Run
Excitation method	White noise and burst random excitation produced similar results, bounded by hammer impact tests with and without load cell.	White noise excitation
Excitation string length	No dependence on string length.	0.24 m tensioned string
Excitation string tension	Dependence on excitation string tension only occurs if cable is displaced; range of DC offset to change tension was not large enough to displace cable.	Medium setting on DC offset, causing string to be snug without causing displacement of cable
Cable tension	Slack cables behave differently than tensioned cables; increasing cable tension slightly increases frequency.	8.89 N of tension applied while cable is loaded in fixture
Cable tie size	No dependence on cable tie size.	TY-Rap 525M 7" cable ties used.
Cable tie tightness	Loose cable ties produce different dynamic response than tight cable ties and show less repeatability from trial to trial.	Cable ties tightened to uniform tight setting with cable tie gun.
Cable orientation	Helical cables show a correlation between natural frequency and orientation of the coil plane.	Cable orientation must be controlled if helical cables are used; contra-helical cables were used for all subsequent testing to eliminate this variation.

5.4 Unbaked Cable Tests

Once all preliminary tests were completed and the standard run was developed, the standard run could be applied with confidence to test multiple samples of each of four different cable types to compile a database of cable frequency responses and provide pre-bakeout data for comparison.

As discussed in detail in Chapter 3, four cable geometries were investigated: single strand cables of small (1X7), medium (1X19) and large (1X48) sizes, and a large multi-strand (7X7) cable. Five samples of each cable type were provided at cost from Southern California Braiding Co., made with MIL27500-26TG2T14. The cables were made on a planetary machine, were tied every 4-6" with white lacing ties, and were machine-wrapped with Kapton with a 50% overlap. Figure 5.17 shows the flight-quality space cable samples used for the cable tests.

Figure 5.17: Samples of each of 1X7, 1X19, 1X48 and 7X7 spaceflight cables, in sets of five samples for each cable; single samples laid out to show uniformity of Kapton wrap.

One change from the preliminary test cable type was the use of machine-manufactured contra-helical cables instead of helically twisted cables. As Figure 3.3 illustrated, the helically twisted cable, in which all of the layers have the same left-hand lay, has an inherent curvature when it is in a relaxed state. The contra-helical cable alternates lay direction for each layer, and thus hangs straight in a relaxed state. This straightness was desirable for two reasons: first, it was shown previously that the curved plane of the helical cable resonated at a different frequency than the perpendicular plane, and second,

since the test fixture is straight, attaching a curved cable with cable-ties introduces elements of torque to keep the cable straight, which are not accounted for in the model (although they could be introduced as applied moments at the connection nodes) and are therefore undesirable.

The test cables were mounted to a Bosch test fixture with cable-ties and TC105 tabs, following the standard run procedure developed previously. Excitation was provided via a suspended modal shaker and tensioned wire, and output was measured with a non-contact laser vibrometer. The 20 cable samples were tested over several weeks, with care taken to keep the cables straight and never excessively bent (since that could cause individual wires to slip into a new equilibrium position). Between 14 and 18 trials were run for each cable section with the output measured at the driving point, and at least 4 scans were taken for each cable to show the operating deflection shapes at each resonance. These tests resulted in over 50 frequency response function test runs per cable type, presented in the results section of this work.

5.5 Cable Bakeout Procedure

Since the bakeout process required for flight hardware was reported to change cable stiffness, a comparison of cable dynamic response before and after bakeout was conducted. Common bakeout procedures include planetary protection bakeout, necessary for biological decontamination, and low-Earth orbit bakeout, used for objects that will not be venturing further than 2,000 km from the Earth's surface. A low-Earth orbit bakeout was used for this study, as cabling on satellites is of particular interest, and satellites are maintained at low-Earth orbit.

To do so, the three cables from each section with the most consistent results from the unbaked cable trials were selected and baked out at 105 degrees Celsius for 72 hours, the requirements for bakeout for low-earth orbit. Mass of the cable was measured before and after the bakeout process with no evident change recorded. Figures 5.18, 5.19, and 5.20 show the cables on the bakeout rack, the bakeout chamber used for the test, and one day's

worth of thermograph record that showed the temperature and pressure readings for the chamber.

Figure 5.18: Cables on bakeout rack.

Figure 5.19: Vacuum bakeout chamber.

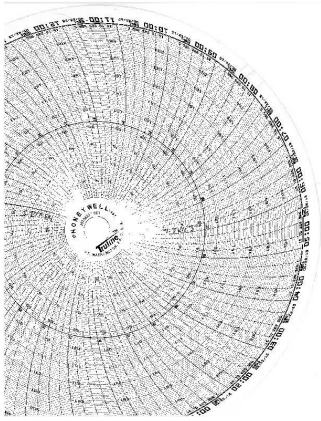

Figure 5.20: Bakeout thermograph record.

5.6 Two-Point and Four-Point Fixture Baked Cable Tests

Once the cable samples were baked out, they experienced additional rounds of testing in two different test fixtures. First, the four-point fixture tests were repeated for a direct comparison; the same standard run procedure was followed for the baked cables in the four-point fixture, with 10-15 trials per cable section, measured at the driving point, and 6 scans run per cable to compare the operating deflection shapes and make sure that the frequencies were being directly compared. Figure 5.21 shows the scan comparisons for the major first and second modes of the 1X19 cable; although the natural frequency for

this mode shape is 15% lower for both modes after bakeout, the mode shape is identical before and after bakeout, which makes it clear that the frequency values can be compared since they are identifying the same mode. A slight reduction in amplitude is apparent for the second mode, identifying an increase in damping. The complete results from the baked out cable tests are presented in Chapter 6 as a direct comparison with the unbaked cable tests.

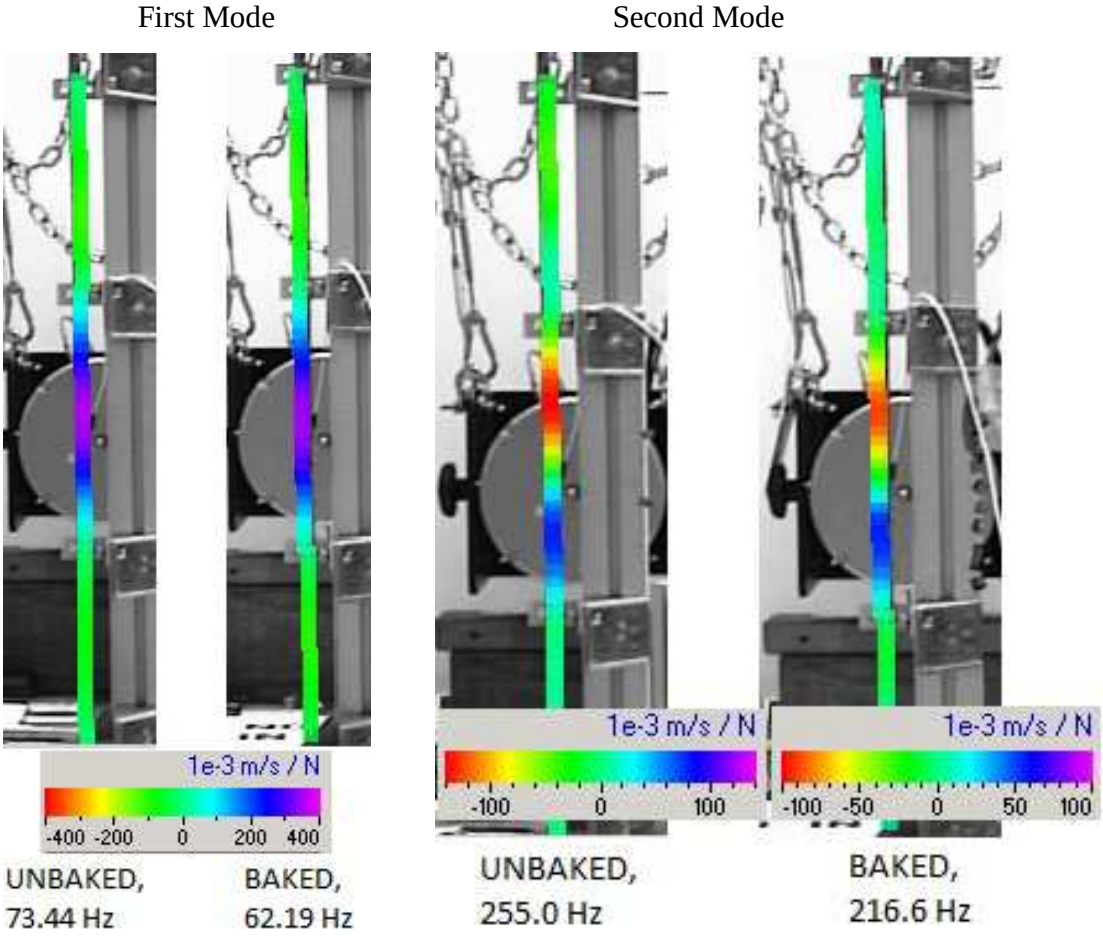

Figure 5.21: Scan comparison showing the mode shape for the unbaked and baked cable for the major first mode (left) and second mode (right); despite a frequency reduction of 15%, mode shape is the same between pre- and post-baked cables.

When comparing the four-point fixture tests to models, the uncertainty in the attachment stiffness was problematic. Therefore, a two-point fixture was designed that would use only two attachment points closer to the ends of the cable. This would reduce some of

the uncertainty due to the attachment points and would allow for comparisons between calculations of the cable frequencies with pinned ends to ensure that the calculated cable parameters were effective for cable modeling, as well as reduce any effects from the free ends of the cable. Figure 5.22 shows the 1X48 cable in the two-point test fixture. For the two-point fixture tests, the standard run was followed with the only change being the location and number of the attachment points. Five scans were run for each two-point fixture test, giving not only frequency response data, but mode shape data for all trials. When the two-point and four-point test data was used in conjunction with the attachment point stiffness experiments described in Section 5.7, a complete characterization of the entire cable and test fixture was achieved with confidence.

Figure 5.22: 1X48 cable in the two-point test fixture.

5.7 Attachment Point Experiments

When comparing the results from the models developed in Chapter four to the four-point fixture cable experiments described herein, it quickly became apparent that knowing the

cable parameters was not enough for accurate modeling. Standard "pinned" or "clamped" boundary conditions did not adequately describe the cable connection points, so another contribution of this work was the determination of attachment point characteristics. Although several experiments were conducted by the Air Force Research Laboratory to establish tie-down stiffness of the attachment points, an overall conclusion from [1] was that a better methodology was needed to establish tie-down stiffness.

The attachment points for the cable and cabled beam consisted of an aluminum TC105 tab and a cable tie, tightened to a specific tension setting with a cable tie gun. Figure 5.23 shows the cable attachment to "ground" (actually a large Bosch test fixture with an easily identifiable fixture frequency).

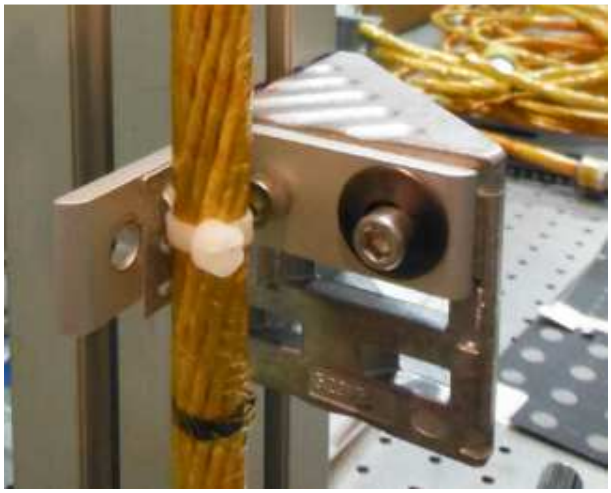

Figure 5.23: Cable secured to support via cable tie and TC105 tab.

Several sets of experiments were required to determine the linear and rotational stiffness of the attachment points to use as the model constraint inputs. First, static deflection tests measured the displacement of a small piece of cable in the attachment fixture when a load was applied to the center of the cable, and rotational stiffness was determined by applying a moment to the cable attachment and measuring the angular deflection. Next, dynamic stiffness tests measured the deflection of the small piece of cable due to sine wave excitation. Plotting the force-displacement ellipses gave information about the damping and linear stiffness of the attachment. However, both of these tests had values that varied by several orders of magnitude depending on frequency, so a more applicable

test was conducted in which solid rods of known material properties were tested in the two-point and four-point cable fixtures using the same attachment methods.

5.7.1 Direct Static and Dynamic Measurement

Experiments to measure the attachment stiffness directly included both static and dynamic measurements of displacement for an applied force. The static test involved hanging weight from a small section of cable mounted with the typical attachment method as shown in Figure 5.24. Different weights were applied to non-stretching string snugged around the cable alongside the cable tie so that the force would be applied to the edge of the cable against the TC105 tab; Figure 5.25 shows the cable harness method that was determined to most effectively transmit the force as closely as possible to the intended location at the cable-attachment point interface. Sections of small, medium and large cable were used, as well as a small piece of solid Acetron rod. These experiments resulted in values of 0.1 * 10^4 N/m for the stiffness of the attachment for the multi-stranded cable, 1-2 *10^4 N/m for the small and medium cable sections, and 0.5-2 *10^5 N/m for the Acetron piece. As this was one of the initial experiments run to determine attachment stiffness, the range and discrepancy between trials and cables was concerning, so further experiments for linear stiffness were conducted using dynamic excitation. Results for rotational stiffness had much less variation; regardless of cable type used, when a force was applied at one end of the cable section to cause a moment and the angle of deflection was measured, the result for all cables was between 1 and 3 N-m/rad, so the average value of 2 N-m/rad was used for the rotational stiffness model constraint input for all cables. Rotational stiffness was measured by hanging the various weights from one side of the cable and measuring the resulting upward deflection at a specified distance on the other end of the cable so that the resulting angle of rotation could be determined and used in the equation $M = k_\theta \theta$, where M is the applied moment, θ is the resulting angular displacement, and k_θ is the rotational stiffness.

Figure 5.24: Static deflection test using laser displacement sensor to measure the deflection of the cable tie from an applied force due to hanging weight.

Figure 5.25: String harness for application of force for linear stiffness static and dynamic testing.

To get more information about the linear stiffness of the attachment, dynamic direct measurement tests were performed. For these, the same cable attachment was used, but instead of a weight, the loading string harness was attached to a dynamic load cell and shaker. The shaker could be driven at varying amplitudes and frequencies, with the laser

displacement sensor measuring the resulting deflection in real time. The force and displacement curves were plotted to form hysteretic ellipses where the angle of the axis of the resulting ellipse is related to the slope and the area of the ellipses is related to the damping loss. Figure 5.26 shows just a few of the test set up iterations that were used for these tests, and Figure 5.27 shows the resulting hysteresis loops for shaker excitation of a sine wave at 1 Hz with varying amplitudes, where larger amplitudes result in larger loops. Thus, damping in the attachment point is related to both frequency and amplitude of the input force.

Figure 5.26: Test fixture iterations for dynamic testing of the attachment point linear stiffness.

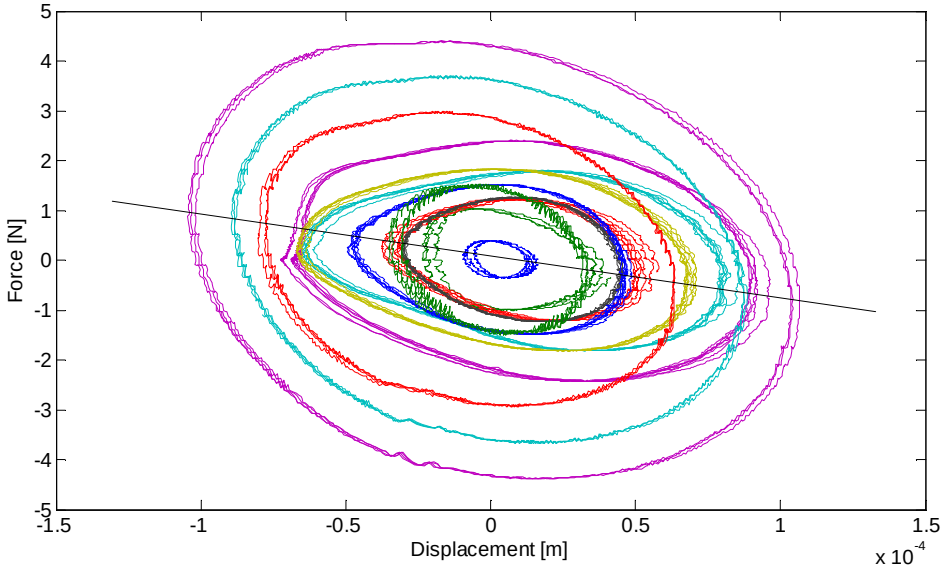

Figure 5.27: Force versus displacement hysteresis loops for various amplitude 1 Hz sine excitation input to TC105 tab and cable tie assembly.

Force-displacement plots were created for input voltage amplitudes of 0.1, 0.3, 0.4, and 0.6 volts for input frequencies of 1, 10, 40, 50, 70, 85, and 100 Hz. Figure 5.27 is an especially good example of the results, since the 1 Hz input is close to static. Higher frequency results showed much greater variation in slope values for different input amplitudes. A plot of the measured average attachment stiffness for the different frequency values finally offered some insight; Figure 5.28 shows the attachment stiffness trend rise and then fall over the range of frequencies tested, with a distinct downward trend evident for higher frequencies. Theoretically, as frequency input increases, the input amplitude decreases and cable motion would be on the level of the individual wires rather than the cable as a whole. Based on this data it is reasonable to infer that the higher frequency inputs could have lower attachment stiffness since the individual wires are moving within the cable tie and are less constrained, as opposed to the lower frequencies that would be exciting the cable as a whole which is constrained more completely by the cable tie that encircles the cable as a whole.

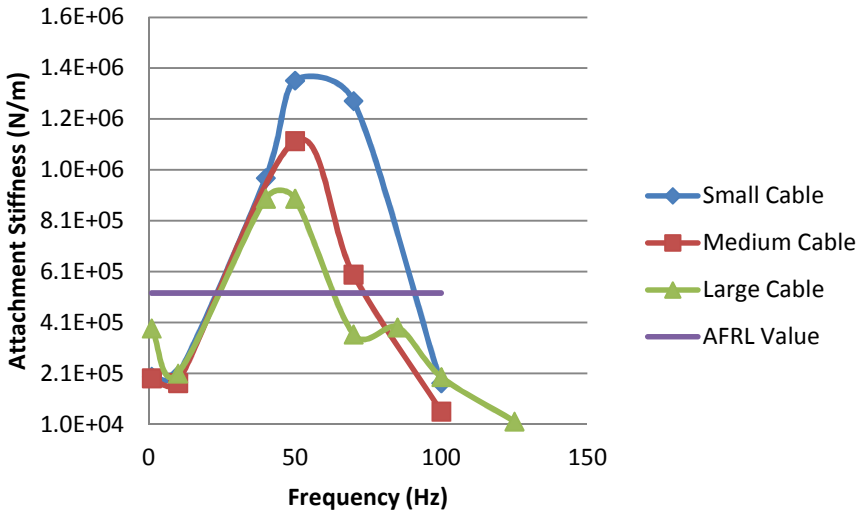

Figure 5.28: Measured stiffness of the tie-down attachment from dynamic measurement showing order of magnitude range over a relatively narrow frequency range.

Of particular interest for this study was the comparison for the value used for linear attachment stiffness by the AFRL; past studies determined tie down stiffness through experimental comparison of a known system, but the stiff value calculated for finite

element analysis in [1] and shown as a horizontal line in Figure 5.28 did not represent the experimental connection points well for these experiments (although it did represent the average stiffness over the frequency range quite nicely).

Overall, the direct measurement techniques provided useful values for the rotational stiffness, concrete evidence that the attachment points add damping to the system based on the large hysteresis loops, and confirmation that the linear attachment stiffness is a function of excitation frequency and cable size.

5.7.2 Rod in Fixture Tests

The direct measurement experiments certainly added to knowledge about the characteristics of the attachment points, but further testing was needed in order to have a single constraint input value for the developed models. Solid rods of tool steel and Acetron GP of similar size to the test cables were put in the same attachment point configurations as the cables had been tested in, with two attachment points (attached at ends only) or four attachment points; Figure 5.29 shows the tool steel and Acetron rods in the different fixtures. Stainless steel and brass rods were also tested. The properties of the solid rods were known, so the attachment point stiffnesses were the only variables. Attachment point stiffnesses were tuned until the model frequency response function and mode shapes for the modeled rods matched the experimental data for both fixtures. The required stiffness for the very flexible Acetron was lower than the stiffness required for the tool steel; this gave a clear indication that the attachment stiffness would vary depending on the cable size and flexibility. Bending stiffness of the tool steel rod was significantly higher than any of the cables, and its attachment stiffness value was ~10^6 N/m. Bending stiffness of the Acetron rod similar to the bending stiffness of the 1X19 and 7X7 cables, and its attachment stiffness value was ~10^5 N/m. These provided confirmation of the values used determined from the dynamic tests. Since the cable is modeled as a free-free beam with attachments to ground, when the attachment stiffness is very low (essentially zero), there is a rigid body mode; as the stiffness increases, the rigid body mode disappears. If the attachment stiffness is further increased, the initial

frequency increases and then splits into multiple frequencies, which matched with the larger cables' responses well.

Figure 5.29: Tool steel in four-point fixture and Acetron in two-point fixture for rod-in-fixture tests designed to determine attachment point stiffness.

5.8 Cabled Beam Tests

Since the motivation behind this research involves modeling cables on space structures, dynamic responses were also tested for cables attached to a simple structure, an aluminum beam measuring 0.0064 m by 0.102 m by 0.8 m. The beam was sized so that the four types of test cable attached would represent the 4-30% typical cable mass ratio for space structures [1, 2]. Table 5.2 gives the cable mass percentage for the cabled beam system for each case, showing that all cables were in the typical range for space structure cabling. Five tie-down attachment points were used at 0.04, 0.22, 0.4, 0.58, and 0.76 m locations, holding the cable off the beam at a height of 0.015 m. Care was taken to ensure that the cable did not contact the beam in any other location, as that would lead to significant variation and possible non-linearities in the response. The beam was suspended to approximate free boundary conditions at each end with the supporting

strings attached at two nodal points to minimize swinging motion of the beam. The length of the supporting strings were very long to give a rigid-body mode swinging frequency of 0.56 Hz, well below the first bending frequency of the beam which was around 50 Hz. The beam was excited via modal shaker with a long solid stinger or tensioned string terminating in a load cell screwed into a very small tapped hole in the beam. The mass of the load cell was very small compared to the cables. A 0.1 volt white noise excitation input was used to excite the beam; excitation of the cable was achieved only through the five connection points between the beam and cable. The beam was first tested without the cable to verify that the response was as expected for a free beam and could be modeled correctly with the cabled-beam model without a cable, as successfully shown in Chapter 4. The bare beam bending frequencies occurred at 50, 137, 277, and 450 Hz, which are referred to as the major structure modes to distinguish them from the smaller amplitude additional frequencies caused when a cable is added to the structure.

Next, a solid rod was attached to the beam and the response measured. This was largely to confirm the attachment point stiffness values were still valid from the rod in fixture tests conducted to determine the attachment stiffness. Finally, each type of cable was attached to the beam using tight cable ties and the frequency response for the cabled-beam systems were recorded. A dense scan was run for the bare beam and the beam with each cable attached; the dense scan had 125 points in five rows of 25 points each, in two rows above the cable, a row on the cable, and two rows below the cable. Ten additional sparse scans were run with 57 points in three rows of 19 points each, with a row above the cable on the beam, a row on the cable, and a row below the cable on the beam. Figure 5.30 shows the cabled-beam test set up. Figure 5.31 shows the transfer function for each of the four cabled-beam systems as measured on the cable coincident with the driving point on the beam. Figure 5.32 shows the operating deflection shapes for the 7X7 cabled beam as experimentally measured from a dense scan. The dominant major structure beam modes are easily visible (i.e. modes 1 and 3), but additional mode shapes are also present due to the cable's interaction with the beam; in these modes the motion of the cable can be seem relative to the beam deflection (i.e. modes 2, 4 and 5). Comparison

between the cabled-beam model and the experimental data frequency response functions and mode shapes are presented in Chapter 6.

Table 5.2 Cable mass percentage for cabled-beam system.

Cable Type	1X7	1X19	1X48	7X7
Cable Mass % of System Total Mass	5.0%	12.2%	24.5%	26.5%

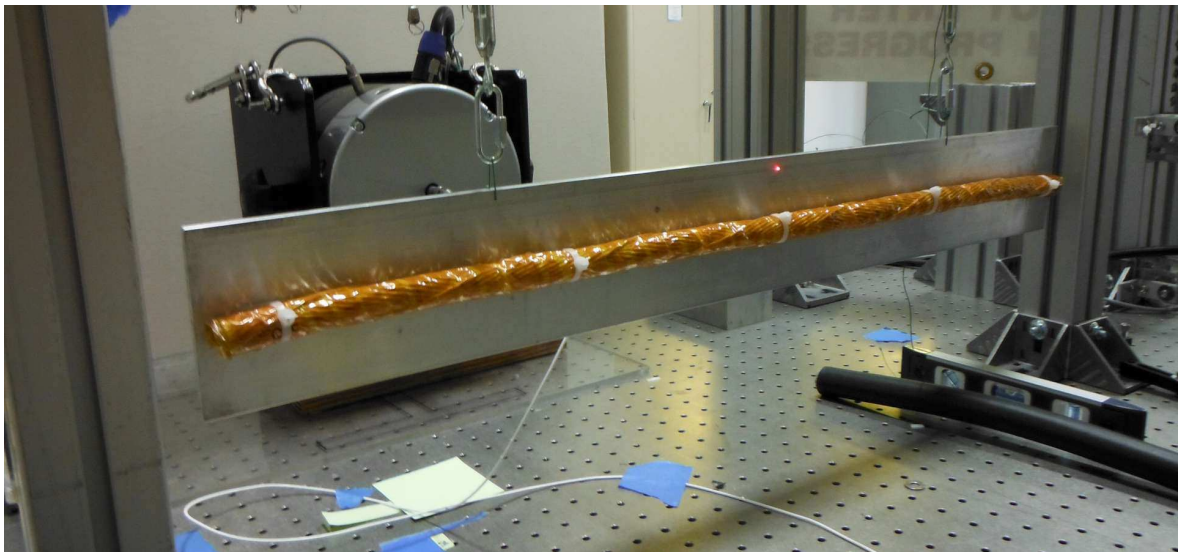

Figure 5.30: Experimental set up for the cabled-beam set up; excitation is via suspended modal shaker terminating in a load cell mounted to a tapped hole in the beam.

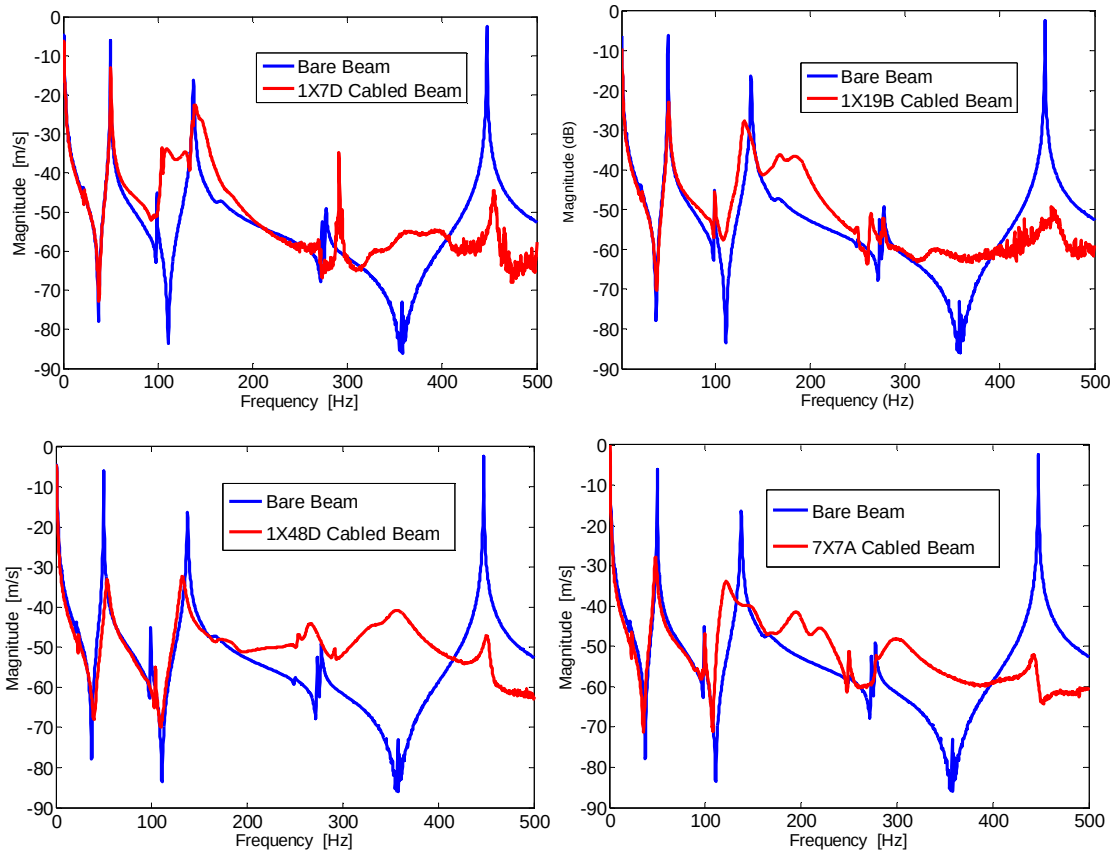

Figure 5.31: Comparison between bare beam and cabled beam transfer function for four cable types, measured at the driving point; clockwise from top left: 1X7 cabled beam, 1X19 cabled beam, 7X7 cabled beam, and 1X48 cabled beam.

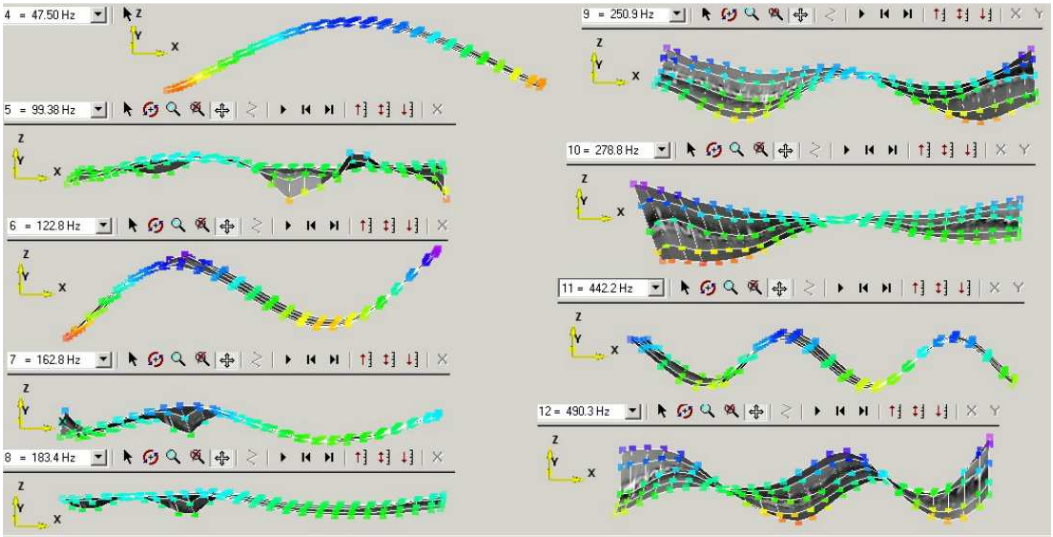

Figure 5.32: Experimental operating deflection shapes for the 7X7 cabled beam.

5.9 Use of ME Scope and Data Processing

Once data were taken with the laser vibrometer, Polytec PSV Software, MATLAB and ME'Scope software were used for analysis. Figure 5.33 shows the frequency response functions taken at every point overlaid together for one of the 1X19 cable sections. Whenever possible, data was used in original and raw form; noisy test data was eliminated only if it was so noisy that no useful data could be extracted. Due to careful test set up and wise software analysis choices, only 4 cable test trials and 2 cabled beam trials were eliminated or re-run due to noise.

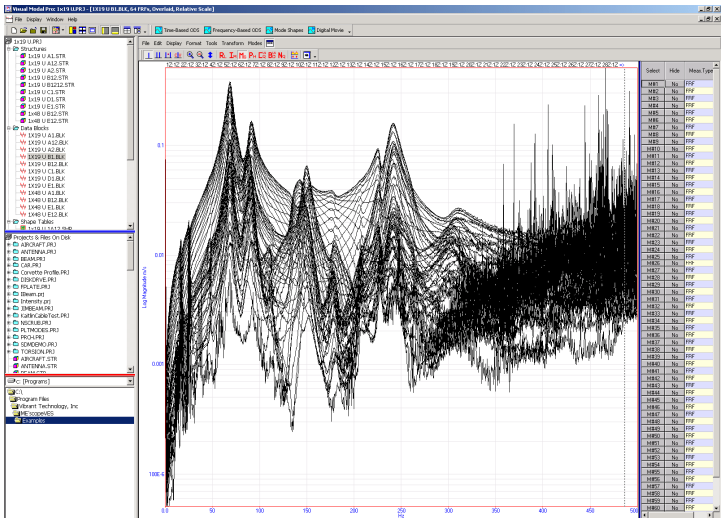

Figure 5.33: Frequency response functions for 1X19 cable for each scan point along the cable as displayed in ME'Scope.

ME'Scope was used to determine the modes and damping ratios for the various cables. The unknown parameters of modal frequency, modal damping and mode shapes were matched to the experimental data using partial fraction expansion. The FRF matrix can be written in the following partial fraction expansion form

$$[H(\omega)] = \sum_{k=1}^{modes} \left[\frac{R(k)}{j\omega - p(k)} + \frac{[R(k)]}{j\omega - p(k)^*} \right]$$

where ω is the frequency variable, $p(k)$ is the pole location for mode k, $p(k)^*$ is the complex conjugate of $p(k)$, and $[R(k)]$ is the residue matrix for mode k. This expression

shows that the FRF matrix is a summation of matrix pairs, each pair containing the contribution of a mode *k* [122].

ME'Scope can also calculate mode indicator functions using multiple measurement points. The mode indicator function provides a single smooth curve from multiple single point measurements along the length of the cable in order to identify those frequencies that are most likely to be natural resonances with associated modes. Figure 5.34 shows the mode indicator function for a 7X7 cable scan. The modal peaks function sums together all of the real parts of the velocity/force transfer functions. All of the scan data for a single test cable was included in the modal indicator, and the ortho-polynomial method was used to estimate modal frequencies and damping. This multi-degree of freedom method simultaneously estimates the modal parameters of two or more modes from the FRFs. The polynomial method curve fits the FRFs directly by performing a least squared error curve fit from multiple FRFs and estimates the coefficients of the FRF denominator polynomial. Modal frequency and damping estimates are then extracted as roots of that polynomial. Modes were selected in small groups for greater accuracy in modal parameter estimation. Damping percentage for each mode was calculated by ME'Scope software and confirmed with hand calculations by applying the half-power point method for damping to the vibrometer data.

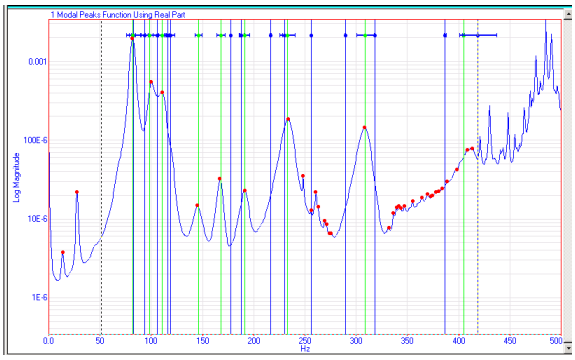

Figure 5.34: Mode indicator function for 7X7 cable with relevant modes highlighted in green.

The experimental data from cables and cabled beams was used to find frequency response functions, natural frequencies, and damping percentages for each mode, and the

results were compared with model results. Mode shapes were compared using the modal assurance criterion (MAC) from Ewins [106], given by

$$MAC(A,X) = \frac{\left|\sum_{j=1}^{n}(\Phi_X)_j(\Phi_A)_j{}^*\right|^2}{\left(\sum_{j=1}^{n}(\Phi_X)_j(\Phi_X)_j{}^*\right)\cdot\left(\sum_{j=1}^{n}(\Phi_A)_j(\Phi_A)_j{}^*\right)}$$

where Φ_X and Φ_A are the experimental and analytical (model) mode shapes. Appendix D contains the MATLAB program files used for processing of the experimental and model data and subsequent modal assurance criterion calculation. Natural frequencies were compared directly and the frequency response functions were compared both visually and using a cumulative RMS value method, since using an FRF assurance criterion is sensitive to slight shifts in the frequency peaks and does not necessarily indicate good or poor agreement clearly. Chapter 6 presents the results of all comparisons.

5.10 Summary of Experiments

For this research, dynamic testing was performed on cables and cabled beams. Cables were tested before and after a bakeout treatment to determine the effect of bakeout on the cable response. Solid rods were also tested in the various fixtures for model comparison. Experiments to determine the characteristics of the attachment points were developed and provided useful values for the models, but also showed the frequency dependence of the connection stiffness. This experimental data is useful not only for comparison with the developed models, but also to provide insight to the effects of cables on structures. The large number of cable trials provide a useful database for further cable study. The frequency response functions for a bare structure, a rod on the structure, and a cable on the structure show differences that validate the need for better understanding and modeling of cable effects.

6. Results

This research resulted in both experimental and theoretical contributions as the synthesis of cable parameters, cable and structure modeling, and test data occurred. Results are presented here for the calculated cable parameters, as well as the resulting cable and cabled-beam models. Undamped and damped models are compared to experimental data for both two-point and four-point cable fixtures and the cabled beams. The experimental comparison between unbaked and baked out cables is also presented. Although the focus is on the utility of the cable and cabled beam models, the experimental results on their own offer insight into the physical phenomena of cable dynamics as well, so the experimental data from the bakeout comparison and the cabled beams are examined in detail.

6.1 Cable Parameter Results

Based on the methods of Chapter 3, parameters for area, density, bending stiffness, and shear rigidity were calculated as maximums and minimums for each type of cable. Table 6.1 gives the property calculation results, as well as the stiffness values used for the cables in the two- and four-point fixture connections and for the cables in the cabled beam model. The cable stiffness varies from fixture to fixture since the curvature of the cable is different depending on the span and deflection experienced by the cable. Bending stiffness is higher for the cable in the four-point fixture due to the shorter span sections that prevent static displacement and curvature of the cable. The cable was attached to the beam at five points, giving an even shorter span length and thus slightly higher bending stiffness, as expected. Notice that the minimum frequency bound is the result of using the minimum bending stiffness and maximum area and density values, while the maximum frequency is the result of using the maximum bending stiffness and the minimum values for area and density.

Table 6.1 Inputs for cable properties for minimum and maximum frequencies calculated for each cable based on the methods introduced herein, and the material properties and cable measurements introduced in Chapter 3.

		1x7		1x19		1x48		7x7 (multi-strand)	
		Min Freq.	Max Freq.	Min Freq.	Max Freq.	Min Freq.	Max Freq.	Min Freq.	Max Freq.
Area, m^2	A	$4.35*10^{-5}$	$3.44*10^{-5}$	$1.27*10^{-4}$	$9.33*10^{-5}$	$3.27*10^{-4}$	$2.36*10^{-4}$	$3.66*10^{-4}$	$2.41*10^{-4}$
Density, kg/m^3	ρ	3323	2677	3528	2624	3049	2456	3295	2654
Wire Modulus of Elasticity, GPa	E_L	19.1	23.7	19.1	23.7	19.1	23.7	19.1	23.7
Bending Stiffness (2 Pt), $kg\text{-}m^3/s^2$	EI	0.34	0.37	1.09	1.18	4.73	5.10	2.14	2.30
Bending Stiffness (4 Pt), $kg\text{-}m^3/s^2$	EI	0.40	0.44	1.55	1.71	7.52	8.13	2.60	2.82
Bending Stiffness (Cabled Beam), $kg\text{-}m^3/s^2$	EI	0.46	0.51	1.94	2.16	16.82	18.25	3.48	3.83
Shear Rigidity, Pa	κAG	$2.69*10^4$	$2.13*10^4$	$7.87*10^4$	$5.78*10^4$	$2.02*10^5$	$1.46*10^5$	$2.27*10^5$	$1.49*10^5$
Cxn Stiffness Value, Rotational	k_{rot}	2 N/m-rad		2 N/m-rad		2 N/m-rad		2 N/m-rad	
Cxn Stiffness Value, Linear	k	$1*10^4$ N/m-rad		$6*10^4$ N/m-rad		$1*10^6$ N/m-rad		$6*10^5$ N/m-rad	

From these parameters, the bound for each frequency was calculated using the cable model for the two-point and four-point fixtures. As an example, Figure 6.1 shows the maximum and minimum frequency response functions that result from the model for the 1X19 cable parameters in the two-point and four-point fixtures. The range of frequency prediction is smallest for the first frequency, but increases with each successive frequency in the two-point model. The four-point model has a more uniform frequency range for the frequencies shown.

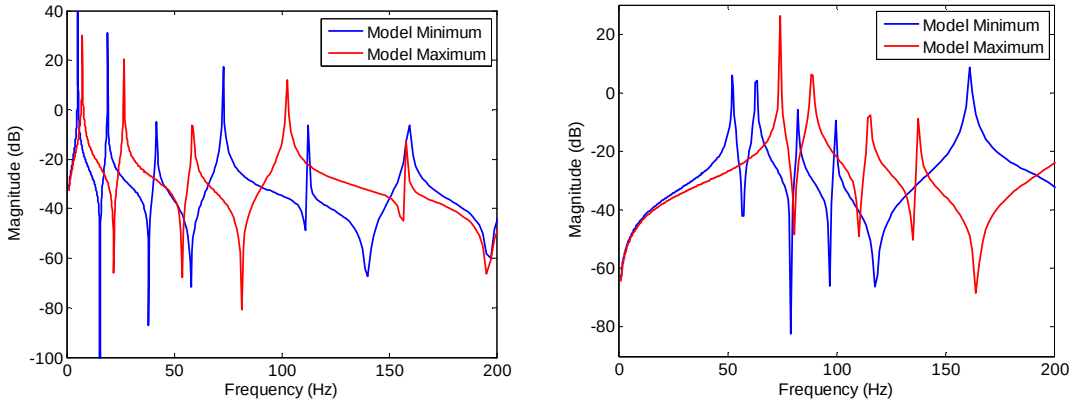

Two-Point Model Four-Point Model

Figure 6.1: Model frequency response functions using minimum frequency cable parameters (blue) and maximum frequency parameters (red) for the two-point model (left) and the four-point model (right).

6.2 Comparison of Undamped Model with Cable Response

The value of calculating cable parameters without having to conduct extensive vibration testing depends on using those cable parameters to predict the cable frequencies in various fixtures or mounting configurations. Thus, the cable model was run in two-point and four-point configurations as described in Chapter 4 and shown above, and the range of frequency values was compared to the respective two-point or four-point experimental configuration. Addition of cables to structures changes both the resonance frequencies and damping ratios, so the most useful comparison between model results and experimental data is a direct frequency value comparison and comparison of frequency response functions (FRFs) [2]. However, for a more rigorous study and confirmation that frequencies are being compared appropriately, the mode shapes should also be compared. A direct comparison of frequencies is only useful if the frequencies being compared actually correspond to the same mode; thus, a modal assurance criterion (MAC) was run for each case that compared the experimental and model mode shapes at each natural frequency to ensure that frequencies were being compared directly correctly. Torsional modes were not evident in the frequency response functions for the cables, which was as expected since the lowest calculated torsional modes for the cables were higher than the frequency range of interest.

To show the comparison of the predicted frequencies to the experimental data, the model frequency ranges are overlaid as black bars on the experimental frequency response functions of the two-point cables; the black bars represent the range between the minimum and maximum frequency values for each peak that were shown in Figure 6.1 as an example. Model amplitudes were not compared until damping was added, since the experimental cable damping was significant; therefore, the position of the black bars on the following graphs serves only to put the bars near the frequency peak of interest, not to indicate amplitude of the model. Five experimental trials are shown for the two-point cables, giving an idea of the variability inherent from trial to trial and the value of having frequencies calculated as a range rather than a single value. The experimental data is shown as frequency response transfer functions where resonance frequencies are indicated by peaks in the data and amplitude is indicated by the relative magnitude of the peak.

The modal assurance criterion is displayed as a top view of a grid of experimental and model modes; for perfect agreement, the diagonal row of the MAC should be 1 and all other squares should be 0. In practice, due to experimental uncertainty and the use of raw data, bright diagonal and dark off-diagonal squares indicate good mode agreement for the entire model, where bright squares indicate high mode correlation with MAC values above 0.7 and dark squares indicate minimal mode correlation with MAC values below 0.3.

6.2.1 Cables in Two-Point Fixture

The two-point fixture had only two attachment points, reducing the variation due to attachment uncertainty and allowing the cable to respond with typical and easily recognizable bending modes.

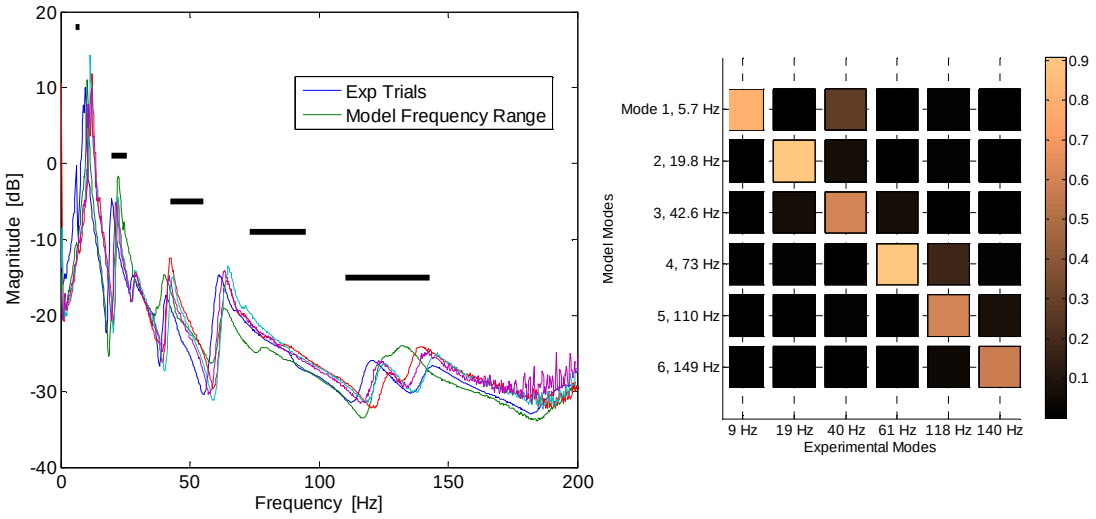

Figure 6.2: Frequency response function (FRF) comparison and MAC for 1X7 cable in two-point fixture.

Based on the experimental trials shown in Figure 6.2, it is clear that the cable response is not perfectly repeatable from trial to trial, but there are certainly frequency peaks that appear clearly and could be predicted by a frequency range. Figure 6.2 shows the comparison between the frequency response functions for five experimental trials with the predicted model frequencies shown as black bars to indicate the predicted frequency range, as well as the MAC that compares the experimental and model mode shapes of the 1X7 cable. The frequency values for the experimental data and minimum model values are listed along the axes of the MAC chart to indicate the frequency at which the mode shape was determined for comparison purposes. The first frequency range is reasonable but narrow, and the second frequency range is an excellent representation. The third and fourth experimental frequencies (at about 40 Hz and 60 Hz) are lower than predicted by the model ranges, but addition of damping or a percentage knockdown of the bending stiffness due to bakeout [108] could bring these into alignment, and the MAC shows good agreement for these modes, so they are compared correctly. Notice that the small peak at about 25 Hz is not included in the prediction; the peak at 25 Hz in this and all subsequent frequency response plots is the frequency of the cable fixture, and should show up only in the experimental data and not the model. For the 1X7 cable in the two-

point fixture, MAC agreement was excellent between model and experimental mode shapes for the six modes compared. Frequency values were also reasonable for such a small cable.

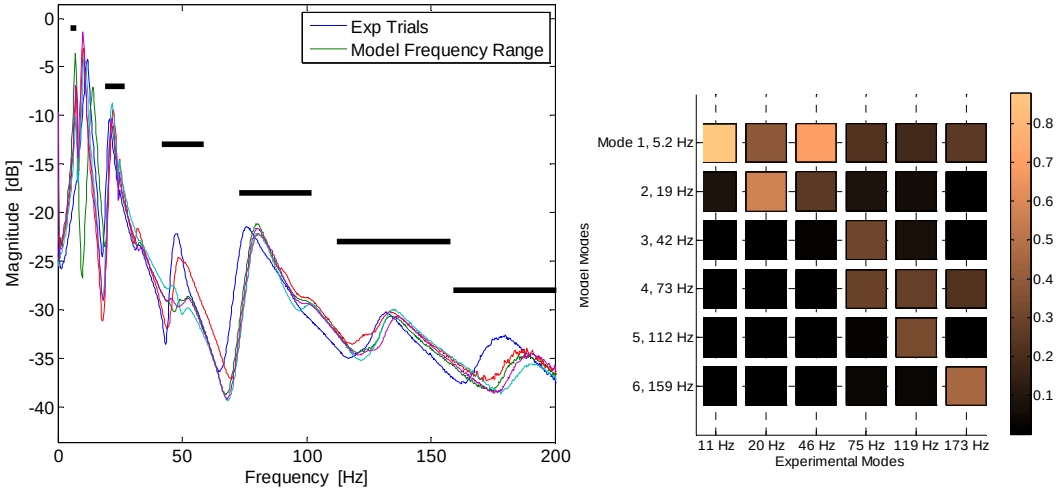

Figure 6.3: FRF experimental and model range comparison and MAC for 1X19 cable in two-point fixture.

The agreement between the model and experimental data of the medium sized 1X19 cable is shown in Figure 6.3. This cable, being larger and more beam-like, showed improved results with the same cable parameter calculation method used for the 1X7 cable. Again, the frequencies of greatest amplitude are predicted with the narrowest range, which is useful since many applications are only concerned with the highest amplitude mode. MAC values for the 1X19 cable in the two-point fixture showed good agreement of mode shapes for similar frequencies, although the first mode tended to dominate the nearby modes, showing that the first mode was excited to some degree for almost all frequencies.

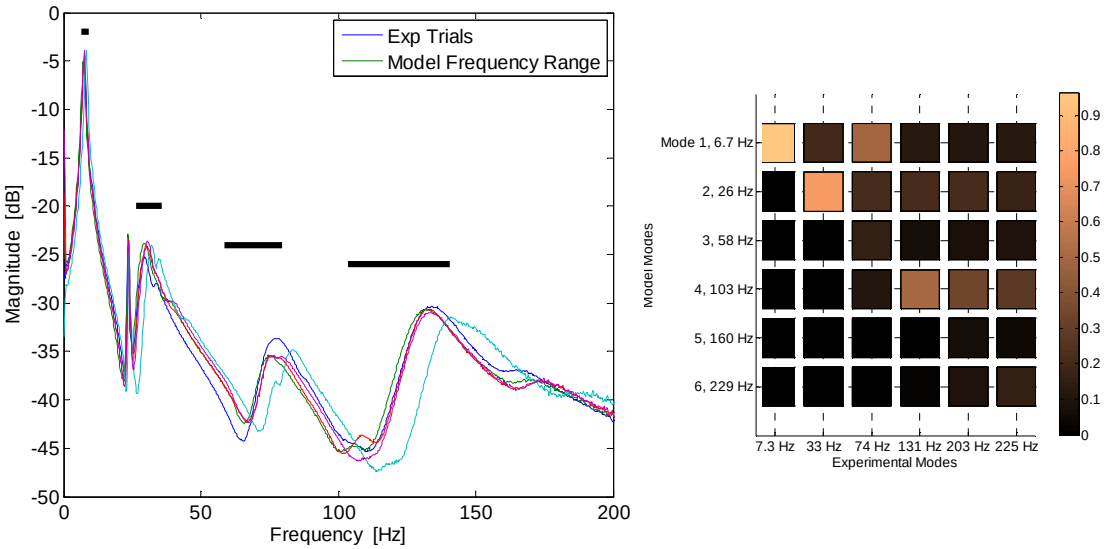

Figure 6.4: Frequency response function and MAC for 1X48 cable in two-point fixture.

The 1X48 cable was the stiffest of the cables tested and showed fewer modes in the same frequency range. Predicted frequency ranges shown in Figure 6.4 for the 1X48 cable attached at two points agree with the experimental data. As noted before, the spike at 25 Hz is a structural mode from the cable test fixture, and is not included in the model. Mode agreement for this case is good for modes 1, 2, and 4, with modes 5 and 6 dominated by the much larger fourth mode. Despite the less than perfect MAC, visual comparison of the mode shapes showed enough agreement to be confident in the natural frequency comparison.

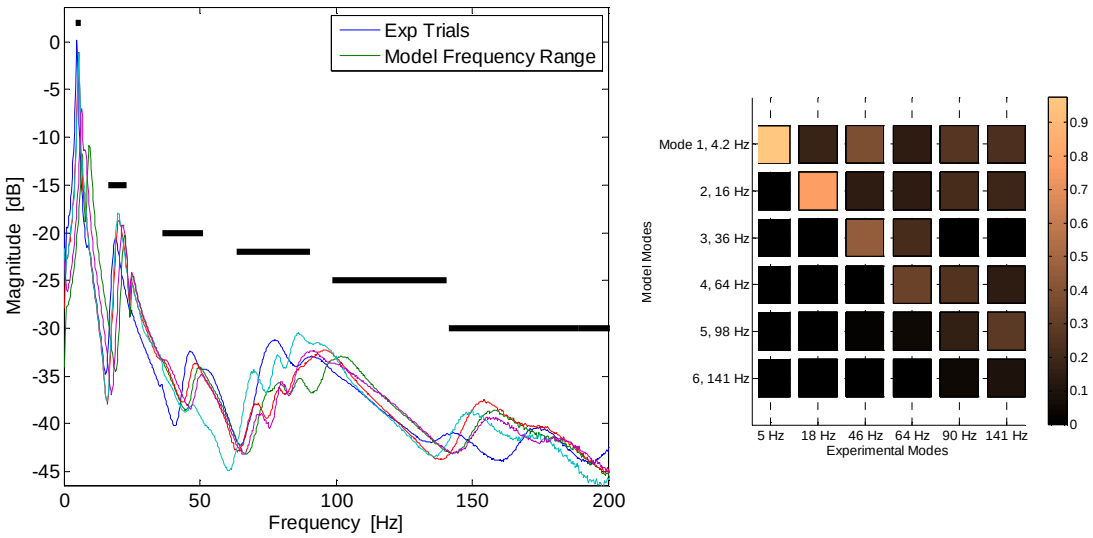

Figure 6.5: Experimental FRF and model range comparison and MAC for 7X7 cable in two-point fixture.

As a multi-stranded cable, the 7X7 was not as beam-like as the single-stranded cables in that it showed greater variation between trials and non-standard experimental modes. The first few natural frequencies are adequately predicted, as shown in Figure 6.5, but the fifth model mode is too high, and the model fails to capture the 2-3 additional internal modes between 60 Hz and 100 Hz. Since the amplitude of the frequency response is so much greater for the first mode, this model is still deemed useful for multi-stranded cables, with the caveat that above the first few modes, additional modes may not be captured. The MAC for the 7X7 two-point cable confirms that agreement for the modeled modes is good, but additional experimental modes between 60 and 100 Hz were not captured. However, mode correlation between the modeled modes is still high and thus the multi-stranded model can be used with the understanding that additional low amplitude modes may be present.

The above results are useful for predicting the first several frequencies, but for many applications, only the first frequency with the highest amplitude is of interest. The use of circular or elliptical wire calculations as first discussed in Chapter 3 results in similar frequency predictions, but different frequency ranges. The range for the first frequency

predicted with the elliptical wire calculations is narrow; using the circular wire calculations sets wider bounds on the predicted frequency range. Figure 6.6 shows the experimental FRF and model range comparison for the model with circular wire calculations used for each of the cable types in the two-point fixture. The first frequency range is wider, but the model ranges for the higher frequencies are too wide to be of practical use. Thus, the elliptical wire calculations are recommended unless a wider predicted range for the first frequency is desired.

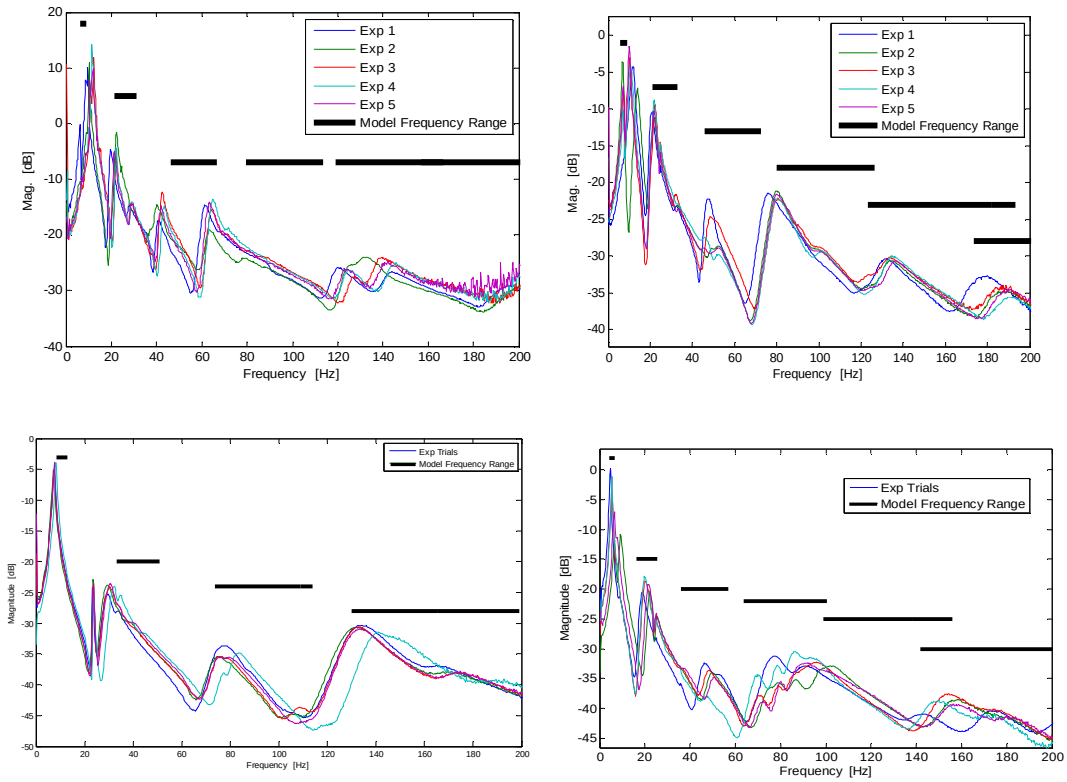

Figure 6.6: FRF and frequency range comparisons for all cables showing the larger range resulting from the use of circular wire calculations. Clockwise from top left: 1X7 cable, 1X19 cable, 7X7 cable, and 1X48 cable.

Overall, predictions from the model for natural frequency using elliptical wire calculations were good for single-stranded cables, and adequate for the multi-stranded cable. Natural frequency results are better for larger, more beam like cables; this agrees

with previously published work that found that the calculation of bending stiffness became more accurate as the number of wires in a given layer increases [123].

6.2.2 Cables in Four-Point Fixture

For the four-point cables, difficulty arises in comparison of the model results to the experimental data because of the inherent variation in cable behavior, augmented by the lack of precision of the attachment method. Although all of the cables show clear large frequency response function peaks at the first bending mode of the center section, the interaction modes (smaller amplitude modes occurring due to the stranded nature of the cable) for the four-point cables tests between the first and second center section beam modes are erratic; for instance, one section of cable might show two interaction modes between the first and second center section beam modes, while another sample of the same type of cable shows three. Figure 6.7 shows the typical appearance of the four-point cable frequency response function where the large first and second modes are separated by interaction modes. The interaction modes are characterized by small amplitude standard beam modes within each span section, where the major first and second beam modes are characterized by a standard mode over the center test section with much larger amplitude. Figure 6.8 shows the experimental mode shapes for the first few modes of a 1X7 cable, showing the major beam modes as large amplitude standard string mode shapes in the center sections, while the interaction modes have larger displacements in the buffer sections. For the larger cables, the shape and number of the interaction modes is different, but the first and second beam-like mode shapes always appear at the high amplitude frequency peaks. Even within the results from the same cable section the number of interaction modes varies. Therefore, the most reliable way to compare frequencies between model and experimental data for the four-point cables was to find the easily identifiable first and second beam-mode mode shapes that occurred in the center test section, and compare those frequencies. The larger cables showed multiple peaks near the first beam mode, and seem to be modeled more appropriately with the stiff connection values that cause additional frequencies at the first mode.

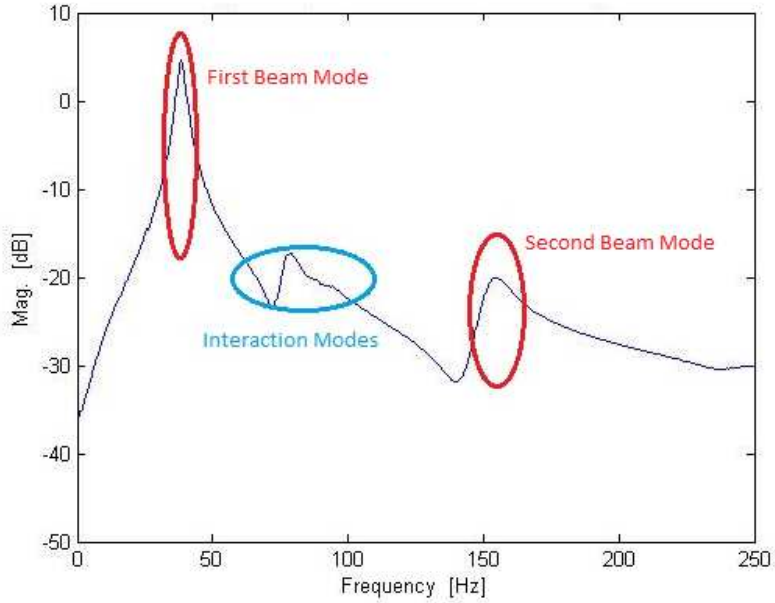

Figure 6.7: Anatomy of a frequency response function for a smaller cable in the multi-span four-point fixture.

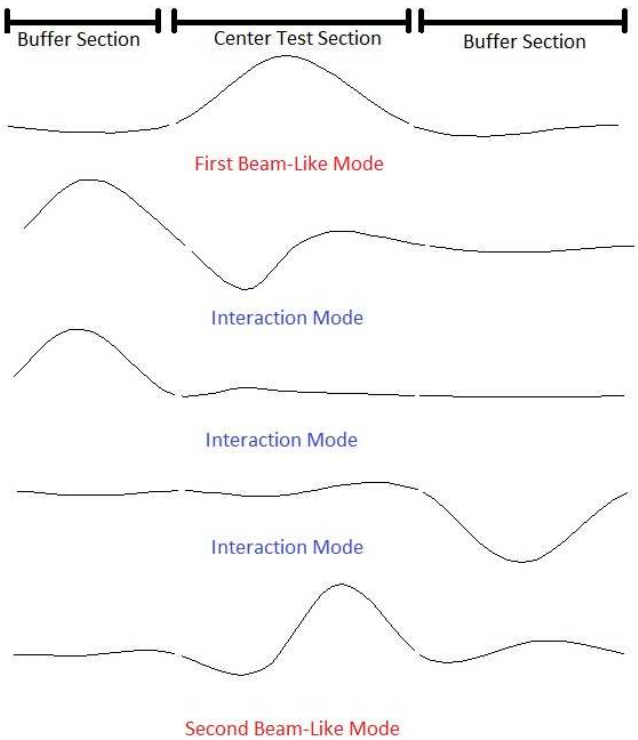

Figure 6.8: Representative 1X7 experimental mode shapes showing the difference between beam-like major amplitude modes and interaction modes for the multi-span four-point fixture.

Comparison of predicted model ranges and experimental data and MAC chart for the 1X7 cable attached at four points are shown in Figure 6.9. The first model frequency range was too high; inclusion of damping or a bakeout correction factor, which would affect the first mode the most, may adjust this prediction accordingly. The second, third and fourth frequencies correspond to the multiple (usually three) interaction modes between 50 and 100 Hz. The MAC for the 1X7 cable attached at four points showed that the experimental modes are dominated by the two largest-amplitude frequencies, the first and fifth frequency. In an effort to determine whether mode interaction was occurring in the experimental data, the first model mode was added to the three interaction modes and the modal assurance criterion was run for these blended modes against the experimental modes. The results were very clear; the blended interaction modes 2, 3, and 4 had MAC values of 0.7166, 0.8356, and 0.7565 respectively, high enough to show strong correlation. Comparison of natural frequencies for the four-point fixture is most effective when the two frequencies with the highest local peak amplitude are identified and compared to the corresponding model modes.

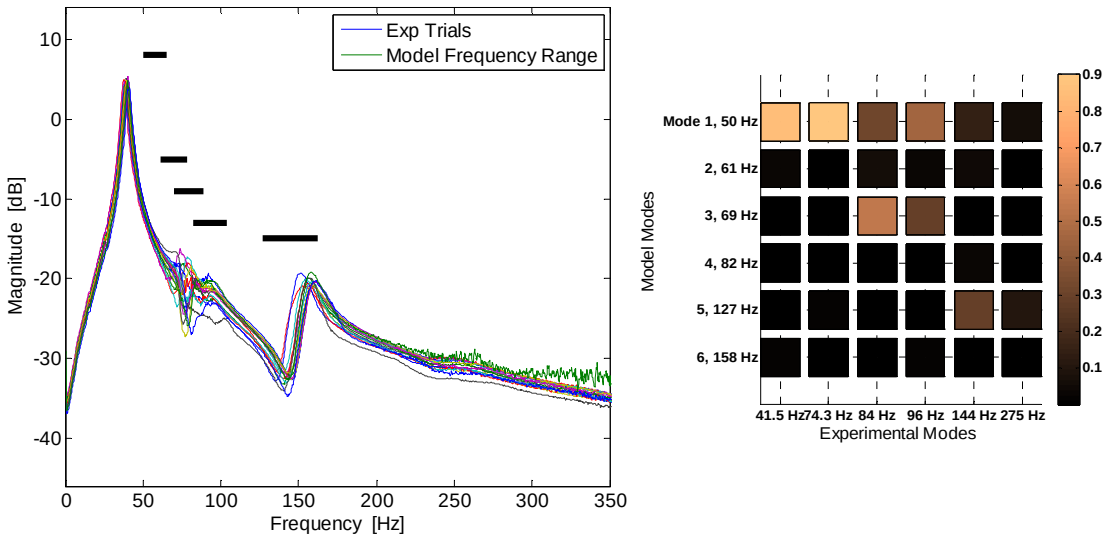

Figure 6.9: Frequency response function and MAC for 1X7 cable in four-point fixture.

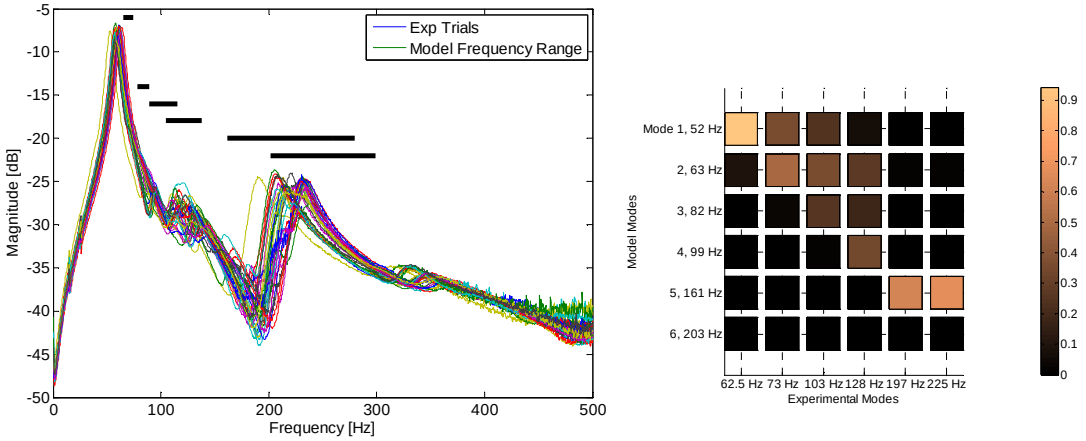

Figure 6.10: Frequency response function and MAC for 1X19 cable in four-point fixture.

Figure 6.10 shows the comparison of experimental data and model for the 1X19 cable attached at four points. In this case, the model predicts three interaction modes between the major large amplitude modes. Just as with the 1X7 cable, the large amplitude experimental modes dominate the other modes, so the MAC for the 1X19 cable showed more concentrated agreement around those first and fifth model modes. Again, mode interaction seemed likely, so the first model mode was added to the second and third interaction modes to test this hypothesis. This resulted in MAC comparison values of 0.9424 for the second interaction mode and 0.5485 for the third interaction mode, giving strong support to the theory that mode interaction is prevalent in stranded cables. This is further supported by the fact that mode interaction is common in non-linear systems, such as stranded cables. The fifth natural frequency range and mode correlates to both the fifth natural frequency in the FRF and fifth experimental mode, showing that the frequencies are being compared correctly.

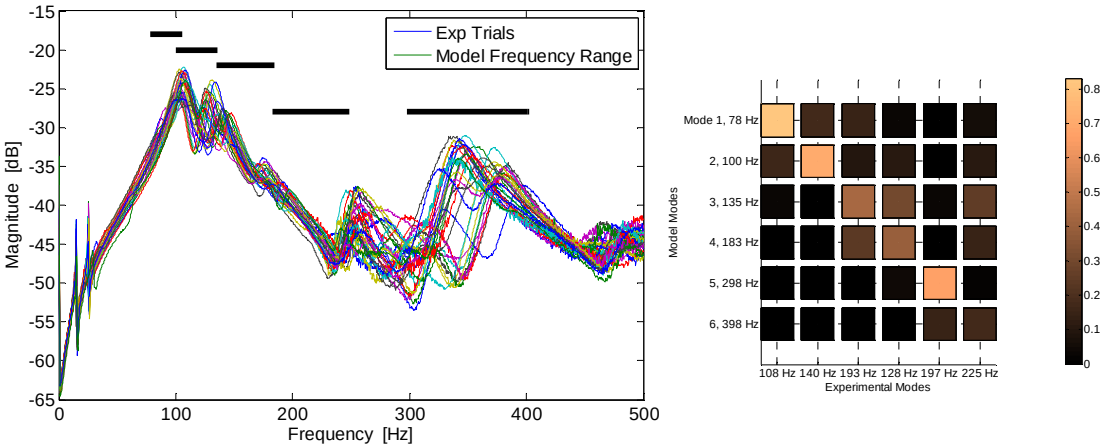

Figure 6.11: Frequency response function and MAC for 1X48 cable in four-point fixture.

The larger 1X48 and 7X7 cables showed several large modes of similar amplitude instead of the single large amplitude frequency peak shown by the smaller cables. This was modeled in part by the higher bending stiffness, but also shows the importance of the attachment stiffness, since only higher values for attachment stiffness correctly modeled the multiple high amplitude peaks. For the larger cables the variability from sample to sample and even trial to trial of the same sample is quite large, with varying numbers of modes at certain frequencies. The modeled frequencies are approximations at best and may not capture all of the small interaction frequencies that are evident. Figure 6.11 shows the comparison between the model and experimental frequencies for the 1X48 cable attached at four points. The three large amplitude peaks are modeled and the fourth and fifth frequencies are captured. The MAC for the 1X48 cable in the four-point fixture showed excellent correlation for the large amplitude first, second, and fifth modes.

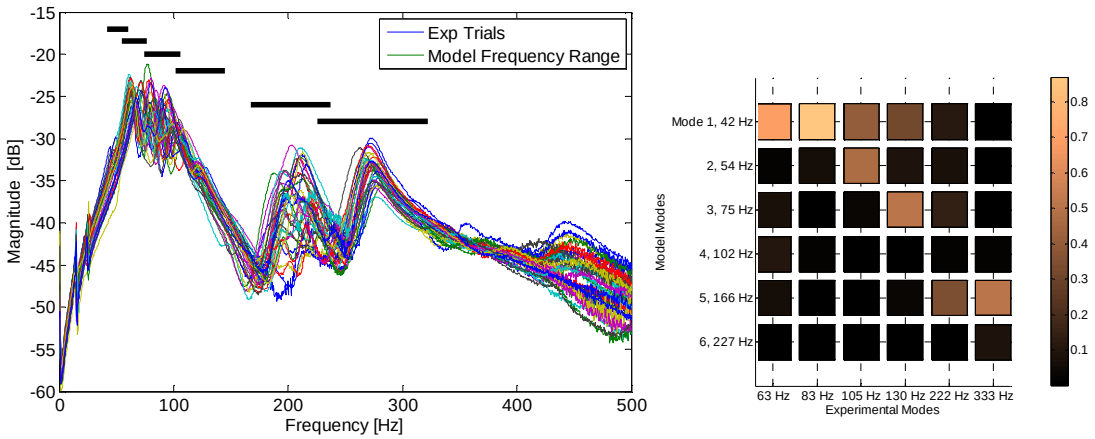

Figure 6.12: Frequency response function and MAC for 7X7 cable in four-point fixture.

The comparison between the model results and the experimental results for the 7X7 cable attached at four points is shown in Figure 6.12. The first four mode shapes correspond to the large amplitude frequencies overall, of which 3-4 are always present in the experimental trials. The fifth and sixth frequency range correlates with the higher frequency large amplitude peaks at about 200 and 300 Hz, respectively. From the correlation of the MAC values between the first four experimental modes and the first model mode, it is clear that the first four large amplitude modes all have some element of the first model mode. Adding the first model mode to the subsequent model modes results in higher MAC correlations for these blended modes; adding model modes 1 and 2 and comparing to experimental mode 2 results in a MAC value of 0.8541. The results for the 7X7 cable comparison in the four-point fixture are significantly better than the results in the two-point fixture. For the multi-stranded cable, it appears that smaller span lengths can help to make the cable behave more like a beam.

Phase information for both two-point and four-point cable tests was also recorded. Figure 6.13 shows a representative mobility frequency response function and the associated phase plot for a 1X48 two-point cable trial. The modes were very clear when identified by the mode shapes at the peak frequencies, and the phase diagram corresponded with these frequencies. Figure 6.14 shows the phase diagram for a trial of a

1X48 cable in the four-point fixture. Phase diagrams were less useful than mode shape analysis for these cases due to the heavy damping that made phase shifts less obvious.

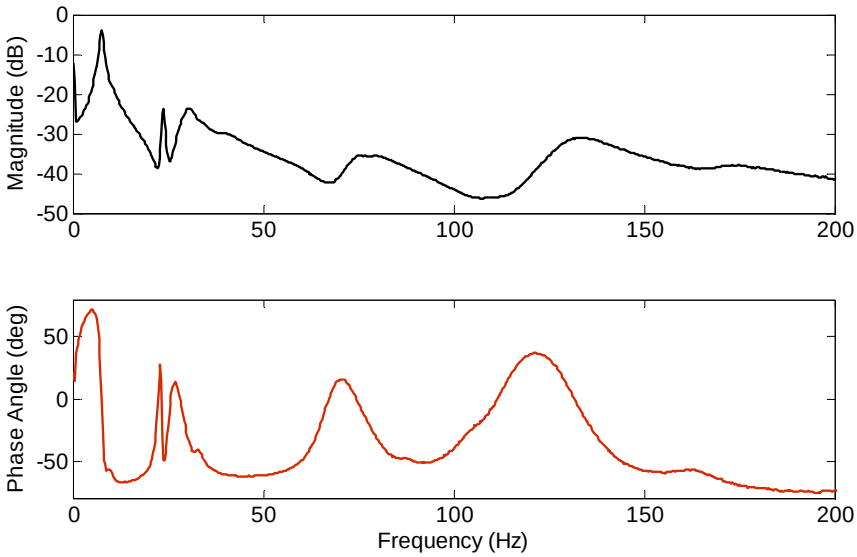

Figure 6.13: Frequency response and associated phase angle plot for 1X48 cable trial in two-point fixture.

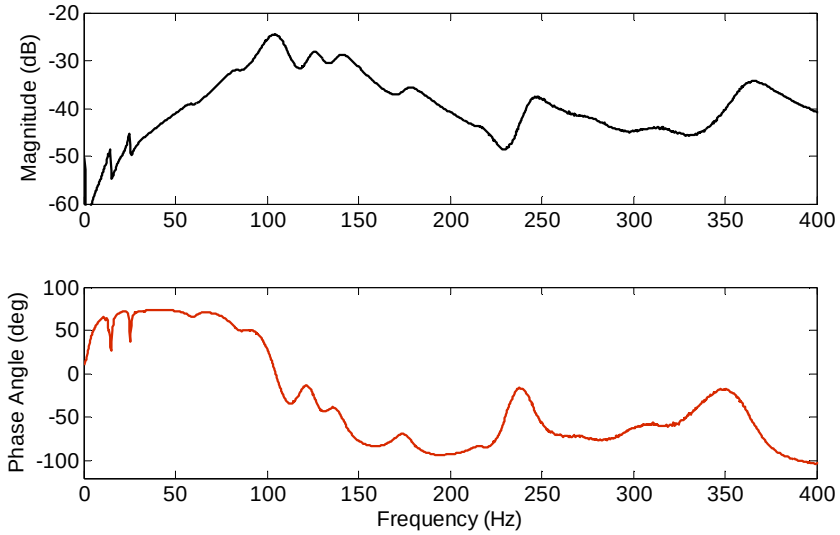

Figure 6.14: Frequency response and associated phase angle plot for 1X48 cable trial in four-point fixture.

The four-point cables are more difficult to compare frequencies directly with confidence due to the variability of the interaction modes, but the largest amplitude responses are

certainly captured by the derived cable model, and interaction modes are identified. The four-point models serve less to predict the exact frequency of any given interaction mode, and more to validate the cable parameters that were shown to be effective for the two-point cable tests. Since the eventual goal for this work is to model cables attached to host structures at multiple points, it is important that the cable parameters calculated still represent the cable well when it is attached as a multi-span beam. Just as exhibited by the two-point cables, results are still best for the larger, more beam-like cables.

The results for the two-point single-span cables show correct cable parameters calculated from cable measurements and reasonably predictive frequency ranges, and the results for the four-point multi-span cables verify that this parameter calculation approach and model method is still valid for cables attached at multiple points as they would be when attached to a host structure.

6.3 Effect of Bakeout on Cable Dynamics

As discussed in Chapter 3, the bakeout process was hypothesized to have an effect on spaceflight cable stiffness. Based on the experiments conducted as part of this research, bakeout reduces the bending stiffness and changes the frequency response function of spaceflight cables as illustrated herein. Results for the experimental comparison of the pre- and post-bakeout cables are presented in this section, with all trials of each cable type shown in a single figure. Appendix E contains the comparisons for individual cable sections.

6.3.1 Single Stranded 1X7 Cable

Figure 6.15 shows the comparison for all of the 1X7 cable sections in which red dashed lines are the unbaked cable responses and blue solid lines show the cable responses after bakeout. For every section of the 1X7 cable, the first and second natural frequencies shifted to the left beyond the variation between the cable sections. The first and second beam modes are much more consistent in frequency and amplitude than the interaction modes. This is likely due to interaction modes being very dependent on the constriction of the cable at the attachment points; although cable tie tension was kept constant, the

random way that the individual wires were compressed as the tie was tightened for each installation of the cable in the test fixture may have contributed to the interaction mode variation. After bakeout, the Kapton tape is said to set, which may hold the wires more snugly and reduce some of this variation.

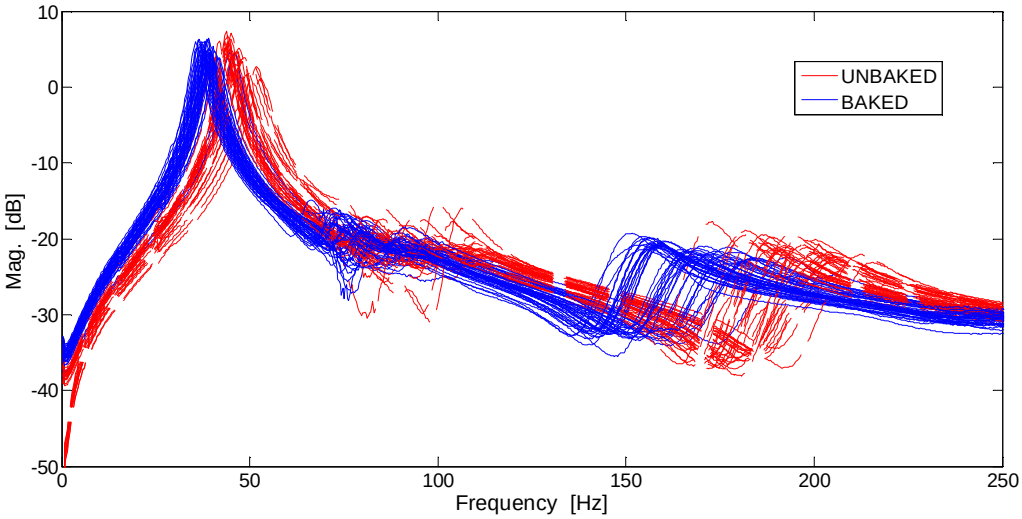

Figure 6.15: Comparison of cable frequency response functions before and after bakeout, showing a decrease in natural frequencies for 1X7 cable.

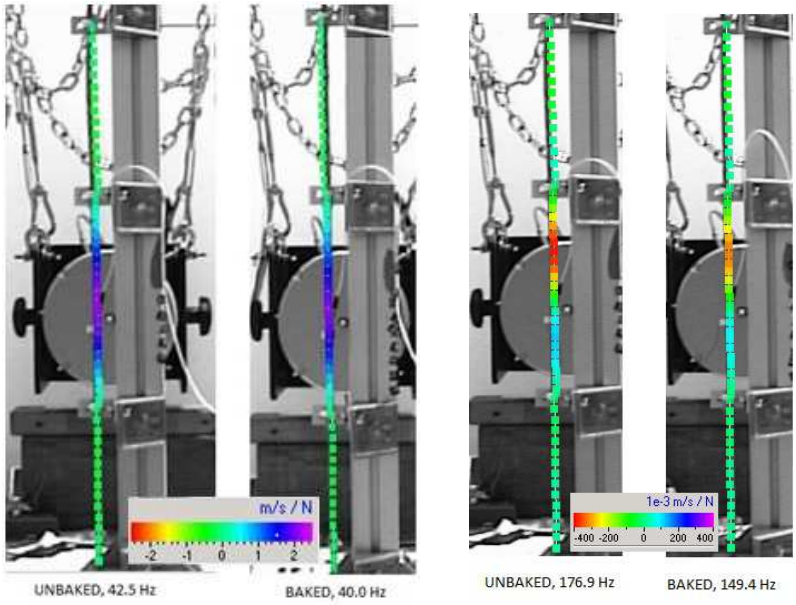

First Mode Second Mode

Figure 6.16: Comparison between first and second major beam modes for 1X7 unbaked (left) and baked (right) modes.

To show where the first and second major beam modes occur, the cable was scanned and mode shapes were identified. The cable showed clear beam modes which were used to identify the modes of the test section. The unbaked cable first frequency occurs around 45 Hz and the second frequency occurs around 180 Hz. The modes that occur between 50 and 100 Hz are interaction modes, in which the buffer zones show larger displacements than the center section. This is valuable information since cables are usually attached in multiple places and would show these interaction modes in practice as well. The first mode can be differentiated from the interaction modes by the lack of activity shown in the buffer zones at this point. Figure 6.16 shows the mode shapes for the 1X7 cable as measured using Polytec laser vibrometer software; the left side of each image is an unbaked cable and the image on the right side is the same cable section after bakeout, showing the same beam mode at a reduced frequency and slightly reduced amplitude. The reduced amplitude that is readily apparent in the second mode indicates greater damping in the baked out cable.

Figure 6.17 shows a graph of the first natural frequency value taken from single point data for all of the unbaked and baked trials for the 1X7 cables, again showing a clear decrease in frequency for the baked cables. The 1X7 section C cable was the only cable that showed a downward trend in frequency for the first few unbaked trials. This is likely due to the "bedding in" effect, in which continued vibration of the cable changes the frictional force between the wires and thus decreases the natural frequency. The term "bedding in" is used throughout Raoof's research on spiral strands and differentiates an old cable that has experienced vibration from a newly manufactured cable [69]. After the first five trials, it appears that the cable is completely bedded in. All cables were excited by the same amount and same duration to eliminate any differences due to bedding in. It should also be noted that section C of the 1X7 set was the most poorly behaved of all of the cable samples, which is observed in its unusually high frequency values at trials 10 and 12 of the baked cable testing. Overall though, it still follows the general trend shown clearly by 1X7 sections D and E, which show an average decrease in first natural frequency of 12.7% and 17.2% respectively.

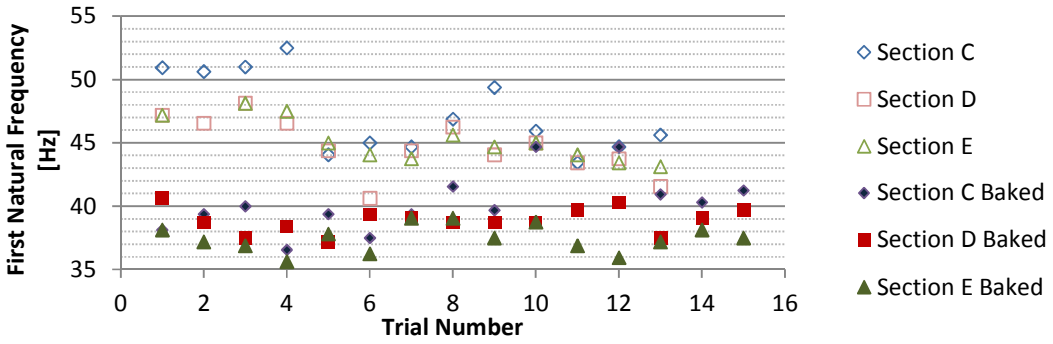

Figure 6.17: First natural frequencies for 1X7 cable sections, showing lower frequency trend of baked cables for all trials.

6.3.2 Single Stranded 1X19 Cable

Frequency response functions, mode shapes, and natural frequencies were inspected for the 1X19 cables before and after bakeout as well. The frequency response functions for all baked and unbaked 1X19 trials are shown in Figure 6.18, again showing a decrease in effective stiffness for both first and second beam mode frequencies.

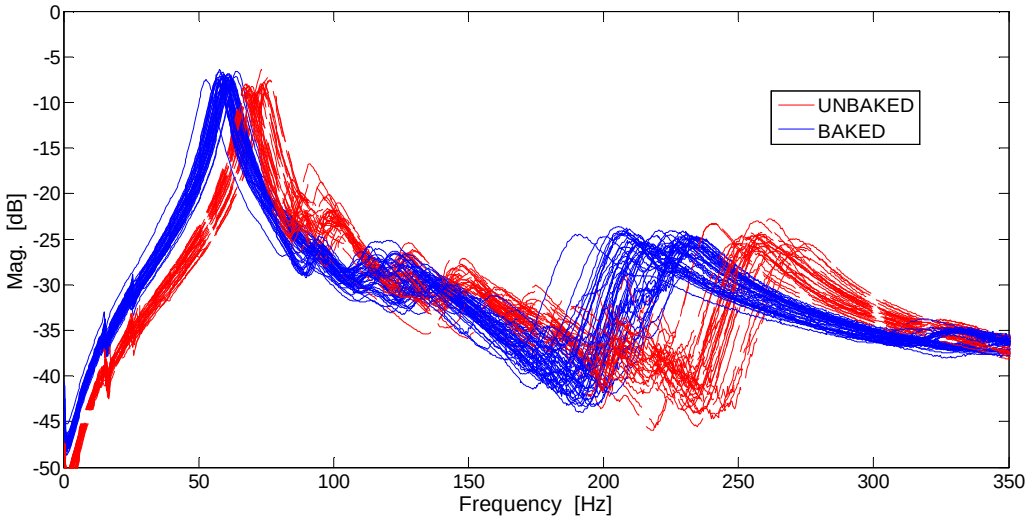

Figure 6.18: Comparison of cable frequency response functions before and after bakeout, showing a decrease in natural frequencies for 1X19 cable.

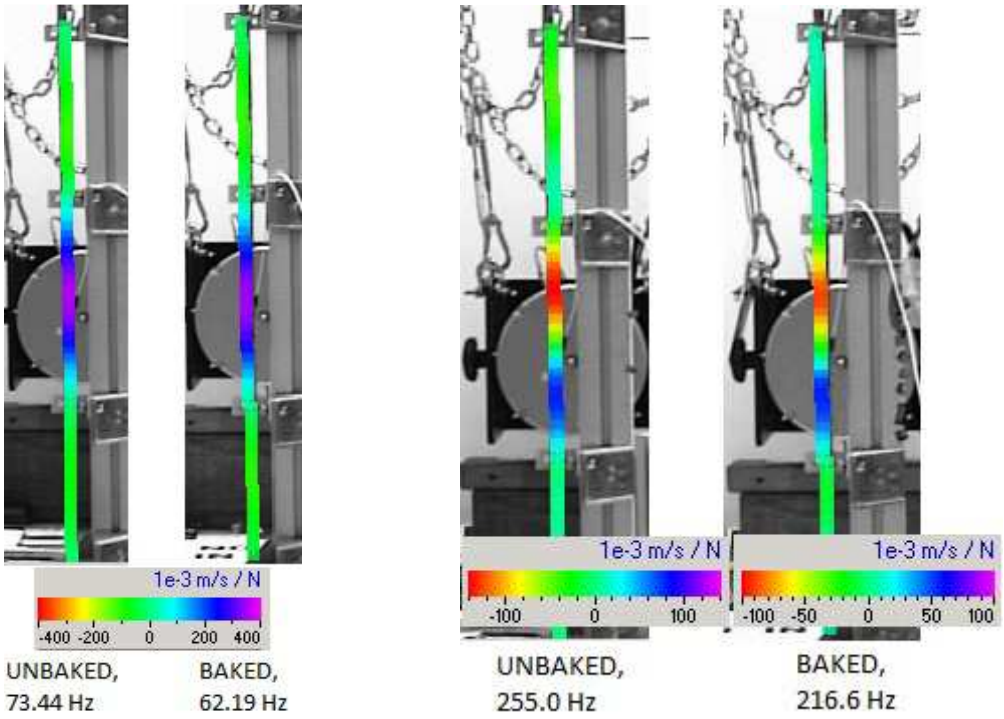

First Mode Second Mode

Figure 6.19: Comparison between first and second major beam modes for 1X19 unbaked (left) and baked (right) modes.

Figure 6.19 shows the matching mode shapes for the first and second beam modes with a 15% reduction in the frequency of the baked cable shown on the right side of each figure for each mode. Figure 6.20 shows the trend in first natural frequency as compared between the unbaked and baked cable trials from the single point data of the 1X19 trials. The frequency difference here ranged from 13.2% to 16.2% and in no trial was the baked cable frequency ever higher than the unbaked cable frequency. This cable, being the medium sized cable that the standard run was designed for, showed excellent repeatability and a clear trend through all trials. No bedding in effect was observed.

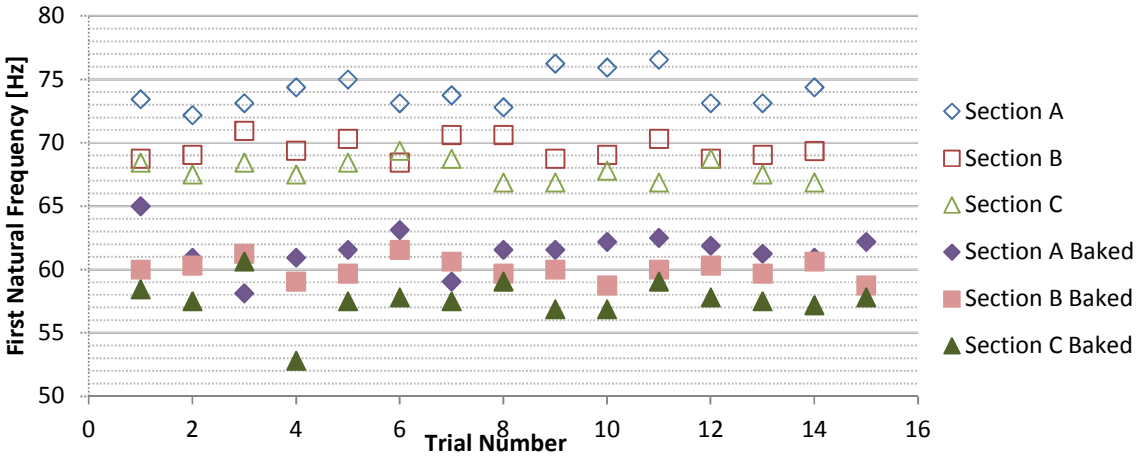

Figure 6.20: First natural frequencies for 1X19 cable sections, showing lower frequencies of baked cables for all trials.

6.3.3 Single Stranded 1X48 Cable

The much stiffer cable showed frequency response functions with modes that could not be as easily identified by inspection alone. This is where the identification of the matching mode shapes became necessary since there was ambiguity in the peaks of the frequency response functions. Figure 6.21 shows the FRFs of all of the 1X48 trials, where the first beam mode of the cable test section is no longer as clearly defined due to the close proximity of the interaction modes (which occurs because this cable is much stiffer and larger, and experiences less constriction at the pinned connections between the buffer zones and test section). Figure 6.22 shows the 1X48 cable's first and second mode shapes, respectively. The unbaked cable resonated at 117.2 Hz for the first beam mode and 389.1 Hz for the second beam mode, while the same cable after bakeout resonated at 107.8 Hz and 348.1 Hz, differences of 8% and 10.5% for the first and second modes. Figure 6.23 shows a graph of the first peak frequency values from single point data. As with the other single-strand cables, every baked trial showed lower frequency values than every unbaked trial.

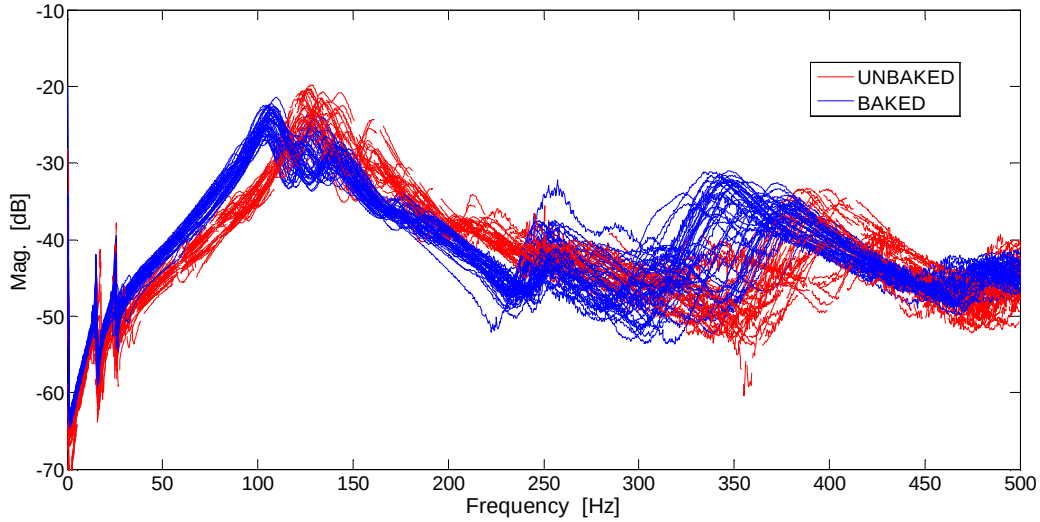

Figure 6.21: Comparison of cable frequency response functions before and after bakeout, showing a decrease in natural frequencies for 1X48 cable.

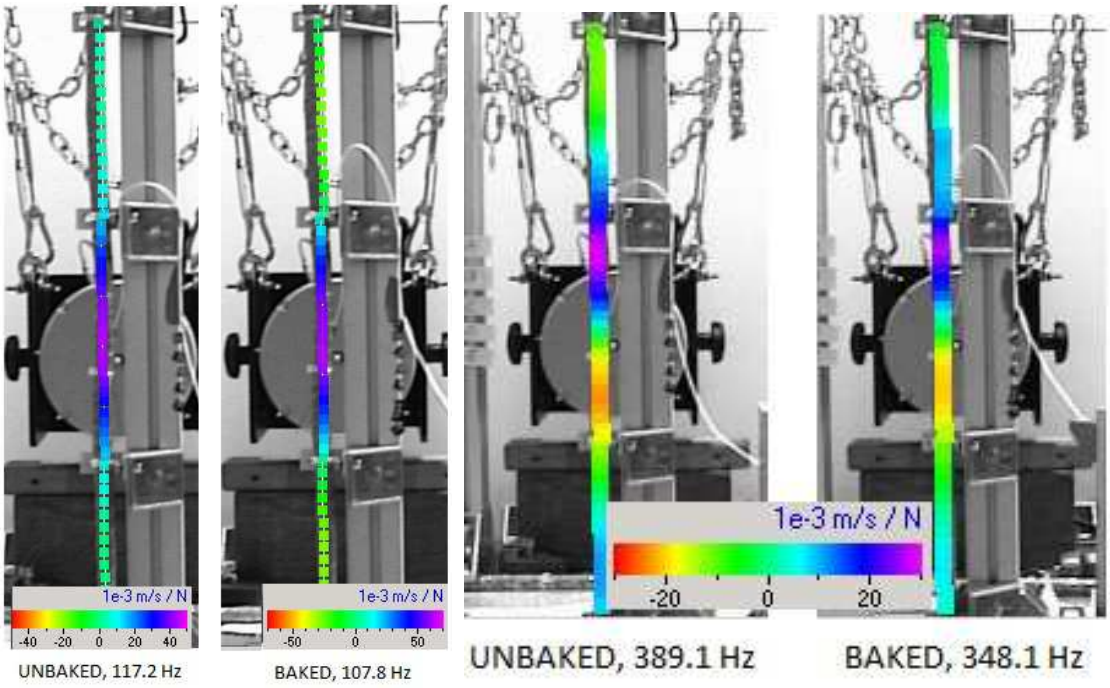

First Mode Second Mode

Figure 6.22: Comparison between first and second major beam modes for 1X48 unbaked (left) and baked (right) modes.

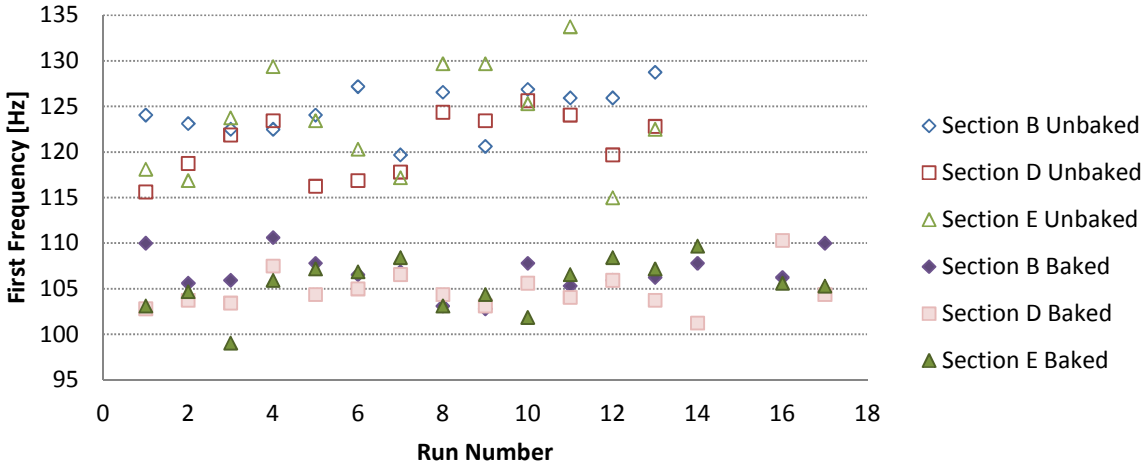

Figure 6.23: First natural frequencies for 1X48 cable sections, showing lower frequencies of baked cables for all trials.

6.3.4 Multi Stranded 7X7 Cable

The 1X48 cable was made to compare to the 7X7 cable; although both cables have about the same number of wires, the multi-stranded cable is significantly more flexible since it is made up of strands instead of individual wires. The data collected were consistent with the theory; the multi-strand cable was less stiff with lower first and second natural frequencies than the single-strand cable of the same size.

Proximity of the interaction modes becomes an even greater issue for the 7X7 cable, and inspection of the mode shapes is necessary to determine which frequencies correspond to the first and second beam modes of the cable test section. Figure 6.24 shows the FRFs for all 7X7 cable trials, still showing a left shift for the baked cables. The more flexible multi-stranded configuration does show a lower natural frequency than the 1X48 cable with similar wire count as expected. Although the interaction modes appear larger and in different locations than for the single stranded cables, the overall pattern of frequency decrease still occurs.

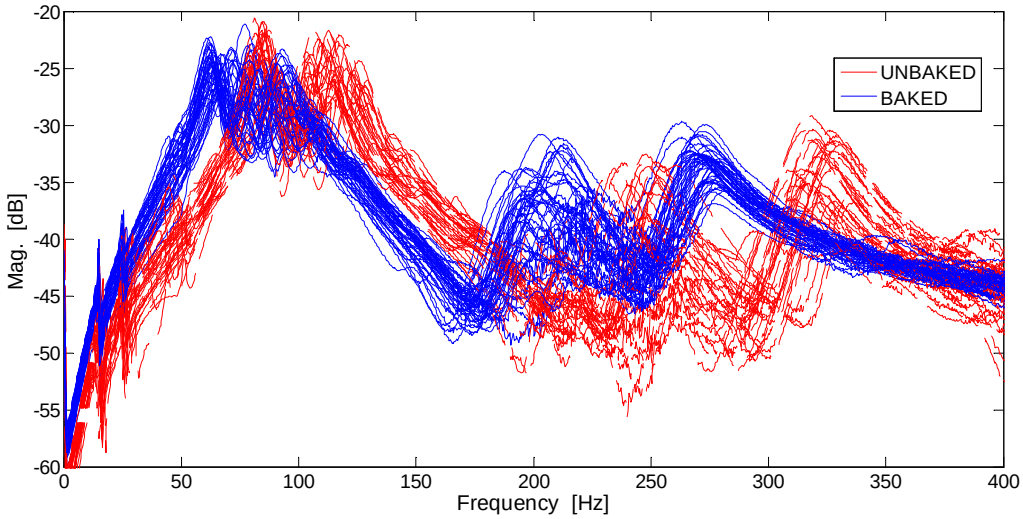

Figure 6.24: Comparison of unbaked and baked cables, showing a decrease in natural frequencies for 7X7 cable.

It is not necessarily the highest peak in the FRF that corresponds to the first frequency, which indicates that the interaction modes may be just as important in these larger cables to consider when determining maximum amplitude. Figure 6.25 shows the scan result for the first and second modes of the 7X7 cable. The first frequency is reduced from 81.9 Hz to 63.7 Hz, and the second frequency is reduced from 234 Hz to 194 Hz, differences of almost 23% and 18% respectively. Figure 6.26 shows another clear separation between baked and unbaked cable frequencies, with all baked frequencies for the 7X7 cable significantly lower than the unbaked frequencies.

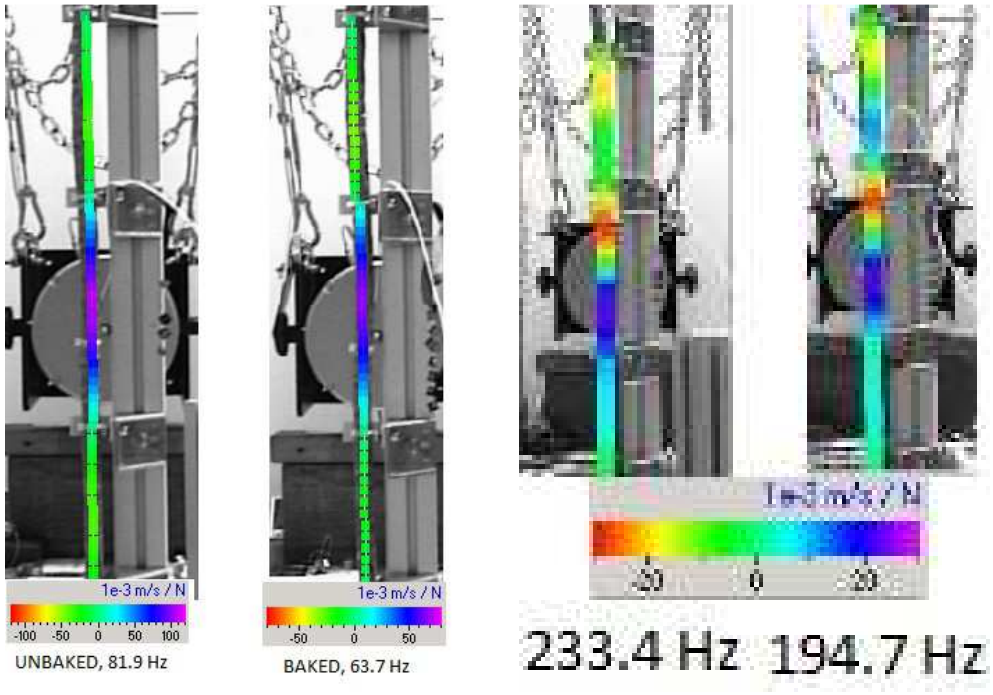

First Mode Second Mode

Figure 6.25: Comparison between first and second major beam modes for 7X7 unbaked (left) and baked (right) modes.

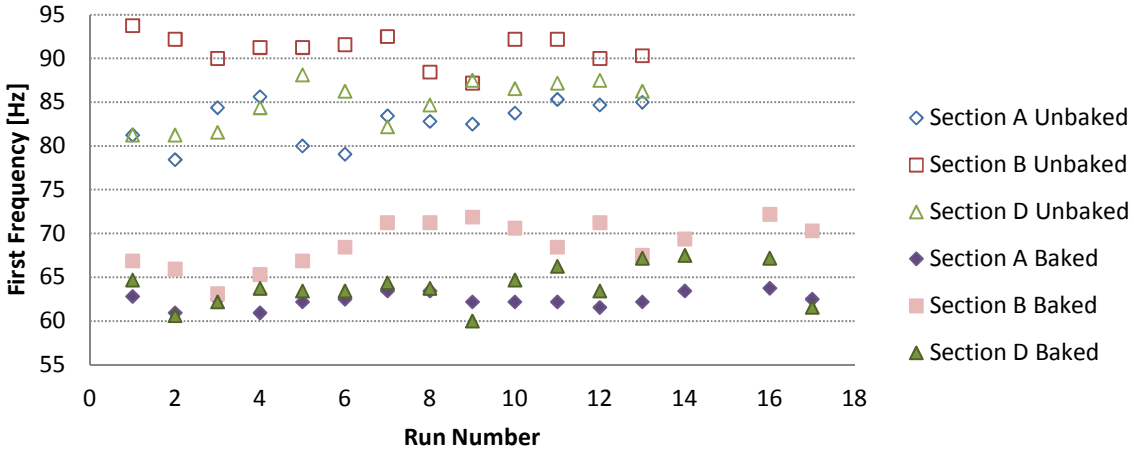

Figure 6.26: First natural frequencies for 7X7 cable sections, showing lower frequencies of baked cables for all trials.

6.3.5 Bakeout Effect Conclusions

Results from the comparison of the pre- and post-bakeout cable trials were conclusive. Data were taken in the form of multiple single-point runs and scans of the entire cable. The results from the single point data agreed well with averages taken from the laser scans and those evaluated using ME'Scope. The frequency response functions showed a clear shift left and natural frequency values decreased, both of which indicate a decrease in bending stiffness. The change in frequencies was consistent; all unbaked first frequencies for single stranded cables decreased between 14% and 15% after bakeout on average. However, the multi-stranded cable showed a more significant reduction in frequency at both the first and second beam modes. Table 6.2 presents the average first and second frequency values for each cable before and after bakeout. These averages are based on 39-54 runs per cable type, removed and remounted in the test section each time. Based on the percentage decrease in the natural frequencies, a bakeout correction factor of 0.8 could be included with the calculation of bending stiffness to take this effect into account.

Coefficient of variation was calculated for the baked trials, the unbaked trials, and then for all of the trials together for each cable. The coefficient of variation ranges from 0.015 to 0.06 for the unbaked trials, from 0.02 to 0.05 for the baked trials, and from 0.05 to 0.2 for combined unbaked and baked trials. The coefficient of variation for the combined trials for each frequency for each cable was larger than for the baked or unbaked trials in every case, and was almost always larger by a factor of 2 to 4. The frequency change exhibited by the baked out cables was greater than what could be expected due to only experimental variation. The list of coefficients of variation for each section and for each type of cable overall can be found in Appendix E; cable sections were compared directly before and after bakeout to ensure that changes were due only to bakeout and not cable section variation. More data are available from scans of the entire cable, but as the frequencies were within the distribution of the single point data and agreed with the overall results, the additional scans were considered superfluous.

Table 6.2 First and second frequencies, in Hz, for baked and unbaked cases for four cable types with percent reduction for each.

	Average First Frequency, Hz			Average Second Frequency, Hz		
Cable	Unbaked	Baked	% Reduction	Unbaked	Baked	% Reduction
1X7	46.1	39.3	14.8%	195.6	166.8	14.7%
1X19	70.5	59.9	14.9%	257.9	220.5	14.5%
1X48	122.9	105.7	14.0%	394.5	360.4	8.6%
7X7	86.3	65.1	24.6%	247.9	206.0	16.9%

Damping values were also investigated by using ME'Scope to determine damping percentage at the first mode. While the magnitude of the frequency response functions did not indicate a clear trend for damping behavior after bakeout, the percent damping calculated using ME'Scope showed an increase in damping percentage for all cables after bakeout. Table 6.3 presents the average damping percentage for the first frequency for each cable. This information is based on cable scan data.

Table 6.3 Percent difference in first frequency average damping for each cable type.

	First Frequency	
	Average %	Average %
Cable	Damping, Unbaked	Damping, Baked
1X7	3.40	3.72
1X19	4.96	5.74
1X48	3.65	7.05
7X7	4.83	9.07

This damping ratio data agree very well with previously published data of roughly 4% for unbaked cables of similar sizes [3], but bakeout treatment pushes the larger cables outside of this range, providing further evidence that bakeout effects should be taken into account for modeling and design purposes. Based on this data, bakeout can nearly double damping percentage for large cables, while small cables see only a slight increase in damping due to bakeout.

There are a few likely mechanisms to explain the cable stiffness softening effect exhibited. First, it was observed that the Tefzel insulation coating had shrunk down

around the wire after bakeout, indicating that the Tefzel coating may have shrunk overall, binding the individual conductors more snugly but providing more interstitial space in between the individual wires. The increase in space may lead to a decrease in the radial pressure holding the wires together, thus making the individual wires act more like a flexible set of wires and less like a stiff solid beam. Another hypothesis relates to the outgassing of plasticizers in cable insulation, but since plasticizers are not present in the Tefzel insulation used for these wires, that is unlikely to be a mechanism that contributes to the changes observed. The Kapton overwrap may also experience changes due to the bakeout treatment; the Kapton becomes more brittle after heat treatment, which may lead to the perception that the cable is stiffer even though its dynamic stiffness has decreased. It was observed that when holding baked and unbaked cables out as cantilevered beams, the baked cable showed a larger amount of end displacement, providing further verification that the baked out cables become less stiff after bakeout.

To match the frequency reduction exhibited by the baked out cables, the theoretical cable model requires a reduction in the bending stiffness value, with the baked out cables having a bending stiffness of about 80% of the unbaked cable when connection stiffness is on the order of $5*10^4$ N/m. This change in bending stiffness value should be incorporated into cabled structure models if the other model inputs (such as connection stiffness, density, and area) remain the same. Figure 6.27 shows the effect of adding a 0.8 bakeout correction factor to the cable model frequency response function for the four-point 1X19 cable model, a representative graph of the cables investigated.

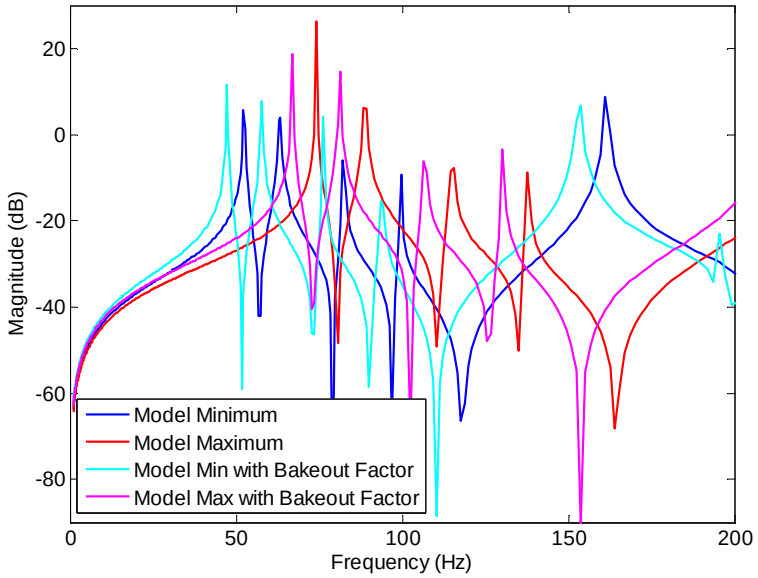

Figure 6.27: Effect of including the bakeout correction factor on the four-point 1X19 cable model; including the bakeout factor in the bending stiffness input decreases natural frequencies similar to the decrease in experimental frequency response function results for baked out cables.

6.4 Cable Damping

While the undamped cable models provide adequate ranges for natural frequency prediction, the amplitudes of the model responses do not reflect the experimental data well unless damping is included. As discussed in Chapter 3, the viscous damping model that approximates damping due to the motion of the cable in its surrounding medium is not adequate to capture the internal damping and material damping in cables, since cables have both friction between the wires and viscoelastic material as insulation. In addition, this viscous air damping would be entirely absent in the vacuum of space where spaceflight cables are used. Cables dissipate more energy than a similarly sized solid rod, experiencing greater hysteresis. To determine the damping term coefficients for the hysteretic form of cable damping, the damped model was fit to the experimental cable response average for the two-point cable. Those damping coefficients were then applied to the damped four-point cable model and the cabled beam model. Fitting the coefficients to the specific experimental data for each configuration (two-point, four-

point, or cabled beam) could result in better damped models for the four-point cable model and cabled beam, but since one of the goals of this work was to reduce the need for experimental cable testing, only the two-point data was used for damping parameter determination to evaluate whether damping could be extrapolated from the two-point data for at least the first mode of the other configurations.

Since bakeout appears to have an effect on the cable damping, the bakeout correction factor must be included for all damped cable models, which actually improves the model agreement and supports the idea that damping can be partly incorporated through appropriate variable bending stiffness calculation.

6.4.1 Determination of Cable Hysteretic Damping Coefficients

Figures 6.28 - 6.31 show the fitted damped cable model FRFs with the average of the experimental scan FRFs for each cable in the two-point fixture. The damped model included the bakeout correction factor and the model FRF shown in the following figures is based on the cable inputs for the minimum frequency response; the darker blue bars above each frequency show the damped frequency range. Table 6.4 lists the damping coefficients for the GHM hysteretic damping form used for the damped two-point cable models in Figures 6.28 - 6.31.

In each of the damped cable model comparisons, the amplitudes for the first three frequencies are matched very well, with the exception of the 1X19 cable, which had a second frequency that was higher than predicted due to the interaction of the structure mode that occurs at the same location as the second mode of the 1X19 cable and thus increases the amplitude. Not only are the amplitudes matched, the damped frequency ranges were generally able to span the experimental frequency. The lower frequencies were better matched by the minimum model, while higher frequencies tended toward the maximum value model. Thus, the minimum to maximum model span seems to be a decent method to evaluate the first 3-5 modes of the cable. If prediction of fewer modes was required, the minimum model could be used with confidence for the first two modes in each case.

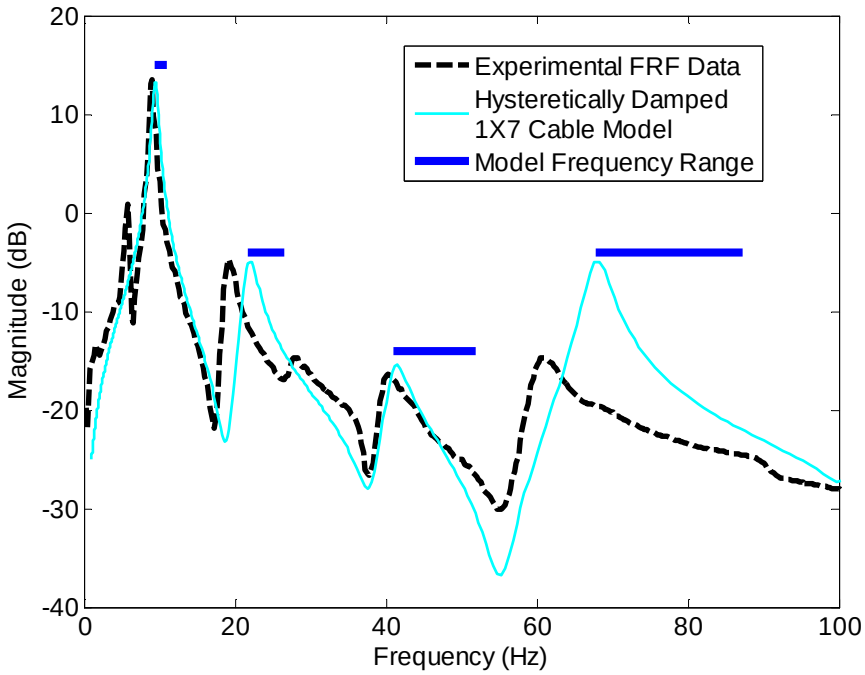

Figure 6.28: Comparison of experimental data and hysteretically damped cable model for the 1X7 cable in two-point fixture configuration.

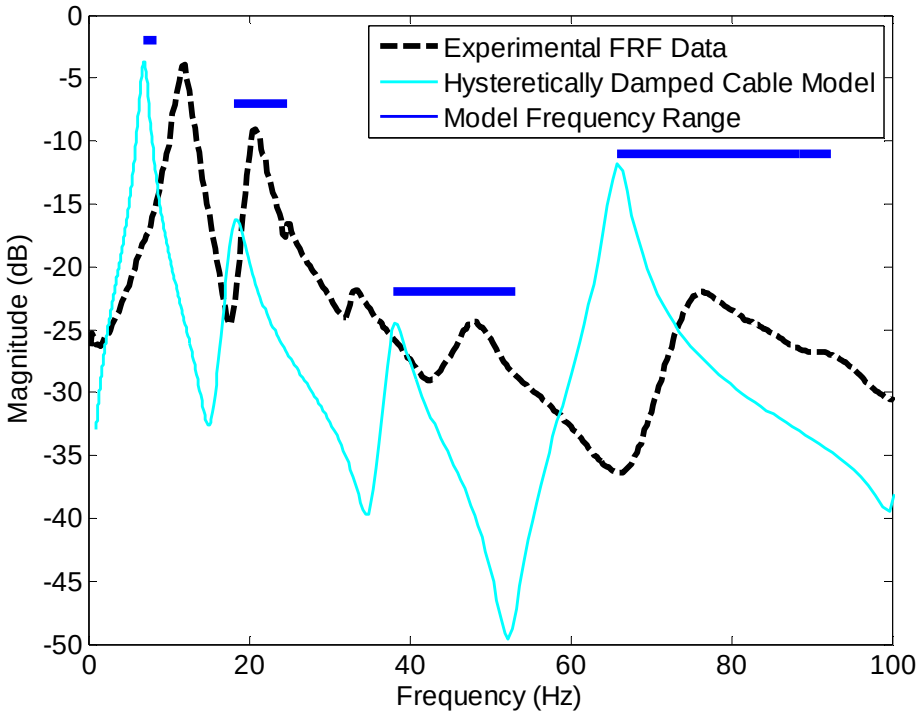

Figure 6.29: Comparison of experimental data and hysteretically damped cable model for the 1X19 cable in two-point fixture configuration.

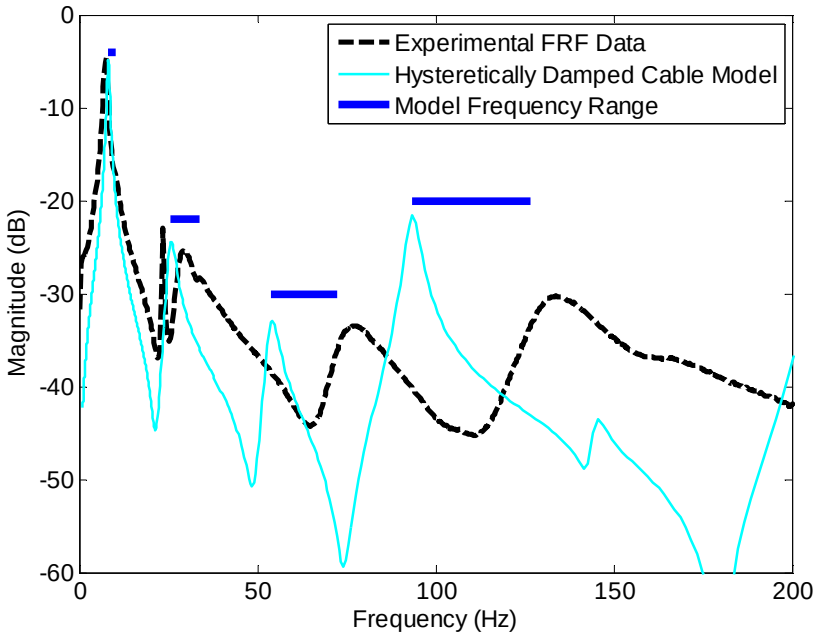

Figure 6.30: Comparison of experimental data and hysteretically damped cable model for the 1X48 cable in two-point fixture configuration.

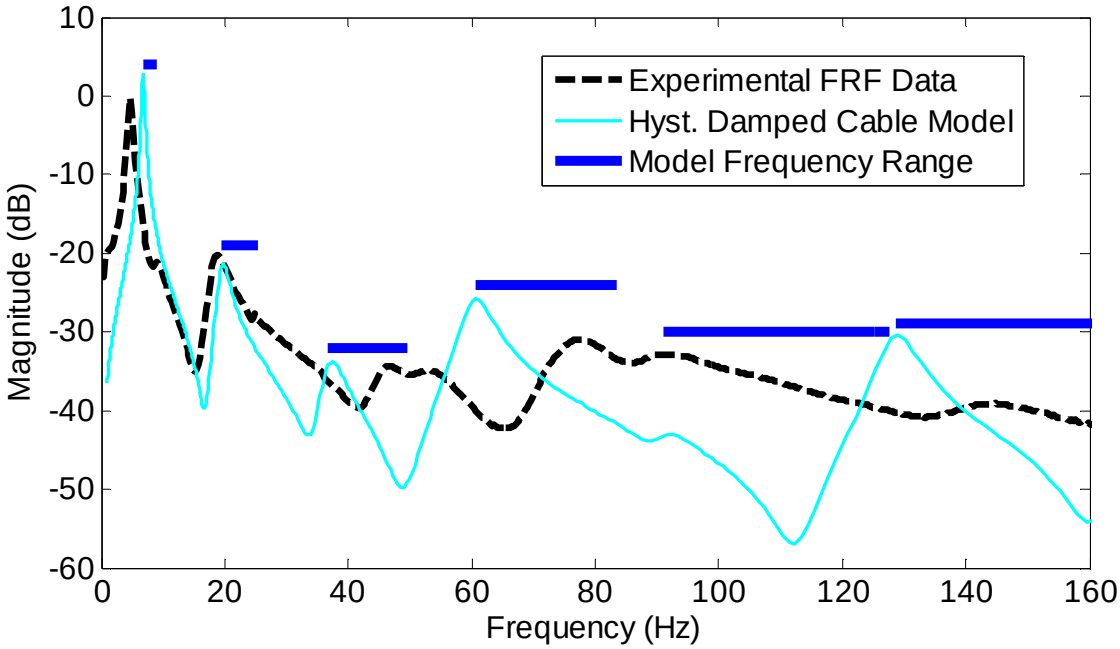

Figure 6.31: Comparison of experimental data and hysteretically damped cable model for the 7X7 cable in two-point fixture configuration.

Recall the form of time hysteretic damping from Chapter 3, where the hysteretic cable damping was modeled in the form

$$G(s) = \frac{\alpha s^2 + \gamma s}{s^2 + \beta s + \delta}$$

Table 6.4 contains the coefficients for each hysteretic damping term for each cable, as determined from fitting the model data to the experimental data for the two-point fixture configuration. The gamma term had the greatest effect on matching the second and third mode amplitudes once the first mode amplitude was matched sufficiently. The delta term could shift the model frequencies to some degree without significantly changing the amplitude of the model. A more sophisticated curve fitting program could probably improve the damping parameters determined for the two-point cables, especially if more terms were added to the hysteretic damping form to improve the curve fit over a larger frequency. The GHM method was initially developed for finite element analysis, so it is typical to include a sum of terms of the form in $G(s)$, instead of the single term as used here since the finite element method was not used. More terms in the GHM damping model could improve the damping fit for the cable models.

Table 6.4 Hysteretic damping coefficients based on fitting of model to experimental data.

	Numerator Terms		Denominator Terms		
Cable Type	$\alpha * s^2$	$\gamma * s$	s^2	$\beta * s$	δ
1X7	25	9000	4	1	-8000
1X19	70	6000	5	2	2000
1X48	180	40000	2	2	-9000
7X7	140	60000	2	2	-15000

Appendix F shows the results from applying the two-point fixture damping expressions (listed in Table 6.4 for each cable) to the four-point model; agreement is good for the first mode when damping coefficients determined from the two-point comparison are applied in the four-point model, but other than the first mode, it appears that damping characteristics cannot be extended from the simpler experiments. Further study would be

needed to determined whether differences in the damping of the cable in different fixtures can be determined without requiring dynamic testing.

As an illustration of the complexity of cable damping, a comparison of the time hysteretic damping used and typical viscous damping is shown for the 1X7 cable in Figure 6.32. Hysteretic damping yields correct FRF amplitudes for at least the first three modes in general, whereas viscous damping can only reasonably approximate the FRF amplitude for one mode at a time. The cyan hysteretically damped model shows good amplitude agreement for the first three modes, and even the fourth mode is not overly high. In contrast, two values for viscous damping were run to show that viscous damping can only be matched to one amplitude at a time; for instance, the red viscously damped model with cv = 0.4 matches the first frequency amplitude with a damping ratio of about 4.0%, but all other amplitudes are too high. The green viscously damped model matches the amplitude of the third mode, but the first and second modes are then modeled as being lower than reality. Viscous damping can only match one mode, while hysteretic damping can model more modes more accurately. Structural damping was also compared, with better results than the viscous damping model; for the 1X7 cable, using an alpha value of 2.5 and a beta value of $8*10^{-4}$ resulted in decent agreement for one or two modes, but the hysteretic damping method still matches more modes. Figure 6.33 compares structural damping to hysteretic damping for the 1X7 cable.

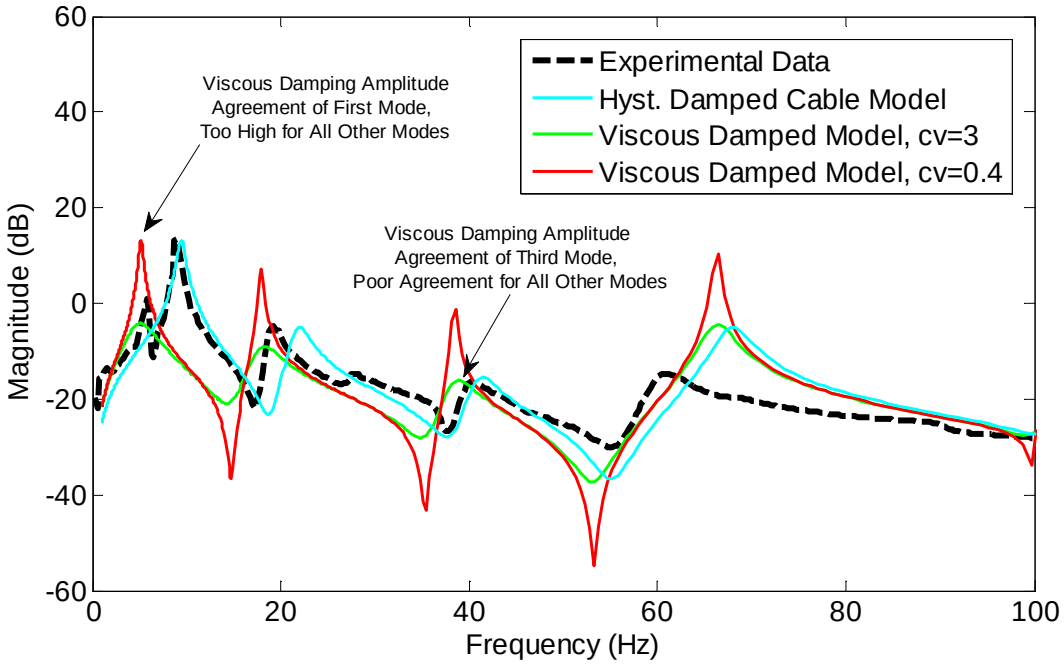

Figure 6.32: Comparison of hysteretic and viscous damping for the 1X7 cable model; the cyan hysteretically damped cable model matches amplitudes for first three modes, while the viscous damping model can only match one mode at a time.

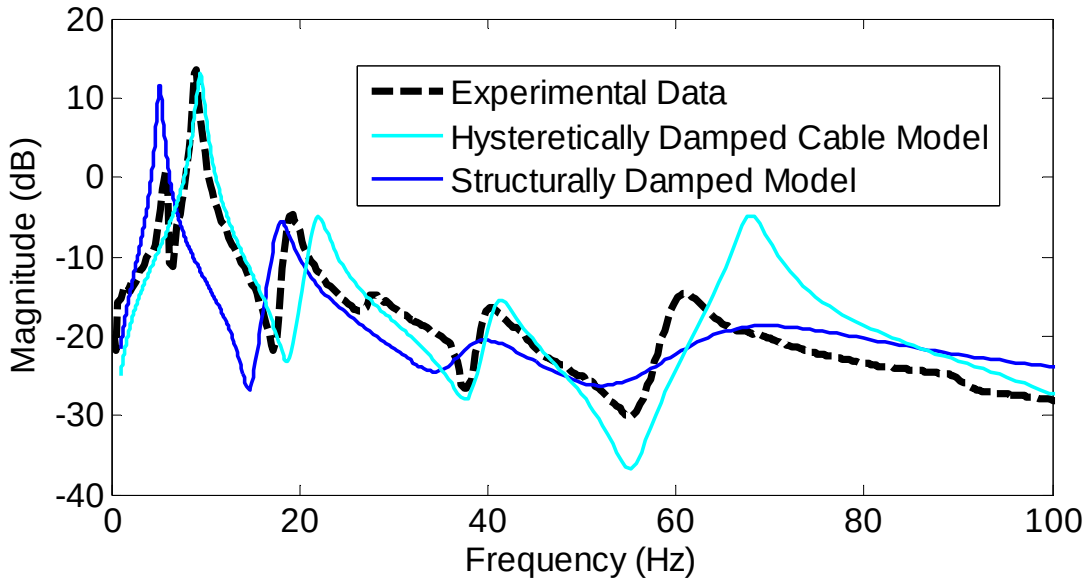

Figure 6.33: Comparison of hysteretic and structural damping for the 1X7 cable model; structural damping is an acceptable choice for cable modeling, but still does not match as many modes as closely as a hysteretic damping model.

6.4.2 Experimentally Determined Cabled Structure Damping

Since one of the overarching objectives of this research is to quantify the effect of cables on cabled structures, before attempting to model the damping of a cabled structure, it is useful to know how heavily the structure is damped. Table 6.5 gives the average damping percentages for 10 scans of the bare beam and the cabled beam for each cable type. In general, larger cables have more damping, but no clear trend is established.

Table 6.5 Average damping percentages for each bending mode for bare beam and cabled beams.

Bending Mode	Bare Beam	1X7	1X19	1X48	7X7
1	0.01	0.35	1.27	3.20	2.10
2	0.43	1.13	2.80	2.00	4.10
3	0.02	0.29	0.40	0.72	0.08
4	0.01	0.26	1.49	0.62	0.70

6.5 Cabled Beam Experimental Results

The effects of adding cables to structures are not completely understood; therefore, before presenting the comparison between the cabled beam model and experimental cabled beam results, it is beneficial to investigate the purely experimental results of cables attached to beams. Figure 6.34 shows the experimental comparison between the bare beam and the four types of cables, based on a dense scan. Appendix G contains plots of the mobility transfer functions (TFs) for the ten sparse scans of each cabled beam as measured on the beam near the driving point, and as measured on the cable, shown with the average frequency response function for all trials. It is clear that the bending modes of the bare beam still appear, but may be shifted due to the addition of the cable. The cable also causes additional modes where the cable experiences resonance. Torsional modes are evident (based on observation of the mode shapes as well as the FRFs) for the bare beam and all cables at about 250 Hz and 490 Hz, which agrees with the theoretically calculated torsional modes of 246 Hz and 492 Hz for the bare beam. Table 6.6 lists the experimental torsional frequencies for the bare beam and cabled beams. None of the cabled beams showed shifts in the torsional frequency of more than 1.2% from the bare beam values; this was expected since the cable was attached at the

centerline of the beam specifically to minimize any changes in the torsional response since torsional response was not modeled.

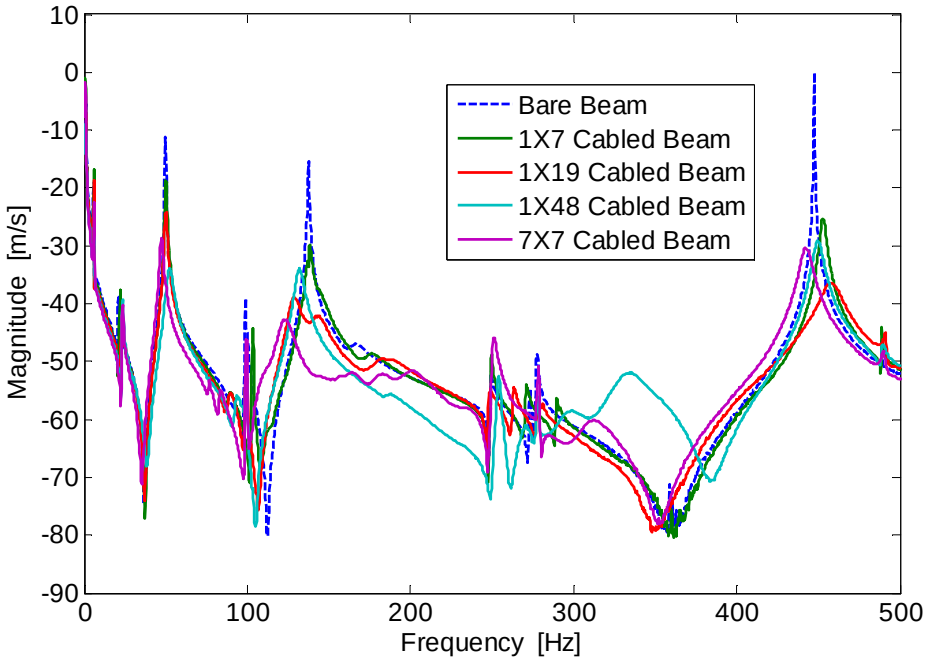

Figure 6.34: Comparison of experimental data from bare beam and each cable attached to the beam, measured close to the driving point on the beam.

Table 6.6 Experimental average torsional frequencies of the bare and cabled beams, in Hz.

	First Torsional Mode		Second Torsional Mode	
	Frequency (Hz)	% Difference from Bare Beam	Frequency (Hz)	% Difference from Bare Beam
Bare Beam	249.1	-	489.1	-
1X7 Cabled Beam	250.0	0.36%	490.0	0.18%
1X19 Cabled Beam	248.8	0.12%	491.3	0.45%
1X48 Cabled Beam	251.8	1.08%	488.5	0.12%
7X7 Cabled Beam	252.0	1.16%	490.3	0.25%

Different size cables do not affect the system frequency response in the same way. Additional cable modes from the 1X7 cable occur below the first bending frequency of the system, while the additional modes from the other cables add small magnitude resonance frequencies above the first system bending mode. The damping added by the

cable is significant, and larger cables add more damping to the structure at most system bending modes. Although the cable was attached to the beam the same way for each trial, results between cabled beam trials showed variation similar to the variation shown by the grounded cables. Figure 6.35 shows the transfer function plot for the 7X7 cabled beam with the dense scan trial and ten sparse scan trials overlaid on the average of the trials. The major beam frequencies are repeatable, but the small magnitude additional frequencies due to the cable (between 150 and 200 Hz, for instance) have significant variation from trial to trial. For model comparison purposes, the average of the 11 total trials is used to represent the experimental data.

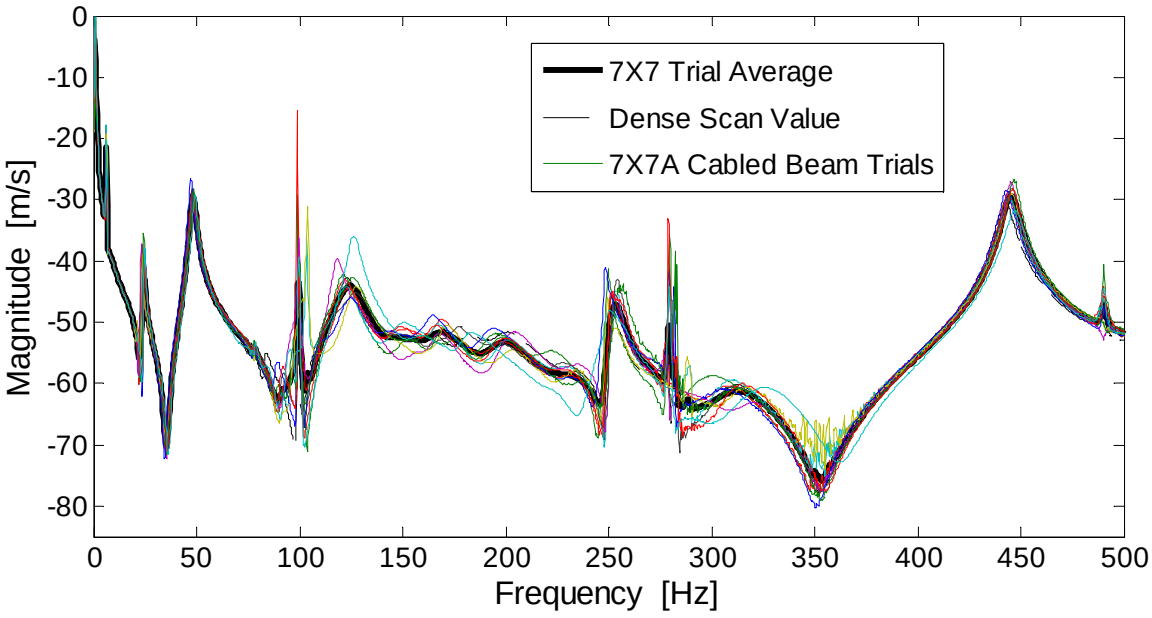

Figure 6.35: Transfer frequency response function for the 7X7 multi-stranded cable showing the variation between trials for small amplitude modes.

Figure 6.36 shows the frequency response function and associated phase angle plots for the bare beam and the 1X48 beam from dense scan data measured at the driving point. Additional modes are indicated around 350 Hz by the approach of the phase value to 0 degrees, as expected for phase angle measured for a mobility transfer function using measured velocity. Note that this is different than a transfer function based on measurement of displacement, where a natural frequency is indicated by a 90 degree phase shift.

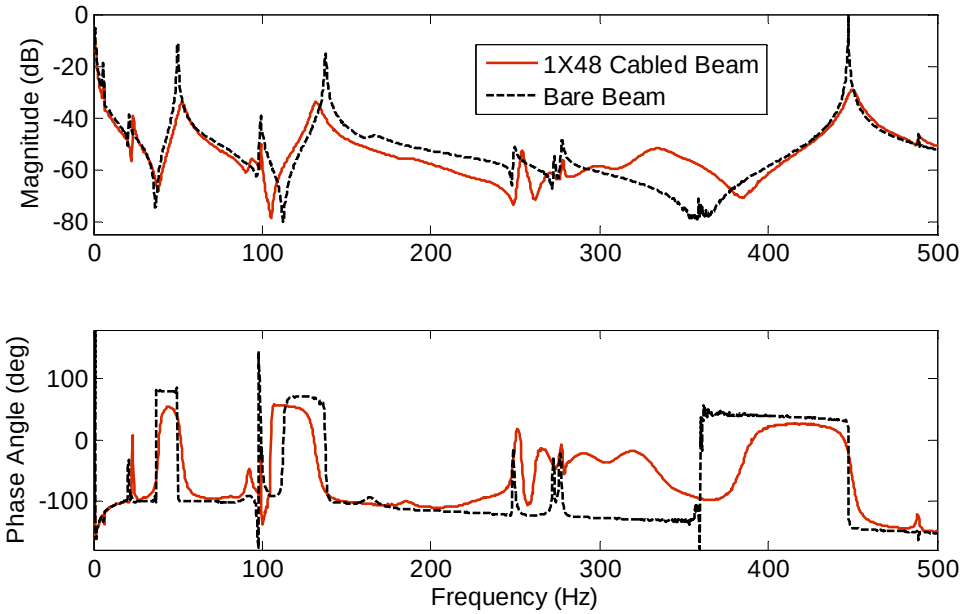

Figure 6.36: Frequency response function and associated phase angle plots for the bare beam and 1X48 beam measured at the driving point.

As a valuable illustration to show the complexity of stranded cables as compared to solid materials and the importance of bending stiffness calculation for cable models, solid material rods of similar size, weight, and/or bending stiffness were attached to the beam and scanned to obtain the frequency response functions. Figure 6.37 shows the comparison between the 1X19 cable on the beam and the Acetron rod. The Acetron rod had similar mass and bending stiffness to the 1X19 cable, and the results have similarities in terms of frequency shifts and amount of damping added, but the cabled beam has more additional system frequencies than the rod does, particularly around the second and third bending modes. Figure 6.38 shows the comparison between the 1X48 cable and a 316 stainless steel rod, which had very similar mass, but much higher bending stiffness than the cable. The results show differences between a cable and a rod attached to the beam; in each case, the solid rod exhibits fewer additional modes than the cable does when compared to the bare beam. The solid rods also stiffen the structure at all low frequencies, shifting the natural frequencies higher despite the additional mass. The

cables do not uniformly stiffen nor soften the structure, but affect each mode somewhat differently.

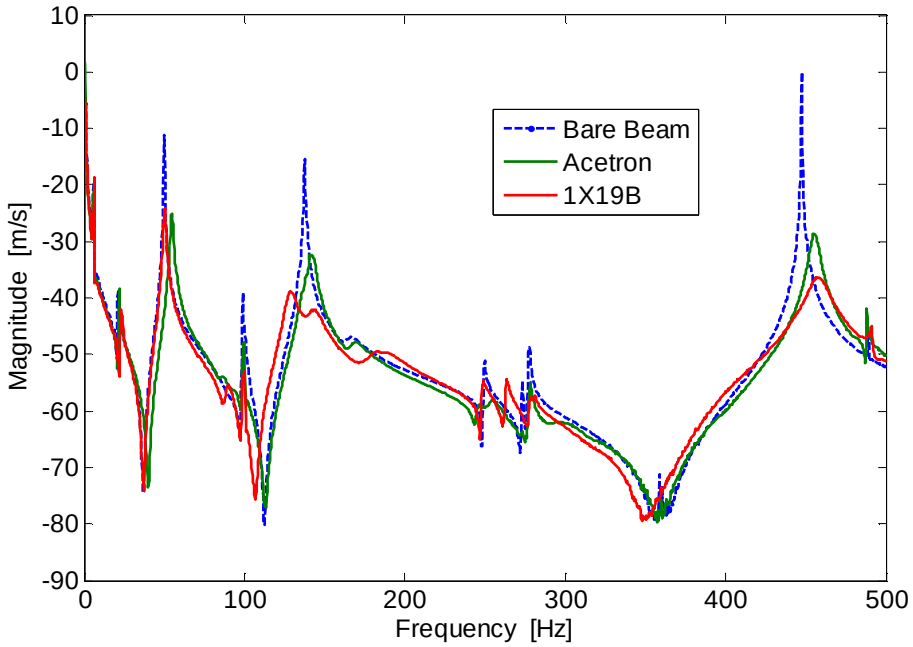

Figure 6.37: Frequency response comparison between the 1X19 cable on the beam and an Acetron rod of similar mass and bending stiffness on the beam.

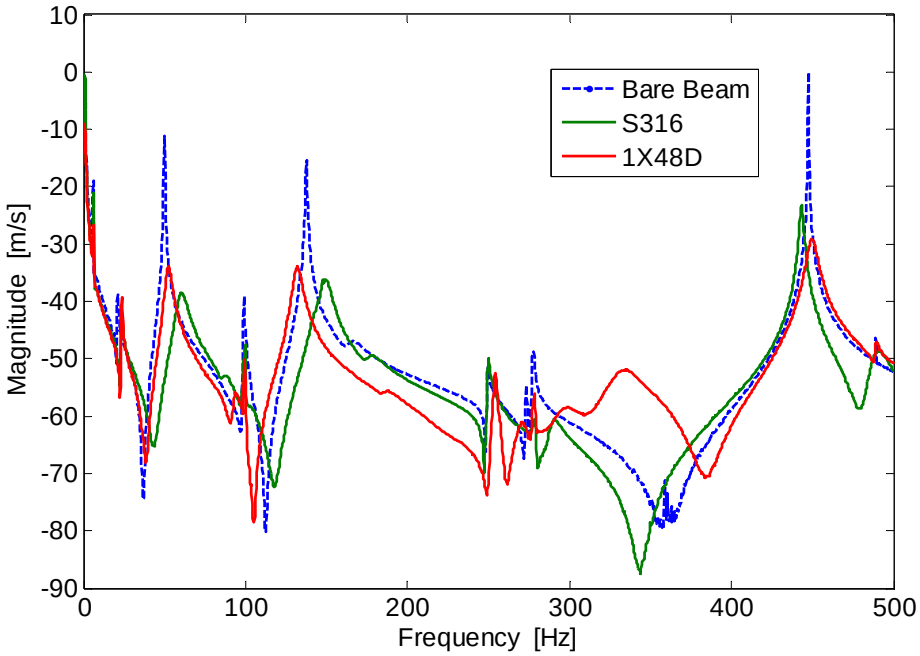

Figure 6.38: Frequency response comparison between the 1X48 cable on the beam and a stainless steel 316 rod of similar mass, but much higher bending stiffness, on the beam.

The importance of the cable bending stiffness is further illustrated by comparisons between the similarly sized single strand and multi-strand cables. Figure 6.39 shows five trials of each of the two types of large cables compared to the bare beam. The 1X48 cable and 7X7 cable have a mass difference of only 46 grams (about 3% of the mass of the beam) and yet they shift the first natural frequency of the cabled-beam system in opposite directions, as shown in detail in Figure 6.40. In addition, the multi-strand cable has additional modes around 200 Hz that are nearly equal in magnitude to the second cabled-beam bending frequency around 140 Hz that the single-strand cable does not exhibit. Although the mass is very similar for these cables, the 7X7 cable is significantly more flexible with much lower bending stiffness. The difference between the 1X48 and 7X7 cable FRFs underscore the importance of taking cable configuration and thus, cable bending stiffness, into account for cable modeling; simply modeling the cable as a rod with a single bending stiffness value would not capture the differences between these cable configurations.

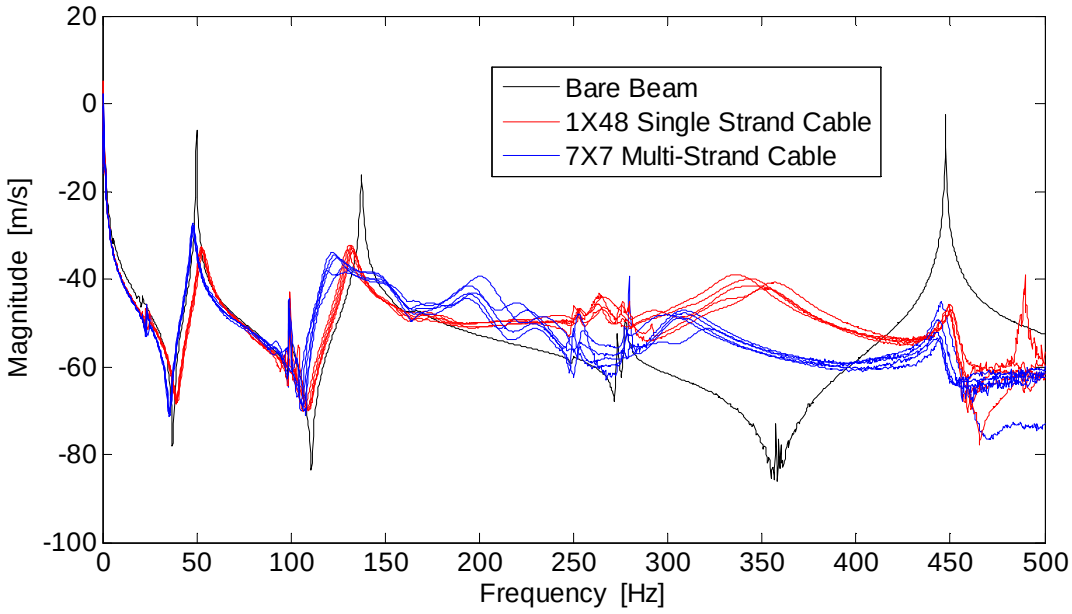

Figure 6.39: Comparison between five 7X7 and five 1X48 cabled beam trials to show differences between similar mass cables with different wire configurations, particularly in the first mode where the stiff 1X48 cable has a higher frequency despite the additional mass.

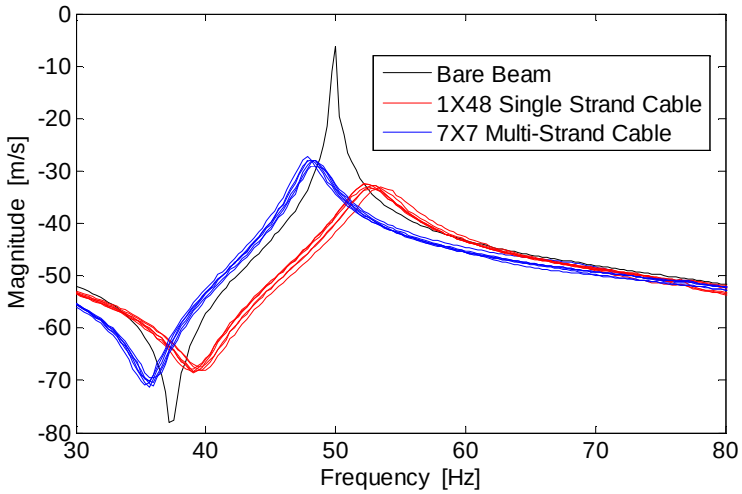

Figure 6.40: Enlarged view of FRF near first natural frequency, showing the consistent and clear frequency shifts for the cabled beam when single or multi-stranded cable is attached.

Just as with the cable experiments, mode shapes must be examined to ensure that frequencies between bare beam and cabled beam are being compared correctly. Mode shapes were observed for both the dense scans and all sparse scan trials. Figure 6.41 shows the mode shapes for the bare beam, while Figure 6.42 shows mode shapes representative for a cabled beam, specifically the beam with the 1X48 D cable attached. Additional modes where the cable is experiencing resonance are identified with a red arrow. Appendix H contains the mode shapes for the other cabled beams. The bending modes are clearly exhibited for all cabled beams, along with additional cable modes.

For all cables, the first and second mode shapes were dominated by the beam, and the cable flexed in phase with the beam. Additional combined modes were observed in which the beam showed some bending while the cable showed relatively large deflections out of phase with the beam. The addition of a cable to the beam also increased the interaction between the torsional mode and the third bending mode. The fourth bending mode was relatively unchanged from the bare beam mode shape. Having identified the experimental effects of cables on the beam structure, the developed cable model can be evaluated and compared.

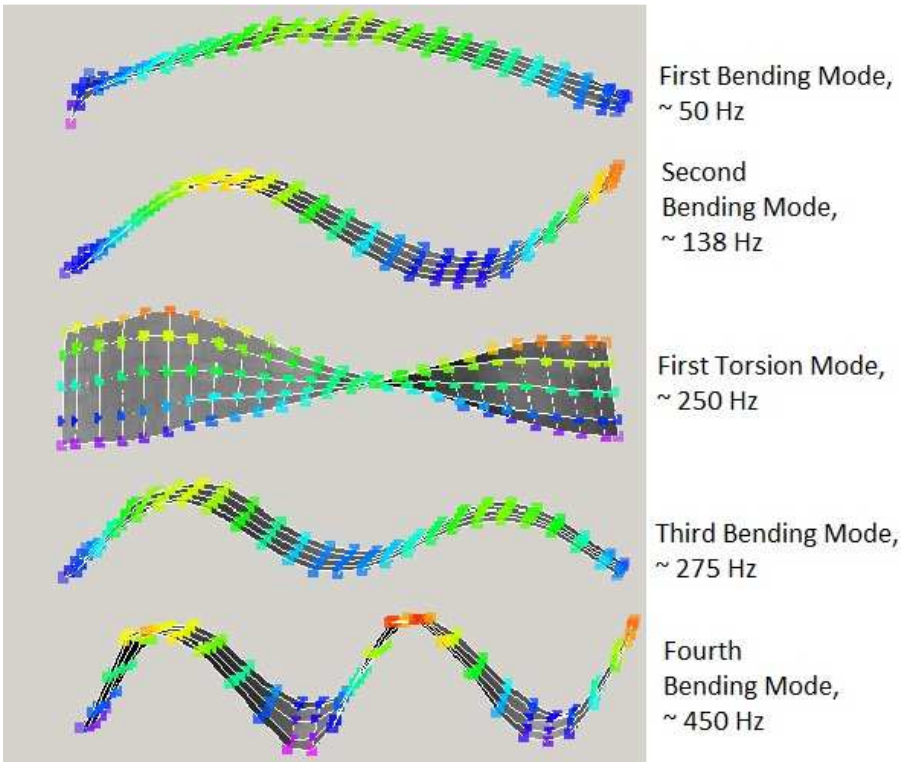

Figure 6.41: Mode shapes of the bare beam from dense scan.

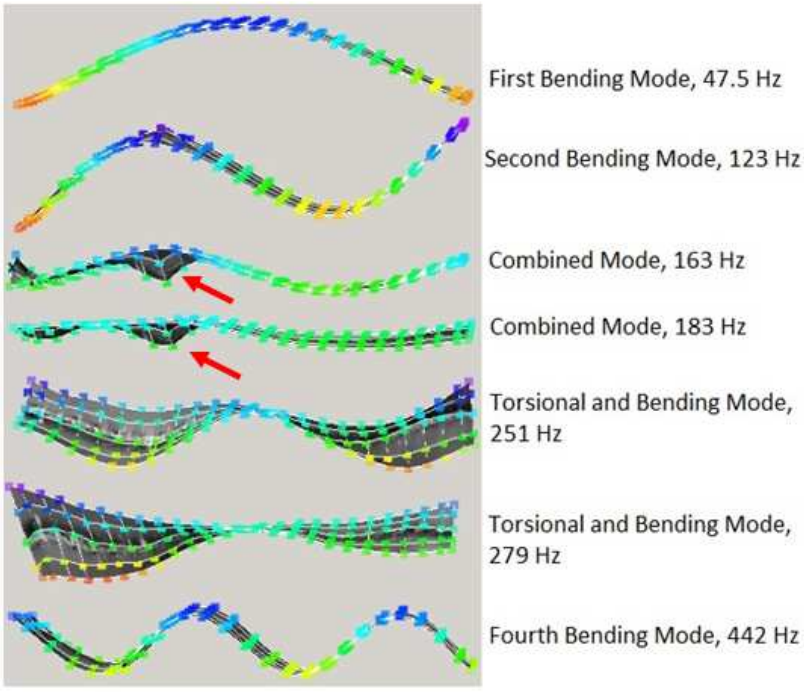

Figure 6.42: Mode shapes of the 1X48 cabled beam from the dense scan, with areas of noticeable cable deflection identified by red arrows.

6.6 Cabled Beam Model Results

This section presents comparisons between the cabled beam model and experiments. First, the rod-on-cable experimental data and model results are shown and discussed briefly. Then the cabled beam experimental data and model are compared and discussed, and finally the currently used distributed mass model is shown in comparison to the DTFM cabled beam model and experimental data. The limitations of the distributed mass model and DTFM models are discussed, including recommendations about which model is more appropriate depending on cable size and desired output information.

6.6.1 Rod-on-Beam Comparison

Before evaluating the DTFM model's effectiveness for the cabled beam, the cabled beam model was evaluated with a solid Acetron rod in place of the cable to ensure that the basic rod-on-beam system was adequately modeled before adding the complexity of the cable parameters. The rod and beam were both modeled as Euler-Bernoulli beams with linear and rotational connection stiffness included using the values determined from the rod tests. As shown in Figure 6.43, the rod on beam model was able to capture the experimentally determined natural bending frequencies of the structure within 10% , acceptable considering the simplicity of the model, use of connection values determined from prior results, and only light viscous damping included.

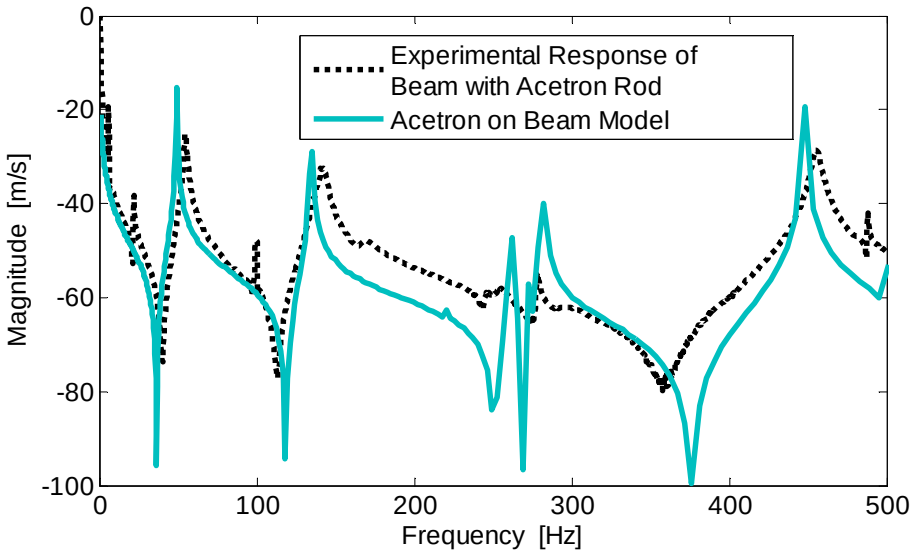

Figure 6.43: Comparison of experimental and model transfer functions for Acetron rod attached to beam, with Acetron rod modeled as an Euler-Bernoulli beam.

6.6.2 Distributed Transfer Function Cabled Beam Model Comparison

The distributed transfer function method cabled beam model consists of a DTFM cable attached with linear and rotational stiffness to an Euler-Bernoulli beam. The use of the distributed transfer function model for the cable allows for inclusion of cable properties such as bending stiffness and shear rigidity, parameters that are absent in lumped or distributed mass models. The cabled beam model could be run to output minimum, middle, or maximum values by choosing the minimum, middle, or maximum values calculated by the cable parameters. The middle value used the middle calculations for area and density, and the average value for bending stiffness. Bending stiffness was calculated based on the equations presented in Chapter 3 and the span of the cable between connection points to determine the maximum displacement, with the bakeout factor included and damping included as calculated for the two-point fixture cables. Viscous damping was added to the stiffer cables for improved curve fit.

Due to the complexity of the cabled beam transfer functions, only the damped average (middle) value transfer function is shown for clarity, with the minimum and maximum frequency range shown with horizontal bars. It is important to note that the frequencies must be compared using both the transfer functions and the mode shapes, since frequencies that appear to be similar in value may actually represent different modes. To that end, modal assurance criteria were run for each cabled beam structure. The averaging of the experimental data sometimes smoothes areas where multiple frequencies are present, so Appendix I contains the undamped and damped minimum and maximum models compared to the 11 cabled beam trials for each cabled beam.

Figure 6.44 presents the damped average transfer function response for the 1X7 cabled beam. The average experimental data is shown with a black dashed line; the model average is shown as a purple line, and the range of natural frequency values based on the minimum and maximum cable input parameters are shown as red range bars above the respective frequencies. Note the very narrow range for the first bending frequency (around 50 Hz) and the eighth frequency (around 450 Hz). In fact, all of the major structure bending frequencies that occur similar to the bare beam are modeled with a very

narrow result; the additional modes that are introduced due to the addition of the cable on the structure have a much wider range, which corresponds to the uncertainty in the cable parameters.

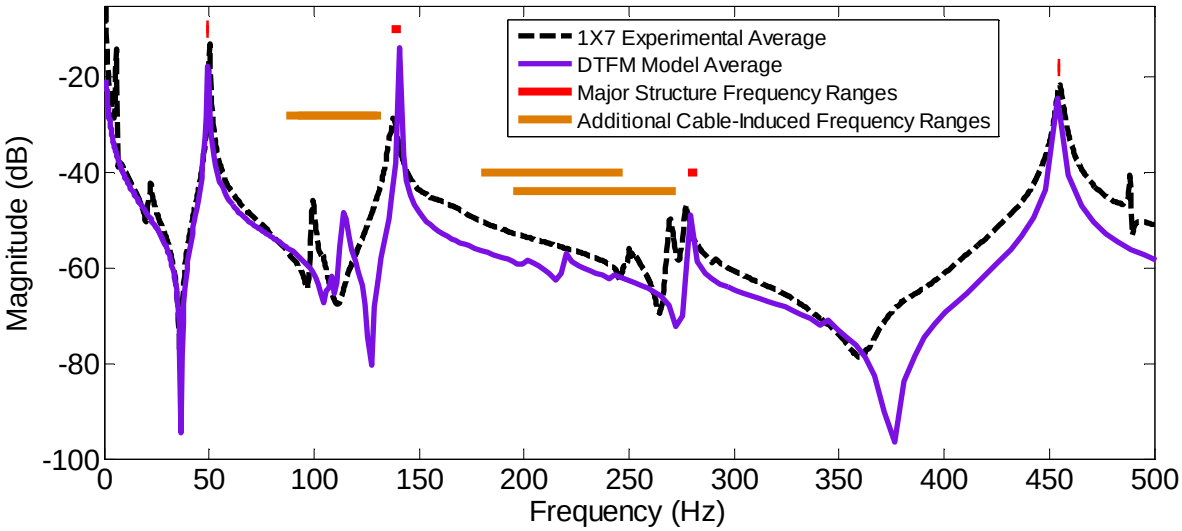

Figure 6.44: Damped average cabled beam model compared to experimental data for 1X7 cabled beam, with ranges for the natural frequency values shown as bars.

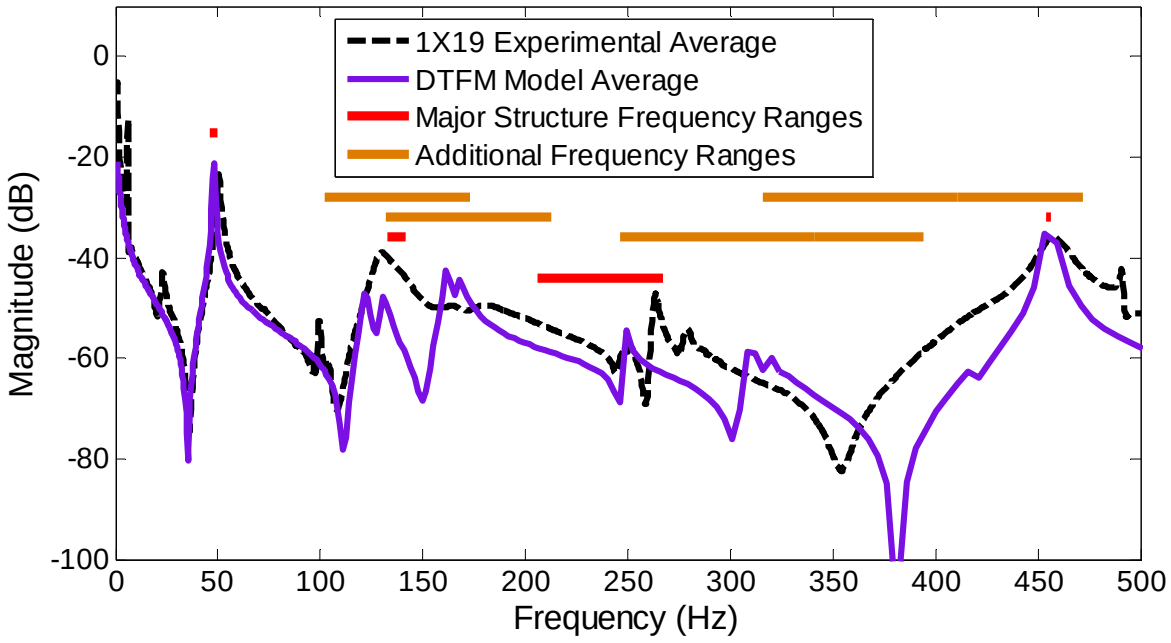

Figure 6.45: Damped average cabled beam model compared to experimental data for 1X19 cabled beam, with ranges for the natural frequency values shown as bars.

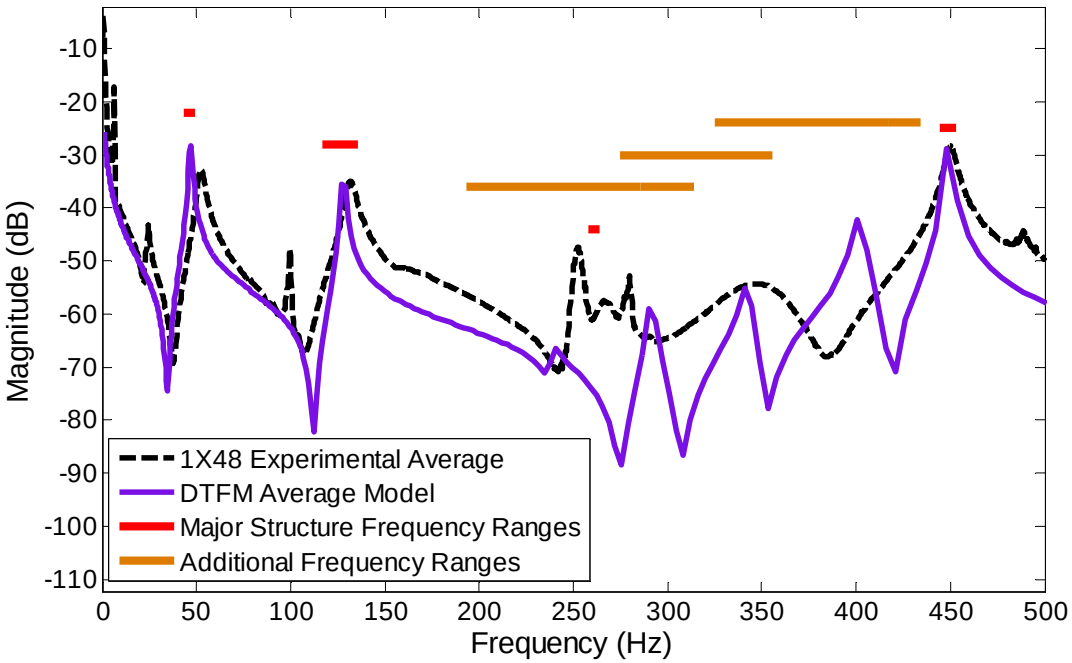

Figure 6.46: Damped average cabled beam model compared to experimental data for 1X48 cabled beam, with ranges for the natural frequency values shown as bars.

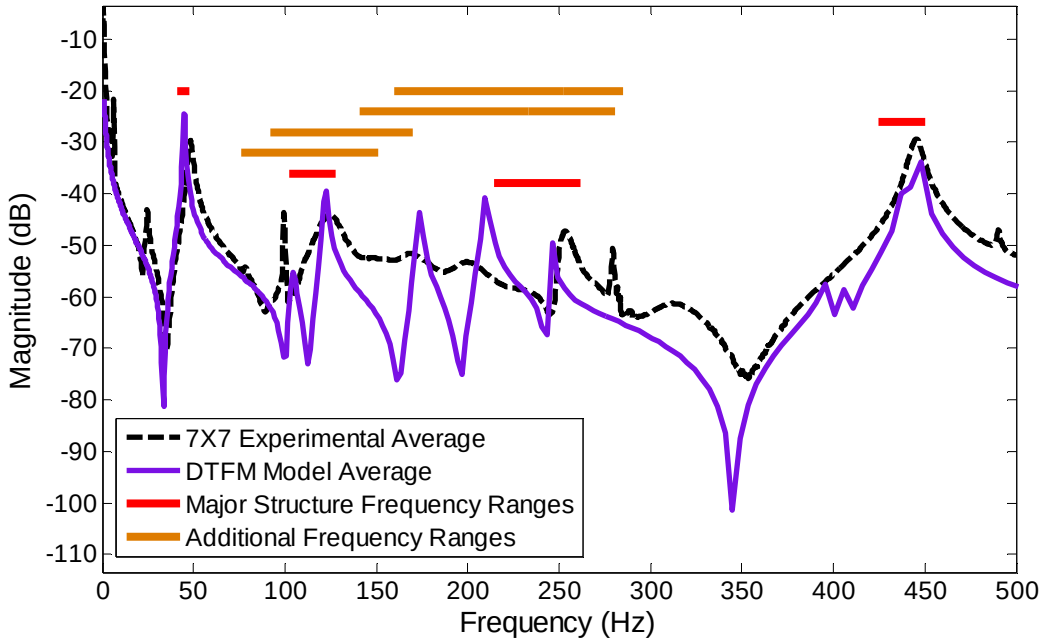

Figure 6.47: Damped average cabled beam model compared to experimental data for 7X7 cabled beam, with ranges for the natural frequency values shown as bars.

Just as with the cable models, it is important to compare mode shapes as well as natural frequencies to ensure legitimate comparison between model and experimental data. This is especially important for the cabled beam as the number of frequencies predicted with the minimum and maximum cable parameter values as inputs will not necessarily be the same; the minimum cable parameter values tend to have additional lower modes. Only mode shapes that were clearly matched for both minimum and maximum inputs are shown as additional frequency ranges in Figures 6.44 through 6.47. To compare the mode shapes, modal assurance criteria were run for each cabled beam structure, where the raw experimental shapes of both the cable and the beam were compared to the model shapes. Figure 6.48 shows the MAC for the bare beam model as compared to the experimental data. Note that the torsional mode at 250 Hz is not captured by the bending model. The bare beam MAC shows high correlation between the experiment and model mode shapes for the major structural modes at about 50 Hz, 140 Hz, 275 Hz, and 450 Hz. Modes at 99 Hz and 375 Hz are present in the bare beam experimental data, but not in the model, a trend that continues with the cabled beam cases. These modes are likely due to the modes of the test fixture or noise in the test equipment.

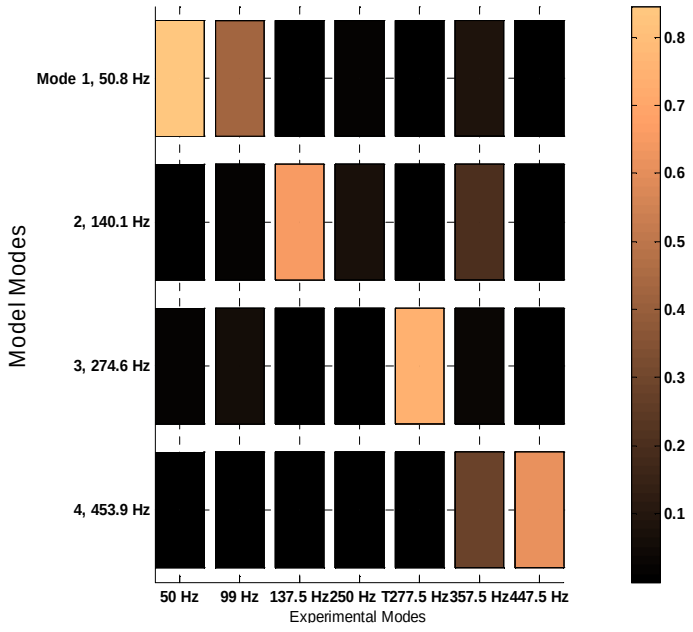

Figure 6.48: Modal assurance criterion for bare beam model modes against bare beam experimental modes with all modes shown; note that the model only finds bending modes.

Modal assurance criteria for the four cabled beams are shown in Figure 6.49 through 6.52. Best agreement occurs for the major structural modes at around 50 Hz, 140 Hz, 270 Hz, and 450 Hz, but agreement is evident for many of the modes that are added due to the addition of the cable. Figure 6.49 shows the MAC for the 1X7 cabled beam using middle values for the cable parameter inputs and showing the difference between the undamped and damped model mode shapes. The undamped model has mode agreement for the major structural modes, but also shows weak correlation for the additional cable modes. When the mode shapes of the damped model are compared, the additional modes due to the cable are not as prominently correlated, while the major structural modes still stand out. In both cases, the torsional experimental mode at 250 Hz is included in the experimental data, and shows no correlation to the model modes since torsional modes are not modeled. Thus, the torsional experimental mode column is removed for all subsequent MAC calculations.

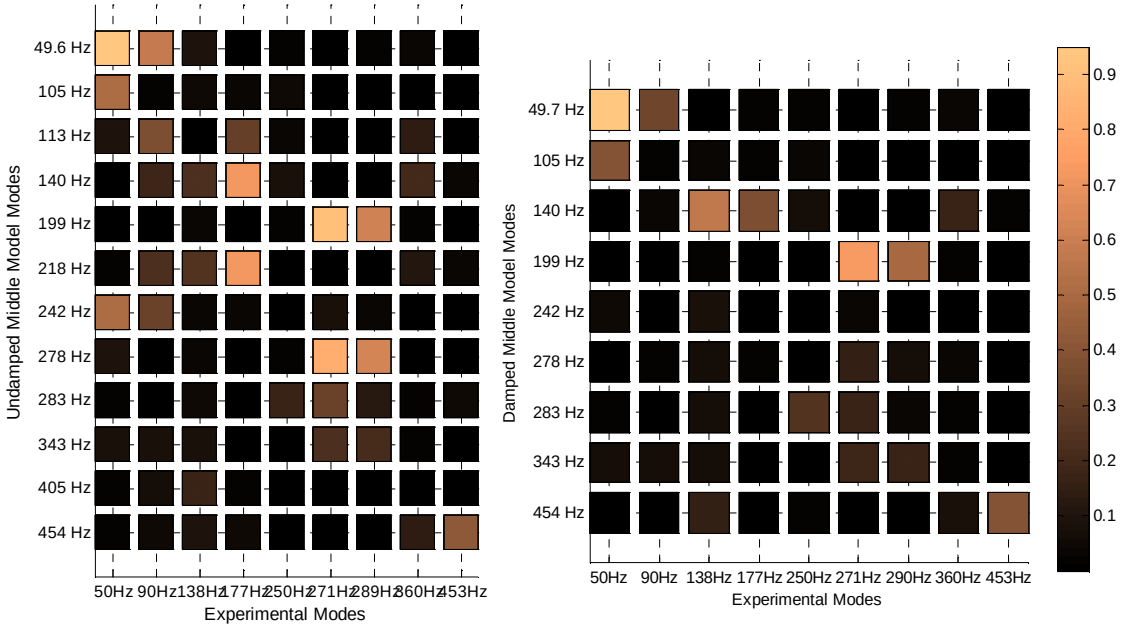

Figure 6.49: Undamped and damped model MAC for 1X7 cabled beam; comparison between undamped middle model and experimental modes from the dense scan on the left side, and comparison using damped middle model on the right.

The cable models can be run with different cable parameters to give minimum, middle, or maximum frequency values. As seen from the cabled beam transfer functions, the use of

different parameters can add, shift, and split modes of the model. As such, the MACs calculated from the different model inputs show differences in modal correlations. Figure 6.50 shows the MACs for the 1X19 cable for the minimum, middle, and maximum cable parameters inputs. In each case, the correlation for the first mode is excellent, and the major structure modes correlate well between experimental and model data, but the additional cable modes show varying degrees of correlation. This is in part due to the greater noise exhibited by the experimental mode shapes for low amplitude modes. In addition, trying to represent all of the modes with a single model is ambitious; cable modes that are represented well by the minimum cable parameters are not usually represented as well by the maximum cable parameters, and vice versa. In Figure 6.50, experimental mode shapes for the 1X19 cable were observed at 50, 90, 128, 143, 182, 263, 281, and 458 Hz, where column 1, 4, 6, and 8 represent the major structure modes.

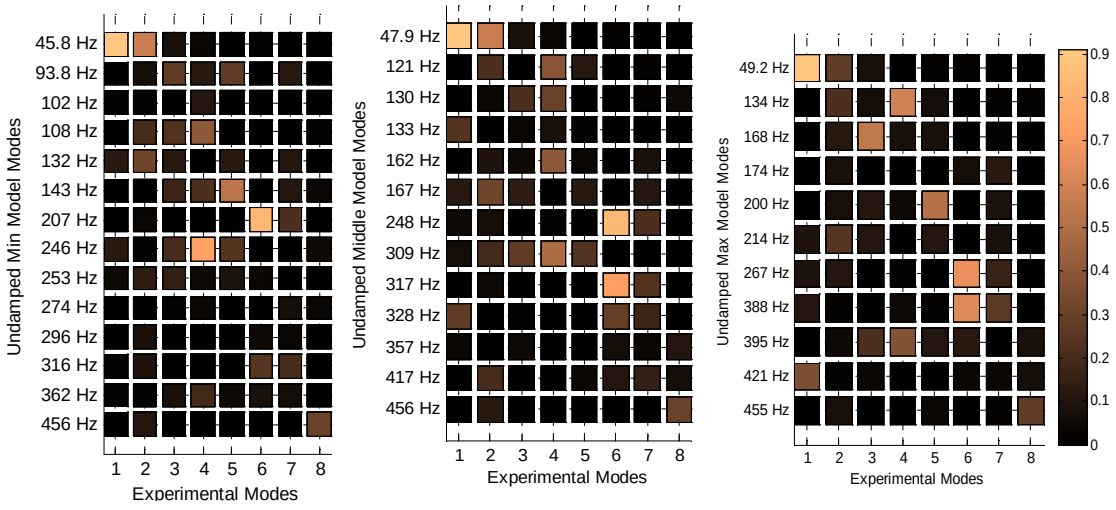

Figure 6.50: MAC for 1X19 cabled beam; comparison between minimum, middle, and maximum values of undamped model and experimental modes from the dense scan.

Figure 6.51 shows the complete array of MACs that can be created for each experimental scan; the top row has the undamped model minimum, middle, and maximum values, and the bottom row has the damped model comparisons.

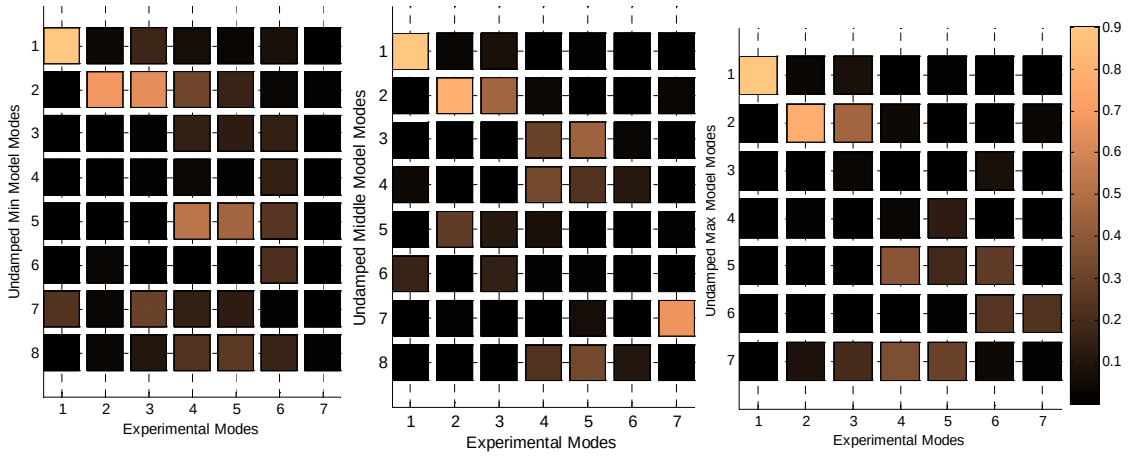

UNDAMPED MACs

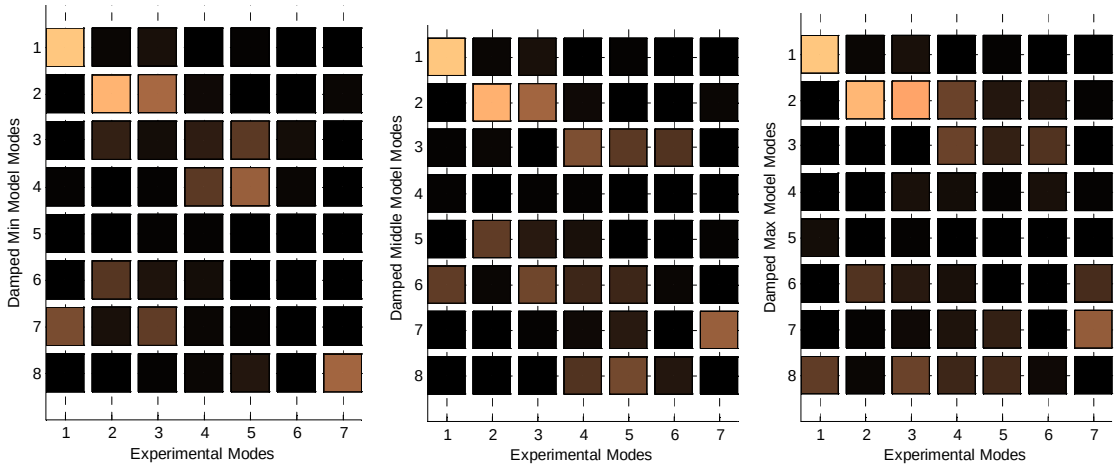

DAMPED MACs

Figure 6.51: MAC for 1X48 cabled beam; comparison between minimum, middle, and maximum values of undamped model (top row) or damped model (bottom row) and experimental modes from the dense scan.

Figure 6.52 shows the MAC resulting from comparison of the maximum undamped model and the experimental mode shapes. Table 6.7 contains a few representative graphic depictions of the model and experimental mode shapes used to calculate the MAC, where the cable shape is shown in red on each plot. The model mode shapes are normalized by the beam maximum displacement for both beam and cable, while the experimental mode shapes are normalized by the beam and cable displacement for each respective section.

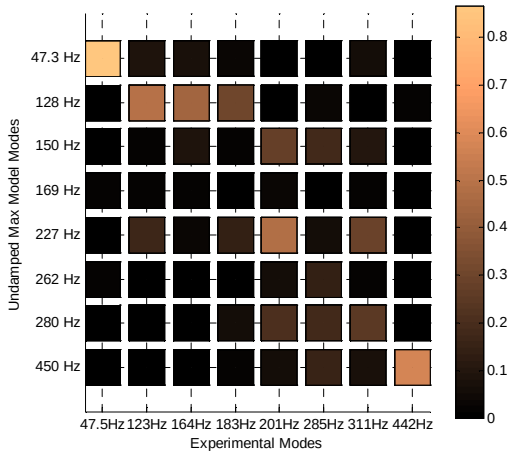

Figure 6.52: MAC for 7X7 cabled beam comparing maximum undamped model modes with experimental modes.

Table 6.7 Examples of model and experimental mode comparison for cabled beam major structural modes and additional modes due to cable.

	Experimental Mode Shape	Model Mode Shape
First Major Structure Mode, 7X7 (~ 50 Hz)	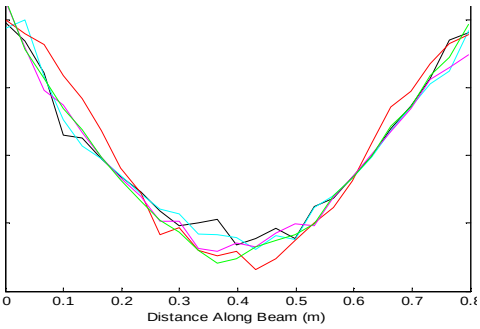	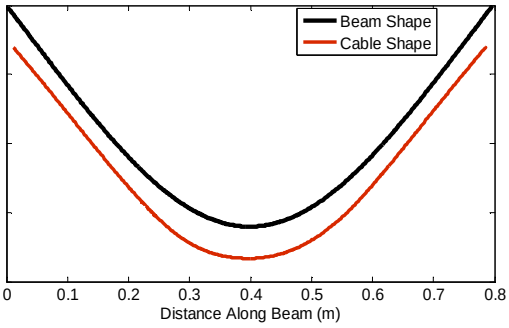
Second Major Structure Mode, 1X48 (~130 Hz)	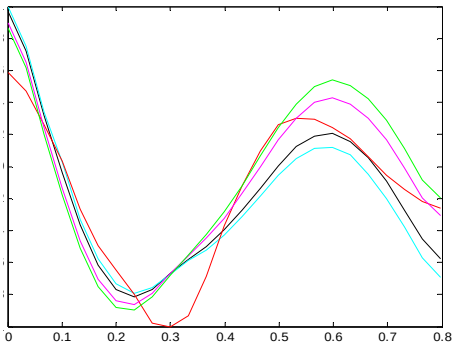	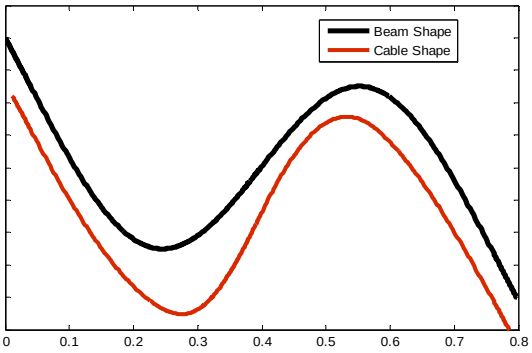

Additional Mode Due to Cable, 1X19 (~140 Hz)

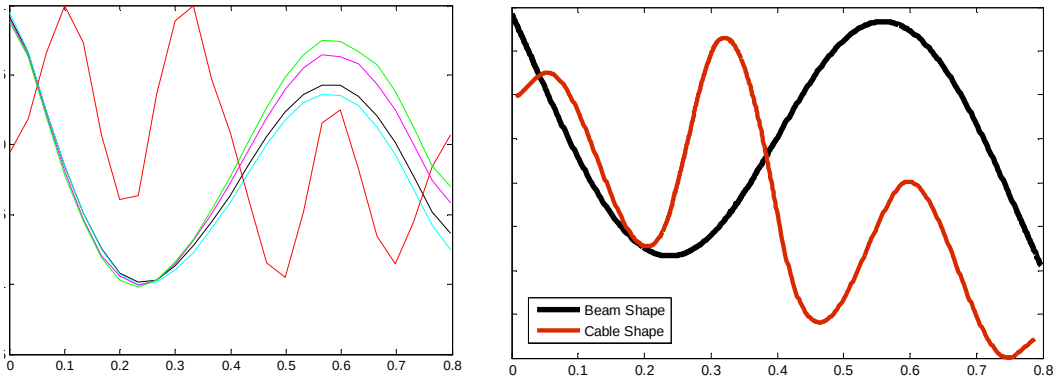

4th Major Structure Mode, 7X7 (~ 450 Hz)

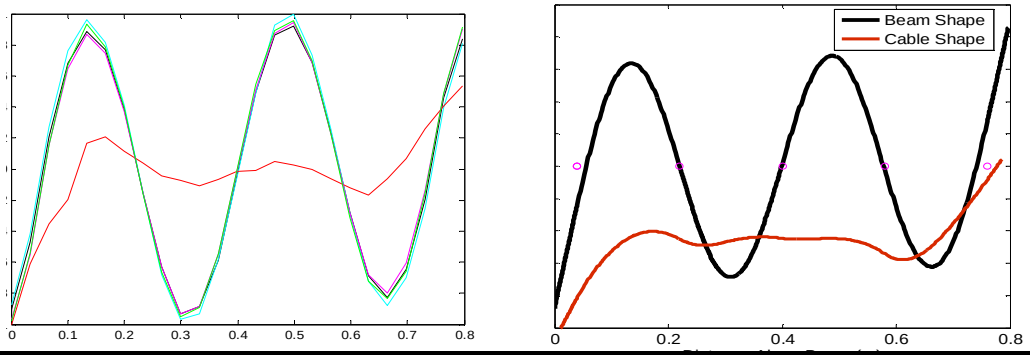

6.6.3 Distributed Mass Model Comparison

To show the value of the DTFM cabled beam model, it must show improvement when compared to existing models. The best current commonly used model is the distributed mass model; in this model, the mass of the cable is added to the beam by changing the density of the beam wherever cables are present. Note that this is a better technique than the previously used lumped mass model, where the cable mass was simply added at the center of gravity of the structure. As Figure 6.53 shows, the distributed mass model simply shifts the natural frequencies of the bare structure; the greater the mode number, the larger the frequency decrease due to the additional mass. Figure 6.53 also shows the lack of distinction between the two large cables; although these cables have different stiffness values and affect the structure differently, the distributed mass model does not capture that difference.

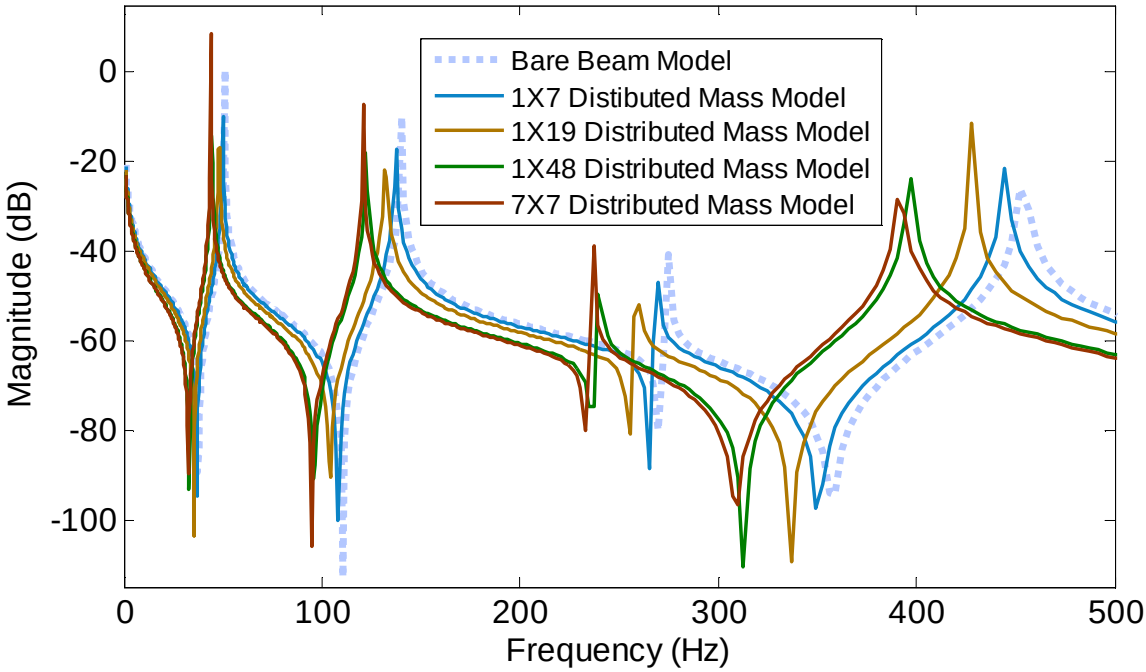

Figure 6.53: Distributed mass model transfer function for the four cable types, showing a downward shift in all frequencies for all cables.

The distributed mass model treats the cable as though it has no stiffness and is continuously attached, neither of which reflect the reality of cable attachment. This method is acceptable for the first one or two modes of a small mass addition, but does not capture the additional modes that arise due to the interaction between the cable and the host structure, fails to predict frequencies accurately at higher modes, and does not capture the difference between the stiff single stranded large cable and the much more flexible multi-stranded large cable that we observed in the experimental trials shown in Figure 6.40. To illustrate these points, the distributed mass model is compared to the average DTFM cabled beam model and experimental data in the following figures. Figure 6.54 compares the experimental data and both models for the 1X7 cable. For this small cable, the differences in the model frequencies for the first two bending modes are near negligible, although the DTFM model does capture additional modes and shows closer agreement for the third and fourth bending mode frequencies.

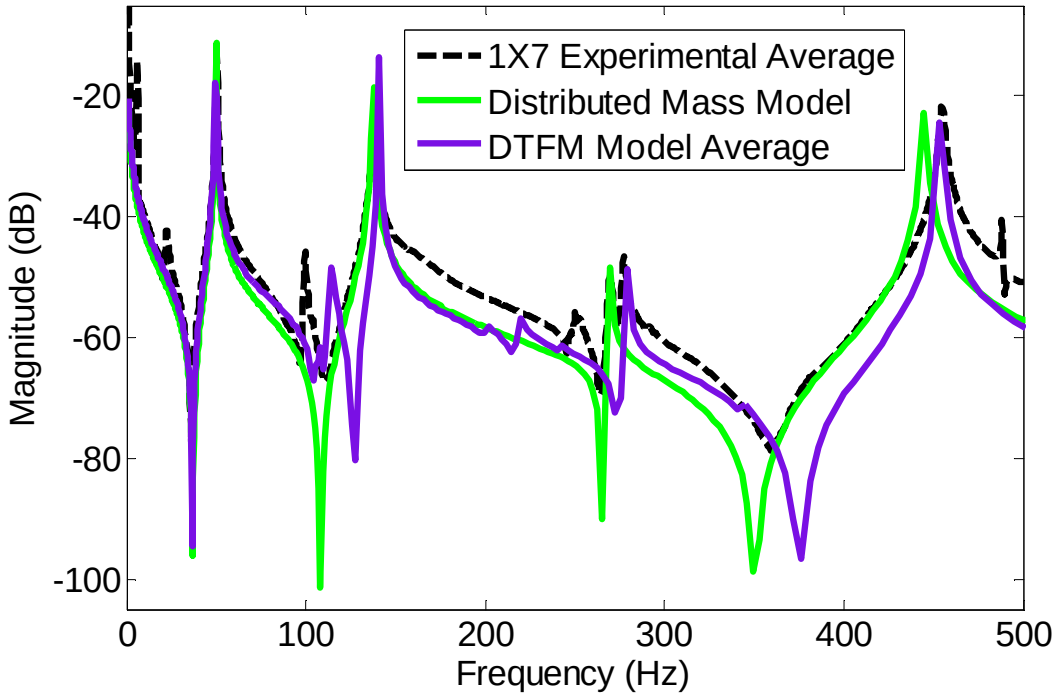

Figure 6.54: Comparison of distributed mass model and DTFM cabled beam model with experimental data for 1X7 cable.

Figure 6.55 and Figure 6.56 compare the distributed mass model and DTFM cabled beam model for the 1X48 and 7X7 cables, respectively. Figure 6.55 clearly shows the addition of modes around 350 Hz, which is not captured at all by the distributed mass model. The mode at 350 Hz appears to be a single mode, but in reality the many cabled beam trials showed one to three modes in this area, showing good agreement with the DTFM average model. In addition, all of the bending modes are predicted more accurately by the DTFM cabled beam model for the 1X48 cable. The real strength of the DTFM model is shown in Figure 6.56, the comparison of the models and experimental data for the 7X7 model. Here, the heavy but very flexible cable has several additional modes in the 100-200 Hz range, and all bending frequencies are predicted closely by the the DTFM model. While the 1X48 and 7X7 distributed mass models are nearly identical, the DTFM model manages to capture the differences between the cabled beams more clearly and more closely to the experimental data.

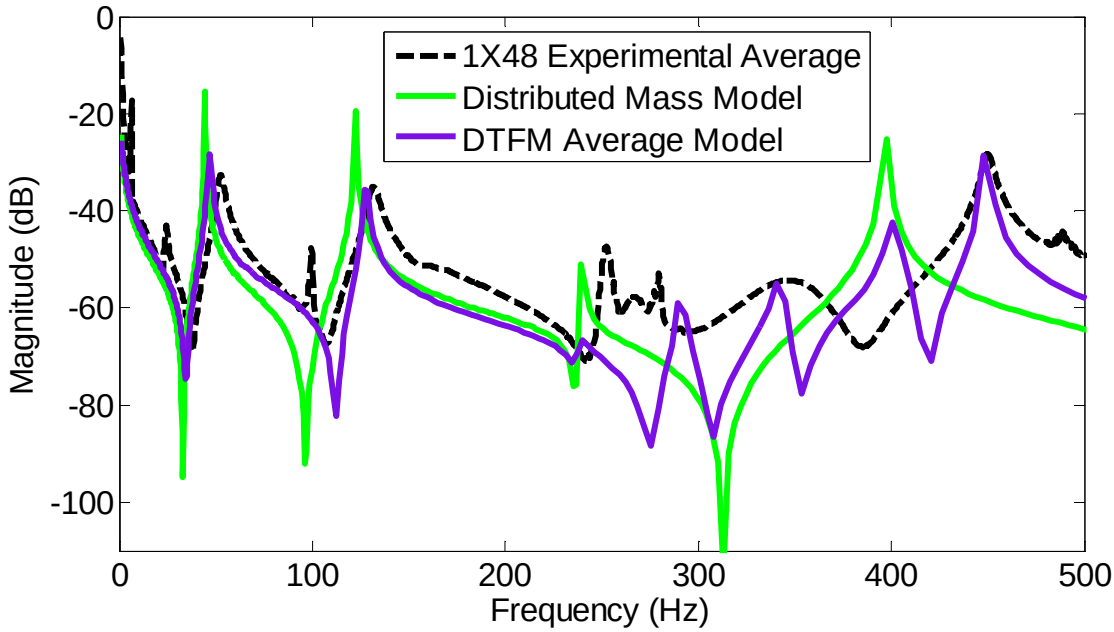

Figure 6.55: Comparison of distributed mass model and DTFM cabled beam model with experimental data for 1X48 cable.

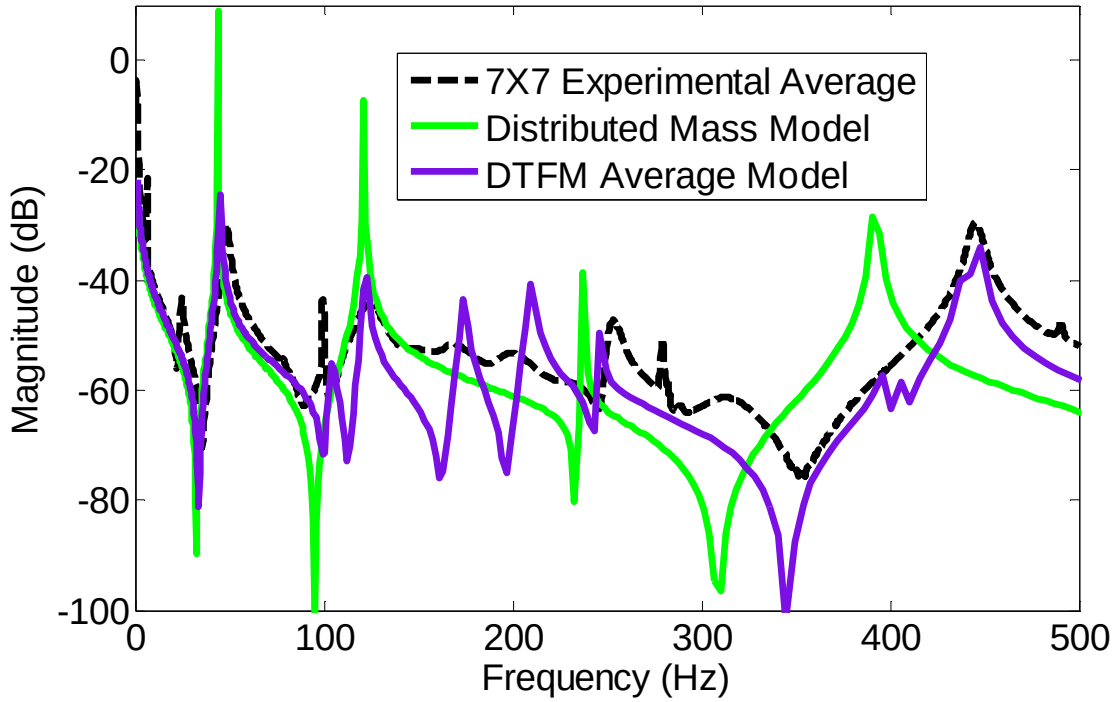

Figure 6.56: Comparison of distributed mass model and DTFM cabled beam model with experimental data for 7X7 cable.

There are several ways to perform quantitative comparisons between FRF results, including FRF assurance criterion, difference comparison, and cumulative value comparison. FRF assurance criterion does not adequately compare FRFs if frequencies are shifted slightly, so difference and cumulative comparisons were used. Figure 6.57 shows a representative result for the difference calculation comparison between the DTFM and distributed mass models for the 1X48 cable. The difference between the model and experimental FRF value for each frequency is plotted, and the zero value (for which the experimental and model data would be identical) is shown by a black line. Overall, the DTFM model has smaller difference values across the frequency range.

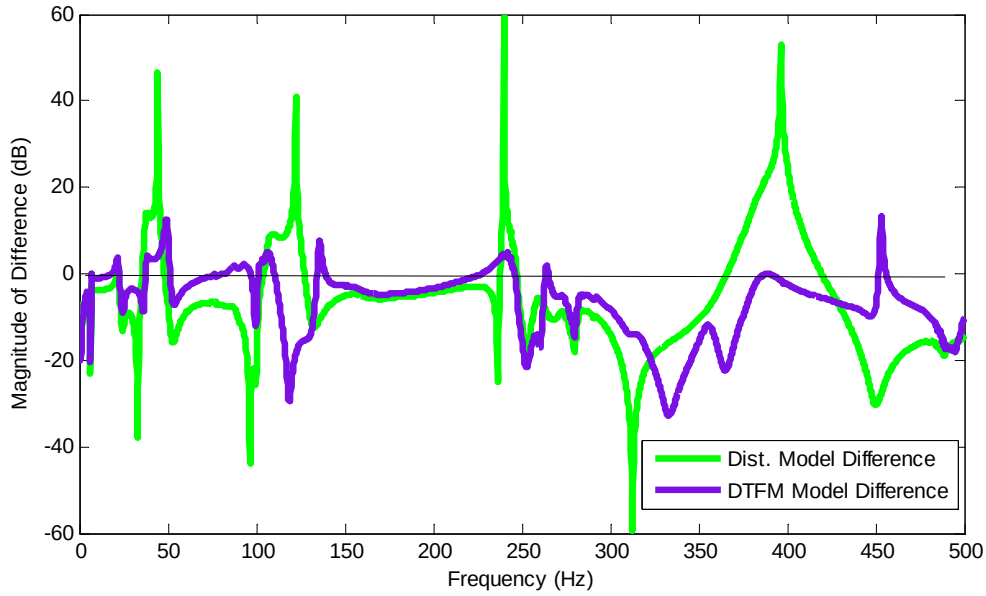

Figure 6.57: Difference between experimental and model FRF values for the 1X48 middle DTFM cabled beam model results and the 1X48 distributed mass model results.

For each of the cabled beam configurations, the cumulative values of the FRF results were also plotted for the experimental data and the models. Figure 6.58 and Figure 6.59 show the cumulative comparison between the experimental and model data for the 1X7 and 7X7 cabled beams, respectively. For both cabled beams, the DTFM model values were closer to the experimental data for the entire frequency range, and the shape of the experimental cumulative value curve is followed more closely by the DTFM models. Results were similar for the 1X19 and 1X48 cabled beams. Figures 6.58 and 6.59 also show the effect of comparing the different cable parameter ranges, showing the middle

values to be best for 1X7 cabled beam and maximum values to be best for the 7X7 cabled beam.

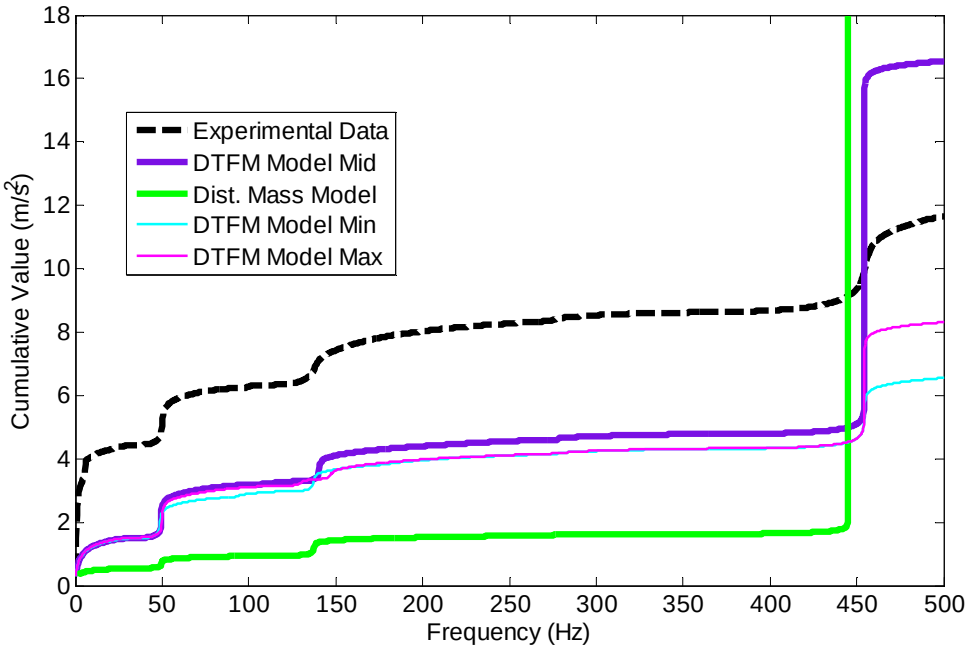

Figure 6.58: Cumulative values for the 1X7 cabled beam.

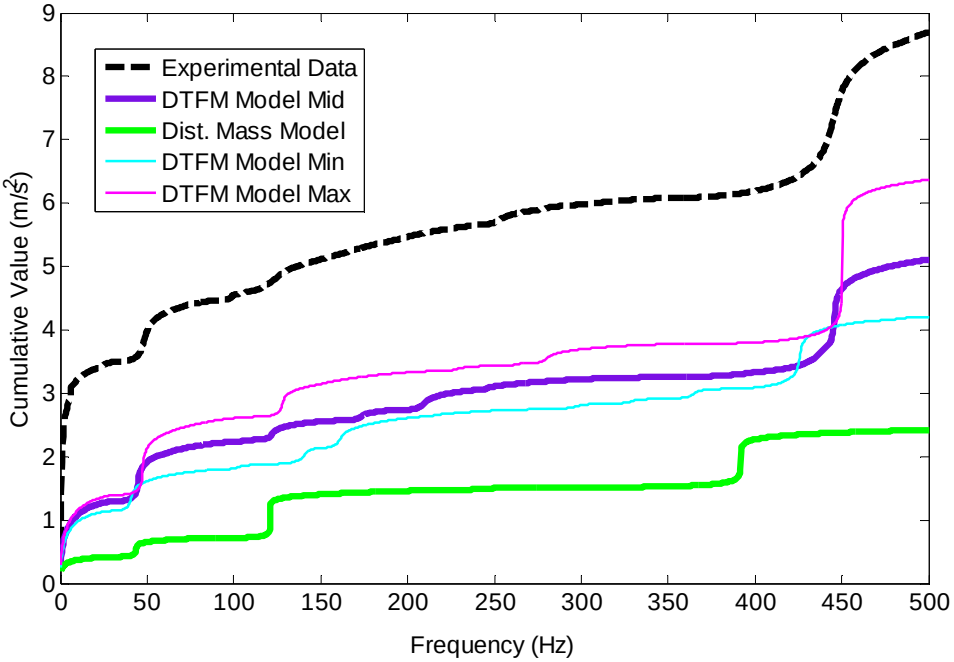

Figure 6.59: Cumulative values for the 7X7 cabled beam.

For the smaller cables with less mass, the distributed mass model predicts the frequency shift adequately for the lowest modes, but for higher modes and all modes of larger cables, the frequency shift is not captured as correctly as by the DTFM model. This is clearly shown by the drastic rise in amplitude value at 450 Hz in Figure 6.58. The DTFM model also provides a range of values, which can capture the inherent variability of cables more completely; for clarity, only the average DTFM value was shown in the prior FRF comparison plots. The distributed mass model does not capture additional modes caused by the addition of the cables and is not as accurate at predicting natural frequencies for cables of varying stiffnesses. Therefore, there is value in the development of the DTFM cabled beam model to correct these inadequacies.

6.7 Discussion

Overall, results from the DTFM cabled beam model showed good agreement with the experimental data. The DTFM cabled beam model shows improvement over the distributed mass model both in terms of natural frequency prediction and ability to identify locations of additional modes due to cable attachment. When the difference between the experimental data TF and the distributed mass model TF was compared to the difference between experimental data and the DTFM model, the DTFM model had less total error. Although the distributed mass model may be useful for small cables, the DTFM cabled beam model can incorporate cable bending stiffness and shear rigidity, and thus provides more information and a more accurate prediction for larger cables or higher modes. Table 6.8 gives the bending frequencies from the experimental data, distributed mass model, and the minimum and maximum DTFM cabled beam model.

For the case of the bare beam with no cable attached, the distributed mass model and DTFM model give the same results (as expected), with only 0.8% to 2.3% difference from the experimental frequencies. The distributed mass model results are quite acceptable for the small 1X7 cabled beam, but the DTFM model captures the 1X7 cabled structure resonances just as well within its range. As the cable gets larger, the distributed mass model deviates from experimental data widely, up to 16% difference (mode 3 of

7X7), whereas the maximum difference between a range boundary and the experimental data is less than 6% (mode 4 minimum of 7X7) for the DTFM cabled beam model.

Table 6.8 Comparison of natural frequencies from experimental data, distributed mass model, and minimum and maximum DTFM model.

Type of Cable on Beam	Bending Mode	Experimental Natural Frequency (Hz)	Distributed Mass Model Frequency (Hz)	DTFM Minimum Frequency (Hz)	DTFM Maximum Frequency (Hz)
None	1	50.0	50.8	50.8	
	2	136.9	140.1	140.1	
	3	276.9	274.6	274.6	
	4	450.0	453.9	453.9	
1X7	1	50.28	49.8	48.9	50.2
	2	138.1	137.3	137.2	142.0
	3	269.0	269.2	272.0	282.8
	4	455.0	445.0	454.3	454.4
1X19	1	50.5	48.2	45.9	49.8
	2	130.0	132.9	133.8	142.9
	3	263.1	260.6	246.1	267.5
	4	456.5	430.7	455.6	455.7
1X48	1	52.5	44.7	43.3	49.3
	2	131.6	123.1	116.8	135.6
	3	262.9	241.4	258.4	263.9
	4	450.0	399.0	444.6	453.1
7X7	1	48.3	43.9	40.8	47.7
	2	123.4	120.9	103.0	127.74
	3	280.2	237.0	214.3	262.3
	4	445.1	391.8	425.7	450.3

In evaluating the results from the DTFM cable and cabled beam models, the minimum range value usually matched the cable experimental data, while the maximum range value was closer to experimental data for the cabled beam structure. Therefore, the frequencies predicted by using the range of cable parameters seem to agree well for the variety of fixtures that the cable was mounted in. In addition, the damping parameters determined from the two-point fixture testing were used successfully for the cabled beam

model. These findings support the goal of being able to model a variety of structures with cable parameters calculated from direct measurements instead of testing.

Chapter 7: Conclusions, Contributions, and Considerations

Although this research was focused on spaceflight cables, the methods and models developed are applicable to many types of stranded cable and thus have application outside the realm of space structure design. The conclusions drawn from this research, advantages and limitations of application, contributions of this Dissertation, and considerations for future work are presented here.

Upon revisiting the questions raised in the first chapter, this research has provided conclusive answers and expanded our knowledge of cable dynamics. It is possible to calculate cable parameters based on cable measurements, and cables can be modeled with damping well enough to predict natural frequency ranges. Hysteretic damping certainly improves on viscous damping and structural damping for cables, but additional hysteretic damping mechanisms could be even more effective. Machine-manufactured cables are as identically constructed as possible, but still show variation between cable sample responses. Finally, an effective cable model can be incorporated into a structural model for prediction of system frequencies with results showing slight improvement over previous methods.

7.1 Dissertation Summary

This Dissertation has experimentally and theoretically investigated the dynamic behavior and modeling of stranded cables and of a simple cabled structure. The variety of existing cable modeling approaches were described and explored, followed by an in-depth discussion of how to calculate cable parameters to model a non-homogenous stranded cable with a homogenous shear beam model. Several types of spaceflight cables were dynamically tested, and different factors affecting the dynamic response were identified. Curved helical cable construction affected frequency results and previous studies used hand-built cables that showed high variability in results, so machine manufactured contra-helical cables secured with lacing ties and wrapped with Kapton were procured to provide the most consistent dynamic results. Dynamic testing was performed on five samples of each of four cable configurations, and then the cables were baked out. The

baked out cables were tested in several different fixtures, including two- and four-point fixtures where the cable was attached to ground, and a free-free cabled beam fixture, in which the cable was mounted to a free-swinging aluminum beam. Differences in the cable response due to bakeout were identified, and the effects of the different types of cables on the simple beam structure were quantified including shifts in major frequencies, differences between single and multi-stranded cables, and the amount of damping observed.

From a theoretical standpoint, the method to determine beam parameters for a cable proved useful for the cable and cabled structure models that were developed. The cable itself was modeled as a shear beam, and the distributed transfer function method was used to incorporate the TC105 attachment points and solve for the cable response, including natural frequencies, transfer function response and mode shapes. The distributed transfer function models were capable of describing the cable and cabled beam responses, and addition of hysteretic damping and rotational and linear stiffness for the attachment points further improved the model capabilities. Hysteretic damping was shown to be capable of matching multiple modes of the cable response, and was superior to both viscous and structural damping for modeling cable damping.

7.2 Application Discussion

In the interest of practical application, the strengths and limitations of the cable model should be highlighted. The DTFM determines exact analytical solutions, so error between the model and reality depends on the input parameters for the model and not on number of elements as a finite element model would. In comparison to the distributed mass model, for the first one or two modes of small cables (6% of total structure mass or less), the DTFM model does not show marked improvement in frequency prediction since the small cable has less effect on the structure and is less beam-like. However, for higher modes of small cables and all modes of larger, more beam-like cables, the DTFM model is superior.

The author realizes that the DTFM is not commonly used, but there is value in the research for commercially available finite element (FE) modeling of cables as well. Whether the DTFM model or a commercially available FE code is used, the results are only as good as the input parameters used. This research has shown that the parameter of bending stiffness must not only be included as input, but has introduced a method of combining the calculation of bending stiffness for steel ACSR cables with the material properties of composite materials and the displacement of the cable to yield a realistic value. In addition, the elements used for the cable must include shear, and the connection point elements should include rotational degrees of freedom.

7.3 Contributions

The major contributions of this research are as follows:

- Developed a method to calculate cable properties that are suitable to use for modeling purposes from direct physical measurements of cables. Cable parameters of mass properties, bending stiffness, and shear rigidity were determined for typical spaceflight cables.
- Created a standard run procedure for testing of cables with verification of factors that would influence cable dynamic response and showed that machine made cables did not fully eliminate variability in the dynamic response.
- Produced a database of cable responses for typical spaceflight cables from over 70 trials of dynamic testing which are available for further investigation.
- Determined the effect of bakeout on spaceflight cable response, identified bakeout as a source of frequency response changes, and quantified the amount of frequency shift and damping ratio changes due to bakeout.
- Extended the distributed transfer function shear model to include shear effects, tension, and a variety of damping mechanisms to model cables or other damped shear beams.
- Developed a distributed transfer function cabled beam model that combines the shear beam cable model with attachment point models that have the capability to include both linear and rotational stiffness and damping.

- Compared the developed distributed transfer function cabled beam models to the currently used distributed mass models to show the slight improvement in frequency prediction and identification of additional modes by the new distributed transfer function cabled beam model.
- Investigated the influence of the attachment points, verified that the attachment points did not act as pinned constraints, and revealed results for the attachment stiffness as a function of frequency.

7.4 Future Work and Considerations

As the field of precision space structures continues to grow and more engineering applications involve increasingly complex signal and power cabling, the need to model cables is likely to continue requiring refinement and improvement for the aerospace industry and beyond.

A logical next step for these models is the use of statistical analysis to replace the range of cable responses with a predicted distribution of the cable response. This work used the minimum and maximum input values to bound the frequency response, but myriad combinations of the cable parameters are possible within those bounds. With the large number of experimental trials conducted for this research, it would be valuable to determine a statistical distribution for the experimental results. The DTFM model could be run in conjunction with a statistical program such as Sandia National Laboratory's Dakota project that could take the range of input values and produce a statistical likelihood for frequency predictions and mode shapes.

Further recommended refinement involves the measurement of the cable attachment points. This research determined values for TC105 tabs, but there was great variation in the results and there are other types of mounting brackets for cables being developed. In the future, concrete and effective measurement techniques for determining cable mounting techniques for any type of cable mount would greatly improve the predictive ability of cable models, as the connection points had a great effect on the model response.

Attempts to improve damping modeling are ongoing for all structures, and damping of cables is no exception. Although this Dissertation showed that hysteretic damping was more effective for stranded cables than viscous or hysteretic damping, there are other hysteretic damping mechanisms that could be evaluated. Additional damping mechanisms that should be incorporated in the DTFM cable model and evaluated are spatial hysteresis and geometric rotation-based damping, which has been suggested for cable damping specifically. To improve the utility of the damped cabled structure models, a method to determine cable damping parameters a priori would be valuable. This could involve performing material testing on the cables or constituent cable wires to gain information about the viscoelastic damping properties of the wires and internal frictional losses and develop equations for damping parameters based on these damping characteristics. If this method proved successful, the damping parameters determined from simple material testing could be used for the more complicated cabled structure damping terms without requiring additional dynamic testing.

From modeling to testing, the field of cable dynamics is becoming increasingly critical for spacecraft applications. This Dissertation has added to the knowledge of cable dynamics and provides a step forward on the path to useful predictions of cabled structure response.

References

[1] Babuska V., Coombs D.M., Goodding J.C., Ardelean E., Robertson L.M., Lane S.A., 2010, "Modeling and experimental validation of space structures with wiring harness," Journal of Spacecraft and Rockets, **47**(6), pp. 1038-1052.

[2] Coombs D.M., Goodding J.C., Babuska V., Ardelean E., Roberston L.M., Lane S.A., 2011, "Dynamic modeling and experimental validation of a cable-loaded panel," Journal of Spacecraft and Rockets, **48**(6), pp. 958-973

[3] Goodding J.C., Ardelean E.V., Babuska V., Robertson L.M., Lane S.A., 2011, "Experimental techniques and structural parameter estimation studies of spacecraft cables," Journal of Spacecraft and Rockets, **48**(6), pp. 942-957.

[4] Triantafyllou M. S., 1984, “Linear dynamics of cables and chains,” The Shock and Vibration Digest, **16**(3), pp. 9–17.

[5] Starossek U., 1994, “Cable dynamics- A review,” Structural Engineering International, (3), pp. 171–176.

[6] Rega G., 2004, “Nonlinear vibrations of suspended cables — Part I: Modeling and analysis,” Applied Mechanics Review, **57**(6), pp. 443–478.

[7] Rega G., 2004, “Nonlinear vibrations of suspended cables — Part II: Deterministic phenomena,” Applied Mechanics Review, **57**(6), pp. 479–514.

[8] Raj T. M., and Parthasarathy N. S., 2007, “A complete review on friction models of composite cables,” International Journal of Mechanics of Composite Materials and Constructions, Russian Academy of Applied Mechanics and Sciences, **13**(3), pp. 356–384.

[9] Spak K.S., Agnes G.S., Inman D.J, 2013, "Cable modeling and internal damping developments," Applied Mechanics Reviews, **65**(1), pp. 1-18. doi:10.1115/1.4023489

[10] Triantafyllou M. S., 1987, “Dynamics of cables and chains,” The Shock and Vibration Digest, **19**(12), pp. 3–5.

[11] Irvine H. M., and Caughey T. K., 1974, “The linear theory of free vibrations of a suspended cable,” Proceedings of the Royal Society of London, **341**, pp. 299–315.

[12] Benedettini F., and Rega G., 1986, “Non-linear dynamics of an elastic cable under planar excitation,” International Journal of Non-Linear Mechanics, **22**(6), pp. 497–509.

[13] Hagedorn P., and Schafer B., 1980, “On non-linear free vibrations of an elastic cable,” International Journal of Non-Linear Mechanics, **15**, pp. 333–340.

[14] Koh C. G., and Zhang Y., 1999, “Low-tension cable dynamics: Numerical and experimental studies,” Journal of Engineering Mechanics, **125**(3), pp. 347–354.

[15] Luongo A., Rega G., and Vestroni F., 1984, “Planar non-linear free vibrations elastic cable,” International Journal of Non-Linear Mechanics, **19**(1), pp. 39–52.

[16] Starossek U., 1991, “Dynamic stiffness matrix of sagging cable,” Journal of Engineering Mechanics, **117**(12), pp. 2815–2829.

[17] Utting W. S., and Jones N., 1987, “The response of wire rope strands to axial tensile loads- Part 1. Experimental results and theoretical predictions,” International Journal of Mechanical Sciences, **29**(9), pp. 605–619.

[18] Erdonmez C., and Imrak C. E., 2011, “A finite element model for independent wire rope core with double helical geometry subjected to axial loads,” Sadhana, **36**(6), pp. 995–1008.

[19] Velinsky S. A., 1985, “General nonlinear theory for complex wire ropes,” International Journal of Mechanical Sciences, **27**, pp. 497–507.

[20] Velinsky S. A., 1989, “On the design of wire rope,” Journal of Mechanisms, Transmissions, and Automation, **111**(9), pp. 382–388.

[21] Costello G. A., 1990, Theory of Wire Rope, Springer, New York.

[22] Chiang Y. J., 1996, “Characterizing simple-stranded wire cables under axial loading,” Finite Elements in Analysis and Design, **24**, pp. 49–66.

[23] Sathikh S., Moorthy M. B. K., and Krishnan M., 1996, “A symmetric linear elastic model for helical wire strands under axisymmetric loads,” The Journal of Strain Analysis, **31**(5), pp. 389–399.

[24] Huang N. C., 1978, “Finite extension of an elastic strand with a central core,” Transactions of the ASME, **45**, pp. 852–858.

[25] Raoof M., and Hobbs R. E., 1988, “Analysis of multilayered structural strands,” Journal of Engineering Mechanics, **114**(7), 1166-1182.

[26] Jolicoeur C., and Cardou A., 1996, “Semicontinuous mathematical model for bending of multilayered wire strands,” Journal of Engineering Mechanics, **122**(7), pp. 643–650.

[27] Jolicoeur C., 1997, “Comparative study of two semicontinuous models for wire strand analysis,” Journal of Engineering Mechanics, **123**(8), pp. 792–799.

[28] Raoof M., and Kraincanic I., 1994, “Critical examination of various approached used for analysing helical cables,” The Journal of Strain Analysis for Engineering Design, **29**(1), pp. 43–55.

[29] Dreyer T. P., and Van Vuuren J. H., 1999, “A comparison between continuous and discrete modeling of cables with bending stiffness,” Applied Mathematical Modeling, **23**, pp. 527–541.

[30] Hover F. S., and Triantafyllou M. S., 1999, “Linear dynamics of curved tensioned elastic beams,” Journal of Sound and Vibration, **228**(4), pp. 923–930.

[31] Ashkenazi R., Weiss M. P., and Elata D., 2004, “Torsion and bending stresses in wires of non-rotating tower crane ropes,” OIPECC Bulletin No. 87, **41**(5-6), pp. pp. 1157–1172.

[32] Elata D., Eshkenazy R., and Weiss M. P., 2004, “The mechanical behavior of a wire rope with an independent wire rope core,” International Journal of Solids and Structures, **41**, pp. 1157–1172.

[33] Usabiaga H., and Pagalday J. M., 2008, “Analytical procedure for modeling recursively and wire by wire stranded ropes subjected to traction and torsion loads,” International Journal of Solids and Structures, **45**, pp. 5503–5520.

[34] Huang C., and Knapp R. H., 2006, “Parametric modeling of double and triple helical strands,” Proceedings of the Sixteenth International Offshore and Polar Engineering Conference, San Francisco CA, pp. 139–144.

[35] Koh C. G., and Rong Y., 2004, “Dynamic analysis of large displacement cable motion with experimental verification,” Journal of Sound and Vibration, **272**(1-2), pp. 187–206.

[36] Srinil N., Rega G., and Chucheepsakul S., 2004, “Three-dimensional non-linear coupling and dynamic tension in the large-amplitude free vibrations of arbitrarily sagged cables,” Journal of Sound and Vibration, **269**, pp. 823-852.

[37] Sun J. F., Wang G. L., and Zhang H. O., 2008, “FE analysis of frictional contact effect for laying wire rope,” Journal of Materials Processing Technology, **202**, pp. 170–178.

[38] Sauter D., 2003, “Modeling the dynamic characteristics of slack wire cables in Stockbridge dampers,” TU Darmstadt. Dissertation.

[39] Zhong M., 2003, “Dynamic analysis of cables with variable flexural rigidity.” University of Hawaii. Thesis.

[40] Liu X., 2004, “Cable vibration considering internal friction,” University of Hawaii. Thesis.

[41] Knapp R. H., and Liu X., 2005, “Cable vibration considering interlayer coulomb friction,” International Journal of Offshore and Polar Engineering, **15**(3), pp. 229–234.

[42] Crossley J. A., Spencer A. J. M., and England A. H., 2003, “Analytical solutions for bending and flexure of helically reinforced cylinders,” International Journal of Solids and Structures, **40**, pp. 777–806.

[43] Ghoreishi S. R., Messager T., Cartraud P., and Davies P., 2007, “Validity and limitations of linear analytical models for steel wire strands under axial loading, using a 3D FE model,” International Journal of Mechanical Sciences, **49**, pp. 1251–1261.

[44] Inagaki K., Ekh J., and Zahrai S., 2007, “Mechanical analysis of second order helical structure in electrical cable,” International Journal of Solids and Structures, **44**, pp. 1657–1679.

[45] Lacarbonara W., Paolone A., and Vestroni F., 2007, “Non-linear modal properties of non-shallow cables,” International Journal of Non-Linear Mechanics, **42**(3), pp. 542–554.

[46] Lacarbonara W., and Pacitti A., 2008, “Nonlinear modeling of cables with flexural stiffness,” Mathematical Problems in Engineering, **2008**, pp. 1–22.

[47] Jiang W., Warby M. K., and Henshall J. L., 2008, “Statically indeterminate contacts in axially loaded wire strand,” European Journal of Mechanics and Solids, **27**, pp. 69–78.

[48] Jiang W.G., 2012, “A concise finite element model for pure bending analysis of simple wire strand,” International Journal of Mechanical Sciences, **54**(1), pp. 69–73.

[49] Papailiou K. O., 1997, “On the bending stiffness of transmission line conductors,” IEEE Transactions on Power Delivery, **12**(4), pp. 1576–1588.

[50] Shibu G., Mohankumar K. V., and Devendiran S., 2011, “Analysis of a three layered straight wire rope strand using finite element method,” Proceedings of the World Congress on Engineering, **3**.

[51] Argatov I., 2011, “Response of a wire rope strand to axial and torsional loads”: Asymptotic modeling of the effect of interwire contact deformations,” International Journal of Solids and Structures, **48**(10), pp. 1413–1423.

[52] Johnson E. A., Christenson R. E., and Spencer B. F., 2003, “Semiactive damping of cables with sag,” Computer-Aided Civil and Infrastructure Engineering, **18**, pp. 132–146.

[53] Boston C., Weber F., and Guzzella L., 2011, “Optimal semi-active damping of cables with bending stiffness,” Smart Materials and Structures, **20**.

[54] Yu A., 1949, “Vibration damping of stranded cable,” Lehigh University. Dissertation.

[55] Diana G., Falco M., Cigada A., and Manenti A., 2000, “On the measurement of over head transmission lines conductor self damping,” IEEE Transactions on Power Delivery, **15**(1), pp. 285–292.

[56] Otrin M., and Boltežar M., 2007, “Damped lateral vibrations of straight and curved cables with no axial pre-load,” Journal of Sound and Vibration, **300**(3-5), pp. 676–694.

[57] Pivarov I., Vinogradov O.G., 1985, "The phenomenon of damping in stranded cables," Proceedings of the 26th AIAA Structures, Structural Dynamics, and Materials Conference, Orlando FL, AIAA Paper 85-0660, pp. 232-237.

[58] Vinogradov O., Pivarov I., 1986, "Vibrations of a system with non-linear hysteresis," Journal of Sound and Vibration, **111**(1), pp 145-152.

[59] Urchegui M. A., Tato W., and Gomez X., 2008, “Wear evolution in a stranded rope subjected to cyclic bending,” Journal of Materials Engineering and Performance, **17**(4), pp. 550–560.

[60] Ramsey H., 1990, “Analysis of interwire friction in multilayered cables under uniform extension and twisting,” International Journal of Mechanical Sciences, **32**(8), pp. 709–716.

[61] Raoof M., and Huang Y. P., 1992, “Upper bound prediction of cable damping under cyclic bending,” Journal of Engineering Mechanics, **117**(12), pp. 2729–2747.

[62] Raoof M., and Huang Y. P., 1992, “Free bending characteristics of axially preloaded spiral strands,” Proceedings of the Institution of Civil Engineers, Structures and Buildings, **94**(4), p. 469.

[63] Kumar K., and Botsis J., 2001, “Contact stresses in multilayered strands under tension and torsion,” Journal of Applied Mechanics, **68**, pp. 432–440.

[64] Labrosse M., Nawrocki A., and Conway T., 2000, “Frictional dissipation in axially loaded simple straight strands,” Journal of Engineering Mechanics, **126**(6), pp. 641–646.

[65] Zhu Z. H., and Meguid S. A., 2007, “Nonlinear FE-based investigation of flexural damping of slacking wire cables,” International Journal of Solids and Structures, **44**, pp. 5122–5132.

[66] Cutchins M. A., Cochran J. E., Kumar K., Fitz-Coy N. G., and Tinker M. L., 1987, "Initial investigations into the damping characteristics of wire rope vibration isolators," NASA Technical Report, Auburn University, Alabama.

[67] Goodding J. C., 2008, “Spacecraft electrical cable harness structural test and analysis methods,” IMAC: Conference and Exposition on Structural Dynamics, pp. 437–443.

[68] Raoof M., and Huang Y. P., 1992, “Axial and free-bending analysis of spiral strands made simple,” Journal of Engineering Mechanics, **118**(12), pp. 2335–2351.

[69] Raoof M., and Davies T. J., 2006, “Simple determination of the maximum axial and torsional energy dissipation in large diameter spiral strands,” Computers and Structures, **84**, pp. 676–689.

[70] Rawlins C. B., 2009, “Flexural self-damping in overhead electrical transmission conductors,” Journal of Sound and Vibration, **323**, pp. 232–256.

[71] Gnanavel B. K., and Parthasarathy N. S., 2011, “Effect of interfacial contact forces in radial contact wire strand,” Archive of Applied Mechanics, **81**, pp. 303–317.

[72] Gnanavel B. K., and Parthasarathy N. S., 2012, “Effect of interfacial contact forces in single layer cable assemblies,” International Journal of Mechanics and Materials in Design, **8**, pp. 183–195.

[73] Dastous J.B., 2005, “Nonlinear finite-element analysis of stranded conductors with variable bending stiffness using the tangent stiffness method,” IEEE Transactions on Power Delivery, **20**(1), pp. 328–338.

[74] Papailiou K. O., 1995, “Bending of helically twisted cables under variable bending stiffness due to internal friction, tensile force and cable curvature,” Eidgenossische Technische Hochschule Zurich. Dissertation.

[75] Lanteigne J., 1986, “Theoretical estimation of the response of helically armored cables to tension, torsion, and bending,” Journal of Applied Mechanics, **52**(6), pp. 423–432.

[76] Hong K., Kiureghian A. D., and Sackman J. L., 2005, “Bending behavior of helically wrapped cables,” Journal of Engineering Mechanics, **131**(5).

[77] Jayakumar C. V., Sathikh S., Jebaraj C., and Jolicoeur C., 1999, “Discussion of ‘Comparative study of two semicontinuous models for wire strand analysis’,” Journal of Engineering Mechanics, **125**(3), pp. 369–370.

[78] Johansen V., Ersdal S., Sørensen A. J., and Leira B., 2006, “Modeling of inextensible cable dynamics with experiments,” International Journal of Non-Linear Mechanics, **41**(4), pp. 543–555.

[79] Cardou A., Papailiou K. O., Hong K., Kiureghian A. D., and Sackman J. L., 2006, “Discussion of ‘Bending behavior of helically wrapped cables’,” Journal of Engineering Mechanics, **132**, pp. 790–792.

[80] Filiatrault A., and Stearns C., 2005, “Flexural properties of flexible conductors interconnecting electrical substation equipment,” Journal of Structural Engineering, **131**(1), pp. 151–160.

[81] Yamaguchi H., and Adhikari R., 1994, “Loss factors of damping treated structural cables,” Journal of Sound and Vibration, **176**(4), pp. 487–495.

[82] Yamaguchi H., and Adhikari R., 1995, “Energy-based evaluation of modal damping in structural cables with and without damping treatment,” Journal of Sound and Vibration, **181**(1), pp. 71–83.

[83] Barbieri N., de Souza O. H., and Barbieri R., 2004, “Dynamical analysis of transmission line cables. Part 1 — linear theory,” Mechanical Systems and Signal Processing, **18**, pp. 659–669.

[84] Castello D. A., and Matt C. F. T., 2011, “A validation metrics based model calibration applied on stranded cables,” Journal of the Brazilian Society of Mechanical Scientists and Engineers, **33**(4), pp. 417–427.

[85] Goodding J.C., Babuska V., Griffith D.T., Ingram B.R., Robertson L.M., 2007, "Study of free-free beam structural dynamics perturbations due to mounted cable harnesses," 48th AIAA/ASME/ASCE/AHS/ASC Structures, Structural Dynamics, and Materials Conference, Honolulu HI, AIAA-2007-2390.

[86] Smith A.M., Davis R.B., LaVerde B.T., Fulcher C.W., Jones D.C., Waldon J.M., Craigmyle B.B., 2012, "Validation of measured damping trends for flight-like vehicle panel/equipment including a range of cable harness assemblies," 53rd AIAA/ASME/ASCE/AHS/ASC Structures, Structural Dynamics and Materials Conference, Honolulu HI, AIAA 2012-1643.

[87] Robertson L.M., Lane S.A., Ingram B.R., Hansen E.J., Babuska V., Goodding J., Mimovich M,. Mehle G., Coombs D., Ardelean E.V., 2007, "Cable effects on the dynamics of large precision structures," 48th AIAA/ASME/ASC Structures, Structural Dynamics, and Materials Conference, Honolulu HI, AIAA-2007-2389.

[88] Griffin M.D., French J.R., 2004, Space Vehicle Design, 2nd ed., AIAA, Blacksburg VA.

[89] Ardelean E., Goodding J.C., Coombs D.M., Griffee J.C., Babuska V., Robertson L.M., Lane S.A., 2010, "Cable effects study: Tangents, rat holes, dead ends, and

valuable results," 51st AIAA/ASME/ASC Structures, Structural Dynamics, and Materials Conference, Orlando FL, AIAA-2010-2806.

[90] Goodding J.C., Griffee C., Ardelean E.V., 2008, "Parameter estimation and structural dynamic modeling of electrical cable harnesses on precision structures," 49th AIAA/ASME/ASCE/AHS/ASC Structures, Structural Dynamics, and materials Conference, Schaumburg IL, AIAA-2008-1852.

[91] Lesieutre G. A., 2010, “Frequency-independent modal damping for flexural structures via a viscous geometric damping model,” Journal of Guidance, Control, and Dynamics, **33**(6), pp. 1931–1935.

[92] Kauffman J. L., Lesieutre G. A., and Babuska V., 2012, “Damping models for shear beams with applications to spacecraft wiring harnesses,” 53rd AIAA/ASME/ASCE/AHS/ASC Structures, Structural Dynamics and Materials Conference, Honolulu HI, pp. 1–10.

[93] Smith A., Davis R.B., LaVerde B., Fulcher C., Jones D., 2012, "Determining damping trends from a range of cable harness assemblies on a launch vehicle panel from test measurements," 27th Aerospace Testing Seminar, Los Angeles CA.

[94] Feyrer K., 2007, Wire Rope: Tension, Endurance, Reliability, Springer, New York.

[95] Department of Defense, 1988, Military Specification MIL-C-27500G, General Specification for Cable, Power, Electrical and Cable Special Purpose, Electrical, Shielded and Unshielded, pp 1-35.

[96] Spak K.S., Agnes G.S., Inman D.J., 2014, "Cable parameters for homogenous cable-beam models for space structures," Topics in Dynamics of Civil Structures, Volume 4: Proceedings of the 32nd IMAC, A Conference on Structural Dynamics, Orlando FL, pp. 7-18.

[97] Spak K.S., Agnes G.S., Inman D.J., 2014, "Inclusion of shear effects, tension, and damping in a DTF beam model for cable modeling," 55th AIAA/ASME/ASCE/AHS/ASC Structures, Structural Dynamics, and Materials Conference, National Harbor MD, AIAA 2014-0491.

[98] Sendeckyj G.P., 1974, "Elastic Behavior of Composites", Mechanics of Composite Materials, Vol. 2, Academic Press, New York and London, pp. 45-83, Chap. 3.

[99] Hutchinson J.R., 2001, "Shear coefficients for Timoshenko beam theory," Journal of Applied Mechanics, **68**(1), pp. 87-92.

[100] Spak K.S., Agnes G.S., Inman D.J., 2013, "Comparison of damping models for space flight cables," Topics in Dynamics of Civil Structures, Volume 4: Proceedings of the 31st IMAC, A Conference on Structural Dynamics, Garden Grove CA, pp. 183-194.

[101] Inman, D.J., 1989, "Vibration analysis of viscoelastic beams by separation of variables and modal analysis," Mechanics Research Communications, **16**(4), pp. 213-218.

[102] McTavish D.J., Hughes P.C., 1992, "Finite element modeling of linear viscoelastic structures: The GHM method," 33rd AIAA/ASME/ASCE/AHS/ASC Structures, Structural Dynamics, and Materials Conference, Dallas TX, **4**, pp. 1753-1763.

[103] Golla D.F., Hughes P.C., 1985, "Dynamics of viscoelastic structures- a time-domain, finite element formulation," Journal of Applied Mechanics, **52**(4), pp. 897-906.

[104] Friswell M.I., Inman D.J., Lam M.J., 1997, "On the realisation of GHM models in viscoelasticity," Journal of Intelligent Material Systems and Structures, **8**(11), pp. 986-993.

[105] Wang Y., Inman D.J., 2013, "Finite element analysis and experimental study on dynamic properties of a composite beam with viscoelastic damping," Journal of Sound and Vibration, **332**(23), pp. 6177-6192.

[106] Ewins D.J., 2000, Modal Testing: Theory, Practice, and Application, 2nd ed., Research Studies Press Ltd., Hertfordshire, England.

[107] NASA MFSC SPEC 1238:2007, 2007, "Thermal vacuum bakeout specification for contamination sensitive hardware," George C. Marshall Space Flight Center.

[108] Spak K.S., Agnes G.S., Inman D.J., 2014, "Bakeout effects on dynamic response of spaceflight cables," Journal of Spacecraft and Rockets, In Print. doi: 10.2514/1.A32780

[109] Susanto K., 2009, "Vibration analysis of piezoelectric laminated slightly curved beams using distributed transfer function method," International Journal of Solids and Structures, **46**, pp. 1564-1573.

[110] Fang H., Lou M., Yang B., Yang Y., 2003, "Modeling of gossamer space structures with distributed transfer function method," Journal of Spacecraft and Rockets, **40**(4), pp. 548-552.

[111] Yang B., 1994, "Distributed transfer function analysis of complex distributed parameter systems," ASME Journal of Applied Mechanics, **61**(3), pp. 84-92.

[112] Yang B., Tan C.A., 1992, "Transfer functions of one-dimensional distributed parameter systems," ASME Journal of Applied Mechanics, **59**(4), pp. 1009-1014.

[113] Yang B., 2005, Stress, Strain and Structural Dynamics, Elsevier Academic Press, Amsterdam, pp. 913-921.

[114] Sciulli D., 1997, "Dynamics and control for vibration isolation design," Virginia Tech. Dissertation.

[115] Timoshenko S., Young D.H., Weaver W., 1974, Vibration Problems in Engineering, 4th ed., John Wiley & Sons, New York, pp. 420-435, 512.

[116] Adhikari S., Lei Y., Friswell M.I., 2005, "Dynamics of non-viscously damped distributed parameter systems," 46th AIAA/ASME/ASCE/AHS/ASC Structures, Structural Dynamics, and Materials Conference, Austin TX, AIAA-2005-1951.

[117] Tan C.A., Chung C.H., 1993, "Transfer function formulation of constrained distributed parameter systems, part I: Theory," ASME Journal of Applied Mechanics, **60**(4), pp. 1004-1011.

[118] Inman D.J., 2008, Engineering Vibration, 3rd ed., Pearson Prentice Hall, Upper Saddle River NJ.

[119] Majkut L., 2009, "Free and forced vibrations of Timoshenko beams described by single difference equation," Journal of Theoretical and Applied Mechanics, **47**(1), pp. 193-210.

[120] Blevins R.D., 2001, Formulas for Natural Frequency and Mode Shape, Krieger Pub. Co., Malabar FL., pp. 140-145.

[121] Spak K.S., Agnes G.S., Inman D.J., 2013, "Towards modeling of cable-harnessed structures: cable damping experiments," 54th AIAA/ASME/ASCE/AHS/ASC Structures, Structural Dynamics, and Materials Conference, Boston MA, AIAA 2013-1889.

[122] Vibrant Technology, Inc., 2003, ME'ScopeVES 4.0 Visual Engineering Series, Volume II- Reference, Vibrant Technology, Inc., Scotts Valley CA, pp. 235-265.

[123] Raoof, M., 1997, "Effect of lay angle on various characteristics of spiral strands," International Journal of Offshore and Polar Engineering, **7**(1).

Appendices

Appendix A. Construction of Global Stiffness Matrix for Pinned Euler-Bernoulli Beam in 3 Subsystems

A solid beam is divided into three subsystems A, B, and C as an example to illustrate the DTFM approach. Length of each section $L_s = 1$, and the total length $L_T = 3$.

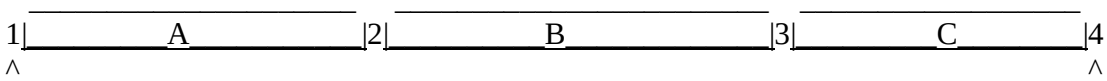

Equation of Motion for an Euler-Bernoulli beam: $\rho A\ddot{w} + EIw'''' = f(x,t)$

The equation of motion is used to make the fundamental matrix as described in Chapter 4, which is the same for each subsystem since they are identical.

$$F_A(s) = F_B(s) = F_C(s) = L_S \begin{bmatrix} 0 & 1 & 0 & 0 \\ 0 & 0 & 1 & 0 \\ 0 & 0 & 0 & 1 \\ -\frac{\rho A}{EI}s^2 & 0 & 0 & 0 \end{bmatrix}$$

Sum of Forces at Each Node:

Node 1: $Q_1^A + Q_1^B + Q_1^C - C_1 * u_1 + p_1 = 0$

Node 2: $Q_2^A + Q_2^B + Q_2^C - C_2 * u_2 + p_2 = 0$

Node 3: $Q_3^A + Q_3^B + Q_3^C - C_3 * u_3 + p_3 = 0$

Node 4: $Q_4^A + Q_4^B + Q_4^C - C_4 * u_4 + p_4 = 0$

There are no additional constraints beyond pinned boundary conditions and no external forces, so C_l and p_l are 0 for all nodes. Q must be evaluated for each section at EACH node for those subsystems that are connected at that node:

Node 1: $x_l = 0$

$Q_1^A = -K_{11}^A * u_1 - K_{12}^A * u_2 - f_1^A$

Q_1^B = NA (Since subsystem B is not connected at node 1)

Q_1^C = NA (Since subsystem C is not connected at node 1)

Node 2: $x_l = 1$

$Q_2^A = -K_{22}^A * u_2 - K_{21}^A * u_1 - f_2^A$

$Q_2^B = -K_{22}^B * u_2 - K_{23}^B * u_3 - f_2^B$

Q_2^C = NA (Since subsystem C is not connected at node 2)

Node 3: $x_l = 2$

Q_3^A = NA (Since subsystem A is not connected at node 3)

$Q_3^B = -K_{33}^B * u_3 - K_{32}^B * u_2 - f_3^B$

$Q_3^C = -K_{33}^C * u_3 - K_{34}^C * u_4 - f_3^C$

Node 4: $x_l = 3$

Q_4^A = NA (Since subsystem A is not connected at node 4)

Q_4^B = NA (Since subsystem B is not connected at node 4)

$Q_4^C = -K_{44}^C * u_4 - K_{43}^C * u_3 - f_4^C$

The global stiffness matrix *K* is made of portions of the transfer function matrix *H*, given by

$$H(x,s) = e^{F(s)*x} * \left(M(s) + N(s) * e^{F(s)}\right)^{-1}$$

where *H* can be partitioned as

$$H(x,s) = \begin{bmatrix} H_{\alpha 0} & H_{\alpha 1} \\ H_{\epsilon 0} & H_{\epsilon 1} \end{bmatrix}$$

Boundary condition matrices $M(s)$and $N(s)$ describe either internal or pinned constraints, depending on the subsystem:

$$M_{Internal} = \begin{bmatrix} 1 & 0 & 0 & 0 \\ 0 & 1 & 0 & 0 \\ 0 & 0 & 0 & 0 \\ 0 & 0 & 0 & 0 \end{bmatrix}, \qquad N_{Internal} = \begin{bmatrix} 0 & 0 & 0 & 0 \\ 0 & 0 & 0 & 0 \\ 1 & 0 & 0 & 0 \\ 0 & 1 & 0 & 0 \end{bmatrix}$$

$$M_{Pin} = \begin{bmatrix} 0 & 0 & EI & 0 \\ 1 & 0 & 0 & 0 \\ 0 & 0 & 0 & 0 \\ 0 & 0 & 0 & 0 \end{bmatrix}, \qquad N_{Pin} = \begin{bmatrix} 0 & 0 & 0 & 0 \\ 0 & 0 & 0 & 0 \\ 0 & 0 & EI & 0 \\ 1 & 0 & 0 & 0 \end{bmatrix}$$

Subsystem A: M_{Pin}, $N_{Internal}$

Subsystem B: $M_{Internal}$, $N_{Internal}$

Subsystem C: $M_{Internal}$, N_{Pin}

At this point, *H* can be calculated for each subsystem, using the appropriate fundamental $F(s)$ matrix, the appropriate M and N matrices, and the *x* value for each node. Recall

$Q_l^N = -R_N * \sigma_N(x_l, s)$ where R is a coordinate transformation matrix. Since

$$\sigma(x,s) = E(s)\int_0^1 G_\epsilon(x,\xi,s)f(\xi,s)d\xi + H_{\epsilon_0}(x,s)\alpha_0(s) + H_{\epsilon_1}(x,s)\alpha_1(s)$$

and

$$\alpha_N(x_l, s) = S_N u_l(s) \ , \qquad \alpha_N(x_i, s) = T_N u_i(s)$$

the nodal force at each node can be written in terms of the displacements α on each end of the subsystem and the transfer matrix as follows.

Node 1: $x_l = 0$

$Q_1^A = -K_{11}^A * u_1 - K_{12}^A * u_2 - f_1^A$

$K_{11}^A = R_A * H_{\epsilon 1}(0,s) * S_A$ with H based on M_{Pin}, $N_{Internal}$, and $F_A(s)$

$K_{12}^A = R_A * H_{\epsilon 0}(0,s) * S_A$ with H based on M_{Pin}, $N_{Internal}$, and $F_A(s)$

Node 2: $x_l = 1$

$Q_2^A = -K_{22}^A * u_2 - K_{21}^A * u_1 - f_2^A$

$Q_2^B = -K_{22}^B * u_2 - K_{23}^B * u_3 - f_2^B$

$K_{22}^A = R_A * H_{\epsilon 1}(1,s) * S_A$ with H based on M_{Pin}, $N_{Internal}$, and $F_A(s)$

$K_{22}^B = R_B * H_{\epsilon 1}(1,s) * S_B$ with H based on $M_{Internal}$, $N_{Internal}$, and $F_B(s)$

$K_{21}^A = R_A * H_{\epsilon 0}(1,s) * T_A$ with H based on M_{Pin}, $N_{Internal}$, and $F_A(s)$

$K_{23}^B = R_B * H_{\epsilon 0}(1,s) * S_B$ with H based on $M_{Internal}$, $N_{Internal}$, and $F_B(s)$

Node 3: $x_l = 2$

$Q_3^B = -K_{33}^B * u_3 - K_{32}^B * u_2 - f_3^B$

$Q_3^C = -K_{33}^C * u_3 - K_{34}^C * u_4 - f_3^C$

$K_{33}^B = R_B * H_{\epsilon 1}(2,s) * S_B$ with H based on $M_{Internal}$, $N_{Internal}$, and $F_B(s)$

$K_{33}^C = R_C * H_{\epsilon 1}(2,s) * S_C$ with H based on $M_{Internal}$, N_{Pin}, and $F_C(s)$

$K_{32}^B = R_B * H_{\epsilon 0}(2,s) * T_B$ with H based on $M_{Internal}$, $N_{Internal}$, and $F_B(s)$

$K_{34}^C = R_C * H_{\epsilon 0}(2,s) * S_C$ with H based on $M_{Internal}$, N_{Pin}, and $F_C(s)$

Node 4: $x_l = 3$

$Q_4^C = -K_{44}^C * u_4 - K_{43}^C * u_3 - f_4^C$

$K_{44}^C = R_C * H_{\epsilon 1}(3,s) * S_C$ with H based on $M_{Internal}$, N_{Pin}, and $F_C(s)$

$K_{43}^C = R_C * H_{\epsilon 0}(3,s) * T_C$ with H based on $M_{Internal}$, N_{Pin}, and $F_C(s)$

Once the subsystem stiffness components are determined, they are assembled in the global stiffness matrix based on the equation $K(s) * u(s) = f(s)$, where u is the displacement vector containing both displacement and slope terms.

$$\begin{bmatrix} K_{11}^A & K_{12}^A & 0 & 0 \\ K_{21}^A & K_{22}^A + K_{22}^B & K_{23}^B & 0 \\ 0 & K_{32}^B & K_{33}^B + K_{33}^C & K_{34}^C \\ 0 & 0 & K_{43}^C & K_{44}^C \end{bmatrix} * \begin{Bmatrix} u_1 \\ u_2 \\ u_3 \\ u_4 \end{Bmatrix} = q(s)$$

The complete global stiffness matrix with individual entries is therefore:

$$\begin{bmatrix} K11Aa & K11Ab & K12Aa & K12Ab & 0 & 0 & 0 & 0 \\ K11Ac & K11Ad & K12Ac & K12Ad & 0 & 0 & 0 & 0 \\ K12Aa & K12Ab & K22A + K22B & K22b & K23Ba & K23Bb & 0 & 0 \\ K12Ac & K12Ad & K22c & K22d & K23Bc & K23Bd & 0 & 0 \\ 0 & 0 & K32Ba & K32Bb & K33B + K33C & K33b & K34Ca & K34Cb \\ 0 & 0 & K32Bc & K32Bd & K33c & K33d & K34Cc & K34Cd \\ 0 & 0 & 0 & 0 & K43Ca & K43Cb & K44Ca & K44Cb \\ 0 & 0 & 0 & 0 & K43Cc & K43Cd & K44Cc & K44Cd \end{bmatrix}$$

$$* \begin{Bmatrix} u_1 \\ \theta_1 \\ u_2 \\ \theta_2 \\ u_3 \\ \theta_3 \\ u_4 \\ \theta_4 \end{Bmatrix} = q(s)$$

The global stiffness matrix can be reduced after the boundary condition rows are eliminated.

$$\begin{bmatrix} K11Ad & K12Ac & K12Ad & 0 & 0 & 0 \\ K12Ab & K22A + K22B & K22b & K23Ba & K23Bb & 0 \\ K12Ad & K22c & K22d & K23Bc & K23Bd & 0 \\ 0 & K32Ba & K32Bb & K33B + K33C & K33b & K34Cb \\ 0 & K32Bc & K32Bd & K33c & K33d & K34Cd \\ 0 & 0 & 0 & K43Cc & K43Cd & K44Cd \end{bmatrix} * \begin{Bmatrix} \theta_1 \\ u_2 \\ \theta_2 \\ u_3 \\ \theta_3 \\ \theta_4 \end{Bmatrix} = q(s)$$

To obtain the various solutions, the stiffness matrix is manipulated in the following ways; more details on these methods are available in Yang's and Sciulli's works:

Natural Frequencies: Solve $\det[K(s)] = 0$ with $s = i\omega$

Mode shapes: Find nontrivial solutions for $K(s) * u(s) = 0$

Frequency Response: $u(j\omega) = K^{-1}(j\omega) * q(j\omega)$ where q is assumed to be a harmonic forcing function.

Time Domain Response: Take the inverse Laplace transform of η

Total solution:

$$\eta(x,s) = [W, W', W'', W''']$$

$$\eta(x,s) = \int_0^1 G(x,z,s) * f(z,s) * dz + H(x,s) * \gamma(s)$$

$$\eta(x,s) = [\alpha; \epsilon]$$

$$\alpha(x,s) = \int_0^1 G_\alpha(x,z,s) * f(z,s) * dz + H_{\alpha 0}(x,s) * \alpha_0(s) + H_{\alpha 1}(x,s) * \alpha_1(s)$$

$$\epsilon(x,s) = E\int_0^1 G_\epsilon(x,z,s) * f(z,s) * dz + H_{\epsilon 0}(x,s) * \alpha_0(s) + H_{\epsilon 1}(x,s) * \alpha_1(s)$$

Appendix B. Combination of Shear Beam Equations

From Chapter 4, the governing equations for a cable as a beam, with tension and damping included, are

$$\rho A \frac{\partial^2 w}{\partial t^2} = -\kappa AG \frac{\partial \psi}{\partial x} + \kappa AG \frac{\partial^2 w}{\partial x^2} + c \frac{\partial w}{\partial t} + q \tag{A.1}$$

$$EI \frac{\partial^2 \psi}{\partial x^2} + T \frac{\partial w}{\partial x} + \int_0^t g(t-\tau) \frac{\partial^3 w}{\partial x^3} dt - \kappa AG\psi + \kappa AG \frac{\partial w}{\partial x} = 0 \tag{A.2}$$

These equations are combined as follows to obtain a single equation in terms of the transverse displacement $w(x,t)$ to be used in the distributed transfer function method.

Solve for $\frac{\partial \psi}{\partial x}$ from first equation (A.1):

$$\frac{\partial \psi}{\partial x} = \frac{\partial^2 w}{\partial x^2} - \frac{\rho}{\kappa G} \frac{\partial^2 w}{\partial t^2} + \frac{c}{\kappa AG} \frac{\partial w}{\partial t} + \frac{q}{\kappa AG} \tag{A.3}$$

Next, take additional spatial derivatives of (A.3) to use in later substitutions:

$$\frac{\partial^2 \psi}{\partial^2 x} = \frac{\partial^3 w}{\partial x^3} - \frac{\rho}{\kappa G} \frac{\partial^3 w}{\partial x \partial t^2} + \frac{c}{\kappa AG} \frac{\partial^2 w}{\partial x \partial t} + \frac{1}{\kappa AG} \frac{\partial q}{\partial x} \tag{A.4}$$

$$\frac{\partial^3 \psi}{\partial x^3} = \frac{\partial^4 w}{\partial x^4} - \frac{\rho}{\kappa G} \frac{\partial^4 w}{\partial x^2 \partial t^2} + \frac{c}{\kappa AG} \frac{\partial^3 w}{\partial x^2 \partial t} + \frac{1}{\kappa AG} \frac{\partial^2 q}{\partial x^2} \tag{A.5}$$

Take spatial derivative of equation (A.2):

$$EI \frac{\partial^3 \psi}{\partial x^3} + T \frac{\partial^2 w}{\partial x^2} + \int_0^t g(t-\tau) \frac{\partial^4 w}{\partial x^4} dt - \kappa AG \frac{\partial \psi}{\partial x} + \kappa AG \frac{\partial^2 w}{\partial x^2} = 0 \tag{A.6}$$

Substitute all terms containing ψ from the derivatives of the first equation (A.1) into (A.6):

$$EI\left(\frac{\partial^4 w}{\partial x^4}-\frac{\rho}{\kappa G}\frac{\partial^4 w}{\partial x^2\partial t^2}+\frac{c}{\kappa AG}\frac{\partial^3 w}{\partial x^2\partial t}+\frac{1}{\kappa AG}\frac{\partial^2 q}{\partial x^2}\right)+T\frac{\partial^2 w}{\partial x^2}$$
$$+\int_0^t g(t-\tau)\frac{\partial^4 w}{\partial x^4}dt \qquad (A.7)$$
$$-\kappa AG\left(\frac{\partial^2 w}{\partial x^2}-\frac{\rho}{\kappa G}\frac{\partial^2 w}{\partial t^2}+\frac{c}{\kappa AG}\frac{\partial w}{\partial t}+\frac{q}{\kappa AG}\right)+\kappa AG\frac{\partial^2 w}{\partial x^2}=0$$

$$\left(EI\frac{\partial^4 w}{\partial x^4}-\frac{\rho EI}{\kappa G}\frac{\partial^4 w}{\partial x^2\partial t^2}+\frac{cEI}{\kappa AG}\frac{\partial^3 w}{\partial x^2\partial t}+\frac{EI}{\kappa AG}\frac{\partial^2 q}{\partial x^2}\right)+T\frac{\partial^2 w}{\partial x^2}$$
$$+\int_0^t g(t-\tau)\frac{\partial^4 w}{\partial x^4}dt+\left(-\kappa AG\frac{\partial^2 w}{\partial x^2}+\rho A\frac{\partial^2 w}{\partial t^2}-c\frac{\partial w}{\partial t}-q\right) \qquad (A.8)$$
$$+\kappa AG\frac{\partial^2 w}{\partial x^2}=0$$

Rearrange terms to move all forcing function terms to the right side, cancel and combine as needed.

$$EI\frac{\partial^4 w}{\partial x^4}-\frac{\rho EI}{\kappa G}\frac{\partial^4 w}{\partial x^2\partial t^2}+\frac{cEI}{\kappa AG}\frac{\partial^3 w}{\partial x^2\partial t}+T\frac{\partial^2 w}{\partial x^2}-\cancel{\kappa AG\frac{\partial^2 w}{\partial x^2}}+\rho A\frac{\partial^2 w}{\partial t^2}-c\frac{\partial w}{\partial t}$$
$$+\int_0^t g(t-\tau)\frac{\partial^4 w}{\partial x^4}dt+\cancel{\kappa AG\frac{\partial^2 w}{\partial x^2}}=q-\frac{EI}{\kappa AG}\frac{\partial^2 q}{\partial x^2} \qquad (A.8)$$

$$EI\frac{\partial^4 w}{\partial x^4}-\frac{\rho EI}{\kappa G}\frac{\partial^4 w}{\partial x^2\partial t^2}+\frac{cEI}{\kappa AG}\frac{\partial^3 w}{\partial x^2\partial t}+T\frac{\partial^2 w}{\partial x^2}+\rho A\frac{\partial^2 w}{\partial t^2}-c\frac{\partial w}{\partial t}$$
$$+\int_0^t g(t-\tau)\frac{\partial^4 w}{\partial x^4}dt=q-\frac{EI}{\kappa AG}\frac{\partial^2 q}{\partial x^2} \qquad (A.9)$$

$$\rho A\frac{\partial^2 w}{\partial t^2}-\frac{\rho EI}{\kappa G}\frac{\partial^4 w}{\partial x^2\partial t^2}+EI\frac{\partial^4 w}{\partial x^4}+\frac{cEI}{\kappa AG}\frac{\partial^3 w}{\partial x^2\partial t}+T\frac{\partial^2 w}{\partial x^2}-c\frac{\partial w}{\partial t}$$
$$+\int_0^t g(t-\tau)\frac{\partial^4 w}{\partial x^4}dt=q-\frac{EI}{\kappa AG}\frac{\partial^2 q}{\partial x^2} \qquad (A.10)$$

Thus, a viscously and hysteretically damped viscoelastic cable in tension can be described with the equation of motion:

$$\rho A\frac{\partial^2 w}{\partial t^2}-\frac{\rho EI}{\kappa G}\frac{\partial^4 w}{\partial x^2\partial t^2}+EI\frac{\partial^4 w}{\partial x^4}+\frac{cEI}{\kappa AG}\frac{\partial^3 w}{\partial x^2\partial t}+T\frac{\partial^2 w}{\partial x^2}-c\frac{\partial w}{\partial t}+\int_0^t g(t-\tau)\frac{\partial^4 w}{\partial x^4}dt$$
$$=q-\frac{EI}{\kappa AG}\frac{\partial^2 q}{\partial x^2}$$

Appendix C. MATLAB Program Files for Cable and Cabled Beam Models Using the Distributed Transfer Function Method

In this section, the cable models are listed first. Two input files are listed, one for the two-point cable, and one for the four-point model. Next, the cable model files are listed. The cabled beam input file is listed next, followed by the cabled beam model files. Finally, the program files common to both cable and cabled beam models (the output files and simple functions) are listed following the model files. Many of these files were built off of functions created by D. Sciulli, whose detailed parameter lists and comments have been retained within the files with thanks.

Two-Point Cable Model Input File

```
% This file initializes cable parameters for one of four types of cable
for
% the two-point fixture
% Last modified 4/25/2014

cabletype=19;
% Cable type options are:
% 7 for 1X7, 19 for 1X19, 48 for 1X48, 749 for 7X7

rangeval=1;
% Range value options are
% 1 for min (min EI and max rho A)
% 2 for avg
% 3 for max (max EI and min rho A)
% 5 for max EI with mid rhoA

% Set whether to include bakeout factor; 1 includes bakeout factor.
bf=1;

if cabletype==7;
% For 1X7 Cable:
len_m=0.7692;

MinDensity=2090; % Note that this is from the rule of mixtures, since
it was less than the minimum rho calculations of 2117.12
DensityMid=3110.6;
MaxDensity=3323.37;

MinArea=2.76803*10^-5; % Calculated based on only wire components
MaxArea=4.34512*10^-5; % Calculated based on OUTER cable diameter
AreaMid=2.95737*10^-5; % Calcuated based on individual wire diameter

EIslipmin=0.34;
EIslipmax=0.37;
```

```
spr_p=1*10^4;

elseif cabletype==19;
len_m=0.7782;
MinDensity=1926.46;
DensityExp=2162;
DensityExp2=2557;
DensityMid=3049;
MaxDensity=3528.353;

MinArea=7.51321*10^-5; % Calculated based on only wire components
MaxArea=1.27076*10^-4; % Calculated based on OUTER cable diameter
AreaMid=8.02715*10^-5; % Calcuated based on individual wire diameter

EIslipmin=1.0846;
EIslipmax=1.1815;
spr_p=6*10^4;
elseif cabletype==48;
len_m=0.7744;

MinDensity=1770.5;
DensityMid=2853.7;
MaxDensity=3048.904;

MinArea=1.898-7*10^-4; % Calculated based on only wire components
MaxArea=3.26851*10^-4; % Calculated based on OUTER cable diameter
AreaMid=2.02791*10^-4; % Calcuated based on individual wire diameter

EIslipmin=4.72633;
EIslipmax=5.1009;
spr_p=1*10^6;
elseif cabletype==749;
len_m=0.7744;

MinDensity=1742.326;
DensityMid=3084.063;
MaxDensity=3295.02;

MinArea=1.93762*10^-4; % Calculated based on only wire components
MaxArea=3.66435*10^-4; % Calculated based on OUTER cable diameter
AreaMid=2.07016*10^-4; % Calcuated based on individual wire diameter

EIslipmin=2.143083;
EIslipmax=2.30292;
spr_p=6*10^5;
else
    disp('Invalid cable type selected, choose 7, 19, 48 or 749')
end

if rangeval==1;
    rhobase=MaxDensity;
    area=MaxArea;
    EI=EIslipmin;
elseif rangeval==2;
    rhobase=DensityMid;
```

```
    area=AreaMid;
    EI=EImid;
elseif rangeval==3;
    rhobase=MinDensity;
    area=MinArea;
    EI=EIslipmax;
elseif rangeval==4;
    % User choice options/ mix n match
    rhobase=DensityExp;
    area=MinArea;
    EI=EImax;
elseif rangeval==5;
    rhobase=DensityMid;
    area=AreaMid;
    EI=EIslipmax;
else
    disp('Invalid selection for min, avg, or max cable frequency
value')
end

l1=0.025; % Length of bottom end piece
l2=0.280; % Length from bottom connection to driving point
l4=0.025; % Length of top end piece
l3=len_m-(l1+l2+l4); % Length from driving point to top connectio

mass=MinDensity*MinArea*len_m; % Mass calculation
Tens=4.45; % Tension applied for two-pint cables
kappag=0.95; % Shear coefficient calculated for all cables
%Gsh=594474058.9; % Calculated G Value min
Gsh=651743193.3; % Calculated G value max
shearrigid=kappag*area*Gsh;
c=0;
% Use cv for viscous damping
cv=0;
rho=rhobase*area;
A=area;
% Inclusion of bakeout factor in EI if bf is set to 1
if bf==1;
Ei=0.8*EI;
elseif bf==0;
Ei=EI
else
    disp('Bakeout factor not specified')
end

num_ev=8; %Number of modes and mode shapes found.
AXIAL=[];               % used for ID matrix if no axial forces

% This is essentially equivalent to no mass, for testing free-free
cable.
%  mass=1e-12;
%  spr_p=1;
% THESE on the other hand are like pinned connections!
% mass=1e12;
% spr_p=1e9;
% Mass value must be very large for correct end condition
```

```
 mass=1*10^12;
% Connection damping can be incorporated here if desired.
zeta_p=0;
damp_p=2*zeta_p*sqrt(spr_p/mass)*mass;
spr_a=0;

 CONSTRAIN(2,:)=[1 1 mass spr_p damp_p 0 1 1 0 0 0 0];
 CONSTRAIN(4,:)=[1 1 mass spr_p damp_p 0 1 1 0 0 0 0];

BC_type=[2 0 0 2];          % type of boundary condtion for each
subsystem, 1 is clamped, 2 is free, 3 is pinned
BC_node_ty=[2 0 0 0 2];

m=4;                % number of subsystems
node=5;             % number of nodes
can=4;              % number of known boundary displacements
dof=2;              % number of dof: wy, w'

% Cable node/attachment point locations
XY = [0 l1 l1+l2 l1+l2+l3 len_m     %X % X,Y position of each node, 2 X
node
    0 0 0 0 0];         %Y      % This is actual x,y not non-
dimensional

% Use this XY value to make equal span lengths for comparison with
Blevins
% XY = [0 len_m/5 2*len_m/5 3*len_m/5 4*len_m/5 len_m % X,Y position of
each node, 2 X node
%   0 0 0 0 0 0];           %Y      % This is actual x,y not
nondimensional

CON=[1 1 2 3 4;0 2 3 4 0];      % which subsystems are connected at
each node

Sub_Con=[1 2 3 4; % Shows how each subsytem is connected to each node
(2 x m)
       2 3 4 5];            %  Top row is x=0 position of subsystem


XX=[0 2 2 2 0];     % the number of subsystems connected at each node
                    %   0 signifies that there is not a connection
                    %   between 2 different subsystems. 1 signifies
                    %   some sort of interface condition (1 x node)

BND_DOF=[1 1;       % Shows which DOF are constrained (node x dof)
        0 0;
        0 0;
        0 0;
        1 1];
```

Four-Point Cable Model Input File

```
% This file initializes cable parameters for one of four types of cable
for
% the four-point fixture
% Last modified 4/2/2014, Added bakeout correction factor 4/18/2014

cabletype=749;
% Cable type options are:
% 7 for 1X7, 19 for 1X19, 48 for 1X48, 749 for 7X7
rangeval=1;
% Range value options are
% 1 for min
% 2 for avg
% 3 for max
% 5 for max EI with mid rhoA

bf=1; % Bakeout factor- if bf=1, bakeout factor is INCLUDED.  If bf=0,
not included!

if cabletype==7;
% For 1X7 Cable:
len_m=0.7692;
MinDensity=2090; % Note that this is from the rule of mixtures, since
it was less than the minimum rho calculations of 2117.12
DensityMid=3110.6;
MaxDensity=3323.37;

MinArea=2.76803*10^-5; % Calculated based on only wire components
MaxArea=4.34512*10^-5; % Calculated based on OUTER cable diameter
AreaMid=2.95737*10^-5; % Calcuated based on individual wire diameter

EIslipmin4pt=0.402;
EIslipmax4pt=0.4385;

EIstickmin=1.65;
EIstickmax=1.87;

spr_p=1*10^4;

elseif cabletype==19;
len_m=0.7782;

MinDensity=1926.46;
DensityExp=2162;
DensityExp2=2557;
DensityMid=3049.738;
MaxDensity=3528.353;

MinArea=7.51321*10^-5; % Calculated based on only wire components
MaxArea=1.27076*10^-4; % Calculated based on OUTER cable diameter
AreaMid=8.02715*10^-5; % Calcuated based on individual wire diameter

EIslipmin4pt=1.55;
EIslipmax4pt=1.71;
```

```
EIstickmax=15.72;
EIstickmin=13.82;

spr_p=6*10^4;

elseif cabletype==48;
len_m=0.7744;

MinDensity=1770.5;
DensityMid=2853.7;
MaxDensity=3048.904;

MinArea=1.898-7*10^-4; % Calculated based on only wire components
MaxArea=3.26851*10^-4; % Calculated based on OUTER cable diameter
AreaMid=2.02791*10^-4; % Calcuated based on individual wire diameter

EIslipmin4pt=7.51748;
EIslipmax4pt=8.13435;

EIstickmin=93.60;
EIstickmax=106.71;

spr_p=1*10^6;

elseif cabletype==749;
len_m=0.7744;

MinDensity=1742.326;
DensityMid=3084.06;
MaxDensity=3295.025;

MinArea=1.93762*10^-4; % Calculated based on only wire components
MaxArea=3.66435*10^-4; % Calculated based on OUTER cable diameter
AreaMid=2.07016*10^-4; % Calcuated based on individual wire diameter

EIslipmin4pt=2.59;
EIslipmax4pt=2.82;

EIstickmin=74.05;
EIstickmax=84.38;

spr_p=6*10^5;

else
    disp('Invalid cable type selected, choose 7, 19, 48 or 749')
end

if rangeval==1;
    rhobase=MaxDensity;
    area=MaxArea;
    EI=EIslipmin4pt;
    %EI=EIstickmin;
elseif rangeval==2;
```

```
    rhobase=DensityMid;
    area=AreaMid;
    EI=EImid;
elseif rangeval==3;
    rhobase=MinDensity;
    area=MidArea;
    EI=EIslipmax4pt;
elseif rangeval==4;
    % User choice options/ mix n match
    rhobase=DensityExp;
    area=MinArea;
    EI=EImax;
 elseif rangeval==5;
    rhobase=DensityMid;
    area=AreaMid;
    EI=EIslipmax4pt;
    %EI=EIstickmax;
else
    disp('Invalid selection for min, avg, or max cable frequency
value')
end

% For Four Point rods
l1=0.025;
l2=0.205;
l3=0.07;
l4=0.184;
l5=0.205;
l6=len_m-(l1+l2+l3+l4+l5);

% % EQUAL SPANS FOR TEST COMPARISON WITH BLEVINS
% spanlngth=len_m/5;
% l1=spanlngth;
% l2=spanlngth;
% l3=spanlngth/2;
% l4=spanlngth/2;
% l5=spanlngth;
% l6=len_m-(l1+l2+l3+l4+l5);

mass=MinDensity*MinArea*len_m;
Tens=8.89; % For 4 pt cable
%Tens=0; % For equal span length
kappag=0.95;
Gsh=651743193.3; % Calculated G value

c=0;
% Use cv for viscous damping
cv=0;

rho=rhobase*area
A=area;
% Bakeout factor
if bf==1;
Ei=0.8*EI
elseif bf==0;
Ei=EI
```

```
else
    disp('Bakeout factor not specified')
end

num_ev=8; % Number of eigenvalues to find

AXIAL=[]; % Used for ID matrix if no axial forces

% This is essentially equivalent to no mass
%  mass=1e-12;
%  spr_p=1;
% THESE on the other hand are like pinned connections!
%mass=1000;
%spr_p=1e9;

% Mass value must be very large for correct end condition.
 mass=1*10^12;
 % Connection damping can be incorporated here if desired.
zeta_p=0;
damp_p=2*zeta_p*sqrt(spr_p/mass)*mass;
spr_a=0;

 % Linear AND rotational spring connection at four points.
CONSTRAIN(2,:)=[1 1 mass spr_p damp_p 0 1 1 0 0 0 0];
CONSTRAIN(3,:)=[1 1 mass spr_p damp_p 0 1 1 0 0 0 0];
CONSTRAIN(5,:)=[1 1 mass spr_p damp_p 0 1 1 0 0 0 0];
CONSTRAIN(6,:)=[1 1 mass spr_p damp_p 0 1 1 0 0 0 0];

BC_type=[2 0 0 0 0 2];          % type of boundary condtion for each
subsystem, 1 is clamped, 2 is free, 3 is pinned
BC_node_ty=[2 0 0 0 0 0 2];

m=6;                % the number of subsystems
node=7;             % the number of nodes
can=4;              % the number of known boundary displacements
dof=2;              % the number of dof: ux, wy, w'

% Cable node/attachment point locations
XY = [0 l1 l1+l2 l1+l2+l3 l1+l2+l3+l4 l1+l2+l3+l4+l5 len_m      %X
% X,Y position of each node, 2 X node
    0 0 0 0 0 0 0];         %Y      % This is actual x,y not
nondimensional

CON=[1 1 2 3 4 5 6;0 2 3 4 5 6 0];      % Which subsystems are
connected at each node

Sub_Con=[1 2 3 4 5 6;           % Shows how each subsytem is connected
to each
       2 3 4 5 6 7];            %   node    (2 x m). top row is x=0
position of subsystem


XX=[0 2 2 2 2 2 0]; % the number of subsystems connected at each node
                    %   0 signifies that there is not a connection
```

```
                    %   between 2 different subsystems. 1 signifies
                    %   some sort of interface condition (1 x node)

BND_DOF=[   1 1;        % Shows which DOF are constrained (node x dof)
        0 0;
        0 0;
        0 0;
        0 0;
        0 0;
        1 1];
```

Cable Stiffness Matrix Assembly Program

```
% This .m file will find the stiffness matrix given a value for the
% frequency which must be in Hz
%
% INPUT
%   ij      frequency in Hz
%
% OUTPUT
%   Kgl     Reduced Global Stiffness Matrix
%   qgl     Reduced Global Force Vector
%
% VARIABLES
%   BC_node_ty  The type of boundary conditions for each node
%   can         the number of known boundary displacements
%   CON         Shows which subsystems are connected to which
%               nodes. '0' means no subsystem
%   CONSTRAIN   Shows how each node is constrained.
%   dof     the number of degrees of freedom of subsystem
%   E       compatibility matrix for subsystem
%   Ea      E*A (Axial Stiffness) for a subsytem
%   Ei      E*I (Flexural Rigidity) for a subsystem
%   evals       Vector of eigenvalues
%   F       matrix built by governing pdes (n x n)
%   F_cstr      Force on equipment
%   filename    the name of file that holds initialization data
%   fptu        point force at subsystem in axial direction
%   fptu_pos    location of point force at subsystem in axial direction
%   fptw        point force at subsystem in transverse direction
%   fptw_pos        location of point force at subsystem in axial
direction
%   Gu      Greens' function for axial displacement
%   Ge_u        partioned G matrix
%   Ge_w        partioned G matrix
%   Gw      Green's function for transverse displacement
%   H       transfer function of Eta/Gamma
%   He0     partitioned H matrix
%   He1     partitioned H matrix
%   ii      dummy variable
%   ID      matrix used to assemble Kgl so that nodes with constraints
%           will be wiped out of K (full Stiffness Matrix)
%   jj      dummy variable
%   K       global stiffness matrix (n x n)
%   Kappa   vector used for BC calculation
%   kk      dummy variable
%   Len     length of each subsystems in vector
%   Li      length of each subsystem
%   M       Temporal-spatial operator for left end of subsystem
%   Mgl     Global M for each subsystem
%   m       the total number of subsystems
%   N       Temporal-spatial operator for right end of subsystem
%   Ngl     Global N for each subsystem
%   n       nth order linear pde (4:bendng, 2:axial)
%   node    total number of nodes of system
%   num     current subsystem
%   num_str current subsystem but of type string
%   n1      nth order linear pde for axial vibrations
```

```
%   n2      nth order linear pde for bending vibrations
%   P       nodal forces
%   P_nodal nodal forces
%   pts     the number of displacements of entire system
%   q       global Force vector (n x 1)
%   qgl     Reduced Global Force Vector
%   Rot     Rotation vector of 'rot' values
%   rho     mass per unit length for a subsystem
%   rot     rotation of subsystem wrt horizontal
%   Sub_Con     Shows which subsystems are connected to which nodes (2
x m)
%               A zero value implies some sort of boundary condition
%   t_alpha     Alpha (i.e mass) term for proportional Damping
%   t_beta      Beta (i.e. stiffness) term for proportional damping
%   tmp,tmpi    dummy variables (i=1,2)
%   var     used to convert degrees to radians
%   s       frequency = ij * sqrt(-1)
%   t1      beginning node location for subsystem
%   t2      end node location for subsystem
%   X       location of node points in local coordinates
%   XX      Shows at each node how many subsystems are connected to it.
%

function [Kgl,qgl]=assemble_K(ij)
%ij=10; % This can be used to test a single frequency value.
global node m dof n1 n2 n can XX CON ID Sub_Con qgl Rot BC_type pts;
global Len Ea Ei rho filename BC_node_ty CONSTRAIN CONSTR_SUB_PT X;
global A kappag Gsh cv c Tens;
global Mgl Ngl Kappa P_Nodal F_cstr FPTw FPTwPos;
global COUNT evals t_alpha t_beta;

for ii=1:m,
    tmp=num2str(ii);

eval(['[R',tmp,'1,R',tmp,'2,S',tmp,'1,S',tmp,'2]=Rotation_Calc(Rot(',tm
p,'));'])
end

% Node point locations for each subsystem; start of each subsystem is
0,
% end of each subsystem is 1.  These values are initialized in
freq_resp.m

X = zeros(node,m);
tmp1=[0;1];
for ii=1:m,
    tmp2=Sub_Con(:,ii);
    X([tmp2],ii)=X([tmp2],ii)+tmp1;
end

% Assembly of Stiffness Matrix
s = 1i*ij*2*pi;         % s = jw, s in radians, ij in Hertz

K=zeros(pts);           % Pre-allocate Global Stiffness Matrix
q=zeros(pts,1);         % Pre-allocate Force Vector
```

```
% Stiffness matrix assembled based on equilibrium at each node

for kk=1:node,
    P=P_Nodal(1:dof,kk); % Force input from forces_ file.
    loc1=ID(kk,:);

    % Add nodal forces to q vector
    q(loc1) = q(loc1) + P;

% Constraint forces incorporated into stiffness matrix
% Lumped system connected to a subsystem at two different points
    if (CONSTRAIN(kk,1)==1 && CONSTRAIN(kk,2)==4)
        loc2=ID(CONSTRAIN(kk,11),:);
        K(loc1,loc2)=K(loc1,loc2) + constr_pt(CONSTRAIN(kk,:),s,1);
        loc2=ID(CONSTRAIN(kk,12),:);
        K(loc1,loc2)=K(loc1,loc2) + constr_pt(CONSTRAIN(kk,:),s,2);
        m_cstr=CONSTRAIN(kk,3);
        c_cstr=CONSTRAIN(kk,5);
        k_cstr=CONSTRAIN(kk,4);
        tmp1=c_cstr*s+k_cstr;
        q(loc1)=q(loc1)-(tmp1)/(m_cstr*s^2+tmp1).*F_cstr;
% Lumped system connected to a subsystem at one point - this is what is
used for cable models
    elseif (CONSTRAIN(kk,1)==1 && CONSTRAIN(kk,2)~=5)
        Cl=constr_pt(CONSTRAIN(kk,:),s);
        K(loc1,loc1) = K(loc1,loc1) + Cl;
        m_cstr=CONSTRAIN(kk,3);
        c_cstr=CONSTRAIN(kk,5);
        k_cstr=CONSTRAIN(kk,4);
        tmp2=c_cstr*s+k_cstr;
        q(loc1)=q(loc1)+tmp2/(m_cstr*s^2+tmp2).*F_cstr;
% Two subsystems connected together at single point - this is what is
used for cabled beam model
    elseif (CONSTRAIN(kk,1)==1 && CONSTRAIN(kk,2)==5)
        loc2=ID(CONSTRAIN(kk,11),:);
        K(loc1,loc2)=K(loc1,loc2) +constr_pt(CONSTRAIN(kk,:),s,1);
        loc2=ID(CONSTRAIN(kk,12),:);
        K(loc1,loc2)=K(loc1,loc2) +constr_pt(CONSTRAIN(kk,:),s,2);
    end

% Assemble K matrix for each subsytem connected to that node
    for jj=1:XX(kk),
        num=CON(jj,kk); % Looking at subsystem num
        num_str=num2str(num);   % string version for subsytem num

        t1=Sub_Con(1,num);  % beginning node location for subsystem num
        t2=Sub_Con(2,num);  % end node location for subsystem num

        M=Mgl(1:n,(num-1)*n+1:n*num);
        N=Ngl(1:n,(num-1)*n+1:n*num);

        x=X(kk,num);

        E=[Ei 0;0 -Ei];
```

```
        R=eval(['R',num_str,num2str(x+1)]);
        S=eval(['S',num_str,num2str(x+1)]);

        Kap=Kappa(1:dof,jj);
        L=Len(num);

        fptw=FPTw(1,num);

        fpt_wpos=FPTwPos(1,num);

    % These are damping values that can be used to incorporate
structura damping.
        %t_alpha=2.5;
        %t_beta=8e-4;

% This is the fundamental matrix for a structurally damped Euler-
Bernoulli beam.
        FEB=L*[  0              1   0   0;
                 0              0   1   0;
                 0              0   0   1;
    -rho*s*(s+t_alpha)/(Ei*(1+t_beta*s))    0   0   0];
% This is the fundamental matrix for a structurally damped shear beam.
        FShear1=L*[  0              1   0   0;
                 0              0   1   0;
                 0              0   0   1;
    -rho*s*(s+t_alpha)/(Ei*(1+t_beta*s))    0
((rho*s^2)/(kappag*A*Gsh)+(c*s)/(kappag*A*Gsh))-Tens/Ei 0];
% These are hysteretically damped coefficient entries.
 zetag=0.2;
 wn=5*2*3.14;
 alphag=5;
 gammag=2*alphag*zetag*wn;
 betathg=2*zetag*wn;
 deltathg=wn^2;
 % Selection of hysteretic damping model; must match freq_resp.m file.
Gofs=0;
%Gofs=(alphag*s^2+gammag*s)/(s^2+betathg*s+deltathg);
%Gofs=(25*s^2+9000*s)/(4*s^2+1*s-8000); % For 1X7
%Gofs=(70*s^2+6000*s)/(5*s^2+2*s+2000);  % For 1X19
%Gofs=(180*s^2+40000*s)/(2*s^2+2*s-9000);  % For 1X48
%Gofs=(140*s^2+60000*s)/(2*s^2+2*s-15000);  % For 7X7

%Remember that "rho" means rho*A!
% This is the fundamental matrix for a viscously damped shear beam.
FShearVD=L*[0,1,0,0;0,0,1,0;0,0,0,1;-
(rho*s^2+cv*s)/Ei,0,((rho*s^2)/(kappag*A*Gsh)+(cv*s)/(kappag*A*Gsh))-
Tens/Ei,0];
% This is the fundamental matrix for a hysteretically damped shear
beam.
FShearHyst=L*[0,1,0,0;0,0,1,0;0,0,0,1;-(rho*s^2+cv*s)/(Ei-
(1/s)*Gofs),0,((rho*Ei*s^2)/(kappag*A*Gsh)+(cv*Ei*s)/(kappag*A*Gsh)-
Tens)/(Ei-(1/s)*Gofs),0];

% Set F equal to the fundamental matrix you would like to use.
        F=FShearHyst;
```

```
        eFs=expm(F);
        H=expm(F*x)*inv(M+N*eFs);

        He0=H(n1+n2/2+1:n,1:n/2);
        He1=H(n1+n2/2+1:n,n/2+1:n);

% Evaluate subsystem K matrices at each node
        % NOTE: used if statements to check if this subsystem
        %       has some sort of BC imposed on it. If there
        %       is then need to find how it adds to the global
        %       force vector as well to the global stiffness
        %       matrix

        if (BC_node_ty(Sub_Con(1,num))>0),
            loc2=ID(t2,:);
            K(loc1,loc2)=K(loc1,loc2)+R*E*He1*S;
            q(loc1) = q(loc1) - R*E*He0*S*Kap;
        elseif (BC_node_ty(Sub_Con(2,num))>0),
            loc2=ID(t1,:);
            K(loc1,loc2)=K(loc1,loc2)+R*E*He1*S;
            q(loc1) = q(loc1) - R*E*He0*S*Kap;
        else
            loc2_1=ID(t1,:);
            loc2_2=ID(t2,:);
            K(loc1,loc2_1)=K(loc1,loc2_1)+R*E*He0*S;
            K(loc1,loc2_2)=K(loc1,loc2_2)+R*E*He1*S;
        end

        %   Evaluate q vector for each node from point forces

        if fpt_wpos>x
            Gw=-H*N*expm(F*(1-fpt_wpos));
        else
            Gw=H*M*expm(-F*fpt_wpos);
        end
        Ge_w=Gw(n2/2+1:n,n);
        q(loc1) = q(loc1) - R*E*Ge_w*fptw;

    end
end
Kgl=K(1:pts-can,1:pts-can); % Global stiffness matrix
qgl=q(1:pts-can,1);
detans=det(Kgl); % To check determinant if using a single s input.
```

Cable Constraint Point Program

```
% Function to determine constraint matrix; modified to include
rotational
% damping and stiffness.
% function Cl=constraints(CONSTR,s,tmp)
%
%   CONSTR(1)       0=no constraint, 1=constraint,2=active constraint
%   CONSTR(2)       type of constraint (See below)
%   CONSTR(3)       mass of rigid body
%   CONSTR(4)       stiffness of spring
%   CONSTR(5)       damping of dashpot
%   CONSTR(6)       linear spring in axial direction
%   CONSTR(7)       linear spring in transverse direction
%   CONSTR(8)       linear rotational spring
%   CONSTR(9)       Moment of Inertia for Rigid Body
%   CONSTR(10)      Distance of isolator from cg on Rigid Body
%   CONSTR(11)      node number of connection
%   CONSTR(12)      node number of connection
%
%   NOTE: CONSTR(11,12) are used only for connection between subsystems
%       (as for cabled beam)
%
%   type=1      simple spring, mass, damper connected at 1 point
%   type=2      point mass, no inertia
%   type=3      point mass with inertia
%   type=4      two actuators (spring-damper) connected to lumped
system
%   type=5      spring and/or damper between two continous systems
%
% tmp is 1 or 2. If it is 1 then constraint is at node
% if it is 2 the constraint force is due to attachment
% at other node.

function CL=constr_pt(CONSTR,s,tmp)

global dof;

CL=zeros(dof);
type=CONSTR(2);
m=CONSTR(3);
k=CONSTR(4);
d=CONSTR(5);
x_=CONSTR(6);
y_=CONSTR(7);
rot_=CONSTR(8);
Ir=CONSTR(9);
ax=CONSTR(10);

krots=2; % Rotational connection stiffness
crots=0; % Rotational connection damping
Ibar=1*10^12;

if type==1
    if CONSTR(1)==1,
        Cy=m*s^2*(d*s+k)/(m*s^2+d*s+k);
```

```
    elseif CONSTR(1)==2,
        Cy=(m*s^2+d*s)*k/(m*s^2+d*s+k);
    end
elseif type==2
    Cx=m*s^2;
    Cy=Cx;
elseif type==3
    Cx=m*s^2;
    Cy=Cx;
    Crot=Ir*s^2;
elseif type==4
    num1=k+d*s;
    den1=Ir*s^2 + 2*ax^2*d*s  + 2*ax^2*k;
    den2=m*s^2+2*d*s+2*k;
    if tmp==1
        Cy = num1 - num1^2*ax^2/den1 - num1^2/den2;
    elseif tmp==2
        Cy = num1^2*ax^2/den1 - num1^2/den2;
    else
        disp('Unknown value for tmp-(1)')
    end
elseif type==5
    if tmp==1
        Cy=k+d*s;
    elseif tmp==2
        Cy=-k-d*s;
    else
        disp('Unknown value for tmp-(2)')
    end
end

if y_==1
    CL(2,1)=Cy;
end
if rot_==1
    %CL(1,2)=Crot;
    % This would be added in for a rotational spring and damper.
    CL(1,2)=(Ibar*s^2*(crots*s+krots))/(Ibar*s^2+crots*s+krots);
end
```

Cable Force Input

```
% This is the force input file for the two-point cable.
if COUNT==0
    for iii=1:m,
        if ((BC_type(iii)==1) | (BC_type(iii)==0)),
            eval(['Kap',num2str(iii),'=zeros(dof,1);'])
        end
    end
    % Must have as many Kappa entries as subsystems (i.e., 14 subsystem
    % model needs Kap1 through Kap14.
    Kap1=[0;0];
    Kap2=[0;0];
    Kap3=[0;0];
    Kap4=[0;0];
    Kap5=[0;0];
    Kap6=[0;0];
    Kap7=[0;0];
    % This puts all values of Kap for each subsystem into global
    % matrix called Kappa
    Kappa=[];
    for iii=1:m,
        eval(['Kappa= [Kappa Kap',num2str(iii),'];'])
    end

% These are the pointwise forces and are functions of frequency in Hz
% In this case they are function of the parameter s=frequency

% Note that the only non-zero input force occurs at the driving point;
% for the two-point fixture, input force is on subsystem two.
% For the four-point fixture, input force is on subsystem three.

    fptw_1=0/Ei*Len(1); % magnitude of pointwise force on subsystem
    fpt1_wpos=.9;       % position of pointwise on subsystem

    fptw_2=100/Ei*Len(2);  % USE THIS FOR TWO POINT CABLE
    %fptw_2=0/Ei*Len(2);    % USE THIS FOR FOUR POINT CABLE
    fpt2_wpos=0.999;        % position of pointwise on subsystem

    fptw_3=0/Ei*Len(3);     % USE THIS FOR TWO POINT CABLE
    %fptw_3=700/Ei*Len(3); % USE THIS FOR FOUR POINT CABLE
    fpt3_wpos=0.999;        % position of pointwise on subsystem

    fptw_4=0/Ei*Len(4); % magnitude of pointwise force on subsystem
    fpt4_wpos=.9;       % position of pointwise on subsystem

% Uncomment forces for subsystems 5 and 6 if four-point cable is being
evaluated
%     fptw_5=0/Ei*Len(5);   % magnitude of pointwise force on subsystem
%   fpt5_wpos=.0001;        % position of pointwise on subsystem
%
%     fptw_6=0/Ei*Len(6);   % magnitude of pointwise force on subsystem
%   fpt6_wpos=.9;       % position of pointwise on subsystem

    FPTw=[];
    FPTwPos=[];
```

```
    for iii=1:m,
        eval(['FPTw=[FPTw fptw_',num2str(iii),'];'])
        eval(['FPTwPos=[FPTwPos fpt',num2str(iii),'_wpos];'])
    end
    %These are the nodal forces and are functions of frequency in Hz
% Must have as many P vectors as subsystems.
    P1=[0;0];
    P2=[0;0];
    P3=[0;0];
    P4=[0;0];
    P5=[0;0];
    P6=[0;0];
    P7=[0;0];
    % This puts all nodal forces into a global matrix called P_Nodal
    P_Nodal=[];
    for iii=1:node
        eval(['P_Nodal= [P_Nodal P',num2str(iii),'];'])
    end
    F_cstr=[0;0];
    COUNT=COUNT+1;
end
```

Cable Frequency Response Program

```
% This file determines frequency response functions (FRFs) for cable
and
% cabled beam models.
%
% INPUT:
%   BND_DOF Shows which DOF are constrained (node x dof)
%
% OUTPUT:
%   alpha1  values for local displacement at position x over frequency
range
%
%   alpha       local displacement vector at position x and frequency s
%   CON         Shows which subsystems are connected to which
%               nodes. '0' means no subsystem
%   cnt     dummy counting variable
%   dof     the number of degrees of freedom of subsystem
%   endvalue    the number of subsystems at location of response
%   F       matrix built by governing pdes (n x n)
%   filename    the name of file that holds initialization data
%   fptu        point force at subsystem in axial direction
%   fptu_pos    location of point force at subsystem in axial direction
%   fptw        point force at subsystem in transverse direction
%   fptw_pos    location of point force at subsystem in axial direction
%   freqend the end frequency for frequency response
%   freqst  the start frequency for frequency response
%   G       Greens' function
%   Ga_u        partioned G matrix
%   Ga_w        partioned G matrix
%   H       transfer function of Eta/Gamma
%   Ha0     partitioned H matrix
%   Ha1     partitioned H matrix
%   incr        the incremental frequency for frequency response
%   jj      dummy counting variable
%   K       reduced global stiffness matrix at frequency s
%   Kap     vector used for BC calculation
%   kk      dummy counting variable
%               also current subsystem for response
%   Len     length of each subsystems in vector
%   Li      length of each subsystem
%   M       Temporal-spatial operator for left end of subsystem
%   N       Temporal-spatial operator for right end of subsystem
%   node        total number of nodes of system
%   num_str string of current subsystem for response
%   pts     the number of displacements of entire system
%   q       reduced global force vector at frequency s
%   R0      Rotation Matrix at the left end of the subsystem for Forces
%   R1      Rotation Matrix at the right end of the subsystem for
Forces
%   rho     mass per unit length for a subsystem
%   S0      Rotation Matrix for left end of subsystem for displacements
%   S1      Rotation Matrix for right end of subsystem for
displacements
%   s       frequency = ii * sqrt(-1) * 2 * pi
%   Sub_Con Shows which subsystems are connected to which nodes (2 x m)
%               A zero value implies somer sort of boundary condition
```

```
%   sub     subsystem for which response is taken
%   tt      dummy counting variable
%   Ugl     global displacement vector at frequency s
%   Ugl_0       global displacement vector at right end for current
subsystem
%   Ugl_1       global displacement vector at left end for current
subsystem
%   u       reduced global displacement vector at frequency s
%   X       location of node points in local coordinates
%   XX      Shows at each node how many subsystems are connected to it.
%   x       position of response
%   which_node  if response is required at a node it gives node number
%
function [omega,alpha1]=freq_resp(BND_DOF,type)

global node m dof n1 n2 n can XX CON ID Sub_Con qgl Rot BC_type;
global Len XY Ea Ei rho filename num_ev BC_node_ty AXIAL pts X;
global A kappag Gsh cv c Tens;
global CONSTRAIN Mgl Ngl Kappa P_Nodal F_cstr FPTw FPTwPos;
global COUNT evals t_alpha t_beta;

% Choose subsystem of output response.
sub=2;  % USE THIS FOR TWO POINT CABLE.
%sub=3;  % USE THIS FOR FOUR POINT CABLE.
x=1;        % Local coordinate on subsystem sub
x1=x;

%NOTE: This assumes that the pointwise forces or nodal forces are
harmonic

% The following are the locations of node points connected
% to each subsystem. The start point of each subsystem is 0 and the
% endpoint is 1.
X = zeros(node,m);

tmp1=[0;1];
for ii=1:m,
    tmp2=Sub_Con(:,ii);
    X([tmp2],ii)=X([tmp2],ii)+tmp1;
end

% This checks whether the measured response is at a node and therefore
% needs to have the neighboring subsystems evaluated.
if (x==0) || (x==1)
    which_node=Sub_Con(x+1,sub);    % node number of measured response
end

% Find M and N for each subsystem
    M=Mgl(1:n,(sub-1)*n+1:n*sub);
    N=Ngl(1:n,(sub-1)*n+1:n*sub);

    [R0,R1,S0,S1]=Rotation_Calc(Rot(sub));
    Li=Len(sub);

omega=logspace(0,3,750); % Choose span and density of FRF points.
```

```
% Choose input forces for appropriate model.
% For two-point model:
filenameforce=['C:\Users\Kaitlin\Desktop\Pinned Cables Feb 2014\Cable
2Pinned Model\forces_bmcable.m'];
% For four-point model:
%filenameforce=['C:\Users\Kaitlin\Desktop\Cable Data In Process\Test 2
%Data\Cable 4Pt Model\forces_bmcable.m'];
run(filenameforce);

alpha1=zeros(dof,size(omega,2));

for iji=1:size(omega,2),
    ii=omega(iji);

    s=ii*i*2*pi;

    [K,q]=assemble_K(ii);
    u=inv(K)*q;
    % Place reduced global position and forces at specific frequeny
    %       into actual global position and force vector
    Ugl=zeros(1,pts);

    cnt=1;
    for jj=1:node,
        for kk=1:dof,
            if (BND_DOF(jj,kk) < 1)
            eval(['Ugl(1,dof*(jj-1)+kk)=u(',num2str(cnt),');'])
                cnt=cnt+1;
            end
        end
    end

    alpha=zeros(dof,1);
% FRF calculations begin
    num_str=num2str(sub);
    tmp1=dof*(Sub_Con(1,sub)-1)+1;
    tmp2=dof*(Sub_Con(2,sub)-1)+1;

    % Find the global displacements at each node at x=0,1 for subsystem
    Ugl_0=Ugl(tmp1:tmp1+dof-1);
    Ugl_1=Ugl(tmp2:tmp2+dof-1);

    fptw=FPTw(1,sub);

    fpt_wpos=FPTwPos(1,sub);

    Kap=Kappa(1:dof,sub);

    if (x==0) || (x==1)
        x1=X(which_node,sub);
    end

        t_alpha=0;  % Structural damping values can be included here.
        t_beta=0;
```

```
        FEB=Li*[     0              1   0   0;
                0              0   1   0;
                0              0   0   1;
    -rho*s*(s+t_alpha)/(Ei*(1+t_beta*s))    0   0   0];

        FShear1=Li*[     0              1   0   0;
                0              0   1   0;
                0              0   0   1;
    -rho*s*(s+t_alpha)/(Ei*(1+t_beta*s))    0
((rho*s^2)/(kappag*A*Gsh)+(c*s)/(kappag*A*Gsh))-Tens/Ei 0];

zetag=0.2;
 wn=5*2*3.14;
 alphag=5;
 gammag=2*alphag*zetag*wn;
 betathg=2*zetag*wn;
 deltathg=wn^2;
Gofs=0;
%Gofs=(alphag*s^2+gammag*s)/(s^2+betathg*s+deltathg);

%Gofs=(25*s^2+9000*s)/(4*s^2+1*s-8000); % For 1X7
%Gofs=(70*s^2+6000*s)/(5*s^2+2*s+2000);  % For 1X19
%Gofs=(180*s^2+40000*s)/(2*s^2+2*s-9000);  % For 1X48
%Gofs=(140*s^2+60000*s)/(2*s^2+2*s-15000);  % Adjust For 7X7

%Remember that "rho" actually represents rho*A for these equations!
FShearVD=Li*[0,1,0,0;0,0,1,0;0,0,0,1;-
(rho*s^2+cv*s)/Ei,0,((rho*s^2)/(kappag*A*Gsh)+(cv*s)/(kappag*A*Gsh))-
Tens/Ei,0];
FShearHyst=Li*[0,1,0,0;0,0,1,0;0,0,0,1;-(rho*s^2+cv*s)/(Ei-
(1/s)*Gofs),0,((rho*Ei*s^2)/(kappag*A*Gsh)+(cv*Ei*s)/(kappag*A*Gsh)-
Tens)/(Ei-(1/s)*Gofs),0];

% CHOOSE MODEL FORMULATION
    F=FShearHyst;
    eFs=expm(F);
    %       Find alpha due to displacements
    H=expm(F*x1)*inv(M+N*eFs);

    Ha0=H(1:n2/2,1:n/2);
    Ha1=H(1:n2/2,n/2+1:n);

    if (BC_node_ty(Sub_Con(1,sub))>0),
        alpha=alpha+Ha0*Kap+Ha1*S1*Ugl_1';
    elseif (BC_node_ty(Sub_Con(2,sub))>0),
        alpha=alpha+Ha0*Kap+Ha1*S0*Ugl_0';
    else
        alpha=alpha+Ha0*S0*Ugl_0'+Ha1*S1*Ugl_1';
    end

    %       Find alpha due to pointwise forces
    if abs(fptw) >= 0
        if fpt_wpos>=x1
            Gw=-H*N*expm(F*(1-fpt_wpos));
```

```
        else
            Gw=H*M*expm(-F*fpt_wpos);
        end
        Ga_w=Gw(1:n2/2,n);
        alpha = alpha + Ga_w*fptw;
    end

    type1=CONSTRAIN(which_node,2);
    p_or_a=CONSTRAIN(which_node,1);

    if type1==0
        alpha1(1:dof,iji)=alpha;
    else
        m_cstr=CONSTRAIN(which_node,3);
        kp=CONSTRAIN(which_node,4);
        dp=CONSTRAIN(which_node,5);

        if p_or_a==1
            if type1<4
                num=dp*s+kp;
                den=m_cstr*s^2+num;

                alpha1(1:dof,iji)=(F_cstr+num*alpha)/den;
            elseif type1==4
            end
        elseif p_or_a==2
            ka=CONSTRAIN(which_node,6);
            da=CONSTRAIN(which_node,7);
            gn=CONSTRAIN(which_node,8);
            nmode=CONSTRAIN(which_node,12);

            if type1==1,
                den=m_cstr*s^2+(da+dp)*s+ka+kp+gn/s;
                alpha1(1:dof,iji)=(F_cstr+(kp+dp*s)*alpha)/den;
            elseif type1==2,
                den=m_cstr*s^2+dp*s+kp;
                alpha1(1:dof,iji)=(F_cstr+(kp+dp*s+ka+da*s)*alpha)/den;
            elseif type1==3
                ev=evals(nmode)*2*pi;
                den=m_cstr*s^2+dp*s+kp;
                denppf=s^2+2*da*ka*s+ka^2;
                den2=den+gn*ka^2*ev^2/denppf;
                alpha1(1:dof,iji)=(F_cstr + (kp+dp*s)*alpha)/den2;
            end
        end
    end
end
```

Cable Mode Shape Program

```
% This file evaluates the mode shapes for the calculated eigenvalues,
and
% creates mode shape vectors for use in the modal assurance criterion
% comparison.

function mode_shapeWMAC(BND_DOF)

global node m dof n1 n2 n can XX CON ID Sub_Con qgl Rot BC_type Len XY
Ea Ei rho;
global A kappag Gsh cv c Tens;
global filename BC_node_ty num_ev len_m t_alpha t_beta;
global AddedModes

% Calculated eigenvalues must be loaded to use for mode shape
calculation.
%filename
%eval(['load evalues_',filename])
% Use this for TWO-POINT cable
load('C:\Users\Kaitlin\Desktop\Pinned Cables Feb 2014\Cable 2Pinned
Model\evalues_bmcabletest.mat');
% Use this for FOUR-POINT cable
% load('C:\Users\Kaitlin\Desktop\Cable Data In Process\Test 2
Data\Cable 4Pt Model\evalues_bmcabletest.mat');

pts=node*dof;
AddedModes=[];
%   Redefine K_eval Matrices to Ki matrices for each mode where i
ranges
%   from 1 to num_ev
for ii=1:num_ev,
    b=pts-can;
    c=b*(ii-1)+1;
    eval(['K',num2str(ii),'=K_eval(1:b,c:c+b-1);'])
end

%   This finds the nontrivial solutionn of K(jlam)u(jlam)=0
for ii=1:num_ev,
    eval(['u',num2str(ii),'=null(K',num2str(ii),');'])
   if isempty(eval(['u',num2str(ii)]))
        eval(['[a1,b1]=eig(K',num2str(ii),');'])
        c=min(abs(diag(b1)));
        d=find(c==abs(diag(b1)));
        if size(d,1) > 1;
            d=d(1);
            a1=a1(:,d);
            eval(['u',num2str(ii),'=a1(1:b,1);'])
        else
            eval(['u',num2str(ii),'=a1(1:b,d);'])
        end
   end
end

% Calculate displacements (i.e. mode shapes for each eigenvalue)
incr=.001;
```

```
for ii=1:num_ev,
    x_pos=[];
    y_pos=[];
    Ugl=zeros(1,pts);
    cnt=1;

% Place reduced global position at specific eigenvalue into actual
global
% position vector
    for jj=1:node,
        for kk=1:dof,
            if (BND_DOF(jj,kk) < 1)
                eval(['Ugl(1,dof*(jj-
1)+kk)=u',num2str(ii),'(',num2str(cnt),');'])
                cnt=cnt+1;
            end
        end
    end

% Find mode shape for each subsystem and plot it
    for kk=1:m,
        alpha=[];

        tmp1=dof*(Sub_Con(1,kk)-1)+1;
        tmp2=dof*(Sub_Con(2,kk)-1)+1;

    % Find the global displacements at each node at x=0,1 for subsystem
        Ugl_0=Ugl(tmp1:tmp1+dof-1);
        Ugl_1=Ugl(tmp2:tmp2+dof-1);

    % Find M and N for each subsystem
        [M,N]=MN_Calc(BC_type(kk),kk,Ei,Ea);

    % This section must match the section from the assemble_K file.
        [R0,R1,S0,S1]=Rotation_Calc(Rot(kk));
        Li=Len(kk);
        s=evals(ii)*i*2*pi;

        FEB=Li*[     0              1   0   0;
                0               0   1   0;
                0               0   0   1;
    -rho*s*(s+t_alpha)/(Ei*(1+t_beta*s))    0   0   0];

        FShear1=Li*[     0              1   0   0;
                0               0   1   0;
                0               0   0   1;
    -rho*s*(s+t_alpha)/(Ei*(1+t_beta*s))    0
((rho*s^2)/(kappag*A*Gsh)+(c*s)/(kappag*A*Gsh))-Tens/Ei 0];

zetag=0.1;
 wn=56*2*3.14;
 alphag=5;
 gammag=2*alphag*zetag*wn;
 betathg=2*zetag*wn;
```

```
 deltathg=wn^2;
Gofs=0;
%Gofs=(alphag*s^2+gammag*s)/(s^2+betathg*s+deltathg);
%Gofs=(1000*s^2+161.4*s)/(s^2+10600*s+280900);
%Gofs=(9*s^2+100*s)/(s^2+10*s+1000);

%Remember that "rho" actually represents rho*A in the following
equations!

FShearVD=Li*[0,1,0,0;0,0,1,0;0,0,0,1;-
(rho*s^2+cv*s)/Ei,0,((rho*s^2)/(kappag*A*Gsh)+(cv*s)/(kappag*A*Gsh))-
Tens/Ei,0];
FShearHyst=Li*[0,1,0,0;0,0,1,0;0,0,0,1;-(rho*s^2+cv*s)/(Ei-
(1/s)*Gofs),0,((rho*Ei*s^2)/(kappag*A*Gsh)+(cv*Ei*s)/(kappag*A*Gsh)-
Tens)/(Ei-(1/s)*Gofs),0];

% SELECT WHICH F FORMULATION TO USE - IMPORTANT, CHOOSE WISELY.
        F=FShearHyst;

        eFs=expm(F);
        invers=inv(M+N*eFs);

        XI=0:incr:1;

    % Find mode shape along span of subsystem
        for xi=XI,
            H=expm(F*xi)*invers;

            Ha0=H(1:n2/2,1:n/2);
            Ha1=H(1:n2/2,n/2+1:n);

            if (BC_node_ty(Sub_Con(1,kk))>0),
                alpha=[alpha Ha1*S1*Ugl_1'];
            elseif (BC_node_ty(Sub_Con(2,kk))>0),
                alpha=[alpha Ha1*S0*Ugl_0'];
            else
                alpha=[alpha Ha0*S0*Ugl_0'+Ha1*S1*Ugl_1'];
            end
        end

    % Find mode shape in global coordinates for plotting
        x_beg=XY(1,Sub_Con(1,kk));
        y_beg=XY(2,Sub_Con(1,kk));

        trans=inv(S1)*alpha;
        cc=size(trans,2);

% Find the exact x,y locations and displacements
        Lc=Li*cos(Rot(kk));
            Y_pos=trans(1,:);
            X_pos=(x_beg:(Lc)/(cc-1):Lc+x_beg);

        if kk==1,
            x_pos=[x_pos X_pos];
```

```
            y_pos=[y_pos Y_pos];
        elseif kk>=2,
            tmp=size(X_pos,2);
            x_pos=[x_pos X_pos(2:tmp)];
            y_pos=[y_pos Y_pos(2:tmp)];
        end
    end

% Normalize the modes for better viewing and for appropriate MAC
comparison
    y_pos=y_pos/max(abs(y_pos));

    if real(y_pos(2))<0
        y_pos=-y_pos;
    end
    YYpos=[];
    YYpos=[YYpos;y_pos];
    %For two-point cable
    plot(x_pos,y_pos,XY(1,2),0,'+',XY(1,5),0,'+')
    %For four-point cable, shows connection points as +s
    %plot(x_pos,y_pos,XY(1,2:3),[0,0],'+',XY(1,5:6),[0,0],'+')
    title(['Mode',num2str(ii)])
    xlabel('Distance Along Cable')
    ylabel('Eigenfunction')

    figure
    AddedModes=[AddedModes;y_pos];
    xmodeplot=x_pos;
end
% Build "AddedModes" matrix for use in MAC calculation.
AddedModes=[xmodeplot;AddedModes];
%To evaluate mode interaction for MAC comparison (mode 1 and 3 for
example):
% plot(x_pos,AddedModes(2,:)+AddedModes(4,:))
% title('Mode 1 & 3')
% This line saves the mode shape vectors.
%eval(['save modes_',filename,' evals x_pos YYpos'])
```

Cabled Beam Model Input File

```
% This file provides cable and beam inputs for the 16 node cabled-beam
model.
% Modified with input parameters on 3/28/2014.
% Altered for stiffer cabled beam EI values 4/11/2014.

% Parameters for aluminum beam as host structure:
w=0.101; % width, in meters, of beam
t=0.0064; % thickness, in meters, of beam

Ibeam=1/12*w*t^3;
Ebeam=65E9;
EIbeam=Ebeam*Ibeam;
Abeam=w*t;
rhobeam=2700;

len_beam=0.797;
len_m=0.797;

% Parameters for cable, rod, or no attached structure:
%_____________________________________________________________
% SELECT CABLE TYPE HERE:
cablechoice=0;
% Choose 7,19,48,749 for cables,
% Choose 1,2,3 for Acetron, spring steel, tool steel
% Choose 0 for bare beam.
calcopt=10;
% Choose 1 for min, 5 for max, 3 for mid/avg, 8 for stickmin
% Choose 2 for min with new vals, chose 6 for max with new vals
% Choose 10 for bare beam or rods on beam
%_____________________________________________________________
 if cablechoice==7;
    disp('1X7 Chosen')
    len_cable=0.7692;
    MinDensity=2117.12;
    DensityMid=3110.59;
    MaxDensity=3233.14;
    MinArea=2.76803*10^-5; % Calculated based on only wire components
    MaxArea=4.34512*10^-5; % Calculated based on OUTER cable diameter
    AreaMid=2.95737*10^-5; % Calcuated based on individual wire
diameter

    EIcablestickmin=1.65;
    EIcablestickmax=1.868;
    EIcable4ptslipmin=0.40;
    EIcable4ptslipmax=0.438;

    EIcablebslipmin=0.46;
    EIcablebslipmax=0.51;

    spr_p=1e4;

 elseif cablechoice==19;
    disp('1X19 Chosen')
    len_cable=0.7782;
```

```
    MinDensity=1926.46;
    DensityExp=2162;
    DensityExp2=2557;
    DensityMid=3049;
    MaxDensity=3258;
    MinArea=7.51321*10^-5; % Calculated based on only wire components
    MaxArea=1.27076*10^-4; % Calculated based on OUTER cable diameter
    AreaMid=8.02715*10^-5; % Calcuated based on individual wire
diameter

    EIcablestickmin=13.818;
    EIcablestickmax=15.71687;
    EIcable4ptslipmin=1.55;
    EIcable4ptslipmax=1.7128;

    EIcablebslipmin=1.94;
    EIcablebslipmax=2.16;

    spr_p=6e4;

 elseif cablechoice==48;
    disp('1X48 Chosen')
    len_cable=0.7744;
    MinDensity=1770.5;
    DensityMid=2853.7;
    MaxDensity=3048.9;
    MinArea=1.89807*10^-4; % Calculated based on only wire components
    MaxArea=3.26851*10^-4; % Calculated based on OUTER cable diameter
    AreaMid=2.02791*10^-4; % Calcuated based on individual wire
diameter

    EIcablestickmin=93.6;
    EIcablestickmax=106.7;
    EIcable4ptslipmin=7.517;
    EIcable4ptslipmax=8.1343;

    EIcablebslipmin=16.82;
    EIcablebslipmax=18.25;

    spr_p=1e6;

 elseif cablechoice==749;
    disp('7X7 Chosen')
    len_cable=0.7744;
    MinDensity=1742.326;
    DensityMid=3084.06;
    MaxDensity=3295.025;
    MinArea=1.93762*10^-4; % Calculated based on only wire components
    MaxArea=3.66435*10^-4; % Calculated based on OUTER cable diameter
    AreaMid=2.07016*10^-4; % Calcuated based on individual wire
diameter

    EIcablestickmin=74.047;
    EIcablestickmax=84.38;
    EIcable4ptslipmin=2.596;
```

```
    EIcable4ptslipmax=2.82;

    EIcablebslipmin=3.48;
    EIcablebslipmax=3.83;

    spr_p=6e5;

 elseif cablechoice==0; % This is for bare beam tests...
    rhocable=0.000001;
    Acable=0.00001;
    EIcable=0.0001;
    len_cable=0.780;
    spr_p=1e5;
elseif cablechoice==1; % This is for Acetron rod
    disp('Acetron rod chosen')
    rhocable=1410;
    Acable=1.2728e-4;
    EIcable=3.8028;
    len_cable=0.780;
    spr_p=1.3e6;
    %spr_p=1e5;
elseif cablechoice==2; % This is for spring steel rod
    disp('Spring steel rod chosen')
    rhocable=7990;
    Acable=4.9017e-5;
    EIcable=36.9008;
    len_cable=0.780;
    spr_p=1.3e6;
elseif cablechoice==3; % This is for spring steel rod
    disp('Spring steel rod chosen')
    rhocable=7750;
    Acable=1.2668e-4;
    EIcable=242.6266;
    len_cable=0.782;
    spr_p=1.3e6;
 else
    disp('Invalid cable or attachment choice')
 end
 % SELECTABLE OPTIONS
 if calcopt==1
    Acable=MaxArea
    rhocable=MaxDensity
    EIcable=EIcable4ptslipmin
 elseif calcopt==5;
     Acable=MinArea
     rhocable=MinDensity
     EIcable=EIcable4ptslipmax
 elseif calcopt==3;
     Acable=AreaMid
     rhocable=DensityMid
     EIcable=(EIcable4ptslipmin+EIcable4ptslipmax)/2
 elseif calcopt==8;
     Acable=AreaMid
     rhocable=DensityMid
     EIcable=EIcablestickmin
 elseif calcopt==2;
```

```
    Acable=MaxArea
    rhocable=MaxDensity
    EIcable=EIcablebslipmin
 elseif calcopt==6;
    Acable=MinArea
    rhocable=MinDensity
    EIcable=EIcablebslipmax
 end

       rhoacable=rhocable*Acable;% In case...
kappag=0.95;
Gsh=651743193.3;
cv=0;
Tens=0;

num_ev=8;

% This is connection stiffness info for any damping in connection
stiffness
% Note that spr_p is located within the cable values.
% spr_p=1e5; %ATTACHMENT STIFFNESS OVERRIDE
damp_p=0;
zeta_p=0.0;

if cablechoice~=0;
CONSTRAIN(2,:)=[1 5 0 spr_p damp_p 0 1 1 0 0 2 10];
CONSTRAIN(10,:)=[1 5 0 spr_p damp_p 0 1 1 0 0 10 2];

CONSTRAIN(3,:)=[1 5 0 spr_p damp_p 0 1 1 0 0 3 11];
CONSTRAIN(11,:)=[1 5 0 spr_p damp_p 0 1 1 0 0 11 3];

CONSTRAIN(5,:)=[1 5 0 spr_p damp_p 0 1 1 0 0 5 13];
CONSTRAIN(13,:)=[1 5 0 spr_p damp_p 0 1 1 0 0 13 5];

CONSTRAIN(6,:)=[1 5 0 spr_p damp_p 0 1 1 0 0 6 14];
CONSTRAIN(14,:)=[1 5 0 spr_p damp_p 0 1 1 0 0 14 6];

CONSTRAIN(7,:)=[1 5 0 spr_p damp_p 0 1 1 0 0 7 15];
CONSTRAIN(15,:)=[1 5 0 spr_p damp_p 0 1 1 0 0 15 7];
end

% Three is pinned, two is free
BC_type=[2 0 0 0 0 0 2 2 0 0 0 0 0 2];          % type of boundary
condtion for each subsystem
BC_node_ty=[2 0 0 0 0 0 0 2 2 0 0 0 0 0 0 2];

m=14;                   % the number of subsystems
node=16;                % the number of nodes
%can=7;             % the number of known boundary displacements
can=8;
dof=2;              % the number of dof: ux, wy, w'

xb=len_beam/2;
xe=len_cable/2;
```

```
rhogl=zeros(1,m);
EIgl=zeros(1,m);
rhogl(1,1:(m/2))=rhobeam*Abeam*ones(1,m/2);
rhogl(1,(m/2)+1:m)=rhocable*Acable*ones(1,m/2);
EIgl(1,1:(m/2))=Ebeam*Ibeam*ones(1,m/2);
EIgl(1,(m/2)+1:m)=EIcable*ones(1,m/2);

 XY = [0  0.04 0.22 0.299 0.4 0.58 0.76 len_beam (len_beam-len_cable)/2
0.04 0.22 0.299 0.4 0.58 0.76 len_cable+(len_beam-len_cable)/2     %X
% X,Y position of each node, 2 X node
    0 0 0 0 0 0 0 0 .015 .015 .015 .015 .015 .015 .015 .015 ];
%Y      % This is actual x,y not nondimensional

CON=[1 1 2 3 4 5 6 7 8 8 9 10 11 12 13 14;
     0 2 3 4 5 6 7 0 0 9 10 11 12 13 14 0];     % which subsystems are
connected at each node

Sub_Con=[1 2 3 4 5 6 7 9 10 11 12 13 14 15;         % Shows how each
subsytem is connected to each
         2 3 4 5 6 7 8 10 11 12 13 14 15 16];           %   node    (2
x m). top row is x=0 position of subsystem

XX=[0 2 2 2 2 2 2 0 0 2 2 2 2 2 2 0];           % the number of
subsystems connected at each node
                  %   0 signifies that there is not a connection
                  %   between 2 different subsystems. 1 signifies
                  %   some sort of interface condition (1 x node)

BND_DOF=[   1 1;        % Shows which DOF are constrained (node x dof)
        0 0;        % dof = [wx  wy  theta]
        0 0;
        0 0;
        0 0;
        0 0;
        0 0;
        1 1;
        1 1;
        0 0;
        0 0;
        0 0;
        0 0;
        0 0;
        0 0;
        0 0;
        1 1];
```

Cabled Beam Stiffness Matrix Assembly Program

```
% This file builds the global stiffness matrix for a 16 node cabled
beam.
% Sections 1-7 are beam, sections 8-14 are cable.
% Created on 1/9/2014 Modified 3/15/2014
% INPUT
%   ij      frequency in Hz
%
% OUTPUT
%   Kgl     Reduced Global Stiffness Matrix
%   qgl     Reduced Global Force Vector
%

% P-LIST
%   BC_node_ty  The type of boundary conditions for each node
%   can     the number of known boundary displacements
%   CON         Shows which subsystems are connected to which
%               nodes. '0' means no subsystem
%   CONSTRAIN   Shows how each node is constrained.
%   dof     the number of degrees of freedom of subsystem
%   E       compatibility matrix for subsystem
%   Ea      E*A (Axial Stiffness) for a subsytem
%   Ei      E*I (Flexural Rigidity) for a subsystem
%   evals       Vector of eigenvalues
%   F       matrix built by governing pdes (n x n)
%   F_cstr      Force on system.
%   filename    the name of file that holds initialization data
%   fptu        point force at subsystem in axial direction
%   fptu_pos    location of point force at subsystem in axial direction
%   fptw        point force at subsystem in transverse direction
%   fptw_pos        location of point force at subsystem in axial
direction
%   Gu      Greens' function for axial displacement
%   Ge_u        partioned G matrix
%   Ge_w        partioned G matrix
%   Gw      Green's function for transverse displacement
%   H       transfer function of Eta/Gamma
%   He0     partitioned H matrix
%   He1     partitioned H matrix
%   ii      dummy variable
%   ID      matrix used to assemble Kgl so that nodes with constraints
%               will be removed from K (full blown Stiffness Matrix)
%   jj      dummy variable
%   K       global stiffness matrix (n x n)
%   Kappa       vector used for BC calculation
%   kk      dummy variable
%   Len     length of each subsystems in vector
%   Li      length of each subsystem
%   M       Temporal-spatial operator for left end of subsystem
%   Mgl     Global M for each subsystem
%   m       the total number of subsystems
%   N       Temporal-spatial operator for right end of subsystem
%   Ngl     Global N for each subsystem
%   n       nth order linear pde (4:bendng, 2:axial)
%   node        total number of nodes of system
%   num     current subsystem
```

```
%   num_str current subsystem but of type string
%   n1      nth order linear pde for axial vibrations
%   n2      nth order linear pde for bending vibrations
%   P       nodal forces
%   P_nodal     nodal forces
%   pts     the number of displacements of entire system
%   q       global Force vector (n x 1)
%   qgl     Reduced Global Force Vector
%   Rot     Rotation vector of 'rot' values
%   rho     mass per unit length for a subsystem
%   rot     rotation of subsystem wrt horizontal
%   Sub_Con     Shows which subsystems are connected to which nodes (2
x m)
%               A zero value implies some sort of boundary condition
%   t_alpha     Alpha (i.e mass) term for proportional Damping
%   t_beta      Beta (i.e. stiffness) term for proportional damping
%   tmp,tmpi    dummy variables (i=1,2)
%   var     used to convert degrees to radians
%   s       frequency = ij * sqrt(-1)
%   t1      beginning node location for subsystem
%   t2      end node location for subsystem
%   X       location of node points in local coordinates
%   XX      Shows at each node how many subsystems are connected to it.
%

function [Kgl,qgl]=assemble_K_fbfe_diffbeams14(ij)
% ij=10; %Used for checking a single frequency value.

global node m dof n1 n2 n can XX CON ID Sub_Con qgl Rot BC_type pts;
global Len Ea Ei rho filename BC_node_ty CONSTRAIN CONSTR_SUB_PT X;
global Mgl Ngl Kappa P_Nodal F_cstr FPTw FPTwPos;
global COUNT evals t_alpha t_beta EIgl rhogl;
global cv Acable Gsh kappag Tens;

for ii=1:m,
    tmp=num2str(ii);

eval(['[R',tmp,'1,R',tmp,'2,S',tmp,'1,S',tmp,'2]=Rotation_Calc(Rot(',tm
p,'));'])
end

% The following are the locations of node points connected
% to each subsystem. The start point of each subsystem is 0 and the
% endpoint is 1.
% This is initialized in freq_resp.m

X = zeros(node,m);
tmp1=[0;1];
for ii=1:m,
    tmp2=Sub_Con(:,ii);
    X([tmp2],ii)=X([tmp2],ii)+tmp1;
end

% Assembly of global stiffness matrix
s = 1i*ij*2*pi;         % s = jw
```

```
K=zeros(pts);           % Zero out Global Stiffness Matrix
q=zeros(pts,1);         % Zero out Global Force Vector

for kk=1:node,
    P=P_Nodal(1:dof,kk);

    loc1=ID(kk,:);

    % Add nodal forces to q vector
    q(loc1) = q(loc1) + P;

% Add constraint forces
    if (CONSTRAIN(kk,1)==1 && CONSTRAIN(kk,2)==5)
        loc2=ID(CONSTRAIN(kk,11),:);
        K(loc1,loc2)=K(loc1,loc2) + constr_pt_act(CONSTRAIN(kk,:),s,1);
        loc2=ID(CONSTRAIN(kk,12),:);
        K(loc1,loc2)=K(loc1,loc2) + constr_pt_act(CONSTRAIN(kk,:),s,2);

    elseif (CONSTRAIN(kk,1)==2 && CONSTRAIN(kk,2)<=2)
        l1=ID(CONSTRAIN(kk,11),:);
        l2=ID(CONSTRAIN(kk,12),:);
        if CONSTRAIN(kk,2)==1,
            if CONSTRAIN(kk,11)>CONSTRAIN(kk,12)
                K(loc1,l1)=K(loc1,l1) +
constr_pt_act(CONSTRAIN(kk,:),s,1);
                K(loc1,l2)=K(loc1,l2) -
constr_pt_act(CONSTRAIN(kk,:),s,0);
            else
                K(loc1,l1)=K(loc1,l1) +
constr_pt_act(CONSTRAIN(kk,:),s,0);
                K(loc1,l2)=K(loc1,l2) -
constr_pt_act(CONSTRAIN(kk,:),s,1);
            end
        elseif CONSTRAIN(kk,2)==2,
            if CONSTRAIN(kk,11)>CONSTRAIN(kk,12)
                K(loc1,l1)=K(loc1,l1) +
constr_pt_act(CONSTRAIN(kk,:),s,0);
                K(loc1,l2)=K(loc1,l2) -
constr_pt_act(CONSTRAIN(kk,:),s,1);
            else
                K(loc1,l1)=K(loc1,l1) +
constr_pt_act(CONSTRAIN(kk,:),s,1);
                K(loc1,l2)=K(loc1,l2) -
constr_pt_act(CONSTRAIN(kk,:),s,0);
            end
        end
    elseif (CONSTRAIN(kk,1)==2 && CONSTRAIN(kk,2)==3)
        l1=ID(CONSTRAIN(kk,11),:);
        l2=ID(CONSTRAIN(kk,12),:);
            if CONSTRAIN(kk,11)>CONSTRAIN(kk,12)
                K(loc1,l1)=K(loc1,l1) +
constr_pt_act(CONSTRAIN(kk,:),s,1);
                K(loc1,l2)=K(loc1,l2) -
constr_pt_act(CONSTRAIN(kk,:),s,0);
            else
```

```
                K(loc1,l1)=K(loc1,l1) +
constr_pt_act(CONSTRAIN(kk,:),s,0);
                K(loc1,l2)=K(loc1,l2) -
constr_pt_act(CONSTRAIN(kk,:),s,1);
            end
    end

    % Asemble K matrix for each subsytem connected to each node

    for jj=1:XX(kk),
        num=CON(jj,kk);     % Looking at subsystem num
        % So for this case, num = 1-7 are the beam and num= 8-14 are
        % the cable
        num_str=num2str(num);   % string version for subsytem num

        t1=Sub_Con(1,num);  % beginning node location for subsystem num
        t2=Sub_Con(2,num);  % end node location for subsystem num
    % Determine boundayr condition matrices for each subsystem
        M=Mgl(1:n,(num-1)*n+1:n*num);
        N=Ngl(1:n,(num-1)*n+1:n*num);

        x=X(kk,num);
        R=eval(['R',num_str,num2str(x+1)]);
        S=eval(['S',num_str,num2str(x+1)]);
        Kap=Kappa(1:dof,jj);
        L=Len(num);
        E=[EIgl(num) 0;0 -EIgl(num)];

        fptw=FPTw(1,num);
        fpt_wpos=FPTwPos(1,num);
% This program uses the Euler-Bernoulli formulation for the aluminum
beam,
% and the shear hysteresis model for the cable.
if num > 0 && num < 7.5;
      F=L*[     0               1   0   0;
                0               0   1   0;
                0               0   0   1;
    -rhogl(num)*s*(s+t_alpha)/(EIgl(num)*(1+t_beta*s))  0   0   0];
elseif num > 7.5 && num < 15;
    Gofs=0;
%Gofs=(25*s^2+9000*s)/(4*s^2+1*s-8000); % For 1X7
%Gofs=(70*s^2+6000*s)/(5*s^2+2*s+2000);  % For 1X19
%Gofs=(180*s^2+40000*s)/(2*s^2+2*s-9000);  % For 1X48
%Gofs=(140*s^2+60000*s)/(2*s^2+2*s-15000);  % For 7X7
    FShearHyst=L*[0,1,0,0;0,0,1,0;0,0,0,1;-
(rhogl(num)*s^2+cv*s)/(EIgl(num)-
(1/s)*Gofs),0,((rhogl(num)*EIgl(num)*s^2)/(kappag*Acable*Gsh)+(cv*EIgl(
num)*s)/(kappag*Acable*Gsh)-Tens)/(EIgl(num)-(1/s)*Gofs),0];
    F=FShearHyst;
else
    disp('F matrix not defined for subsection greater than 14')
end

        eFs=expm(F);
        H=expm(F*x)*inv(M+N*eFs);
```

```
        He0=H(n1+n2/2+1:n,1:n/2);
        He1=H(n1+n2/2+1:n,n/2+1:n);

% Evaluate subsystem K matrices at each node
    % NOTE: used if statements to check if this subsystem has some sort
of
    % BC imposed on it. If there is then need to find how it adds to
the
    % global force vector as well to the global stiffness matrix

        if (BC_node_ty(Sub_Con(1,num))>0),
            loc2=ID(t2,:);
            K(loc1,loc2)=K(loc1,loc2)+R*E*He1*S;
            q(loc1) = q(loc1) - R*E*He0*S*Kap;
        elseif (BC_node_ty(Sub_Con(2,num))>0),
            loc2=ID(t1,:);
            K(loc1,loc2)=K(loc1,loc2)+R*E*He1*S;
            q(loc1) = q(loc1) - R*E*He0*S*Kap;
        else
            loc2_1=ID(t1,:);
            loc2_2=ID(t2,:);
            K(loc1,loc2_1)=K(loc1,loc2_1)+R*E*He0*S;
            K(loc1,loc2_2)=K(loc1,loc2_2)+R*E*He1*S;
        end

        %   Evaluate q vector for each node from point forces
        if abs(fptw) >0
            if fpt_wpos>x
                Gw=-H*N*expm(F*(1-fpt_wpos));
            else
                Gw=H*M*expm(-F*fpt_wpos);
            end
            Ge_w=Gw(n2/2+1:n,n);
            q(loc1) = q(loc1) - R*E*Ge_w*fptw;
        end

    end
end
Kgl=K(1:pts-can,1:pts-can);
qgl=q(1:pts-can,1);
```

Cabled Beam Constraint Point Program

```
% This file develops the constraint matrix for the cabled beam model.
% function Cl=constraints(CONSTR,s,tmp)
%
%   CONSTR(1)       0=no constraint, 1=constraint,2=active constraint
%   CONSTR(2)       type of constraint (See below)
%   CONSTR(3)       mass of rigid body
%   CONSTR(4)       stiffness of spring
%   CONSTR(5)       damping of dashpot
%   CONSTR(6)       linear spring in axial direction
%   CONSTR(7)       linear spring in transverse direction
%   CONSTR(8)       linear rotational spring
%   CONSTR(9)       Moment of Inertia for Rigid Body
%   CONSTR(10)      Distance of isolator from cg on Rigid Body
%   CONSTR(11)      node number of connection
%   CONSTR(12)      node number of connection
%
%   NOTE: CONSTR(11,12) are used only for connection between subsystems
%
%   type=1      simple spring, mass, damper connected at 1 point
%   type=2      point mass, no inertia
%   type=3      point mass with inertia
%
% tmp is 1 or 2. If it is 1 then constraint is at node
% if it is 2 the constraint force crops up due to attachment
% at other node.

function CL=constr_pt_act(CONSTR,s,tmp)

global dof;

CL=zeros(dof);
type=CONSTR(2);
m=CONSTR(3);
k=CONSTR(4);
d=CONSTR(5);
x_=CONSTR(6);
y_=CONSTR(7);
rot_=CONSTR(8);
Ir=CONSTR(9);
ax=CONSTR(10);

%krots=20; %This makes frequencies too high
krots=2; % For cabled beam model
crots=0; % Rotational damping
Ibar=1*10^12;

if type==1
    if CONSTR(1)==1,
        Cy=m*s^2*(d*s+k)/(m*s^2+d*s+k);
    elseif CONSTR(1)==2,
        Cy=(m*s^2+d*s)*k/(m*s^2+d*s+k);
    end
elseif type==2
    Cx=m*s^2;
```

```
    Cy=Cx;
elseif type==3
    Cx=m*s^2;
    Cy=Cx;
    Crot=Ir*s^2;
else
    disp('*** WARNING: Unknown Constraint type')
end

if y_==1
    CL(2,1)=Cy;
end
if rot_==1 && type==5
    if tmp==1
    % This is added in for a rotational spring and damper.
    CL(1,2)=(crots*s+krots);
    elseif tmp==2
    CL(1,2)=-(crots*s+krots);
    else
        disp('*** WARNING: Unknown value for tmp-(rot)')
    end
end
```

Cabled Beam Force Input

```
% This is the force input file for the cabled beam model.
global node
if COUNT==0
    for iii=1:m,
        if ((BC_type(iii)==1) || (BC_type(iii)==0)),
            eval(['Kap',num2str(iii),'=zeros(dof,1)']);
        end
    end
    % Since there are 14 subsections, 14 vectors are needed.
    Kap1=[0;0];
    Kap2=[0;0];
    Kap3=[0;0];
    Kap4=[0;0];
    Kap5=[0;0];
    Kap6=[0;0];
    Kap7=[0;0];
    Kap8=[0;0];
    Kap9=[0;0];
    Kap10=[0;0];
    Kap11=[0;0];
    Kap12=[0;0];
    Kap13=[0;0];
    Kap14=[0;0];
% This puts all values of Kap for each subsystem into global matrix
Kappa
    Kappa=[];
    for iii=1:m,
        eval(['Kappa= [Kappa Kap',num2str(iii),'];']);
    end

% These are the pointwise forces and are functions of frequency in Hz
% In this case they are function of the parameter s=frequency

    fptw_1=0/EIbeam*Len(1); % magnitude of pointwise force on subsystem
    fpt1_wpos=.5;       % position of pointwise on subsystem
    fptw_2=0/EIbeam*Len(2); % magnitude of pointwise force on subsystem
    fpt2_wpos=.55;      % position of pointwise on subsystem
     fptw_3=1e5/EIbeam*Len(3);
    fpt3_wpos=.9999;        % position of pointwise on subsystem
    fptw_4=0/EIbeam*Len(4);    % magnitude of pointwise force on
subsystem
    fpt4_wpos=.6;       % position of pointwise on subsystem
    fptw_5=.15e5/EIbeam*Len(5); % magnitude of pointwise force on
subsystem
    fpt5_wpos=.65;      % position of pointwise on subsystem
    fptw_6=0/EIbeam*Len(6); % magnitude of pointwise force on subsystem
    fpt6_wpos=.67;      % position of pointwise on subsystem
    fptw_7=0/EIbeam*Len(7);    % magnitude of pointwise force on
subsystem
    fpt7_wpos=.7;       % position of pointwise on subsystem
    fptw_8=0/EIcable*Len(8);    % magnitude of pointwise force on
subsystem
    fpt8_wpos=.75;      % position of pointwise on subsystem
    fptw_9=0/EIbeam*Len(9); % magnitude of pointwise force on subsystem
    fpt9_wpos=.77;      % position of pointwise on subsystem
```

```
    fptw_10=0/EIbeam*Len(10);   % magnitude of pointwise force on
subsystem
    fpt10_wpos=.8;      % position of pointwise on subsystem
    fptw_11=0/EIcable*Len(11);  % magnitude of pointwise force on
subsystem
    fpt11_wpos=.85;     % position of pointwise on subsystem
    fptw_12=0/EIcable*Len(12);  % magnitude of pointwise force on
subsystem
    fpt12_wpos=.87;     % position of pointwise on subsystem
    if node==15||node==16;
     fptw_13=0/EIcable*Len(13); % magnitude of pointwise force on
subsystem
    fpt13_wpos=.87;     % position of pointwise on subsystem
    end
    if node==16;
     fptw_14=0/EIcable*Len(14); % magnitude of pointwise force on
subsystem
    fpt14_wpos=.87;     % position of pointwise on subsystem
    end

    FPTw=[];
    FPTwPos=[];
    for iii=1:m,
        eval(['FPTw=[FPTw fptw_',num2str(iii),'];'])
        eval(['FPTwPos=[FPTwPos fpt',num2str(iii),'_wpos];'])
    end

    %These are the nodal forces and are functions of frequency in Hz
    % In this case they are function of the parameter s (frequency)
    P1=[0;0];
    P2=[0;0];
    P3=[0;0];
    P4=[0;0];
    P5=[0;0];
    P6=[0;0];
    P7=[0;0];
    P8=[0;0];
    P9=[0;0];
    P10=[0;0];
    P11=[0;0];
    P12=[0;0];
    P13=[0;0];
    P14=[0;0];
    P15=[0;0];
    P16=[0;0];
    % This puts all nodal forces into a global matrix called P_Nodal
    P_Nodal=[];
    for iii=1:node
        eval(['P_Nodal= [P_Nodal P',num2str(iii),'];'])
    end
    F_cstr=[0;0];
    COUNT=COUNT+1;
end
```

Cabled Beam Frequency Response Program

```
% This file calculates frequency response functions for the cabled
beam.
%
% INPUT:
%   BND_DOF Shows which DOF are constrained (node x dof)
%               dof = [wx  wy  theta]
%
% OUTPUT:
%   alpha1  values for local displacement at position x over frequency
%   range
% Parameter List
%   alpha       local displacement vector at position x and frequency s
%   CON         Shows which subsystems are connected to which
%               nodes. '0' means no subsystem
%   cnt     dummy counting variable
%   dof     the number of degrees of freedom of subsystem
%   endvalue    the number of subsystems at location of response
%   F       matrix built by governing pdes (n x n)
%   filename    the name of file that holds initialization data
%   fptu        point force at subsystem in axial direction
%   fptu_pos    location of point force at subsystem in axial direction
%   fptw        point force at subsystem in transverse direction
%   fptw_pos    location of point force at subsystem in axial direction
%   freqend the end frequency for frequency response
%   freqst  the start frequency for frequency response
%   G       Greens' function
%   Ga_u        partioned G matrix
%   Ga_w        partioned G matrix
%   H       transfer function of Eta/Gamma
%   Ha0     partitioned H matrix
%   Ha1     partitioned H matrix
%   incr        the incremental frequency for frequency response
%   jj      dummy counting variable
%   K       reduced global stiffness matrix at frequency s
%   Kap     vector used for BC calculation
%   kk      dummy counting variable
%               also current subsystem for response
%   Len     length of each subsystems in vector
%   Li      length of each subsystem
%   M       Temporal-spatial operator for left end of subsystem
%   N       Temporal-spatial operator for right end of subsystem
%   node        total number of nodes of system
%   num_str string of current subsystem for response
%   pts     the number of displacements of entire system
%   q       reduced global force vector at frequency s
%   R0      Rotation Matrix at the left end of the subsystem for Forces
%   R1      Rotation Matrix at the right end of the subsystem for
Forces
%   rho     mass per unit length for a subsystem
%   S0      Rotation Matrix for left end of subsystem for displacements
%   S1      Rotation Matrix for right end of subsystem for
displacements
%   s       frequency = ii * sqrt(-1) * 2 * pi
%   Sub_Con Shows which subsystems are connected to which nodes (2 x m)
%               A zero value implies somer sort of boundary condition
```

```
%   sub     subsystem for which response is taken
%   tt      dummy counting variable
%   Ugl     global displacement vector at frequency s
%   Ugl_0       global displacement vector at right end for current
subsystem
%   Ugl_1       global displacement vector at left end for current
subsystem
%   u       reduced global displacement vector at frequency s
%   X       location of node points in local coordinates
%   XX      Shows at each node how many subsystems are connected to it.
%   x       position of response
%   which_node  if response is required at a node it gives node number
%
function [omega,alpha1,alphatf]=freq_resp(BND_DOF)

global node m dof n1 n2 n can XX CON ID Sub_Con qgl Rot BC_type;
global Len XY Ea EIgl rho filename num_ev BC_node_ty AXIAL pts X;
global CONSTRAIN Mgl Ngl Kappa P_Nodal F_cstr FPTw FPTwPos;
global COUNT evals t_alpha t_beta len_m;
global cv Acable Gsh kappag Tens rhogl;

%Choose subsystem to evaluate response on.
sub=3;
x=1;
x1=x;

% The following are the locations of node points connected
% to each subsystem. The start point of each subsystem is 0 and the
% endpoint is 1.

X = zeros(node,m);

tmp1=[0;1];
for ii=1:m,
    tmp2=Sub_Con(:,ii);
    X([tmp2],ii)=X([tmp2],ii)+tmp1;
end

if (x==0) || (x==1)
    which_node=Sub_Con(x+1,sub);    % node number of measured response
end

% Find M and N for  subsystem sub

    M=Mgl(1:n,(sub-1)*n+1:n*sub);
    N=Ngl(1:n,(sub-1)*n+1:n*sub);

    [R0,R1,S0,S1]=Rotation_Calc(Rot(sub));
    Li=Len(sub);

%omega=logspace(0,3,500); % Original
omega=logspace(0,2.7,500); %Last number indicates number of points,
higher number = greater resolution
% Initialize parameters from input file.
```

```
filenameforce=['C:\Users\Kaitlin\Dropbox\CABLED BEAM
MODEL\forces_cablebeam14.m'];
run(filenameforce);

alpha1=zeros(dof,size(omega,2));

for iji=1:size(omega,2),
    ii=omega(iji);

    s=ii*i*2*pi;
    snonimag=ii*2*pi;

    [K,q]=assemble_K_fbfe_diffbeams14(ii);
    u=inv(K)*q;

    % Place reduced global position and forces at specific frequeny
    %       into actual global position and force vector
    Ugl=zeros(1,pts);

    cnt=1;
    for jj=1:node,
        for kk=1:dof,
            if (BND_DOF(jj,kk) < 1)
            eval(['Ugl(1,dof*(jj-1)+kk)=u(',num2str(cnt),');'])
                cnt=cnt+1;
            end
        end
    end

    alpha=zeros(dof,1);

    % Begin to calculate frequency response.
    num_str=num2str(sub);
    tmp1=dof*(Sub_Con(1,sub)-1)+1;
    tmp2=dof*(Sub_Con(2,sub)-1)+1;

    % Find the global displacements at each node at x=0,1 for subsystem
    Ugl_0=Ugl(tmp1:tmp1+dof-1);
    Ugl_1=Ugl(tmp2:tmp2+dof-1);

    fptw=FPTw(1,sub);
    fpt_wpos=FPTwPos(1,sub);

    Kap=Kappa(1:dof,sub);

    if (x==0) || (x==1)
        x1=X(which_node,sub);
    end

%Use Euler Bernoulli formulation for the aluminum beam, shear
hysteresis
%model for the cable.
if sub>0 && sub <7.5;
      F=Li*[        0              1   0   0;
```

```
                0               0   1   0;
                0               0   0   1;
    -rhogl(sub)*s*(s+t_alpha)/(EIgl(sub)*(1+t_beta*s))  0   0   0];
elseif sub > 7.5 && sub < 15;
    Gofs=0;
%Gofs=(25*s^2+9000*s)/(4*s^2+1*s-8000); % For 1X7
%Gofs=(70*s^2+6000*s)/(5*s^2+2*s+2000);  % For 1X19
%Gofs=(180*s^2+40000*s)/(2*s^2+2*s-9000);  % For 1X48
%Gofs=(140*s^2+60000*s)/(2*s^2+2*s-15000);  % For 7X7
    FShearHyst=Li*[0,1,0,0;0,0,1,0;0,0,0,1;-
(rhogl(sub)*s^2+cv*s)/(EIgl(sub)-
(1/s)*Gofs),0,((rhogl(sub)*EIgl(sub)*s^2)/(kappag*Acable*Gsh)+(cv*EIgl(
sub)*s)/(kappag*Acable*Gsh)-Tens)/(EIgl(sub)-(1/s)*Gofs),0];
    F=FShearHyst;
else
    disp('F matrix not defined for subsection greater than 14 in
freq_resp')
end

    eFs=expm(F);

    %       Find alpha due to displacements

    H=expm(F*x1)*inv(M+N*eFs);

    Ha0=H(1:n2/2,1:n/2);
    Ha1=H(1:n2/2,n/2+1:n);

    if (BC_node_ty(Sub_Con(1,sub))>0),
        alpha=alpha+Ha0*Kap+Ha1*S1*Ugl_1';
    elseif (BC_node_ty(Sub_Con(2,sub))>0),
        alpha=alpha+Ha0*Kap+Ha1*S0*Ugl_0';
    else
        alpha=alpha+Ha0*S0*Ugl_0'+Ha1*S1*Ugl_1';
    end

    %       Find alpha due to pointwise forces
    if abs(fptw) > 0
        if fpt_wpos>=x1
            Gw=-H*N*expm(F*(1-fpt_wpos));
        else
            Gw=H*M*expm(-F*fpt_wpos);
        end
        Ga_w=Gw(1:n2/2,n);
        alpha = alpha + Ga_w*fptw;
    end

% Displacement of Beam
        alpha1(1:dof,iji)=alpha;
        alphatf(1:dof,iji)=alpha1(1:dof,iji)/FPTw(1,sub);
end
```

Cabled Beam Mode Shape Program

```
% This program finds the mode shapes of the cabled beam systems.
function mode_shape_fbfe(BND_DOF)

global node m dof n1 n2 n can XX CON ID Sub_Con qgl Rot BC_type Len XY
Ea Ei rho rhogl Eigl
global filename BC_node_ty num_ev len_m t_alpha t_beta CONSTRAIN;
global EIgl;
% Load eigenvalues from eigen_find program.
load(['C:\Users\Kaitlin\Dropbox\CABLED BEAM
MODEL\evalues_cabledbeam.mat'])
nosub=[];
YYpos=[];

pts=node*dof;

%   Redefine K_eval Matrices to Ki matrices for each mode
%   where i ranges from 1 to num_ev

for ii=1:num_ev,
    b=pts-can;
    c=b*(ii-1)+1;
    eval(['K',num2str(ii),'=K_eval(1:b,c:c+b-1);'])
end

%   This part is finding the nontrivial sol'n of K(jlam)u(jlam)=0
for ii=1:num_ev,
    eval(['u',num2str(ii),'=null(K',num2str(ii),');'])])
     if isempty(eval(['u',num2str(ii)]))
        eval(['[a1,b1]=eig(K',num2str(ii),');'])
        c=min(abs(diag(b1)));
        d=find(c==abs(diag(b1)));
        if size(d,1) > 1
            d=d(1);
            a1=a1(:,d);
            eval(['u',num2str(ii),'=a1(1:b,1);'])
        else
            eval(['u',num2str(ii),'=a1(1:b,d);'])
        end
    end
end

%   This routine determines if subsystems are not piecewise continuous.
discont=1;
for ii=2:m,
    if (Sub_Con(1,ii) == Sub_Con(2,ii-1))
        discont = [discont 0];
    else
        discont = [discont 1];
    end
end
no = size(find(discont==1),2);

%   Find the number of subsytems in each free subsystem
num=1;
```

```
for ii=2:size(discont,2),
    if discont(ii)==1
        nosub=[nosub num];
        num=1;
    else
        num=num+1;
    end
end
nosub=[nosub num];

% Calculate displacements (i.e. mode shapes for each eigenvalue)
incr=.01;

for ii=1:num_ev,
    x_pos=[];
    y_pos=[];
    x_loc=[];
    y2_pos=[];

    Ugl=zeros(1,pts);
    cnt=1;

% Place reduced global position at specific eigenvalue into
%       actual global position vector
    for jj=1:node,
        for kk=1:dof,
            if (BND_DOF(jj,kk) < 1)
                eval(['Ugl(1,dof*(jj-
1)+kk)=u',num2str(ii),'(',num2str(cnt),');'])
                cnt=cnt+1;
            end
        end
    end

% Find mode shape for each subsystem and plot it
    for kk=1:m,
        alpha=[];
        tmp1=dof*(Sub_Con(1,kk)-1)+1;
        tmp2=dof*(Sub_Con(2,kk)-1)+1;

    % Find the global displacements at each node at x=0,1 for subsystem
        Ugl_0=Ugl(tmp1:tmp1+dof-1);
        Ugl_1=Ugl(tmp2:tmp2+dof-1);

    % FInd M and N for each subsystem
        [M,N]=MN_Calc(BC_type(kk),kk,EIgl(kk),Ea);

        [R0,R1,S0,S1]=Rotation_Calc(Rot(kk));
        Li=Len(kk);
        s=evals(ii)*i*2*pi;
% This program uses Euler-Bernoulli formulation for the aluminum beam
and
% shear hysteresis model for the cable.
if num > 0 && num < 7.5;
      F=Li*[        0              1   0   0;
```

```
                0               0   1   0;
                0               0   0   1;
    -rhogl(num)*s*(s+t_alpha)/(EIgl(num)*(1+t_beta*s))  0   0   0];
elseif num > 7.5 && num < 15;
    Gofs=0;
%Gofs=(25*s^2+9000*s)/(4*s^2+1*s-8000); % For 1X7
%Gofs=(70*s^2+6000*s)/(5*s^2+2*s+2000);  % For 1X19
%Gofs=(180*s^2+40000*s)/(2*s^2+2*s-9000);  % For 1X48
%Gofs=(140*s^2+60000*s)/(2*s^2+2*s-15000);  % For 7X7

    FShearHyst=Li*[0,1,0,0;0,0,1,0;0,0,0,1;-
(rhogl(num)*s^2+cv*s)/(EIgl(num)-
(1/s)*Gofs),0,((rhogl(num)*EIgl(num)*s^2)/(kappag*Acable*Gsh)+(cv*EIgl(
num)*s)/(kappag*Acable*Gsh)-Tens)/(EIgl(num)-(1/s)*Gofs),0];
    F=FShearHyst;
else
    disp('F matrix not defined for subsection greater than 14')
end

        eFs=expm(F);
        invers=inv(M+N*eFs);

        XI=0:incr:1;

    % Find mode shape along span of subsystem
        for xi=XI,
            H=expm(F*xi)*invers;

            Ha0=H(1:n2/2,1:n/2);
            Ha1=H(1:n2/2,n/2+1:n);

            if (BC_node_ty(Sub_Con(1,kk))>0),
                alpha=[alpha Ha1*S1*Ugl_1'];

            elseif (BC_node_ty(Sub_Con(2,kk))>0),
                alpha=[alpha Ha1*S0*Ugl_0'];
            else
                alpha=[alpha Ha0*S0*Ugl_0'+Ha1*S1*Ugl_1'];
            end
        end

% Need to find mode shape in global coordinates for plotting
        x_beg=XY(1,Sub_Con(1,kk));
        y_beg=XY(2,Sub_Con(1,kk));

        trans=inv(S1)*alpha;
        cc=size(trans,2);

% These find the exact x,y locations and displacements
        Lc=Li*cos(Rot(kk));
        Ls=Li*sin(Rot(kk));
        if Ls==0
            Y_pos=ones(1,cc)*y_beg+trans(1,:);
        else
            Y_pos=(y_beg:(Ls)/(cc-1):Ls+y_beg)+trans(1,:);
```

```
        end
        if Lc==0,
            X_pos=ones(1,cc)*x_beg+trans(1,:);
        else
            X_pos=(x_beg:(Lc)/(cc-1):Lc+x_beg);
        end

% This routine ensures that subsystems are added together correctly if
not
% connected.
        if discont(kk) == 1
            x_pos=[x_pos X_pos];
            y_pos=[y_pos Y_pos];
        else
            tmp=size(X_pos,2);
            x_pos=[x_pos X_pos(2:tmp)];
            y_pos=[y_pos Y_pos(2:tmp)];
        end
    end

% Plot mode shape for eigenvalue number ii
    sz_of_x=size(XI,2);
    sz(1)=0;
    izz=1;
    smnosub=0;

    for ijk=1:no,
        sz(ijk+1) = sz_of_x*nosub(ijk)-nosub(ijk)+1;
        smsz=sum(sz(1:ijk));
        y1=y_pos(1+smsz:sz(ijk+1)+smsz);
        x1=x_pos(1+smsz:sz(ijk+1)+smsz);

    % Make all modes start out to be positive
        if real(y1(2))<0
            y1=-y1;
        end

        plot(x1,y1)
        y2_pos=[y2_pos y1];
        hold on

    % Find spring attachment between subsystems
        begno=Sub_Con(1,1+smnosub);
        endno=Sub_Con(2,smnosub+nosub(ijk));
        for iii=1:nosub(ijk)+1,
            if CONSTRAIN(iii,1)~=0
                tmp=find(x1==XY(1,iii));
                if tmp==[]
                    disp('Increment too large')
                end
                if ijk~=1
                    tmp=tmp+smsz;
                end
                x_loc=[x_loc tmp];
            end
        end
```

```
        smnosub=smnosub+nosub(ijk);
% Boundary conditions marked to differentiate BC types
        for iii=1:2
            if iii==1
                xbc=x1(1);
                ybc=y1(1);
            else
                xbc=x1(size(x1,2));
                ybc=y1(size(y1,2));
            end
            if BC_type(izz)==2
                plot(xbc,ybc,'go')
            elseif BC_type(izz)==1 || BC_type(izz)==3
                plot(xbc,ybc,'ro')
            end
            izz=izz+1;
        end
    end

    tmp=size(x_loc,2)/2;
    % Plot connection point locations
    zvec=0;
    for iii=1:tmp,

plot(XY(1,2),zvec,'mo',XY(1,3),zvec,'mo',XY(1,5),zvec,'mo',XY(1,6),zvec
,'mo',XY(1,7),zvec,'mo')
    end

    title(['Mode',num2str(ii)])
    xlabel('Distance along Beam')
    ylabel('Eigenfunction')
    legend(['Mode Shape at ',num2str(evals(ii)),' Hz'])

    YYpos=[YYpos;y2_pos];
    figure
end
% This is used for MAC Calculation.
%AddedModes=[AddedModes;y_pos];
    %xmodeplot=x_pos;

eval(['save modes_ evals x_pos YYpos discont'])
```

Stiffness Matrix Reduction Function

```
% This file determines which displacements need to be determined by
% creating an ID matrix.  If a node has a boundary condition, then the
% displacements at that node can be neglected and removed from the
global
% stiffness matrix.

function ID=identify(BND_DOF,pts)

global node dof can AXIAL

    cnt1=0;
    cnt2=1;
```

```
for ii=1:node,
    for jj=1:dof,
        if BND_DOF(ii,jj) == 1
            ID(ii,jj)=pts-cnt1;
            cnt1=cnt1+1;
        else
            ID(ii,jj)=cnt2;
            cnt2=cnt2+1;
        end
    end
end
```

Boundary Condition Function

```
% Calculation of boundary condition matrices for each subsystem.
%
% INPUT
%       B_user  User supplied BC (optional)
%       Ei      Flexural Rigidity for beam in bending: E*I
%       sub     Subsystem in question
%       type    Numerical value for type of BC
%
% OUTPUT
%       M       Temporal-spatial operator for left end of subsystem
%       N       Temporal-spatial operator for right end of subsystem
%
% type = 0      No Boundary Condition
% type = 1      Clamped Boundary Condition
% type = 2      Free Boundary Condition
% type = 3      Pinned Boundary Condition
%

% PARAMETER LIST
%
%       B_cl        the boundary conditon matrix for clamped end
%       B_fr        the boundary conditon matrix for free end
%       B_pin       the boundary conditon matrix for pinned end
%       B_sl        the boundary conditon matrix for sliding end
%       M_noBC  M matrix when subsystem has no boundary conditions
%       N_noBC  N matrix when subsystem has no boundary conditions
%       n       the order of the subsystem
%       Sub_Con Shows which subsystems are connected to which nodes (2
x m)
%                   A zero value implies somer sort of boundary
condition
%       XX      Shows at each node how many subsystems are connected to
it.
function [M,N]=MN_Calc(type,sub,Ei)

global n1 n2 n Sub_Con XX BC_type BC_node_ty;

    B_cl=[1 0 0 0;0 1 0 0];
    B_fr=[0 0 Ei 0;0 0 0 -Ei];
    B_pin=[1 0 0 0;0 0 Ei 0];

    % The following are M,N for internal nodes (no BCs)
    M_noBC=zeros(n);
    M_noBC(n1/2+1:n/2,n1+1:n1+n2/2)=eye(n2/2);

    N_noBC=zeros(n);
    N_noBC(n/2+n1/2+1:n,n1+1:n1+n2/2)=eye(n2/2);

    %       Select B for the subsystem
    if (type==0)
        M=M_noBC;
        N=N_noBC;
    elseif (type==1)
        B=B_cl;
```

```
    elseif (type==2)
        B=B_fr;
    elseif (type==3)
        B=B_pin;
    else
        disp(' *** Warning **** Unknown Type for Boundary Condition')
        return
    end

    %  Calculate M, N given the type of Boundary Condition
    if (type> 0)
        if (BC_node_ty(Sub_Con(1,sub)) > 0) &&
(BC_node_ty(Sub_Con(2,sub))==0)
            M=[B;zeros(n/2,n)];
            N=N_noBC;
        elseif (BC_node_ty(Sub_Con(2,sub)) > 0) &&
(BC_node_ty(Sub_Con(1,sub)) ==0)
            M=N_noBC;
            N=[B;zeros(n/2,n)];
        end
    end
```

Rotation Function

```
% This .m file will calculate the rotation matrices for a subsystem
% at end 1 and 2. End 1 is the left end of the subsystem and end 2
% is the right end of the subsystem.
%
% INPUT
%   rot     Rotation angle in radians
%
% OUTPUT
%   R1      Rotation Matrix at the left end of the subsystem for Forces
%   R2      Rotation Matrix at the right end of the subsystem for
Forces
%   S1      Rotation Matrix for left end of subsystem for displacements
%   S2      Rotation Matrix for right end of subsystem for
displacements

function [R1,R2,S1,S2]=Rotation_Calc(rot)
ct=cos(rot);
st=sin(rot);

% These are rotation matrices for forces in x,moment in z and
% force in y
R1=[-1 0;0 -ct];
R2=[1 0;0 ct];
% These are the rotation matrices for displacements in x (u),
% y (w) and theta (w') directions
S1=[ct 0;0 1];
S2=[ct 0;0 1];
```

Determinant Function

```
% This file finds the determinant of the global stiffness matrix for a
% given frequency input.
function determ=tmp(ij)
K=assemble_K(ij);
determ=det(K);
```

Eigenvalue Solver

```
% Function to identify and save eigenvalues of the cable system

% INPUT
%   freqst  the first guess for the frequency range start value
%   freqend the last guess for the frequency range end value
%   num_ev  the number of desired eigenvalues
% OUTPUT
%   Evals       vector of eigenvalues
%
function evals=eigen_find(freqst,freqend,num_ev)

global node m dof n1 n2 n can XX CON ID Sub_Con qgl;
global filename;

disp('Calculating Eigenvalues')

%   Search through the initial frequency range to get an
%   estimate of the evalues. The search routine looks for a
%   minimum value whcih may be a possible candidate for an
%               eigenvalue

incr=1;
p=[];
for ii=freqst:incr:freqend+2,
    K=assemble_K(ii);
    p=[p abs(det(K))];
end

omega=[freqst:incr:freqend+2];

col_p=size(p,2);
a=p(1:col_p-2);
b=p(2:col_p-1);
c=[p(3:col_p)];

g=omega(find(b<a & b<c))

% if the desired number of eigenvalue is not within the specified
% range above, this loop will find guesses for the remaining evals
% There may be cass where an initial guess is nowhere near the
% eval. This may lead to two guess going to the same eval. To
% hopefully bypass these occurences, the number of initial guess
% for the evals are incremented by 3
P1=[];
w1=[];
while(size(g,2)<(num_ev+3))
    freqst=freqend+incr;
    freqend=freqend+100;
    for ii=freqst:incr:(freqend+2)
        K=assemble_K(ii);
        P1=[P1 abs(det(K))];
        w1=[w1 ii];
    end
    col_P1=size(P1,2);
```

```
    a=P1(1:col_P1-2);
    b=P1(2:col_P1-1);
    c=P1(3:col_P1);
    g1=w1(find(b<a & b<c));
    g=[g g1];
    g1=[];
    P1=[];
    w1=[];
end

% The Matlab routine fsolve is used to find the values of
% the eigenvalues which make the determinant of the stiffness
% matrix zero. THe following will cycle through until num_ev
% unique evals are found.

disp('Solving for Evalues')
ii=0;
tmp=1;
K_eval=[];

while(tmp<=num_ev)
    ev=fsolve('tmp',g(ii+1))
    if abs(ev) < 1e-3
        disp('Encountered eigenvalue < 1e-3, skipping ....')
    elseif ev <0
        disp('Encountered negative eigenvalue, discarding ...')
    else
%   This if statement ensures that the eigenvalue found is an actual
% solution (since there can be a case where you get a minimum due to
% numerical deficiencies but det(lam) is still large; fixed this by
% checking that the determinant passes through zero at the eigenvalue.

            if det(assemble_K(ev-0.01))<0 && det(assemble_K(ev+0.01))>0
                evals(tmp)=ev;
                K_eval=[K_eval assemble_K(ev)];
                tmp=tmp+1;
            elseif det(assemble_K(ev-0.01))>0 &&
det(assemble_K(ev+0.01))<0
                evals(tmp)=ev;
                K_eval=[K_eval assemble_K(ev)];
                tmp=tmp+1;
            end

    end
    ii=ii+1;
end
% This saves the eigenvalues for use in mode shape calculation.
eval(['save evalues_bmcabletest evals K_eval'])
```

Output File to Run for Eigenvalues, Frequency Response Functions, and Mode Shapes

```
% This is the top level file that runs all cable or cabled beam
functions
% required to find the eigenvalues, mode shapes, or frequency response
% function of a system, all of which can be determined by running this
% program.

% Based on a program originally created by Dino Sciulli, 1996, altered
for
% cable and cabled beam shear beam models by Kaitlin Spak, 2014.

clear all

global node m dof n1 n2 n can XX CON ID Sub_Con qgl Rot BC_type pts;
global Len XY Ea Ei rho filename num_ev BC_node_ty AXIAL CONSTRAIN A
kappag Gsh cv c Tens;
global Mgl Ngl Kappa P_Nodal F_cstr FPTw FPTwPos;
global COUNT evals len_m t_alpha t_beta;
global AddedModes;

% Initialization of Parameters
CONSTRAIN=[];
COUNT=0;

% This is where the selection is made for either the two-point cable,
% four-point cable, or cabled beam model.
% For two-point cable
filename=['C:\Users\Kaitlin\Desktop\Pinned Cables Feb 2014\Cable
2Pinned Model\bmcable.m'];
% For four-point cable
%filename=['C:\Users\Kaitlin\Desktop\Cable Data In Process\Test 2
%Data\Cable 4Pt Model\bmcable.m'];
run(filename);

n1=0;               % nth order linear pde for axial vibrations
n2=4;               % nth order linear pde for bending vibrations
n=n1+n2;            % nth order linear pde (4:bendng, 2:axial)
pts=node*dof;       % the number of displacements of entire system

% Find the length and rotation angle of each subsytem wrt horizontal
% Find M and N matrices for each subsystem
Mgl=[];
Ngl=[];

for kk=1:m,
    tmp1=Sub_Con(1,kk);
    tmp2=Sub_Con(2,kk);
    dx=XY(1,tmp2)-XY(1,tmp1);
    dy=XY(2,tmp2)-XY(2,tmp1);
    Len=[Len sqrt(dx^2+dy^2)];
    Rot=[Rot atan2(dy,dx)];

    [Mtmp,Ntmp]=MN_Calc(BC_type(kk),kk,Ei,Ea);
    Mgl=[Mgl  Mtmp];
    Ngl=[Ngl Ntmp];
```

```
end
%   Create ID Matrix for reducing global stiffness matrix
ID=identify(BND_DOF,pts);

% Build constraint matrix for inclusion of attachment points

a=size(CONSTRAIN,1);
if a < node
    CONSTRAIN=[CONSTRAIN; zeros(node-a,12)];
elseif a==0
    CONSTRAIN=zeros(node,12);
else
    disp('*** Warning CONSTRAIN matrix is too big: dimension should be
(node x 12)');
end

% Load input forces for appropriate model.
% For two-poitn cable
filenameforce=['C:\Users\Kaitlin\Desktop\Pinned Cables Feb 2014\Cable
2Pinned Model\forces_bmcable.m'];
% For four-point cable
%filenameforce=['C:\Users\Kaitlin\Desktop\Cable Data In Process\Test 2
Data\Cable 4Pt Model\forces_bmcable.m'];
run(filenameforce);

% Choose frequency range of interest.
freqst=1;
freqend=500;
incr=1;

% Calculation of eigenvalues, mode shapes, and FRFs.

   evals=eigen_find(freqst,freqend,num_ev)
   mode_shapeWMAC(BND_DOF);

% hold on
figure(num_ev+10) %Ensures that the mode_shapes are not overwritten by
new plots.
[a,alpha1]=freq_resp(BND_DOF,1);
% [a,alpha1,alphatf]=freq_resp(BND_DOF,1); % For cabled beam transfer
% function
g=(20*log10((a/(2*pi)).*abs(alpha1(1,:)))); % For cable
h=(20*log10((a/(2*pi)).*abs(alphatf(1,:)))); % For cabled beam
%semilogx(a,g,'b') % Alternative plotting form
plot(a,g,'c','LineWidth',2) %Use with "hold on" just prior to plot over
cable exp data
%plot(a,h,'c','LineWidth',2) %Use with "hold on" just prior to plot
over cabled beam exp data
%axis([0 160 -60 10])
xlabel('Frequency (Hz)')
ylabel('Magnitude (dB)')
legend('Cable Model')
```

Appendix D. MATLAB Program Files for Modal Assurance Criterion

These are the representative files for data processing of experimental data and modal assurance criterion calculation from the model mode shapes found using the mode_shape files of Appendix C.

Mode Shape From PSV Scan for Four-Point Cable

```
% Kaitlin Spak
% Mar 17, 2014
% M File to Get Mode Shapes from Experimental Data for MAC
% This file is for cables attached at FOUR points
cabletype=749;
%Choose 7, 19, 48, 749 or 45 for tool steel or 11 for acetron
scanum=2;
%Choose 1 through 3 for full scan mode shapes
len1X7=0.7692;
len1X19=0.7782;
len1X48=0.7744;
len7X7=0.7744;

if cabletype==7;
    if scanum==1;
    % Baked, Scan w Rigid Stinger, Scan 1
    filename=['C:/Users/Kaitlin/Desktop/Cable Mode
Scans/Mar17_1X7D_4Pt_Scan1_mtlbScn.mat'];
    elseif scanum==2;
    % Baked, Scan w Tensioned String, Scan 2
    filename=['C:/Users/Kaitlin/Desktop/Cable Mode
Scans/Mar18_1X7D_4Pt_Scan2_mtlbScn.mat'];
    elseif scanum==3;
    % Baked, Scan w Tensioned String, Scan 3
    filename=['C:/Users/Kaitlin/Desktop/Cable Mode
Scans/Mar19_1X7D_4Pt_Scan3_mtlbScn.mat'];
    end
    LENGTH=len1X7;
    disp('1X7 Cable chosen')
 elseif cabletype==19;
    if scanum==1;
    % Baked, Scan w Rigid Stinger, Scan 1
    filename=['C:/Users/Kaitlin/Desktop/Cable Mode
Scans/Mar17_1X19B_4Pt_Scan1_mtlbScn.mat'];
    elseif scanum==2;
    % Baked, Scan w Tensioned String, Scan 2
    filename=['C:/Users/Kaitlin/Desktop/Cable Mode
Scans/Mar18_1X19B_4Pt_Scan2_mtlbScn.mat'];
    elseif scanum==3;
    % Baked, Scan w Tensioned String, Scan 3
    filename=['C:/Users/Kaitlin/Desktop/Cable Mode
Scans/Mar19_1X19B_4Pt_Scan3_mtlbScn.mat'];

    end
    LENGTH=len1X19;
    disp('1X19 Cable chosen')
```

```
elseif cabletype==48;
    if scanum==1;
    % Baked, Scan w Rigid Stinger, Scan 1
    filename=['C:/Users/Kaitlin/Desktop/Cable Mode
Scans/Mar17_1X48D_4Pt_Scan1_mtlbScn.mat'];
    elseif scanum==2;
    % Baked, Scan w Tensioned String, Scan 2
    filename=['C:/Users/Kaitlin/Desktop/Cable Mode
Scans/Mar18_1X48D_4Pt_Scan2_mtlbScn.mat'];
    elseif scanum==3;
    % Baked, Scan w Tensioned String, Scan 3
    filename=['C:/Users/Kaitlin/Desktop/Cable Mode
Scans/Mar19_1X48D_4Pt_Scan3_mtlbScn.mat'];
    end
    LENGTH=len1X48;
    disp('1X48 Cable chosen')
elseif cabletype==749;
    if scanum==1;
    % Baked, Scan w Rigid Stinger, Scan 1
    filename=['C:/Users/Kaitlin/Desktop/Cable Mode
Scans/Mar17_7X7A_4Pt_Scan1_mtlbScn.mat'];
    elseif scanum==2;
    % Baked, Scan w Tensioned String, Scan 2
    filename=['C:/Users/Kaitlin/Desktop/Cable Mode
Scans/Mar18_7X7A_4Pt_Scan2_mtlbScn.mat'];
    elseif scanum==3;
    % Baked, Scan w Tensioned String, Scan 3
    filename=['C:/Users/Kaitlin/Desktop/Cable Mode
Scans/Mar19_7X7A_4Pt_Scan3_mtlbScn.mat'];
    end
    LENGTH=len7X7;
    disp('7X7 Cable chosen')
elseif cabletype==11;
    if scanum==1;
    % Acetron, Scan w Rigid Stinger, Scan 1
    filename=['C:/Users/Kaitlin/Desktop/Cable Mode
Scans/Mar17_Acetron_4Pt_Scan1_mtlbScn.mat'];
    end
    LENGTH=len1X48;
    disp('Acetron Rod chosen')
elseif cabletype==45;
    if scanum==1;
    % Tool Steel, Scan w Rigid Stinger, Scan 1
    filename=['C:/Users/Kaitlin/Desktop/Cable Mode
Scans/Mar17_TS_4Pt_Scan1_mtlbScn.mat'];
    end
    LENGTH=len7X7;
    disp('7X7 Cable chosen')
end

load(filename)

% % % This figure shows all of the scan point FRFs to determine
frequencies to look at.
% figure(20)
% plot(xx.H2veldB,yy.H2veldB)
```

```
% % % This figure takes the average of all points for an overall FRF.
% figure(21)
% plot(xx.H2veldB,mean(yy.H2veldB))
% % And this figure is the driving point
figure(22)
plot(xx.H2veldB,yy.H2veldB(30,:))

if cabletype==7;

[pks,locs]=findpeaks((yy.H2veldB(30,:)),'NPEAKS',6,'MINPEAKDISTANCE',15
);
elseif cabletype==19;

[pks,locs]=findpeaks((yy.H2veldB(30,:)),'NPEAKS',10,'MINPEAKDISTANCE',1
0);
elseif cabletype==48;

[pks,locs]=findpeaks((yy.H2veldB(30,:)),'NPEAKS',18,'MINPEAKDISTANCE',1
0);
elseif cabletype==749;

[pks,locs]=findpeaks((yy.H2veldB(30,:)),'NPEAKS',10,'MINPEAKDISTANCE',1
0);
end

% These are the frequencies to look at
FreqVals=xx.H2(1,locs)

% These are the point locations
Numpoints=size(yy.H2);
dist=LENGTH/(Numpoints(1)-1);
xvals=0:dist:LENGTH;

YValues=[];
pvf=[];
Iyf=[];
for ii=1:length(locs)
    figure(ii)

    normval=max(abs((yy.H2(:,locs(ii)).*sind(yy.Phs(:,locs(ii))))));
    yvalspn=(yy.H2(:,locs(ii)).*sind(yy.Phs(:,locs(ii)))./normval;
    yvalsp=(yy.H2(:,locs(ii)).*sind(yy.Phs(:,locs(ii))));

    plot(xvals,yvalspn)
    title(['Mode Shape at f=',num2str(xx.H2(1,locs(ii))),' Hz'])

    YValues=[YValues,yvalspn];

    xsm=0:0.01:LENGTH;

    % Smoothing and Interpolating Section - for observation only, data
used
    % as raw for MAC comparison
     Iy = interp1(xvals(:),yvalspn(:),0:.01:LENGTH);
     Iyf=[Iyf;Iy];
```

```
hold on
plot(0:.01:LENGTH,Iy,'ro')
plot(0:.01:LENGTH,smooth(Iy,10),'g')

p = polyfit(xvals(:),yvalspn(:),10);
pv = polyval(p,0:.01:LENGTH);

pvf=[pvf;pv];

hold on
plot(0:.01:LENGTH,pv,'m')
legend('Raw Exp Data','Interpolated','Smoothed','PolyFit')
end
% This command will save the mode shape vector information for use in
the
% MAC program.
%eval(['save expmodes_4PT_',filename(43:length(filename)),' xvals
YValues Iy pv FreqVals'])
```

Modal Assurance Criterion for Cable Model

```
% MAC Calculations; this program takes in experimentally determined
mode
% shapes and model mode shapes, processes them ,and prepares a modal
% assurance criterion.
% First, run "ModeShapeFromPSVScanfor..." (Rod, Cable, etc),
% saves xvals, YValues, Iyf pvf
% SECOND, run TF with mode_shapeWMAC to get "AddedModes" file - first
row is the x values, subsequent rows are each mode.
% Must manually load expmodes_filename .mat files for experimental mode
% shapes- make sure that they have YValues

cabletype=749;
%Must choose 7, 19, 48 or 749;
numberofmodelmodes=6;
numberofexperimentalmodes=12;

clear phiExp phiModel phiMod k MAC

indexy=size(YValues);
 for i=1:indexy(1,2);
phiExp(i,:)=YValues(:,i);
% This gives the experimental mode shapes where each row is a mode.
 end

for j=1:numberofmodelmodes;
phiModel(j,:)=AddedModes((1+j),:); %
% AddedModes is a number of modes+1 by 4001 array- using j turns it
into a
% j by 4001 vector
end

% This part finds the locations of the model data to match the number
of
% points from polytec scan.
if cabletype==7;
for k=1:47
%      locsMod(1,length(xvals))=zeros(1,length(xvals));
%      locsMod(1)=0;
locsfinder=find(AddedModes(1,:) <= xvals(k));
nav=size(locsfinder);
locsMod(k)=locsfinder(nav(2));
end
end

if cabletype==19;
for k=1:47
locsfinder=find(AddedModes(1,:) <= xvals(k));
nav=size(locsfinder);
locsMod(k)=locsfinder(nav(2));
end
end

if cabletype==48;
for k=1:47
```

```
locsfinder=find(AddedModes(1,:) <= xvals(k));
nav=size(locsfinder);
locsMod(k)=locsfinder(nav(2));
end
end

if cabletype==749;
for k=1:47
locsfinder=find(AddedModes(1,:) <= xvals(k));
nav=size(locsfinder);
locsMod(k)=locsfinder(nav(2));
end
end

% This figures out the analytical y values to match the experimental
% points.
for jk=1:numberofmodelmodes;
for kj=2:length(xvals)
phiMod(jk,kj)=AddedModes(jk+1,locsMod(kj))
end
end
phiMod=fliplr(phiMod); % The laser vibrometer numbered the points in
the
% opposite direction than the model does, model is flipped to match
% experimental data.

 mdpts=size(phiMod)
 mdptsexp=size(phiExp)
 for k=1:mdpts(1);
 for j=1:6;
 iin=[1,2,3,4,5,7,8] % Choose which experimental vectors are bending
modes.
 i=iin(j);
 % This is the actual MAC calculation.
 numer=(abs(sum(phiExp(i,:).*conj(phiMod(k,:)))))^2;
denomexp=sum(phiExp(i,:).*conj(phiExp(i,:)));
denommod=sum(phiMod(k,:).*conj(phiMod(k,:)));

denom=dot(denomexp,denommod);

MAC(k,j)=numer/denom;
end
 end
 ExpFreqs=FreqVals
 ModFreqs=evals
% This plots the MAC as a bar graph.
figure(21)
bar3cK(MAC)
xlabel('Experimental Modes')
ylabel('Model Modes')
colorbar
```

Modal Assurance Criterion for Cabled Beam Model

```
% MAC Calculations; this program takes in experimentally determined
mode
% shapes and model mode shapes, processes them ,and prepares a modal
% assurance criterion for a cabled beam.

% First, run "ModeShapeFromPSVScanfor..." (Rod, Cable, whatever), saves
% xbeam, xcab, yvalspn YValues FreqVals
% SECOND, run TF with mode_shape_fbfe to get modes_.mat file
% Loading this gives you x_pos and YYpos
% where x_pos(1,1:701) is the beam x position
% and x_pos(1,702:1402) is the cable x position
% and YYpos(mode,1:701) or YYpos(mode,702:1402) is the beam or cable
mode
% shape for the chosen mode.

% Must manually load expmodes_filename .mat files for experimental mode
% shapes- make sure that they have YValues

% MAC CALC
cabletype=11;
%Must choose 7, 19, 48 or 749;
numberofmodelmodes=size(evals,2);
numberofexpmodes=size(YValues);

clear phiExp phiModelBeam phiModelCab phiModBeam phiModCable k MAC
locsMod
clear bmrw1 bmrw2 cabrw bmrw3 bmrw4

YValuest=transpose(YValues);

for ii=1:numberofexpmodes(2);
if length(yvalspn)==125;
      % xbeam has 25 points
         pt=25;
    bmrw1(ii,1:pt)=YValuest(ii,1:25)
    bmrw2(ii,1:pt)=YValuest(ii,26:50);
    cabrw(ii,1:pt)=YValuest(ii,51:75);
    bmrw3(ii,1:pt)=YValuest(ii,76:100);
    bmrw4(ii,1:pt)=YValuest(ii,101:125)
    bmtot=vertcat(bmrw1,bmrw2,bmrw3,bmrw4)
    bmrw(ii,1:pt)=mean(bmtot)

elseif length(yvalspn)==57;
     % xbeam has 19 points
         pt=19;
    bmrw1(ii,1:pt)=YValuest(ii,1:19);
    cabrw(ii,1:pt)=YValuest(ii,20:38);
    bmrw3(ii,1:pt)=YValuest(ii,39:57);
    bmtot=vertcat(bmrw1,bmrw3)
    bmrw(ii,1:pt)=mean(bmtot)

end
end
```

```
% So here bmrw and cabrw are the experimental mode shapes, where each
row
% is a mode.
phiExp=horzcat(bmrw1,cabrw)

xmbeam=x_pos(1,1:701);
xmcable=x_pos(1,702:1402);

for j=1:numberofmodelmodes;
phiModelBeam(j,:)=YYpos(j,1:701);
maxBeam=max(phiModelBeam(j,1:701));
phiModBeam(j,:)=phiModelBeam(j,1:701)./maxBeam;

phiModelCab(j,:)=YYpos(j,702:1402);
maxCable=max(phiModelCab(j,1:701));
phiModCab(j,:)=phiModelCab(j,1:701)./maxCable;
%  figure(j)
%  plot(xmbeam,phiModBeam(j,:),'k')
%  figure(j+10)
%  plot(xmcable,phiModCab(j,:),'y')

% So at this point, phiModBeam and phiModCab are the mode shapes for
the
% beam and the cable, with jX701 size where j is the mode number.

% % This part finds the locations of the model data to match the number
of
% % points from polytec scan.

for k=1:pt
    locsfinder=find(xmbeam<=xbeam(k));
    nav=size(locsfinder);
    locsMod(k)=(nav(2));
    phiModBm(j,k)=phiModBeam(j,locsMod(k));

    locsfinderc=find(xmcable<=(xcab(k)+(xmcable(1,1))));
    navc=size(locsfinderc);
    locsModc(k)=navc(2);
    phiModC(j,k)=phiModCab(j,locsModc(k));
end
%figure(j)
%plot(xbeam,phiModBm(j,:),'k',(xcab+xmcable(1,1)),phiModC(j,:),'r')

%plot(xbeam,phiModBm(j,:),xbeam,bmrw1(j,:))
end
% At this point, I have the model modes for beam and cable as
% phiModBm(j,:) and phiModCab(j,:) against xbeam and xcab
% and experimental modes as bmrw1 etc
phiMod=horzcat(phiModBm,phiModC)

mdpts=size(phiMod,1)

  for kk=1:mdpts;
  for jj=1:numberofexpmodes(2);
% This is the actual MAC calculation.  Note that the cable and beam are
```

```
% comapred as a complete system.
  numer=(abs(sum(phiExp(jj,:).*conj(phiMod(kk,:))))^2;

 denomexp=sum(phiExp(jj,:).*conj(phiExp(jj,:)));
 denommod=sum(phiMod(kk,:).*conj(phiMod(kk,:)));

 denom=dot(denomexp,denommod);

 MAC(kk,jj)=numer/denom;

 end
  end
% Print the experimental and model frequencies to compare.
ExpFreqs=FreqVals
ModFreqs=evals
% Plot the MAC bar graph.
figure(22)
bar3cK(MAC)
title('MAC for Cabled Beam')
xlabel('Experimental Modes')
ylabel('Model Modes')
colorbar
```

Appendix E. Cable Bakeout Results: Individual Section Tables and Graphs of Cable Comparisons by Section

Table E.1 1X7 Cable Section Averages

1X7 Section	Unbaked First Mode Avg Frequency (Hz)	Baked First Mode Avg Frequency (Hz)	% Change	Unbaked Second Mode Avg Frequency (Hz)	Baked Second Mode Avg Frequency (Hz)	% Change
C	47.64	40.78	14.4%	204.40	177.48	13.2%
D	45.14	39.41	12.7%	187.96	157.71	16.1%
E	45.53	37.68	17.2%	194.40	165.21	15.0%
Overall	46.11	39.29	14.8%	195.58	166.80	14.7%

Table E.2 1X7 Cable Coefficients of Variation

	First Mode Unbaked	First Mode Baked	First Mode All Trials	Second Mode Unbaked	Second Mode Baked	Second Mode All Trials
C	0.072	0.039	0.110	0.039	0.036	0.100
D	0.061	0.023	0.096	0.036	0.017	0.124
E	0.043	0.035	0.133	0.041	0.043	0.115
Overall	0.059	0.047	0.113	0.038	0.035	0.112

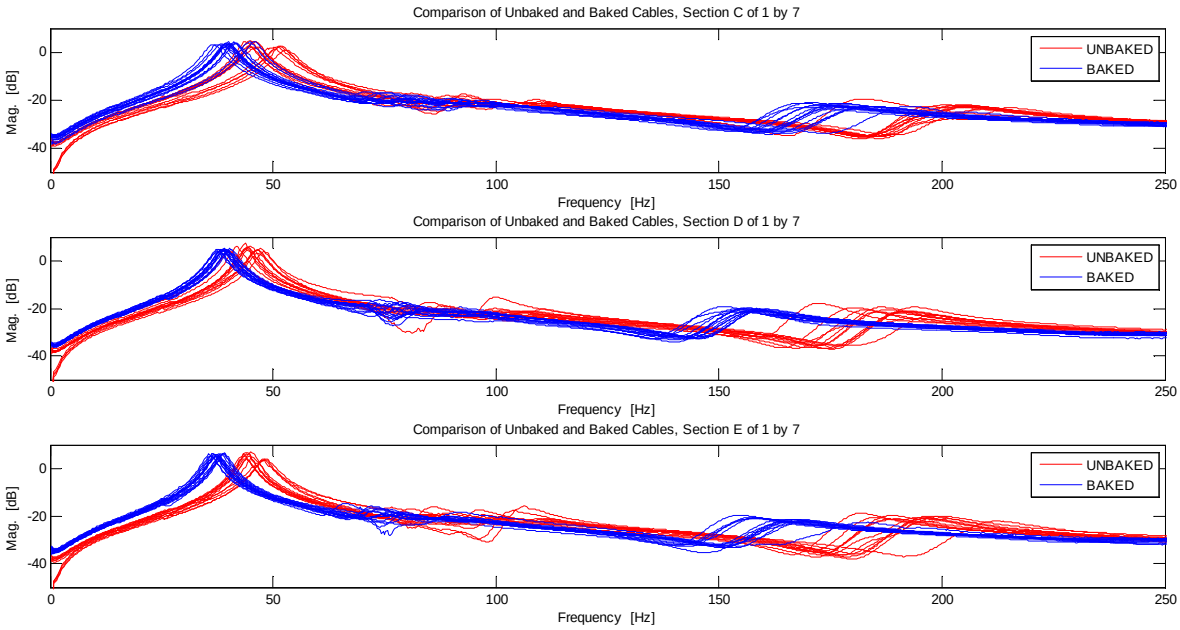

Figure E.1: Baked and unbaked cable comparison for each section of 1X7 cable.

Table E.3 1X19 Cable Section Averages

1X19 Section	Unbaked First Mode Avg Frequency (Hz)	Baked First Mode Avg Frequency (Hz)	% Change	Unbaked Second Mode Avg Frequency (Hz)	Baked Second Mode Avg Frequency (Hz)	% Change
A	73.96	61.95	16.2%	265.06	230.53	13.0%
B	69.57	60.35	13.2%	255.46	223.24	12.6%
C	67.84	57.54	15.2%	253.27	207.81	17.9%
Overall	70.45	59.95	14.9%	257.93	220.53	14.5%

Table E.4 1X19 Cable Coefficients of Variation

	First Mode Unbaked	First Mode Baked	First Mode All Trials	Second Mode Unbaked	Second Mode Baked	Second Mode All Trials
A	0.019	0.027	0.125	0.027	0.030	0.099
B	0.011	0.020	0.100	0.022	0.036	0.095
C	0.011	0.026	0.116	0.018	0.031	0.139
Overall	0.015	0.025	0.115	0.023	0.033	0.111

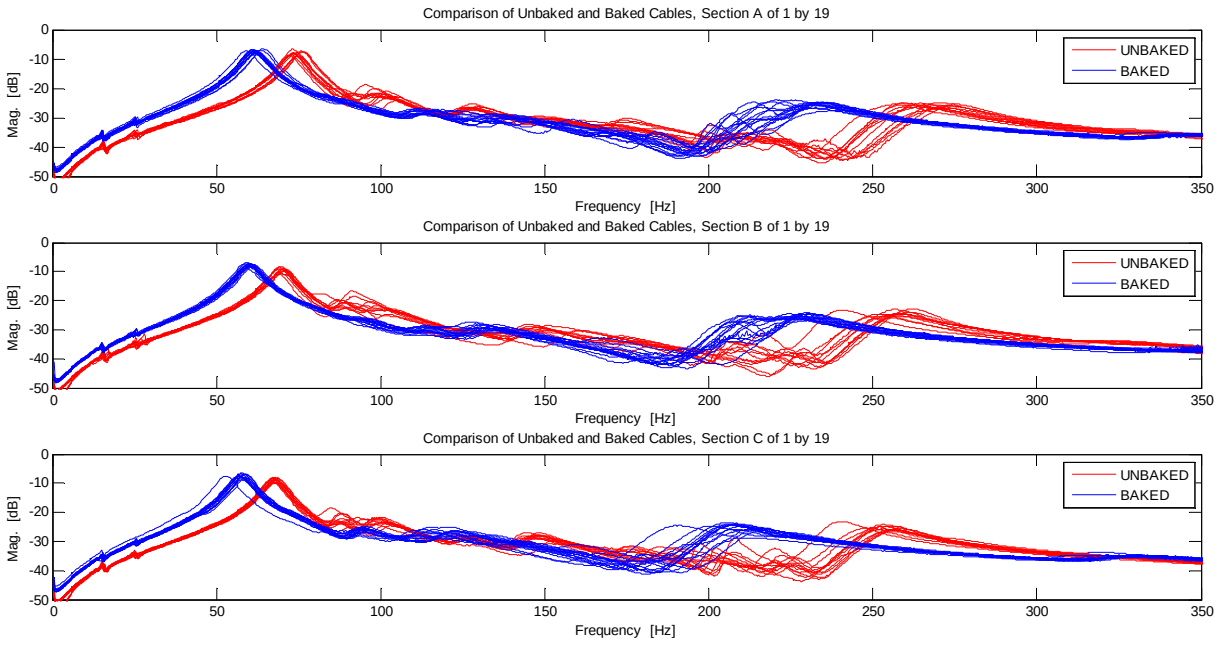

Figure E.2: Baked and unbaked cable comparison for each section of 1X19 cable.

Table E.5 1X48 Cable Section Averages

1X48 Section	Unbaked First Mode Avg Frequency (Hz)	Baked First Mode Avg Frequency (Hz)	% Change	Unbaked Second Mode Avg Frequency (Hz)	Baked Second Mode Avg Frequency (Hz)	% Change
B	124.45	106.80	14.2%	384.06	346.91	9.7%
D	120.82	104.77	13.3%	402.96	379.48	5.8%
E	123.46	105.47	14.6%	396.47	354.90	10.5%
Overall	122.91	105.68	14.0%	394.50	360.43	8.6%

Table E.6 1X48 Cable Coefficients of Variation

	First Mode Unbaked	First Mode Baked	First Mode All Trials	Second Mode Unbaked	Second Mode Baked	Second Mode All Trials
B	0.022	0.021	0.108	0.014	0.021	0.072
D	0.029	0.020	0.101	0.026	0.019	0.051
E	0.048	0.026	0.111	0.021	0.049	0.078
Overall	0.034	0.023	0.107	0.032	0.033	0.065

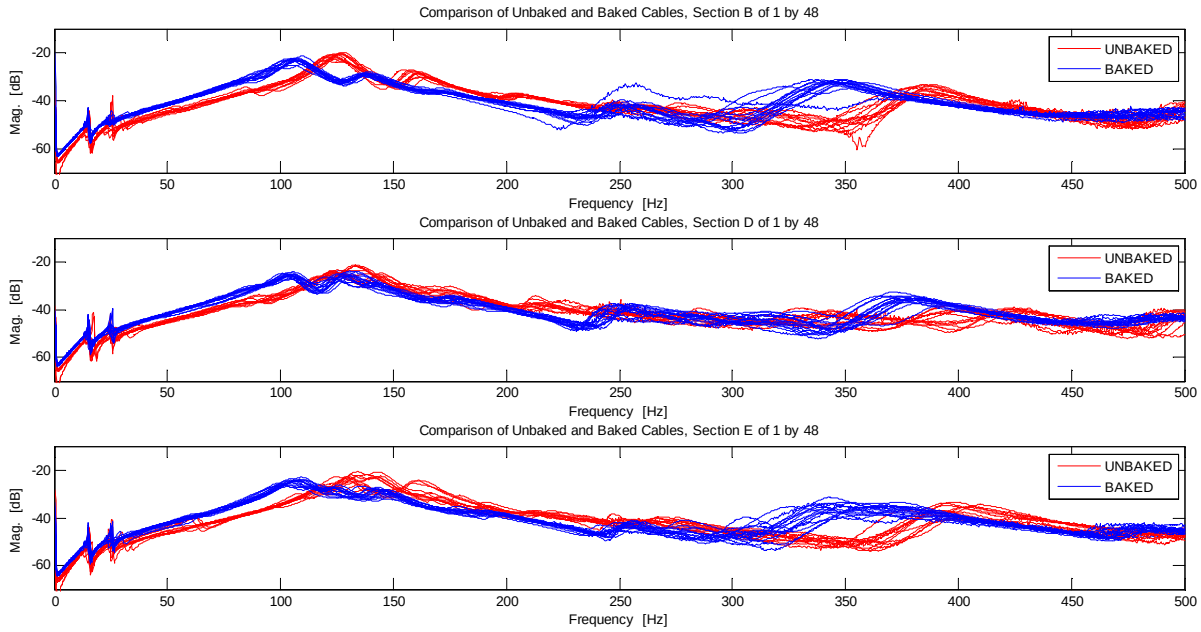

Figure E.3: Baked and unbaked cable comparison for each section of 1X48 cable.

Table E.7 7X7 Cable Section Averages

7X7 Section	Unbaked First Mode Avg Frequency (Hz)	Baked First Mode Avg Frequency (Hz)	% Change	Unbaked Second Mode Avg Frequency (Hz)	Baked Second Mode Avg Frequency (Hz)	% Change
A	82.79	62.42	24.6%	244.83	212.89	13.0%
B	90.99	68.79	24.4%	250.63	207.23	17.3%
D	84.98	64.00	24.7%	248.39	197.89	20.3%
Overall	86.25	65.07	24.6%	247.95	206.00	16.9%

Table E.8 7X7 Cable Coefficients of Variation

	First Mode Unbaked	First Mode Baked	First Mode All Trials	Second Mode Unbaked	Second Mode Baked	Second Mode All Trials
A	0.029	0.013	0.198	0.075	0.051	0.099
B	0.020	0.039	0.196	0.014	0.040	0.134
D	0.031	0.035	0.199	0.074	0.046	0.160
Overall	0.026	0.032	0.198	0.059	0.047	0.131

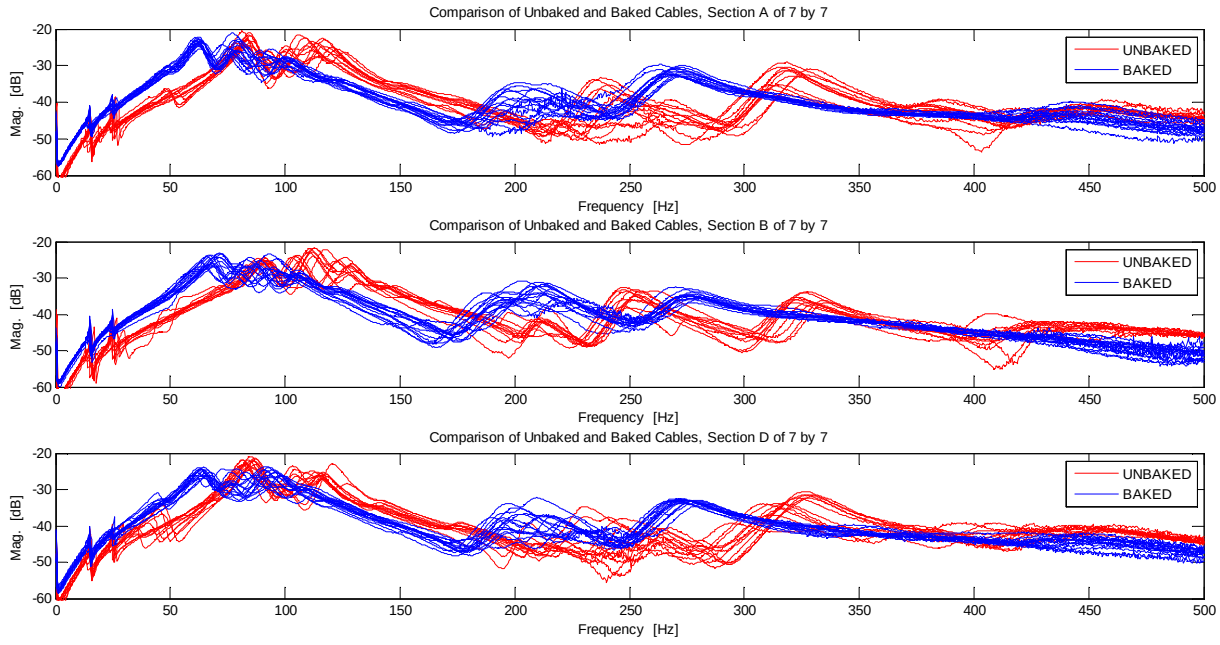

Figure E.4: Baked and unbaked cable comparison for each section of 7X7 cable.

Appendix F. Comparisons Between Four-Point Fixture Experimental Data and Hysteretically Damped Cable Model

Use of the hysteretic damping coefficients determined for the cables in the two-point fixture (shown in Chapter 6) are effective for only the first mode of the four-point fixture, as shown in the following figures.

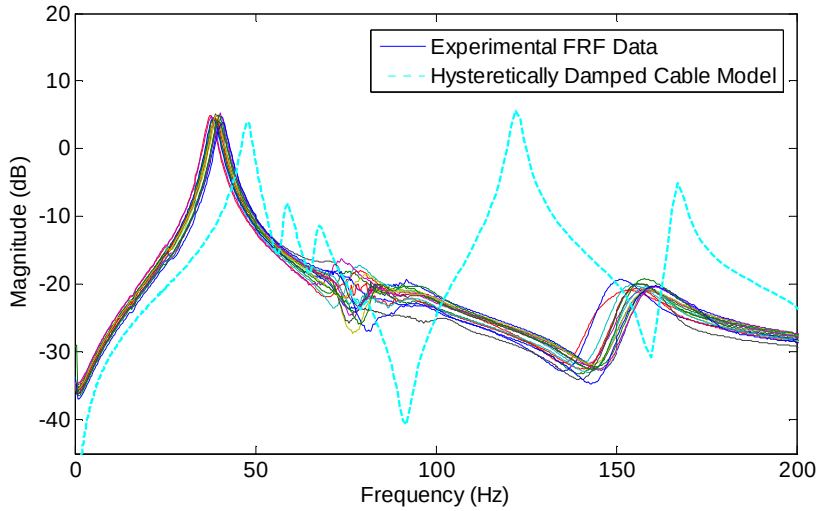

Figure F.1: Comparison of experimental and hysteretically damped model FRFs for 1X7 cable.

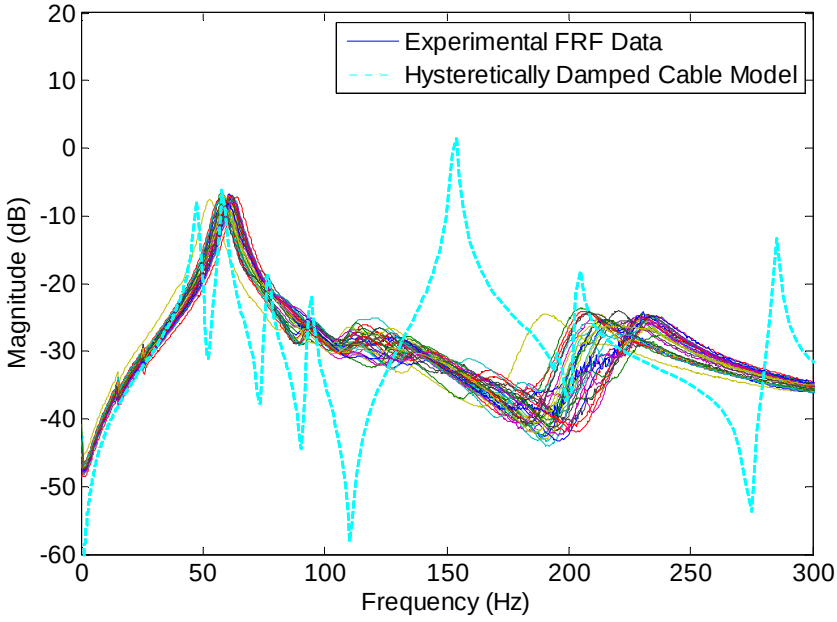

Figure F.2: Comparison of experimental and hysteretically damped model FRFs for 1X19 cable.

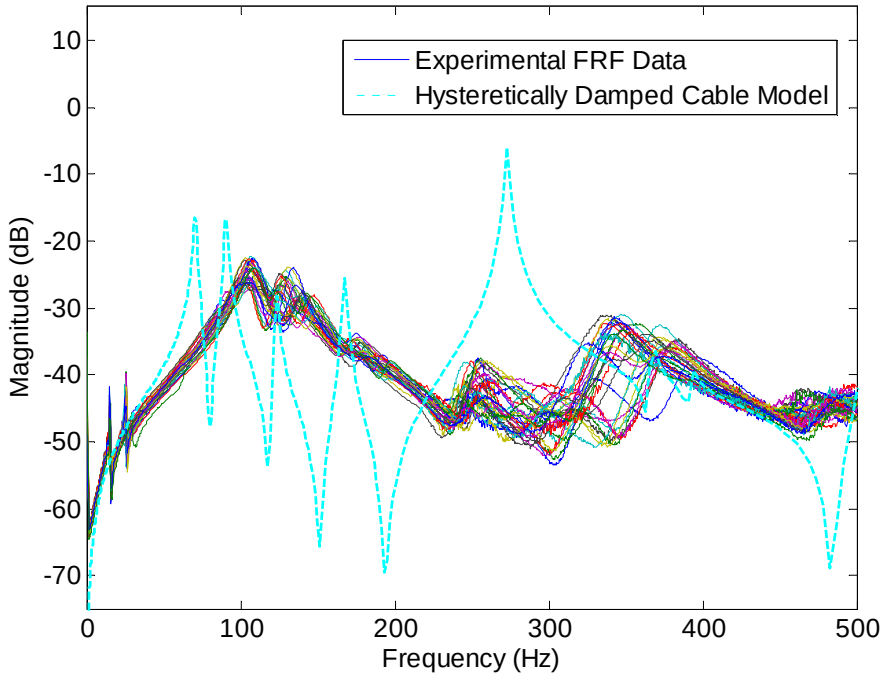

Figure F.3: Comparison of experimental and hysteretically damped model FRFs for 1X48 cable.

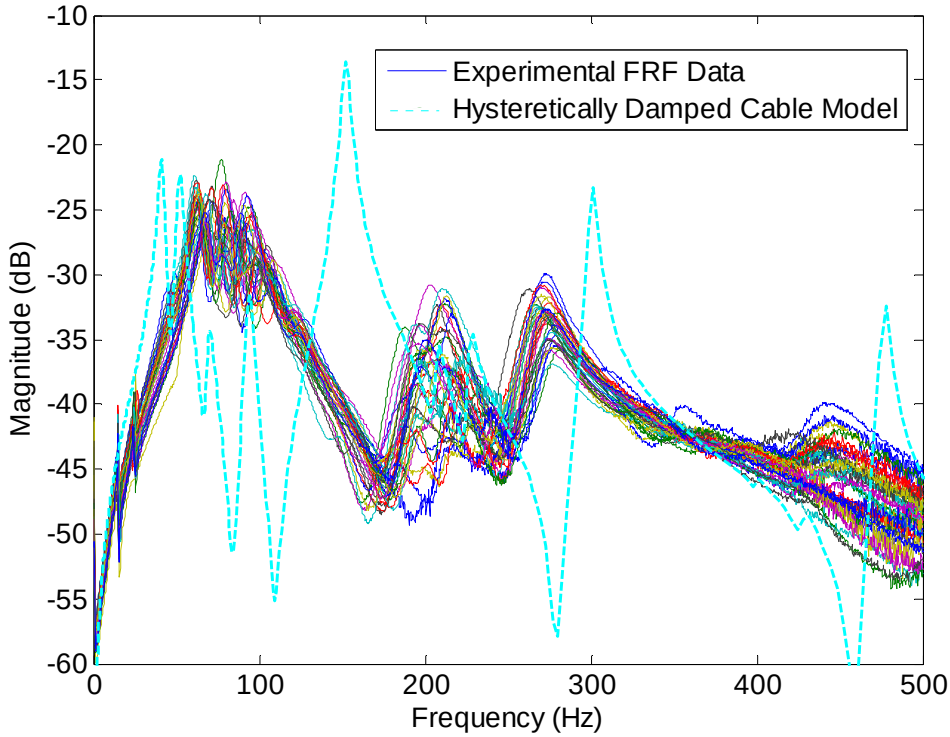

Figure F.4: Comparison of experimental and hysteretically damped model FRFs for 7X7 cable.

Appendix G. Experimental Scans and Average FRFs for Cabled Beams

Figures G.1 through G.4 show the mobility transfer functions for the cabled beam structure as measured on the beam structure. Figures G.5 through G.8 show the trials and average mobility functions as measured on the cable, and Figure G.9 compares the different cable responses on the beam as measured on the cable.

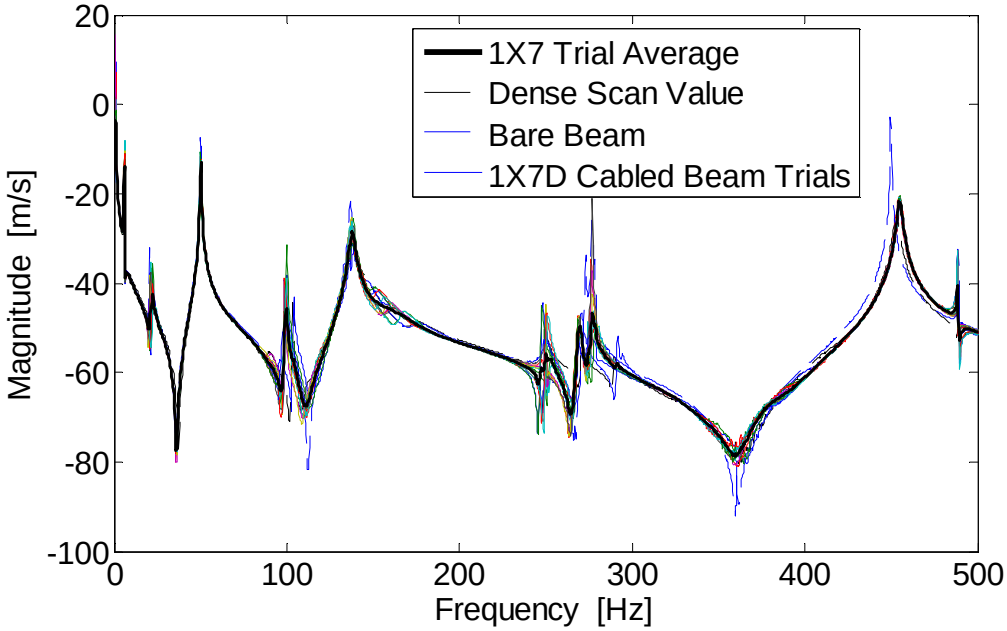

Figure G.1: Frequency response functions measured on the beam for sparse scan experimental trials of beam with 1X7 cable attached with average of 10 trials shown as bold line.

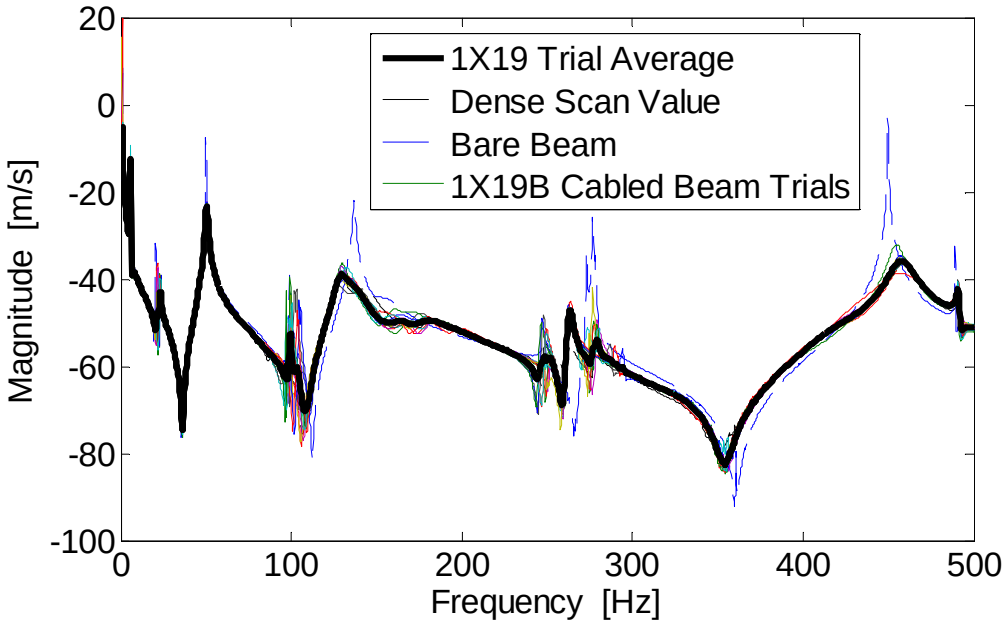

Figure G.2: Frequency response functions measured on the beam for sparse scan experimental trials of beam with 1X19 cable attached with average of 10 trials shown as bold line.

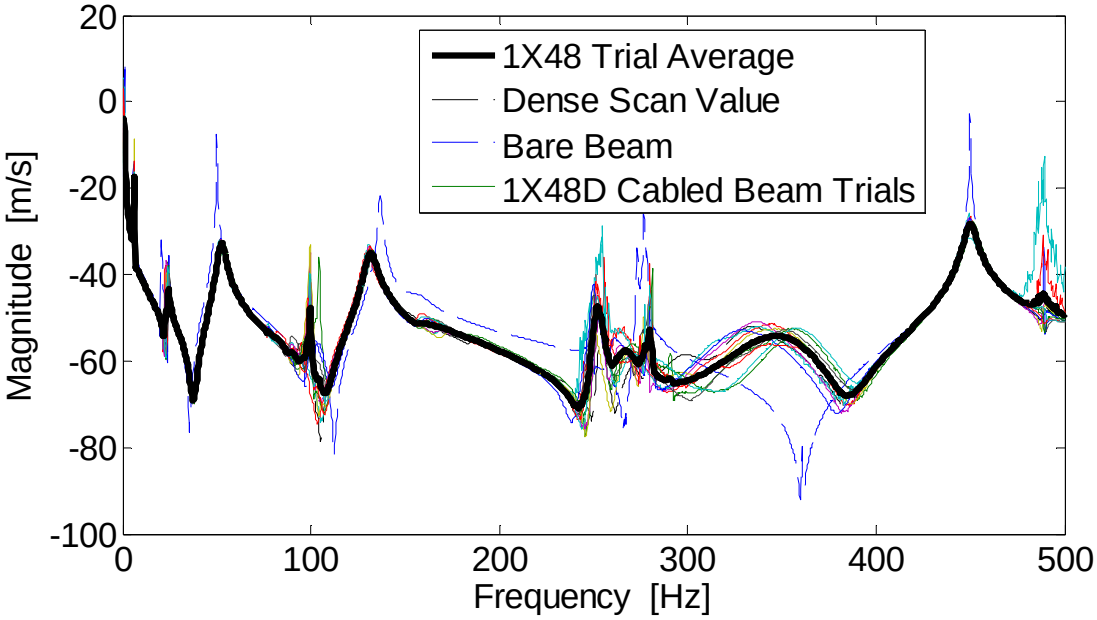

Figure G.3: Frequency response functions measured on the beam for sparse scan experimental trials of beam with 1X48 cable attached with average of 10 trials shown as bold line.

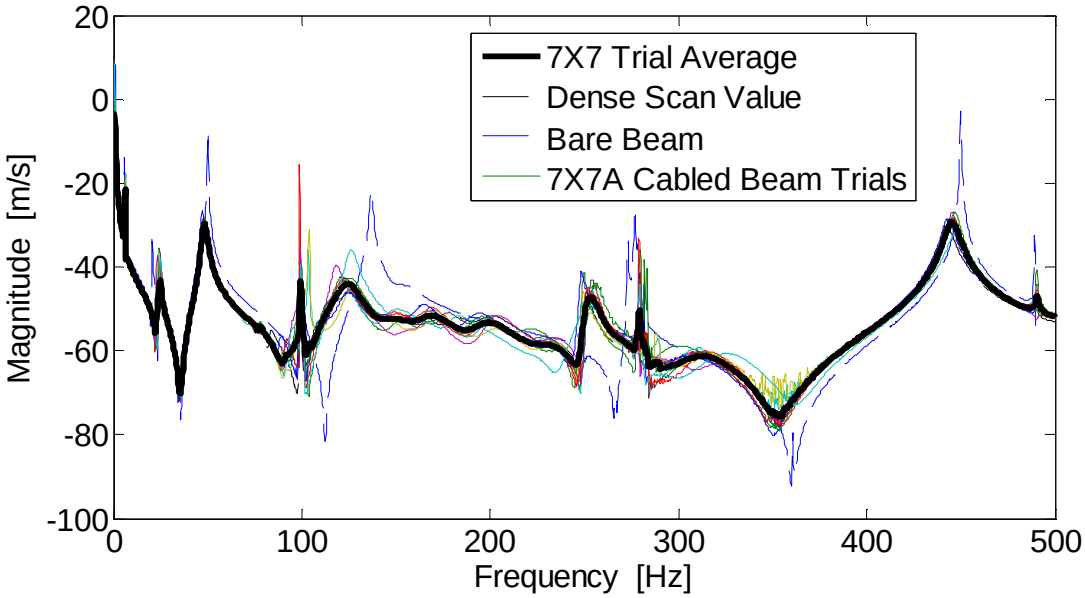

Figure G.4: Frequency response functions measured on the beam for sparse scan experimental trials of beam with 7X7 cable attached with average of 10 trials shown as bold line.

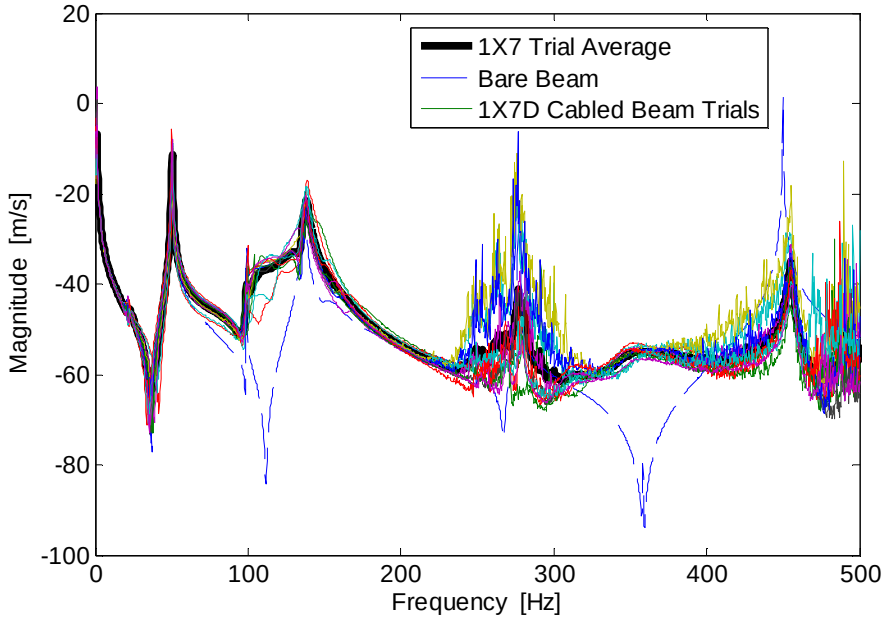

Figure G.5: Frequency response functions measured on the cable for sparse scan experimental trials of beam with 1X7 cable attached with average of 10 trials shown as bold line.

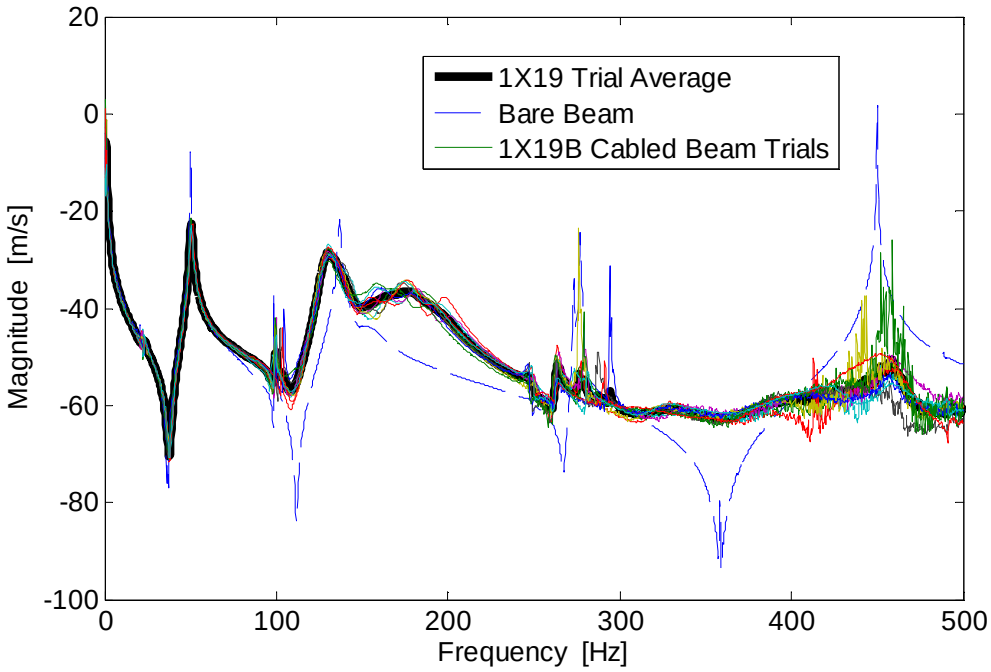

Figure G.6: Frequency response functions measured on the cable for sparse scan experimental trials of beam with 1X19 cable attached with average of 10 trials shown as bold line.

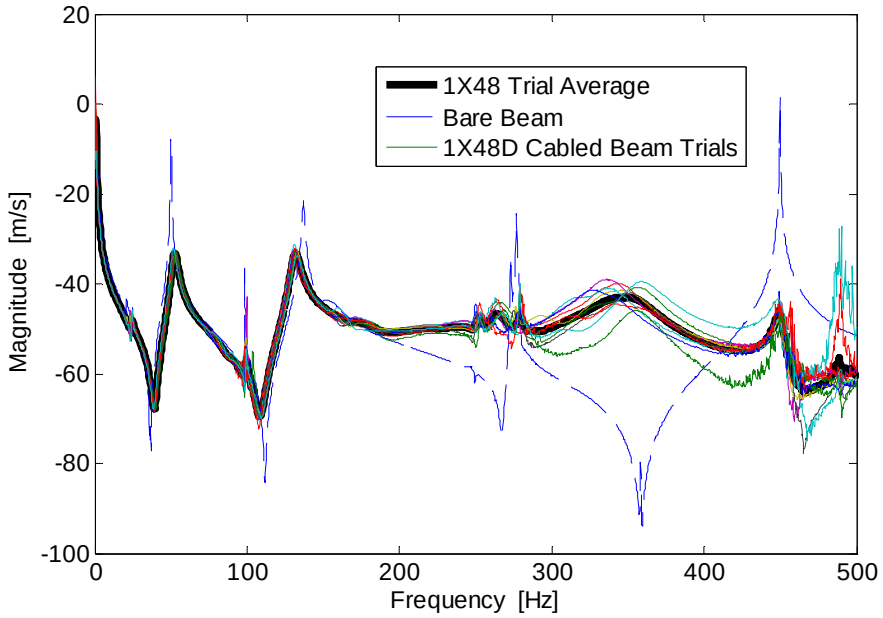

Figure G.7: Frequency response functions measured on the cable for sparse scan experimental trials of beam with 1X48 cable attached with average of 10 trials shown as bold line.

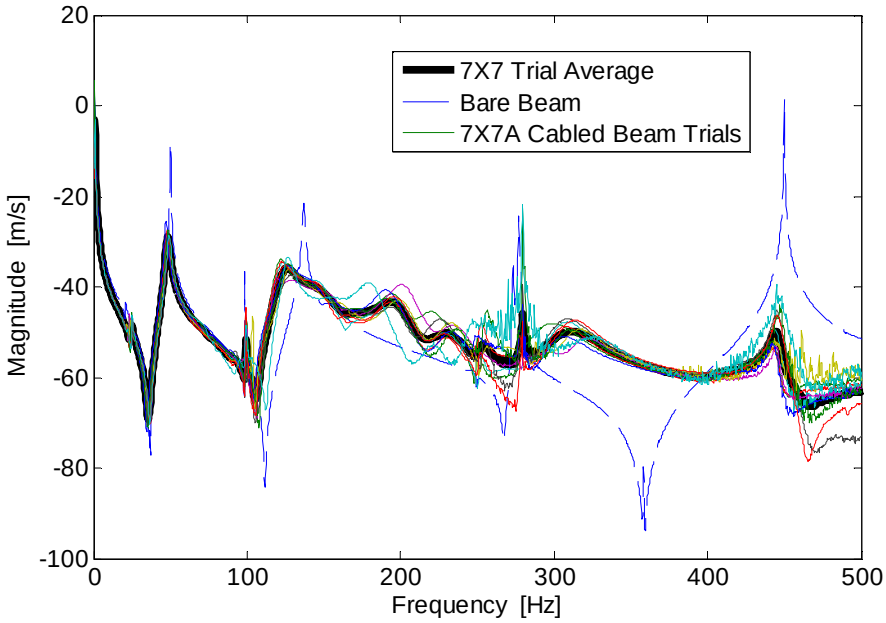

Figure G.8: Frequency response functions measured on the cable for sparse scan experimental trials of beam with 7X7 cable attached with average of 10 trials shown as bold line.

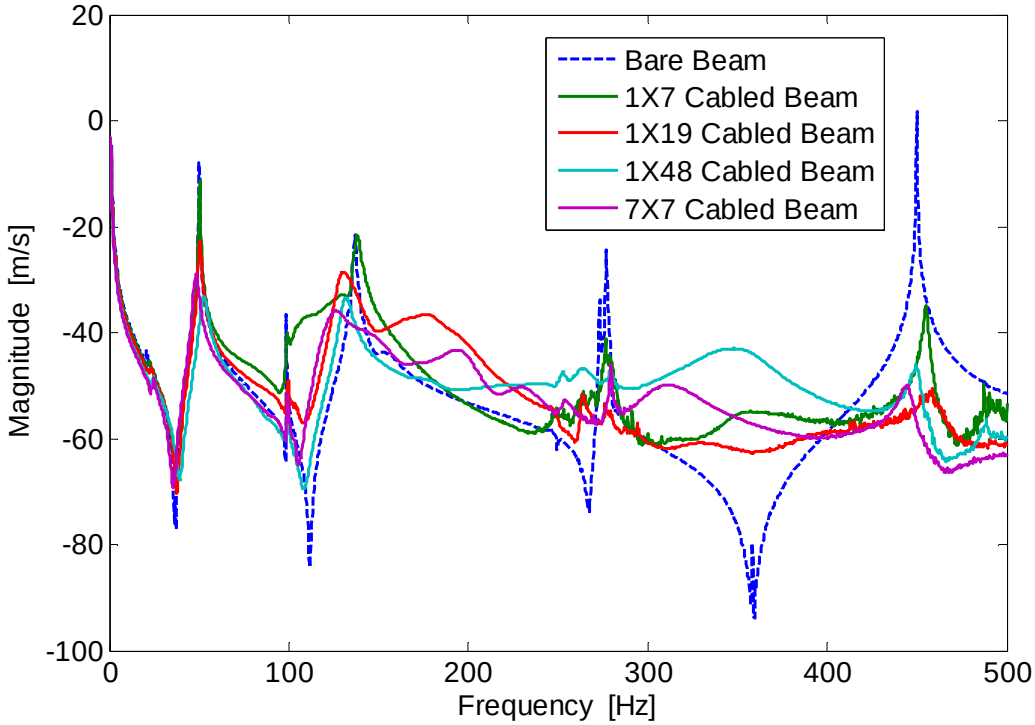

Figure G.9: Bare beam FRF and FRF averages of 10 trials for each cable on beam as measured on the cable.

Appendix H. Mode Shapes of Bare and Cabled Beams from Dense Scans

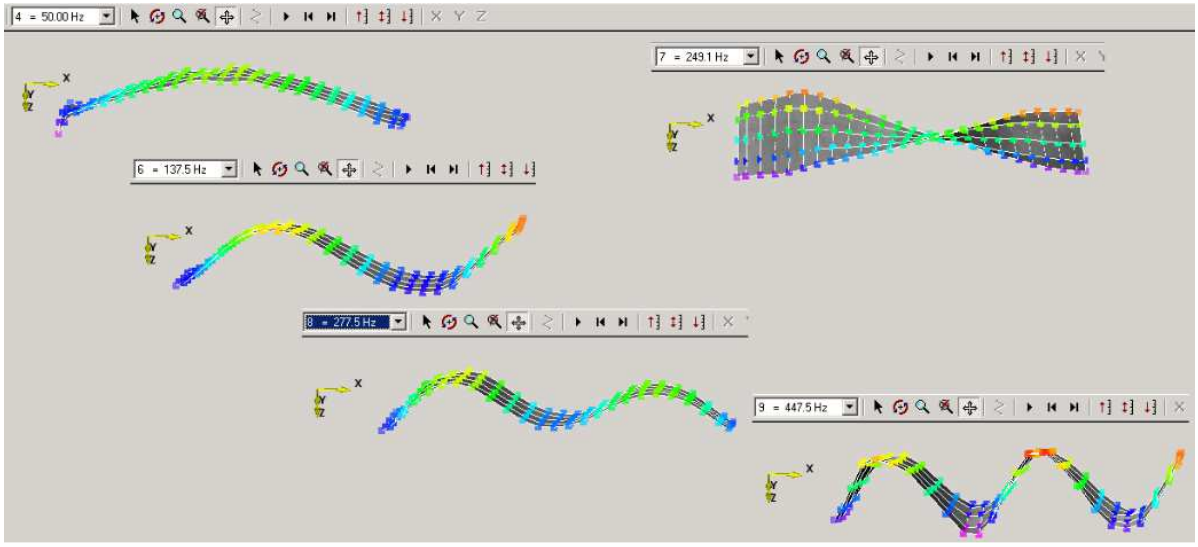

Figure H.1: Mode shapes of bare beam as obtained from dense scan by laser vibrometer.

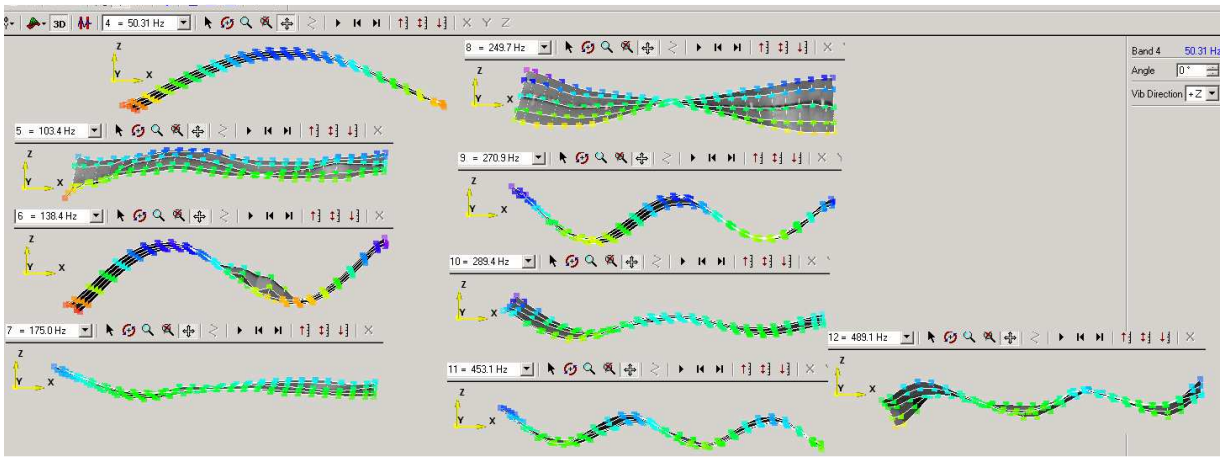

Figure H.2: Mode shapes of 1X7 cabled beam as obtained from dense scan by laser vibrometer.

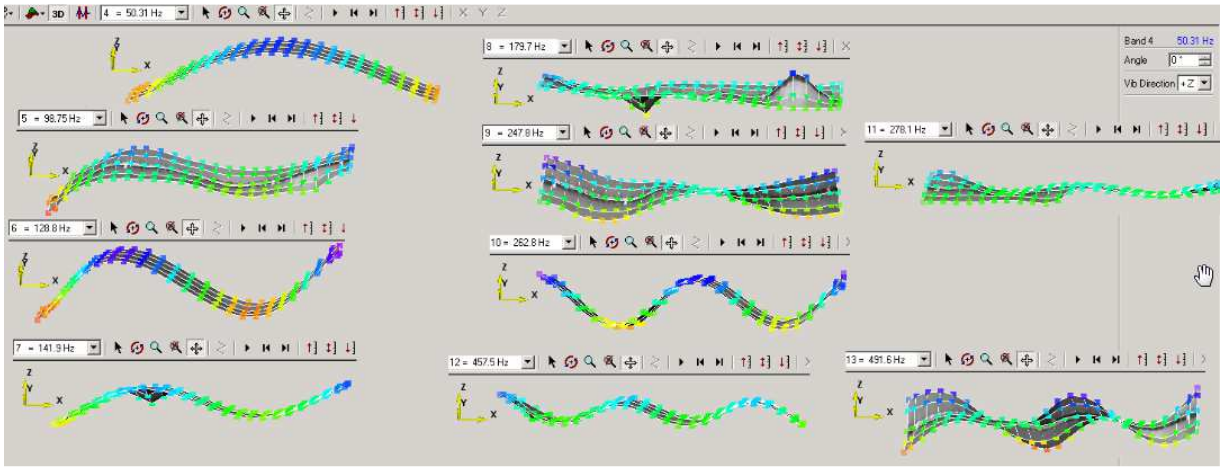

Figure H.3: Mode shapes of 1X19 cabled beam as obtained from dense scan by laser vibrometer.

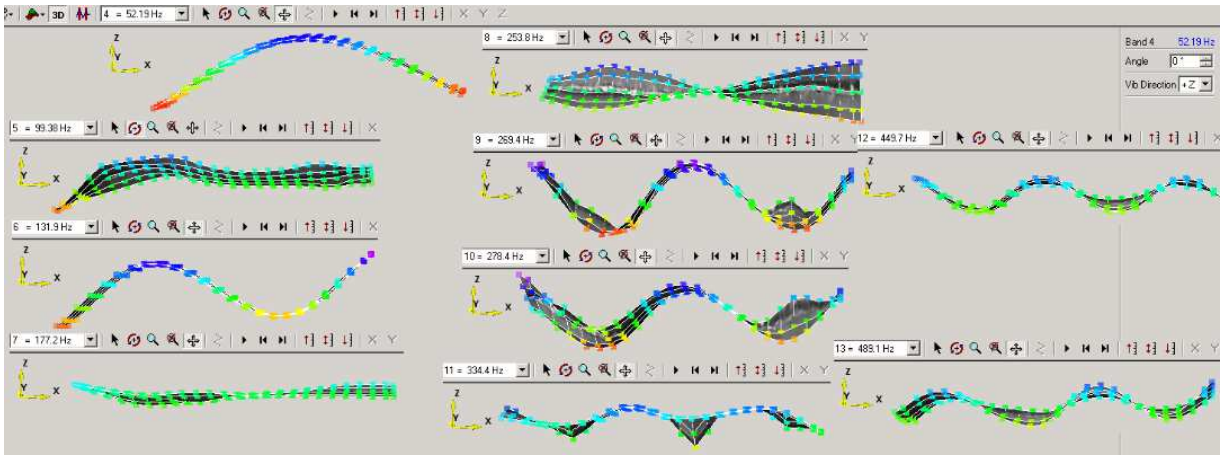

Figure H.4: Mode shapes of 1X48 cabled beam as obtained from dense scan by laser vibrometer.

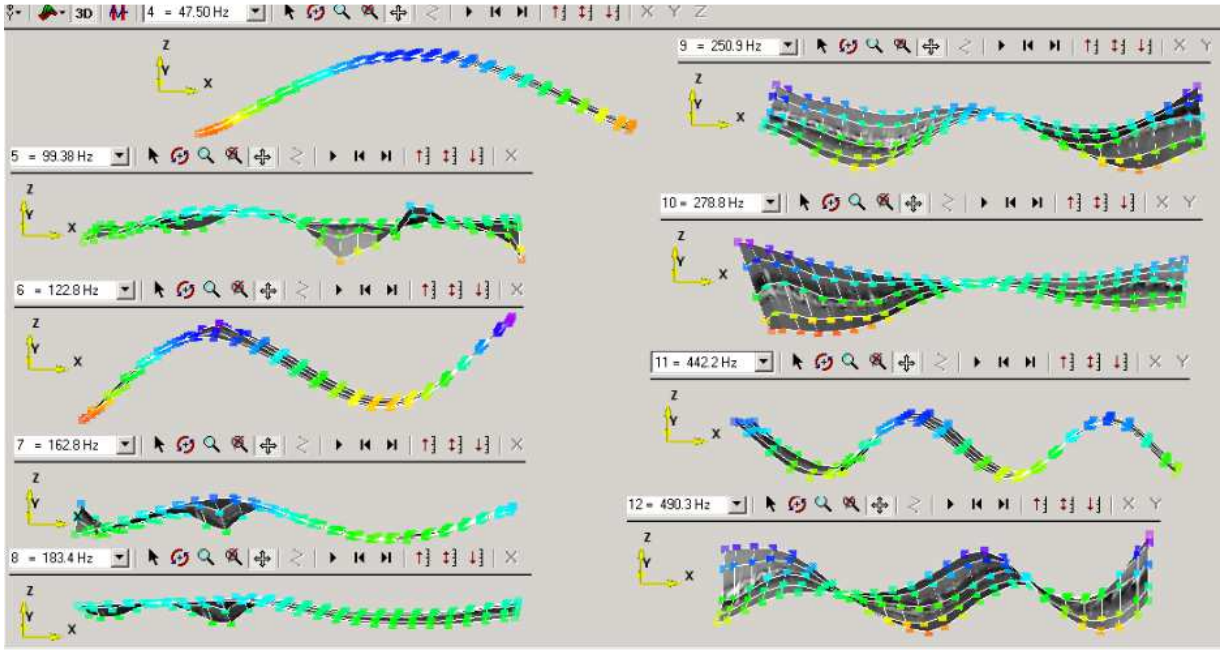

Figure H.5: Mode shapes of 7X7 cabled beam as obtained from dense scan by laser vibrometer.

Appendix I. Comparison of Minimum and Maximum Cabled Beam Models with All Experimental Trials

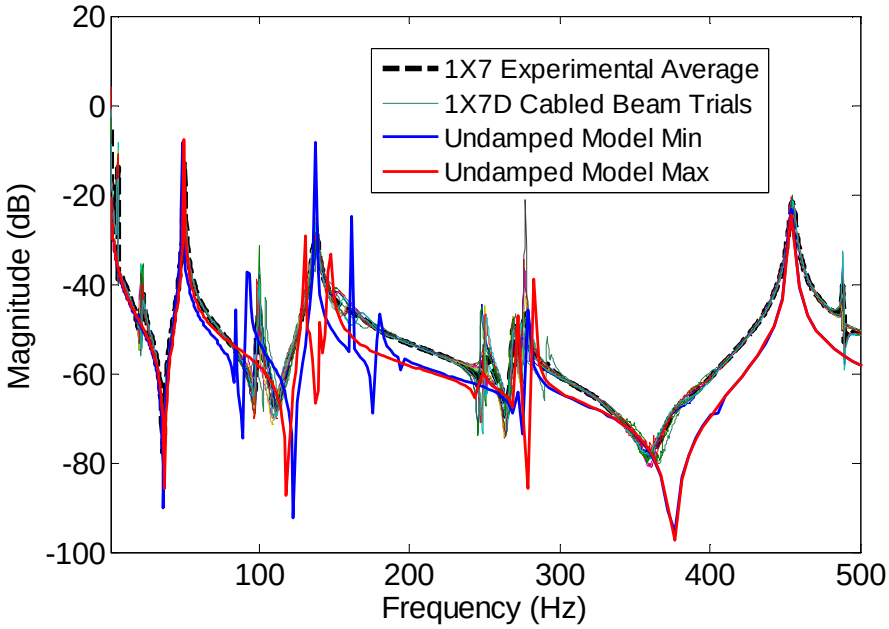

Figure I.1: Undamped DTFM cabled beam model maximum and minimum transfer function results compared to experimental trials for 1X7 cabled beam.

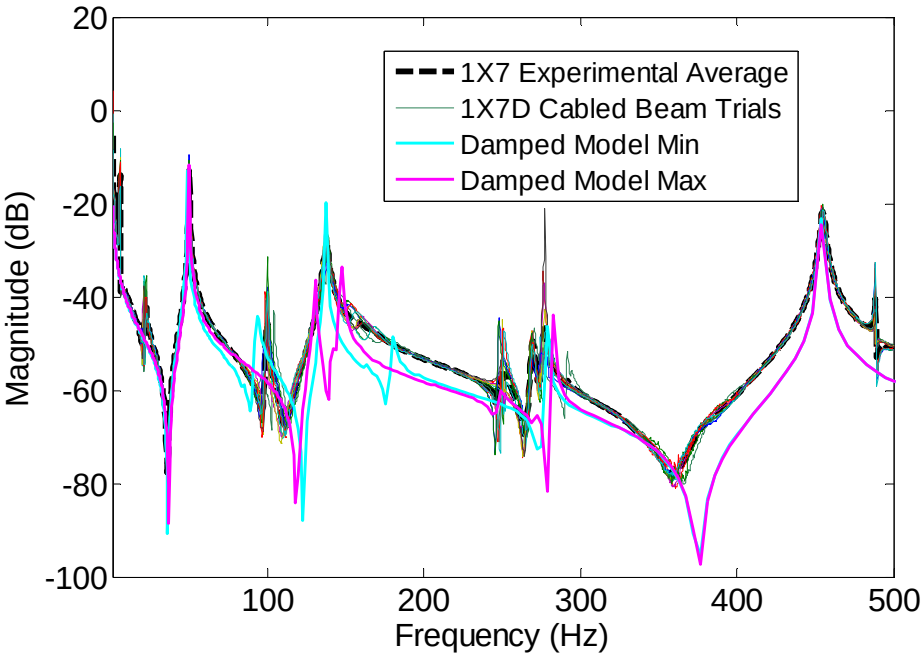

Figure I.2: Damped DTFM cabled beam model maximum and minimum transfer function results compared to experimental trials for 1X7 cabled beam.

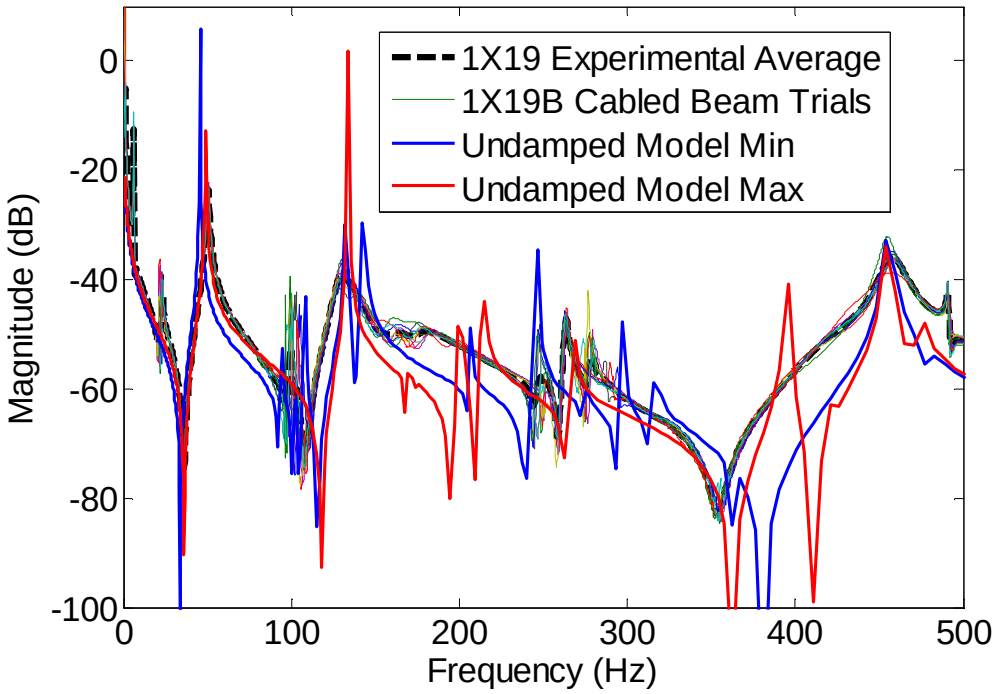

Figure I.3: Undamped DTFM cabled beam model maximum and minimum transfer function results compared to experimental trials for 1X19 cabled beam.

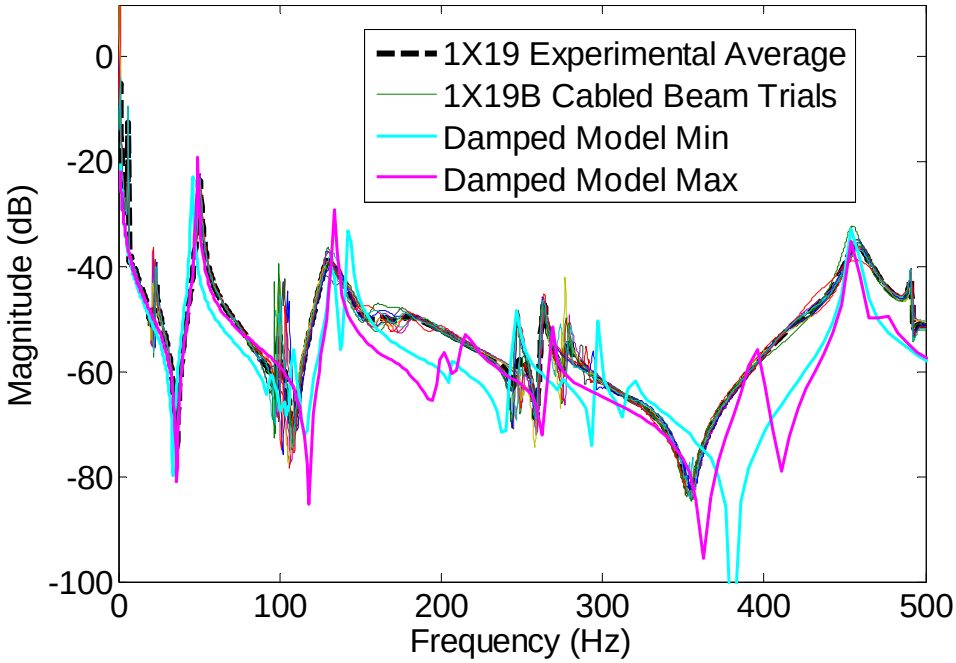

Figure I.4: Damped DTFM cabled beam model maximum and minimum transfer function results compared to experimental trials for 1X19 cabled beam.

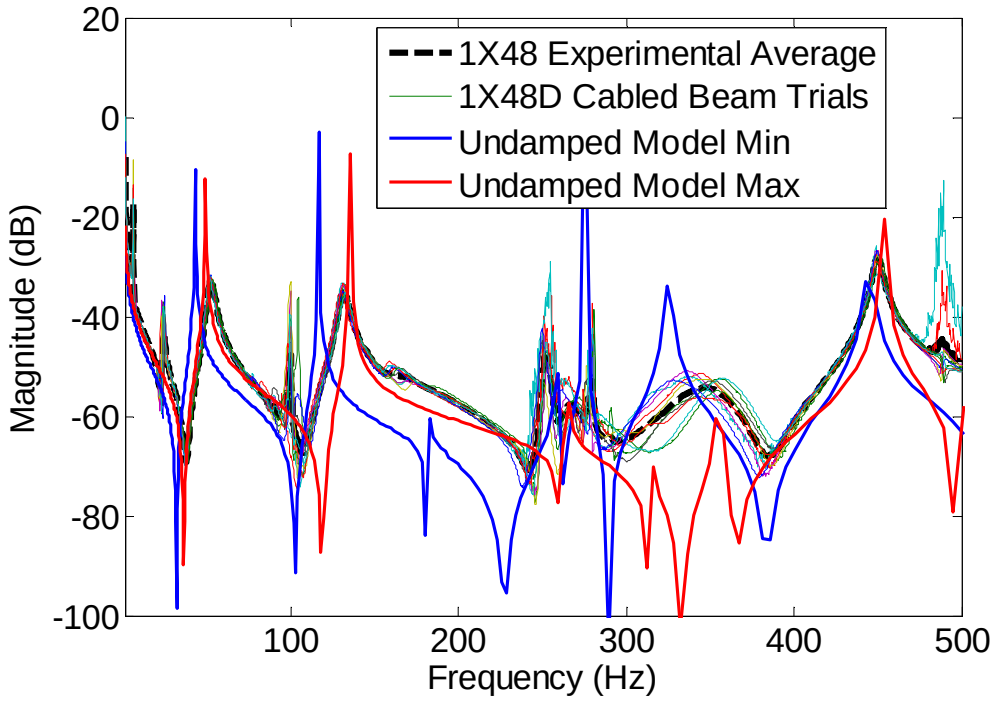

Figure I.5: Undamped DTFM cabled beam model maximum and minimum transfer function results compared to experimental trials for 1X48 cabled beam.

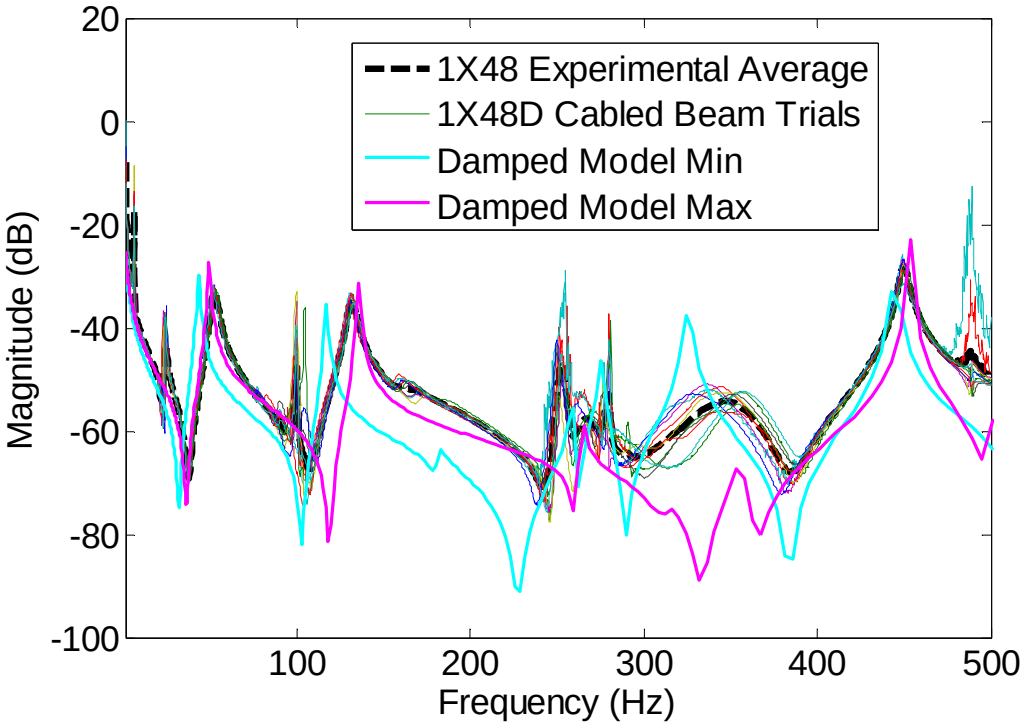

Figure I.6: Damped DTFM cabled beam model maximum and minimum transfer function results compared to experimental trials for 1X48 cabled beam.

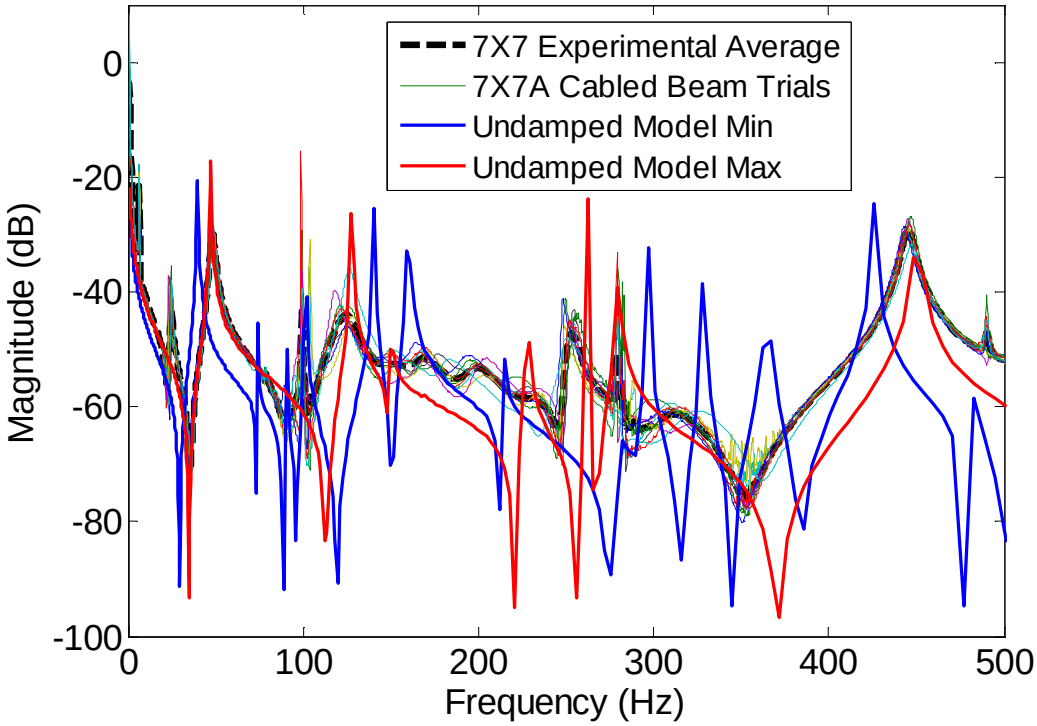

Figure I.7: Undamped DTFM cabled beam model maximum and minimum transfer function results compared to experimental trials for 7X7 cabled beam.

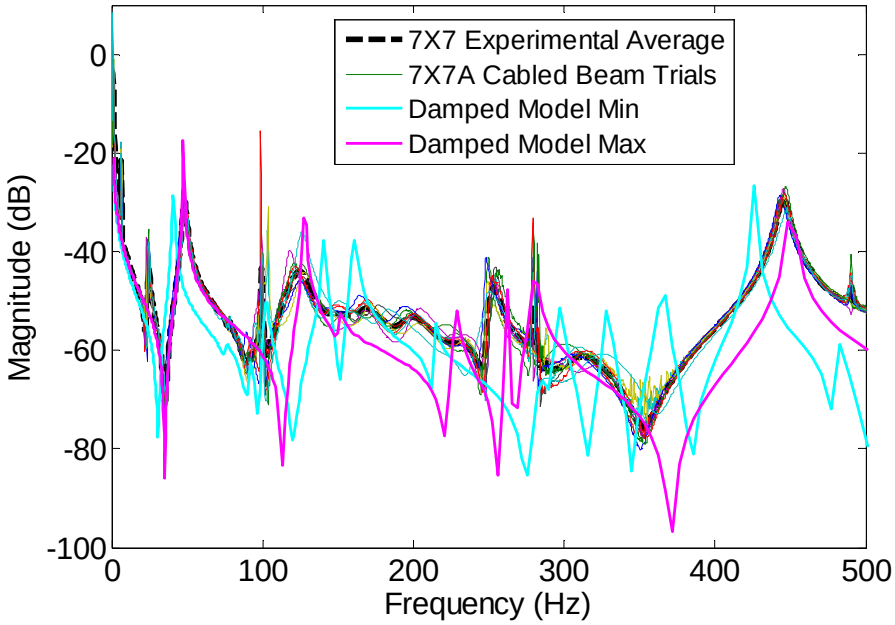

Figure I.8: Damped DTFM cabled beam model maximum and minimum transfer function results compared to experimental trials for 7X7 cabled beam.